

2009-01-20

# Real-Time Adaptive Noise Cancellation in Pulse Oximetry: Accuracy, Processing Speed and Program Memory Considerations

Piyush R. Ramuka  
*Worcester Polytechnic Institute*

Follow this and additional works at: <https://digitalcommons.wpi.edu/etd-theses>

---

## Repository Citation

Ramuka, Piyush R., "Real-Time Adaptive Noise Cancellation in Pulse Oximetry: Accuracy, Processing Speed and Program Memory Considerations" (2009). *Masters Theses (All Theses, All Years)*. 116.  
<https://digitalcommons.wpi.edu/etd-theses/116>

This thesis is brought to you for free and open access by Digital WPI. It has been accepted for inclusion in Masters Theses (All Theses, All Years) by an authorized administrator of Digital WPI. For more information, please contact [wpi-etd@wpi.edu](mailto:wpi-etd@wpi.edu).

**Real-Time Adaptive Noise Cancellation in Pulse Oximetry:  
Accuracy, Processing Speed and Program Memory Considerations**

**A Thesis**

**Submitted to the Faculty of**

**WORCESTER POLYTECHNIC INSTITUTE**

**in partial fulfillment of the requirements for the**

**Degree of Master of Science**

**By**



---

Piyush R. Ramuka  
December 17<sup>th</sup>, 2008



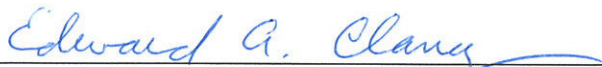
---

**Professor Yitzhak Mendelson, Major Advisor**  
Department of Biomedical Engineering



---

**Professor R. James Duckworth, Committee Member**  
Department of Electrical and Computer Engineering



---

**Professor Edward (Ted) A. Clancy, Committee Member**  
Department of Electrical and Computer Engineering

## ABSTRACT

A wireless, battery operated pulse oximeter system with a forehead mounted optical sensor was designed in our laboratory. This wireless pulse oximeter (WPO) would enable field medics to monitor arterial oxygen saturation ( $SpO_2$ ) and heart rate (HR) information accurately following injuries, thereby help to prioritize life saving medical interventions when resources are limited. Pulse oximeters developed for field-based applications must be resistant to motion artifacts since motion artifacts degrade the signal quality of the photoplethysmographic (PPG) signals from which measurements are derived. This study was undertaken to investigate if accelerometer-based adaptive noise cancellation (ANC) can be used to reduce  $SpO_2$  and HR errors induced by motion artifacts typically encountered during field applications. Preliminary studies conducted offline showed that ANC can minimize  $SpO_2$  and HR errors during jogging, running, and staircase climbing. An 8<sup>th</sup> order LMS filter with  $\mu = 0.01$  was successfully implemented in the WPO's embedded microcontroller. After real-time adaptive filtering of motion corrupted PPG signals, errors for HR values ranging between 60 – 180BPM were reduced from 12BPM to 6BPM. Similarly, ambient breathing  $SpO_2$  errors were reduced from 5% to 2%.

## ACKNOWLEDGEMENT

I express my gratitude to following people for their contribution and support in my research:

My Advisor, Dr. Yitzhak Mendelson, for his expertise, guidance and patience over past two years.

My thesis committee, Dr. R James Duckworth and Dr. Edward Clancy, for their unique perspective and valuable suggestions.

Gary Comtois for helping me transition into the pulse oximeter project.

My Mom and Dad for their encouragement and unwavering support when it was most needed. I dedicate my thesis to my mom. My little sister and brother for their love.

Special thanks to *champu*.

My friends and complete 32-family for believing in me and helping me enjoy my life.

This work was supported by the U.S. Army Medical Research and Material Command under Contract No. W81XWH-07-2-0106. The views, opinions and/or findings are those of the author and should not be construed as an official Department of the Army position, policy or decision unless so designated by other documentation.

## TABLE OF CONTENT

<b>ABSTRACT</b> .....	<b>II</b>
<b>ACKNOWLEDGEMENT</b> .....	<b>III</b>
<b>TABLE OF CONTENT</b> .....	<b>IV</b>
<b>LIST OF FIGURES</b> .....	<b>VII</b>
<b>LIST OF TABLES</b> .....	<b>XVI</b>
<b>GLOSSARY OF ABBREVIATIONS</b> .....	<b>XVIII</b>
<b>1. INTRODUCTION</b> .....	<b>1</b>
<b>2. BACKGROUND</b> .....	<b>4</b>
2.1. PHOTOPLETHYSMOGRAPHY (PPG).....	4
2.2. OPERATING MODES AND MEASUREMENT SITES.....	6
2.3. NONINVASIVE ARTERIAL OXYGEN SATURATION (SPO <sub>2</sub> ) MEASUREMENT.....	7
2.3.1. Significance.....	7
2.3.2. Measurement Theory.....	8
2.4. HEART RATE (HR).....	9
2.4.1. Significance.....	9
2.4.2. Measurement Theory.....	9
2.5. LIMITATIONS TO PULSE OXIMETER.....	9
<b>3. MOTION ARTIFACT</b> .....	<b>11</b>
3.1. EFFECTS OF MOTION ARTIFACTS.....	11
3.2. REDUCING THE EFFECTS OF MOTION ARTIFACTS.....	17
<b>4. ADAPTIVE NOISE CANCELLATION</b> .....	<b>19</b>
4.1. BACKGROUND.....	19
4.2. PRINCIPLE OF ANC.....	19
4.3. DIFFERENT TYPES OF ANC.....	20
<b>5. SIGNAL PROCESSING ALGORITHMS</b> .....	<b>26</b>
<b>6. RESEARCH OBJECTIVES</b> .....	<b>33</b>
<b>7. EXPERIMENTAL SETUP</b> .....	<b>34</b>
7.1. RESTING EXPERIMENTS.....	34
7.2. SITTING EXPERIMENTS.....	37
7.3. CYCLING EXPERIMENTS.....	38
7.4. TREADMILL JOGGING, OUTDOOR RUNNING AND STAIRCASE CLIMBING EXPERIMENTS.....	40
7.5. REAL-TIME ANC.....	41
<b>8. RESULTS</b> .....	<b>43</b>
8.1. RESTING EXPERIMENTS.....	43
8.2. LMS ALGORITHM.....	47
8.2.1. Step-size ( $\mu$ ) selection.....	47

8.2.2. Filter Order (M) selection.....	49
8.2.3. LMS – Sitting Experiments.....	51
8.2.4. LMS – Cycling Experiments.....	61
8.2.5. LMS – Treadmill Jogging Experiments.....	70
8.2.6. LMS – Outdoor Running Experiments.....	81
8.2.7. LMS – Staircase Climbing Experiments.....	83
8.3. CONVENTIONAL LMS RESULTS SUMMARY.....	92
8.4. TV-LMS.....	92
8.4.1. Step-Size Selection.....	92
8.4.2. Results of TV-LMS filter.....	94
8.5. NLMS AND MNLMS.....	94
8.5.1. Step-Size and Filter Order Selection.....	94
8.5.2. Results of NLMS and MNLMS filter.....	97
8.6. RLS ALGORITHM.....	98
8.6.1. Forgetting factor and Filter Order Selection.....	98
8.6.2. Results of RLS filter.....	99
8.7. COMPARATIVE STUDY OF DIFFERENT ANC ALGORITHMS.....	100
8.8. ACCELEROMETER AXIS SELECTION.....	101
8.9. VALIDATION OF REAL-TIME ANC.....	102
8.10. ANC PROCESSING TIME.....	103
8.11. AUTO-TRIGGERING OF ANC.....	104
8.12. REAL-TIME ANC RESULTS.....	106
8.13. LIMITATION OF ANC.....	109
<b>9. DISCUSSION.....</b>	<b>113</b>
9.1. RESTING EXPERIMENTS.....	113
9.1.1. Systolic versus diastolic peak detection.....	114
9.2. LMS ALGORITHM.....	116
9.2.1. Step-size ( $\mu$ ) selection.....	116
9.2.2. Filter Order (M) selection.....	116
9.2.3. LMS – Sitting Experiments.....	117
9.2.4. LMS – Cycling Experiments.....	119
9.2.5. LMS – Treadmill Jogging Experiments.....	120
9.2.6. LMS – Outdoor Running Experiments.....	122
9.2.7. LMS – Staircase Climbing Experiments.....	123
9.3. TV-LMS.....	124
9.3.1. Step-Size Selection.....	124
9.3.2. Results of TV-LMS filter.....	124
9.4. NLMS AND MNLMS.....	125
9.4.1. Step-Size and Filter Order Selection.....	125
9.4.2. NLMS and MNLMS filter results.....	126
9.5. RLS ALGORITHM.....	126
9.5.1. Forgetting factor and filter order selection.....	126
9.5.2. Results of RLS filter.....	127
9.6. COMPARATIVE STUDY OF DIFFERENT ANC ALGORITHMS.....	127
9.7. ACCELEROMETER AXIS SELECTION.....	128
9.8. VALIDATION OF REAL-TIME ANC ALGORITHM.....	129
9.9. ANC PROCESSING TIME.....	129
9.10. AUTO-TRIGGERING OF ANC.....	129
9.11. REAL-TIME ANC RESULTS.....	130
9.12. LIMITATION OF ANC.....	131

<b>10. CONCLUSION .....</b>	<b>133</b>
<b>11. FUTURE RECOMMENDATIONS .....</b>	<b>136</b>
<b>12. REFERENCES.....</b>	<b>139</b>

## LIST OF FIGURES

FIGURE 1.1: WIRELESS PULSE OXIMETER (WPO) DESIGNED IN OUR LABORATORY.....	2
FIGURE 2.1: OPTICAL ABSORBANCE SPECTRA OF $\text{HbO}_2$ AND $\text{Hb}$ [12]. .....	4
FIGURE 2.2: VARIATIONS IN LIGHT ATTENUATION BY TISSUE, ILLUSTRATING THE PPG SIGNAL GENERATION [13].....	5
FIGURE 2.3: TYPICAL PPG SIGNAL ACQUIRED DURING REST.....	6
FIGURE 2.4: OPERATING MODES OF A PULSE OXIMETER.....	6
FIGURE 2.5: EMPIRICAL RELATIONSHIP BETWEEN $\text{SAO}_2$ AND THE NORMALIZED R/IR RATIO [10]. .....	8
FIGURE 3.1: IR PPG SIGNAL DURING REST.....	12
FIGURE 3.2: IR PPG SIGNAL AFFECTED BY MOTION ARTIFACT. ● PPG PEAKS DETECTED BY THE WPO (9-PEAKS), AND ● R-WAVES DETECTED FROM THE ECG WAVEFORM (9-PEAKS).....	13
FIGURE 3.3: EFFECT OF MOTION ARTIFACTS ON HR MEASUREMENTS. ....	14
FIGURE 3.4: EFFECTS OF MOTION ARTIFACTS ON $\text{SpO}_2$ MEASUREMENTS.....	15
FIGURE 3.5: FREQUENCY SPECTRUM OF IR PPG AND REFERENCE ACC SIGNALS ACQUIRED DURING MOTION. ....	16
FIGURE 3.6: FREQUENCY SPECTRUM OF R PPG AND REFERENCE ACC SIGNALS ACQUIRED DURING MOTION. ....	16
FIGURE 4.1: THE ADAPTIVE NOISE CANCELLATION CONCEPT [21].....	20
FIGURE 5.1: PPG SIGNAL PROCESSING FLOWCHART.....	26
FIGURE 5.2: DIGITAL FILTERING FLOW CHART.....	27
FIGURE 5.3: PROPOSED ANC-TRIGGERED ALGORITHM.....	28
FIGURE 5.4: HR AND $\text{SpO}_2$ ESTIMATION ALGORITHM.....	30



FIGURE 7.1: EXPERIMENTAL SETUP FOR INITIAL BENCH TESTING OF THE WPO. ....	35
FIGURE 7.2: EXPERIMENTAL SETUP FOR DATA ACQUISITION .....	36
FIGURE 7.3: EXPERIMENTAL SETUP FOR DATA COLLECTION (SITTING POSITION).....	37
FIGURE 7.4: EXPERIMENTAL SETUP FOR CYCLING EXPERIMENTS. ....	39
FIGURE 7.5: EXPERIMENTAL SETUP FOR DATA COLLECTION DURING TREADMILL JOGGING.....	40
FIGURE 7.6: EXPERIMENTAL SETUP FOR DATA COLLECTION WHILE TESTING REAL-TIME ADAPTIVE FILTERING. ....	42
FIGURE 8.1: TYPICAL HR MEASURED SIMULTANEOUSLY FROM THE WPO (BLUE) AND MPO (GREEN) DURING A RESTING EXPERIMENT.....	43
FIGURE 8.2: TYPICAL HR MEASURED SIMULTANEOUSLY FROM THE WPO (BLUE) AND MPO (GREEN) DURING A RESTING EXPERIMENT. THE HIGHLIGHTED REGION MARKS THE PERIOD OF HYPERVENTILATION THAT RESULTED IN INCREASE IN HR VALUES.....	44
FIGURE 8.3: TYPICAL SPO <sub>2</sub> MEASURED SIMULTANEOUSLY FROM THE WPO (BLUE) AND MPO (GREEN) DURING A RESTING EXPERIMENT. THE HIGHLIGHTED REGION MARKS THE BREATH HOLDING EPISODES TO INDUCE HYPOXIA.....	44
FIGURE 8.4: COMPARISON OF HR VALUES MEASURED BY THE WPO AND MPO DURING REST. THE COLOR CHART ON THE RIGHT REPRESENTS THE FREQUENCY OF DATA POINTS.....	45
FIGURE 8.5: DIFFERENCE BETWEEN HR READINGS FROM THE WPO AND MPO PLOTTED AGAINST MPO VALUES. THE RED LINES INDICATE $M \pm 2SD$ VALUES. ....	46
FIGURE 8.6: DIFFERENCE BETWEEN SPO <sub>2</sub> READINGS FROM THE WPO AND MPO PLOTTED AGAINST MPO VALUES. THE RED LINES INDICATE $M \pm 2SD$ VALUES. ....	46
FIGURE 8.7: AVERAGE MSE IMPROVEMENT IN HR FOR A 16 <sup>ND</sup> ORDER LMS FILTER WITH VARYING STEP-SIZE (M). THE ERROR BARS INDICATE $\pm 1SD$ . THE SHADED REGION CORRESPONDS TO M VALUE THAT WAS SELECTED FOR FURTHER STUDY. ....	48
FIGURE 8.8: AVERAGE MSE IMPROVEMENT IN SPO <sub>2</sub> FOR A 16 <sup>ND</sup> ORDER LMS FILTER WITH VARYING STEP-SIZE (M). THE ERROR BARS INDICATE $\pm 1SD$ . THE SHADED REGION CORRESPONDS TO M VALUE THAT WAS SELECTED FOR FURTHER STUDY. ....	49
FIGURE 8.9: AVERAGE MSE IMPROVEMENT IN HR FOR A LMS FILTER WITH A $M = 0.01$ AND VARYING FILTER ORDER (M). THE ERROR BARS INDICATE $\pm 1SD$ . THE SHADED REGION CORRESPONDS TO M THAT WAS SELECTED FOR FURTHER STUDY. ....	50

FIGURE 8.10: AVERAGE MSE IMPROVEMENT IN $SpO_2$ FOR A LMS FILTER WITH A $\mu = 0.01$ AND VARYING FILTER ORDER ( $M$ ). THE ERROR BARS INDICATE $\pm 1SD$ . THE SHADED REGION CORRESPONDS TO $M$ THAT WAS SELECTED FOR FURTHER STUDY. ....	50
FIGURE 8.11: TYPICAL IR PPG SIGNALS DURING REST (PHASE-1 OF SITTING EXPERIMENT), BEFORE (BLUE) AND AFTER (RED) ANC. NOTE THAT THE BLUE AND RED TRACES COMPLETELY OVERLAP IN THIS FIGURE. ■ MARKS PPG PEAKS DETECTED BY THE WPO AFTER ANC (6-PEAKS) AND ● DENOTES R-WAVES DETECTED FROM THE ECG WAVEFORM (6-PEAKS). ....	51
FIGURE 8.12: TYPICAL IR PPG SIGNALS DURING PHASE-2 OF SITTING EXPERIMENT, BEFORE (BLUE) AND AFTER (RED) ANC. THE ARROWS INDICATE THE ADDITIONAL PEAKS THAT WERE DETECTED ONLY AFTER ADAPTIVE FILTERING. ■ MARKS PPG PEAKS DETECTED BY THE WPO AFTER ANC (9-PEAKS), ● DENOTES PPG PEAKS DETECTED WITHOUT ANC (7-PEAKS), AND ● REPRESENTS R-WAVES DETECTED FROM THE ECG WAVEFORM (9-PEAKS). ....	52
FIGURE 8.13: TYPICAL IR PPG SIGNALS DURING REST (PHASE-3 OF SITTING EXPERIMENT), BEFORE (BLUE) AND AFTER (RED) ANC. NOTE THAT THE BLUE AND RED TRACES COMPLETELY OVERLAP IN THIS FIGURE. ■ PPG MARKS PEAKS DETECTED BY THE WPO AFTER ANC (4-PEAKS), AND ● REPRESENTS R-WAVES DETECTED FROM THE ECG WAVEFORM (4-PEAKS). ....	52
FIGURE 8.14: CHARACTERISTIC FREQUENCY SPECTRUM OF AN IR PPG SIGNAL DURING A SITTING EXPERIMENT. ....	54
FIGURE 8.15: CHARACTERISTIC FREQUENCY SPECTRUM OF AN R PPG SIGNAL DURING A SITTING EXPERIMENT. ....	54
FIGURE 8.16: HR MEASUREMENTS WITHOUT AND WITH ANC DURING A SITTING EXPERIMENT. THE GREEN HIGHLIGHTED REGION SHOWS THE IMPROVEMENT IN HR ESTIMATION AFTER ANC. ....	55
FIGURE 8.17: $SpO_2$ VALUES WITHOUT AND WITH ANC DURING A SITTING EXPERIMENT. ....	56
FIGURE 8.18: COMPARISON OF HR MEASURED BY THE WPO AND AN ECG AS A REFERENCE SOURCE, BEFORE ANC (SITTING EXPERIMENT). ....	57
FIGURE 8.19: COMPARISON OF HR MEASURED BY THE WPO AND AN ECG REFERENCE SOURCE AFTER ANC (SITTING EXPERIMENT). ....	57
FIGURE 8.20: DIFFERENCE IN HR READINGS MEASURED BY THE WPO AND THE ECG HOLTER MONITOR WITHOUT ANC (SITTING EXPERIMENT). THE RED LINES INDICATE THE $M \pm 2SD$ VALUES. ....	58

FIGURE 8.21: DIFFERENCE IN HR READINGS MEASURED BY THE WPO AND THE ECG HOLTER MONITOR WITH ANC (SITTING EXPERIMENT). THE RED LINES INDICATE THE $M \pm 2SD$ VALUES. ....	58
FIGURE 8.22: DIFFERENCE BETWEEN $SpO_2$ READINGS ACQUIRED FROM WPO AND MPO PLOTTED AGAINST MPO VALUES WITHOUT ANC (SITTING EXPERIMENT). THE RED LINES INDICATE THE $M \pm 2SD$ VALUES. ....	59
FIGURE 8.23: DIFFERENCE BETWEEN $SpO_2$ READINGS ACQUIRED FROM WPO AND MPO PLOTTED AGAINST MPO VALUES WITH ANC (SITTING EXPERIMENT). THE RED LINES INDICATE THE $M \pm 2SD$ VALUES. ....	59
FIGURE 8.24: TYPICAL IR PPG SIGNALS DURING PHASE-1 OF CYCLING EXPERIMENT, BEFORE (BLUE) AND AFTER (RED) ANC. NOTE THAT THE BLUE AND RED TRACES COMPLETELY OVERLAP IN THIS FIGURE. ■ MARKS PPG PEAKS DETECTED BY THE WPO AFTER ANC (5-PEAKS), AND ● REPRESENTS R-WAVES DETECTED FROM THE ECG WAVEFORM (5-PEAKS). ....	61
FIGURE 8.25: TYPICAL IR PPG SIGNALS DURING PHASE-2 OF CYCLING EXPERIMENT, BEFORE (BLUE) AND AFTER (RED) ANC. NOTE THAT THE BLUE AND RED TRACES OVERLAP IN THIS FIGURE. ■ MARKS PPG PEAKS DETECTED BY THE WPO AFTER ANC (9-PEAKS), ● DENOTES PPG PEAKS DETECTED WITHOUT ANC (9-PEAKS), AND ● REPRESENTS R-WAVES DETECTED FROM THE ECG WAVEFORM (9-PEAKS). ....	62
FIGURE 8.26: TYPICAL IR PPG SIGNALS DURING PHASE-3 OF CYCLING EXPERIMENT, BEFORE (BLUE) AND AFTER (RED) ANC. NOTE THAT THE BLUE AND RED TRACES OVERLAP IN THIS FIGURE. ■ MARKS PPG PEAKS DETECTED BY THE WPO AFTER ANC (6-PEAKS), AND ● REPRESENTS R-WAVES DETECTED FROM THE ECG WAVEFORM (6-PEAKS). ....	62
FIGURE 8.27: TYPICAL FREQUENCY SPECTRUM OF AN IR PPG OBTAINED DURING CYCLING. NOTE THAT THE RED AND BLUE TRACES OVERLAP COMPLETELY. ....	63
FIGURE 8.28: TYPICAL FREQUENCY SPECTRUM OF AN R PPG OBTAINED DURING CYCLING. NOTE THAT THE RED AND BLUE TRACES OVERLAP COMPLETELY. ....	64
FIGURE 8.29: HR MEASUREMENTS WITHOUT AND WITH ANC DURING CYCLING. NOTE THAT THE RED AND BLUE TRACES OVERLAP COMPLETELY. ....	65
FIGURE 8.30: $SpO_2$ MEASUREMENTS WITHOUT AND WITH ANC DURING CYCLING. NOTE THAT THE RED AND BLUE TRACES OVERLAP COMPLETELY. ....	65
FIGURE 8.31: COMPARISON OF HR MEASURED BY THE WPO AND REFERENCE SOURCE DURING CYCLING BEFORE ANC. ....	66

FIGURE 8.32: COMPARISON OF HR MEASURED BY THE WPO AND REFERENCE SOURCE DURING CYCLING AFTER ANC.....	66
FIGURE 8.33: DIFFERENCE IN HR READINGS MEASURED BY THE WPO AND ECG HOLTER MONITOR DURING CYCLING WITHOUT ANC. THE RED LINES INDICATE THE $M \pm 2SD$ VALUES.....	67
FIGURE 8.34: DIFFERENCE IN HR READINGS MEASURED BY THE WPO AND ECG HOLTER MONITOR DURING CYCLING WITH ANC. THE RED LINES INDICATE THE $M \pm 2SD$ VALUES.....	67
FIGURE 8.35: DIFFERENCE IN $SpO_2$ MEASURED BY THE WPO AND MPO DURING CYCLING WITHOUT ANC. THE RED LINES INDICATE THE $M \pm 2SD$ VALUES. ....	68
FIGURE 8.36: DIFFERENCE IN $SpO_2$ MEASURED BY THE WPO AND MPO DURING CYCLING WITH ANC. THE RED LINES INDICATE THE $M \pm 2SD$ VALUES.....	68
FIGURE 8.37: HR READINGS FOR TRIAL#6. ....	70
FIGURE 8.38: TYPICAL IR PPG SIGNALS DURING PHASE-1 OF TREADMILL JOGGING EXPERIMENT, BEFORE (BLUE) AND AFTER (RED) ANC. NOTE THAT THE BLUE AND RED TRACES COMPLETELY OVERLAP IN THIS FIGURE. ■ MARKS PPG PEAKS DETECTED BY THE WPO AFTER ANC (5-PEAKS), AND ● REPRESENTS R-WAVES DETECTED FROM THE ECG WAVEFORM (5-PEAKS). ....	71
FIGURE 8.39: TYPICAL IR PPG SIGNALS DURING PHASE-2 OF TREADMILL JOGGING EXPERIMENT, BEFORE (BLUE) AND AFTER (RED) ANC. NOTE THAT THE BLUE AND RED TRACES COMPLETELY OVERLAP IN THIS FIGURE. ■ MARKS PPG PEAKS DETECTED BY THE WPO AFTER ANC (8-PEAKS), ● DENOTES PPG PEAKS DETECTED WITHOUT ANC (8-PEAKS), AND ● REPRESENTS R-WAVES DETECTED FROM THE ECG WAVEFORM (8-PEAKS). ....	72
FIGURE 8.40: TYPICAL IR PPG SIGNALS DURING PHASE-3 OF TREADMILL JOGGING EXPERIMENT, BEFORE (BLUE) AND AFTER (RED) ANC. ■ MARKS PPG PEAKS DETECTED BY THE WPO AFTER ANC (9-PEAKS), ● DENOTES PPG PEAKS DETECTED WITHOUT ANC (9-PEAKS), AND ● REPRESENTS R-WAVES DETECTED FROM THE ECG WAVEFORM (9-PEAKS). ....	72
FIGURE 8.41: TYPICAL IR PPG SIGNALS DURING PHASE-4 OF TREADMILL JOGGING EXPERIMENT, BEFORE (BLUE) AND AFTER (RED) ANC. NOTE THAT THE BLUE AND RED TRACES OVERLAP. ■ MARKS PPG PEAKS DETECTED BY THE WPO AFTER ANC (9-PEAKS), ● DENOTES PPG PEAKS DETECTED WITHOUT ANC (9-PEAKS), AND ● REPRESENTS R-WAVES DETECTED FROM THE ECG WAVEFORM (9-PEAKS). ....	73

FIGURE 8.42: TYPICAL IR PPG SIGNALS DURING PHASE-5 OF TREADMILL JOGGING EXPERIMENT, BEFORE (BLUE) AND AFTER (RED) ANC. NOTE THAT THE BLUE AND RED TRACES COMPLETELY OVERLAP IN THIS FIGURE. ■ MARKS PPG PEAKS DETECTED BY THE WPO AFTER ANC (6-PEAKS), AND ● REPRESENTS R-WAVES DETECTED FROM THE ECG WAVEFORM (6-PEAKS). .....	73
FIGURE 8.43: FREQUENCY SPECTRUM OF IR PPG DURING TREADMILL JOGGING.....	74
FIGURE 8.44: FREQUENCY SPECTRUM OF RED PPG DURING TREADMILL JOGGING.....	75
FIGURE 8.45: HR MEASUREMENTS DURING TREADMILL JOGGING WITHOUT AND WITH ANC. ....	76
FIGURE 8.46: SpO <sub>2</sub> VALUES DURING TREADMILL JOGGING WITHOUT AND WITH ANC. ....	76
FIGURE 8.47: COMPARISON OF HR MEASURED DURING TREADMILL JOGGING BY THE WPO AND REFERENCE SOURCE BEFORE ANC.....	77
FIGURE 8.48: COMPARISON OF HR MEASURED DURING TREADMILL JOGGING BY THE WPO AND REFERENCE SOURCE AFTER ANC.....	78
FIGURE 8.49: DIFFERENCE IN HR READINGS MEASURED BY THE WPO AND THE ECG HOLTER MONITOR WITHOUT ANC (TREADMILL JOGGING). THE RED LINES INDICATE THE $M \pm 2SD$ VALUES. ....	78
FIGURE 8.50: DIFFERENCE IN HR READINGS MEASURED BY THE WPO AND THE ECG HOLTER MONITOR WITH ANC (TREADMILL JOGGING). THE RED LINES INDICATE THE $M \pm 2SD$ VALUES. ....	79
FIGURE 8.51: DIFFERENCE IN SpO <sub>2</sub> READINGS MEASURED BY THE WPO AND MPO WITHOUT ANC (TREADMILL JOGGING). THE RED LINES INDICATE THE $M \pm 2SD$ VALUES.....	79
FIGURE 8.52: DIFFERENCE IN SpO <sub>2</sub> READINGS MEASURED BY THE WPO AND MPO WITH ANC (TREADMILL JOGGING). THE RED LINES INDICATE THE $M \pm 2SD$ VALUES. ....	80
FIGURE 8.53: HR READINGS FOR TRIAL#2 DURING OUTDOOR RUNNING.....	82
FIGURE 8.54: SpO <sub>2</sub> READINGS FOR TRIAL#2 DURING OUTDOOR RUNNING.....	82
FIGURE 8.55: TYPICAL IR PPG SIGNALS DURING PHASE-1 OF STAIRCASE CLIMBING, BEFORE (BLUE) AND AFTER (RED) ANC. NOTE THAT THE BLUE AND RED TRACES OVERLAP IN THIS FIGURE. ■ MARKS PPG PEAKS DETECTED BY THE WPO AFTER ANC (5-PEAKS), AND ● REPRESENTS R-WAVES DETECTED FROM THE ECG WAVEFORM (5-PEAKS).....	83

FIGURE 8.56: TYPICAL IR PPG SIGNALS DURING PHASE-2 OF STAIRCASE CLIMBING EXPERIMENT, BEFORE (BLUE) AND AFTER (RED) ANC. ■ MARKS PPG PEAKS DETECTED BY THE WPO AFTER ANC, ● DENOTES PPG PEAKS DETECTED WITHOUT ANC, AND ● REPRESENTS R-WAVES DETECTED FROM THE ECG WAVEFORM.....	84
FIGURE 8.57: TYPICAL IR PPG SIGNALS DURING PHASE-2 OF STAIRCASE CLIMBING EXPERIMENT, BEFORE (BLUE) AND AFTER (RED) ANC. NOTE THAT THE BLUE AND RED TRACES OVERLAP IN THIS FIGURE. ■ MARKS PPG PEAKS DETECTED BY THE WPO AFTER ANC, AND ● REPRESENTS R-WAVES DETECTED FROM THE ECG WAVEFORM.....	84
FIGURE 8.58: FREQUENCY SPECTRUM OF IR PPG DURING STAIRCASE CLIMBING.....	85
FIGURE 8.59: FREQUENCY SPECTRUM OF RED PPG DURING STAIRCASE CLIMBING.....	86
FIGURE 8.60: HR MEASUREMENTS WITHOUT AND WITH ANC DURING A STAIRCASE CLIMBING EXPERIMENT. ....	87
FIGURE 8.61: SpO <sub>2</sub> MEASUREMENTS WITHOUT AND WITH ANC DURING A STAIRCASE CLIMBING EXPERIMENT. ....	87
FIGURE 8.62: COMPARISON OF HR MEASURED DURING STAIRCASE CLIMBING BY THE WPO AND REFERENCE SOURCE BEFORE ANC.....	88
FIGURE 8.63: COMPARISON OF HR MEASURED DURING STAIRCASE CLIMBING BY THE WPO AND REFERENCE SOURCE AFTER ANC.....	89
FIGURE 8.64: DIFFERENCE IN HR READINGS MEASURED BY THE WPO AND THE ECG HOLTER MONITOR WITHOUT ANC (STAIRCASE CLIMBING). THE RED LINES INDICATE THE $M \pm 2SD$ VALUES. ....	89
FIGURE 8.65: DIFFERENCE IN HR READINGS MEASURED BY THE WPO AND THE ECG HOLTER MONITOR WITH ANC (STAIRCASE CLIMBING). THE RED LINES INDICATE THE $M \pm 2SD$ VALUES. ....	90
FIGURE 8.66: DIFFERENCE IN SpO <sub>2</sub> READINGS MEASURED BY THE WPO AND MPO WITHOUT ANC (STAIRCASE CLIMBING). THE RED LINES INDICATE THE $M \pm 2SD$ VALUES.....	90
FIGURE 8.67: DIFFERENCE IN SpO <sub>2</sub> READINGS MEASURED BY THE WPO AND MPO WITH ANC (STAIRCASE CLIMBING). THE RED LINES INDICATE THE $M \pm 2SD$ VALUES.....	91
FIGURE 8.68: AVERAGE MSE IMPROVEMENT IN HR FOR A 16 <sup>ND</sup> ORDER TV-LMS FILTER WITH VARYING STEP-SIZE (M). THE ERROR BARS INDICATE $\pm 1SD$ . THE SHADED REGION CORRESPONDS TO M VALUE THAT WAS SELECTED FOR FURTHER STUDY. ....	93

FIGURE 8.69: AVERAGE MSE IMPROVEMENT IN $SpO_2$ FOR A 16 <sup>ND</sup> ORDER TV-LMS FILTER WITH VARYING STEP-SIZE (M). THE ERROR BARS INDICATE $\pm 1SD$ . THE SHADED REGION CORRESPONDS TO M VALUE THAT WAS SELECTED FOR FURTHER STUDY. ....	94
FIGURE 8.70: AVERAGE MSE IMPROVEMENT IN HR FOR A 16 <sup>ND</sup> ORDER NLMS FILTER WITH VARYING STEP-SIZE (M). THE ERROR BARS INDICATE $\pm 1SD$ . THE SHADED REGION CORRESPONDS TO M VALUE THAT WAS SELECTED FOR FURTHER STUDY. ....	95
FIGURE 8.71: AVERAGE MSE IMPROVEMENT IN $SpO_2$ FOR A 16 <sup>ND</sup> ORDER NLMS FILTER WITH VARYING STEP-SIZE (M). THE ERROR BARS INDICATE $\pm 1SD$ . THE SHADED REGION CORRESPONDS TO M VALUE THAT WAS SELECTED FOR FURTHER STUDY. ....	96
FIGURE 8.72: AVERAGE IMPROVEMENT IN HR MSE FOR A NLMS FILTER WITH A CONSTANT $M = 0.006$ AND VARYING FILTER ORDER (M). THE ERROR BARS INDICATE $\pm 1SD$ . THE SHADED REGION CORRESPONDS TO M VALUE THAT WAS SELECTED FOR FURTHER STUDY. ....	96
FIGURE 8.73: AVERAGE IMPROVEMENT IN $SpO_2$ MSE FOR A NLMS FILTER WITH A CONSTANT $M = 0.006$ AND VARYING FILTER ORDER (M). THE ERROR BARS INDICATE $\pm 1SD$ . THE SHADED REGION CORRESPONDS TO M VALUE THAT WAS SELECTED FOR FURTHER STUDY. ....	97
FIGURE 8.74: AVERAGE MSE IMPROVEMENT IN HR FOR A RLS FILTER WITH $\lambda = 1$ AND VARYING M. THE ERROR BARS INDICATE $\pm 1SD$ . THE SHADED REGION CORRESPONDS TO M VALUE THAT WAS SELECTED FOR DATA ANALYSIS. ....	98
FIGURE 8.75: AVERAGE MSE IMPROVEMENT IN $SpO_2$ FOR A RLS FILTER WITH $\lambda = 1$ AND VARYING M. THE ERROR BARS INDICATE $\pm 1SD$ . THE SHADED REGION CORRESPONDS TO M VALUE THAT WAS SELECTED FOR DATA ANALYSIS. ....	99
FIGURE 8.76: PPG WAVEFORMS OBTAINED FROM A 4 <sup>TH</sup> ORDER LMS ADAPTIVE FILTER IMPLEMENTED IN REAL-TIME. NOTE THAT THE MATLAB (GREEN) AND MC (RED) OUTPUTS OVERLAP COMPLETELY. ....	102
FIGURE 8.77: LMS FILTER PROCESSING TIME FOR VARIOUS FILTER ORDERS INSIDE THE TI-MSP430 MC. ....	104
FIGURE 8.78: AUTO-TRIGGERING OF ANC IN ONE OF THE JOGGING TESTS. ....	105
FIGURE 8.79: HR MEASUREMENTS WITH AND WITHOUT ANC FROM ONE OF THE HEAD MOTION EXPERIMENTS. ....	106
FIGURE 8.80: HR MEASUREMENTS WITH AND WITHOUT ANC FROM ONE OF THE JOGGING TESTS. ....	107

FIGURE 8.81: SpO <sub>2</sub> MEASUREMENTS WITH AND WITHOUT ANC FROM ONE OF THE HEAD MOTION EXPERIMENTS.....	108
FIGURE 8.82: SpO <sub>2</sub> MEASUREMENTS WITH AND WITHOUT ANC FROM ONE OF THE JOGGING TESTS.....	109
FIGURE 8.83: CARDIAC AND MOTION FREQUENCY OVERLAP.....	110
FIGURE 8.84: EFFECTS OF ANC PROCESS IN CASE OF FREQUENCY OVERLAP.....	111
FIGURE 8.85: EFFECT OF FREQUENCY OVERLAP ON HR MEASUREMENTS.....	111
FIGURE 8.86: EFFECT OF FREQUENCY OVERLAP ON SpO <sub>2</sub> MEASUREMENTS.....	112
FIGURE 9.1: HR ESTIMATED FROM SYSTOLIC AND DIASTOLIC PEAKS DURING ONE OF THE JOGGING TRIALS. ....	114
FIGURE 9.2: SpO <sub>2</sub> ESTIMATED FROM SYSTOLIC AND DIASTOLIC PEAKS DURING ONE OF THE JOGGING TRIALS. ....	115
FIGURE 9.3: FREQUENCY SPECTRUM OF IR PPG WAVEFORM DURING OUTDOOR RUNNING. ....	123
FIGURE 11.1: IMPLEMENTATION OF A PHASE DETECTOR ALGORITHM TO BYPASS ANC DURING FREQUENCY OVERLAP.....	137



## LIST OF TABLES

TABLE 4.1: LMS EQUATIONS [22].....	21
TABLE 4.2: TV-LMS EQUATIONS [23, 24].....	22
TABLE 4.3: NLMS EQUATIONS [22, 25].....	23
TABLE 4.4: MNLMS EQUATIONS.....	24
TABLE 4.5: RLS EQUATIONS [22] .....	25
TABLE 5.1: THRESHOLD CONDITION USED IN HR AND SpO <sub>2</sub> ESTIMATION ALGORITHM .....	31
TABLE 7.1: TIME FRAME FOR SITTING EXPERIMENTS (ONE SET).....	38
TABLE 7.2: TIME FRAME FOR CYCLING EXPERIMENTS (ONE SET) .....	39
TABLE 7.3: TIME FRAME FOR TREADMILL JOGGING EXPERIMENTS (ONE SET).....	40
TABLE 7.4: TIME FRAME FOR RUNNING EXPERIMENTS (ONE SET).....	41
TABLE 7.5: TIME FRAME FOR STAIRCASE EXPERIMENTS (ONE SET) .....	41
TABLE 8.1: COMPARISON OF HR AND SpO <sub>2</sub> VALUES OBTAINED FROM THE WPO AND MPO DURING REST.....	47
TABLE 8.2: COMPARISON OF HR AND SpO <sub>2</sub> VALUES OBTAINED AFTER AND BEFORE LMS TYPE ANC. M=16 AND m = 0.01 (SITTING EXPERIMENTS).....	60
TABLE 8.3: COMPARISON OF HR AND SpO <sub>2</sub> VALUES OBTAINED BEFORE AND AFTER ANC USING A LMS FILTER. M=16 AND m = 0.01 (CYCLING EXPERIMENTS).....	69
TABLE 8.4: COMPARISON OF HR AND SpO <sub>2</sub> VALUES OBTAINED BEFORE AND AFTER A LMS TYPE ANC. M=16 AND m = 0.01 (TREADMILL JOGGING).....	80
TABLE 8.5: COMPARISON OF HR AND SpO <sub>2</sub> VALUES OBTAINED BEFORE AND AFTER A LMS TYPE ANC. M=16 AND m = 0.01 (OUTDOOR RUNNING).....	81
TABLE 8.6: COMPARISON OF HR AND SpO <sub>2</sub> VALUES OBTAINED BEFORE AND AFTER A LMS TYPE ANC. M=16 AND m = 0.01 (STAIRCASE CLIMBING EXPERIMENTS).....	91
TABLE 8.7: COMPARISON OF DIFFERENT ANC ALGORITHMS .....	100

TABLE 8.8: PERCENTAGE IMPROVEMENT IN HR AND SpO <sub>2</sub> AFTER ADAPTIVE FILTERING USING DIFFERENT REFERENCE NOISE SIGNALS.....	101
TABLE 8.9: EXECUTION TIME OF THE SIGNAL PROCESSING ALGORITHM INSIDE THE WPO.....	103
TABLE 8.10: PROCESSING TIME OF THE AUTO-TRIGGERED ANC METHOD.....	105
TABLE 8.11: PERCENTAGE IMPROVEMENT IN WPO MEASUREMENT ACCURACY AFTER ANC.....	107
TABLE 8.12: PERCENTAGE IMPROVEMENT IN WPO MEASUREMENT ACCURACY AFTER ANC.....	107
TABLE 9.1: DATA ANALYSIS FOR HR AND SpO <sub>2</sub> VALUES COMPUTED FROM SYSTOLIC AND DIASTOLIC PEAKS.....	115

## GLOSSARY OF ABBREVIATIONS

ACC	Accelerometer
ANC	Adaptive Noise Cancellation
BPF	Band Pass Filter
BPM	Beats Per Minute
CC	Coefficient of Correlation
ECG	Electrocardiograph
FFT	Fast Fourier Transform
Hb	Hemoglobin
HbO <sub>2</sub>	Oxyhemoglobin
HR	Heart Rate
HRV	Heart Rate Variability
IHR	Instantaneous Heart Rate
IR	Infrared
ISpO <sub>2</sub>	Instantaneous Arterial Oxygen Saturation Level
LMS	Least Mean Square
LPF	Low Pass Filter
MNLMS	Modified-Normalized Least Mean Square
MPO	Masimo Pulse Oximeter
MSE	Mean Square Error
N	No / False
NC	No Change
NLMS	Normalized Least Mean Square
PPG	Photoplethysmograph Signal
R	Red
R <sup>2</sup>	Coefficient of Correlation
RLS	Recursive Least Square
RR	Respiration Rate
SD	Standard Deviation
SNR	Signal-to-Noise Ratio
SpO <sub>2</sub>	Arterial Oxygen Saturation Level
Th	Threshold

TVLMS	Time-Varying Least Mean Square
WPO	Wireless Pulse Oximeter
Y	Yes / True
i	Least Mean Square Step-size
iC	Microcontroller

## 1. INTRODUCTION

Monitoring of oxygen supply is critical as death results from lack of oxygen supply. Pulse oximeters use optical means and photoplethysmography to extract continuous arterial oxygen saturation ( $SpO_2$ ). Photoplethysmography is advantageous because it can be used to measure other vital physiological parameters from a single compact sensor. Such data include heart rate (HR), heart rate variability (HRV) and respiration rate (RR). These physiological parameters may provide an early indication of cardiovascular condition in case of physical injury or shock. Physiological measurements from a single sensor allow wearable monitoring devices to be miniaturized for portability and field use.

Pulse oximeters would allow combat medics to continuously monitor the physiological status of soldiers, thereby potentially reducing the medical response time and improve remote triage [1]. During battlefield missions, specifically the Vietnam conflict, 67% of casualties occurred within 10 minutes from the onset of injury, the remaining 33% could have benefited from advanced diagnostic devices [2]. Wearable pulse oximeters will allow medical personnel to monitor several individuals simultaneously, thereby prioritizing medical intervention when resources are limited.

Commercial off-the-shelf pulse oximeters are impractical for field applications as they are typically designed for clinical purposes where the patient remains mostly motionless. In addition, the constraining wires can limit a subject's mobility and interfere with regular activities. Hence, a wireless pulse oximeter (WPO) has been designed in our laboratory. As shown in Figure 1.1, the WPO consists of a forehead worn optical sensor and a USB receiver.

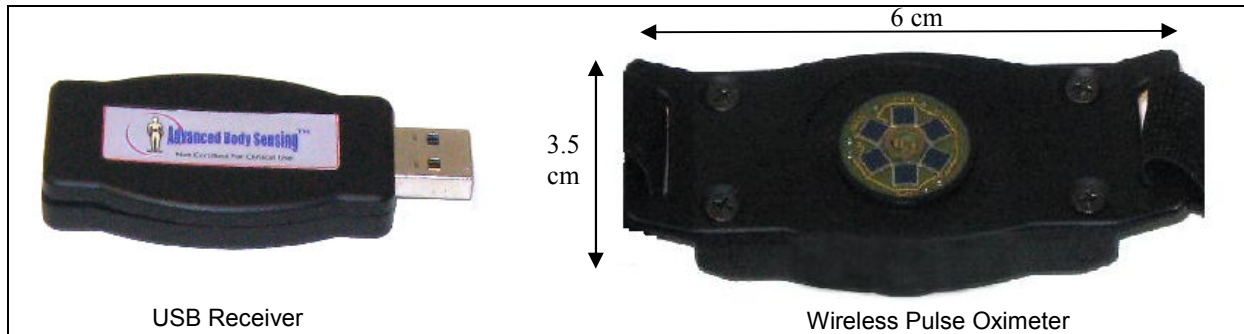


Figure 1.1: Wireless pulse oximeter (WPO) designed in our laboratory.

The WPO consists of two light emitting diodes (LED). These LEDs transmit light at two wavelengths – Red and Infrared (IR). When light is incident on the forehead, some portion of the incident light is absorbed by blood and other tissues, while the rest is reflected back to the sensor. The reflected light is detected by a photodetector and is used to generate photoplethysmographic (PPG) signals. Dedicated algorithms are used to filter the reflected PPG signals and compute HR and SpO<sub>2</sub> based on the relative amplitude and frequency content of the PPG signals. A tri-axial MEMS-type accelerometer (ACC) is embedded within the optical sensor to measure physical activities. The ACC is capable of detecting 3G motion along all three axes. Posture and motion signals, combined with physiological measurements, are valuable indicators to assess the status of an injured person.

Pulse oximeters are highly reliable when used in motionless situations. Pulse oximeters developed for field applications must be resistant to the effects of motion artifacts which are known to considerably degrade the signal-to-noise ratio (SNR) of PPG signals from which the physiological values are derived. Implementation of a robust pulse oximeter for field applications requires sophisticated noise cancellation algorithms to eliminate erroneous readings and false alarms.

Several research groups have suggested use of an ACC-based adaptive noise cancellation (ANC) algorithm [3-9]. These groups have demonstrated that ANC is feasible for reducing the effects of motion artifacts on PPG signals acquired during jogging. However, they have not presented data showing the effectiveness of ANC in real-time implementation within a  $\mu$ C. Therefore, the main focus of this thesis was to determine the feasibility of ANC for real-time implementation in

terms of accuracy, processing time and memory efficiency. The most efficient and feasible algorithm will be implemented in future generations of the WPO for real-time filtering of motion corrupted PPG signals. Employing such a robust signal processing algorithm to reduce the effects of motion artifacts would provide a more suitable platform for field applications.

This thesis begins by discussing the basic principles of pulse oximetry. The effects of motion artifacts and methods to reduce these effects are described in the following chapters. Several ANC algorithms are explained, followed by a brief explanation of the signal processing algorithm utilized to compute HR and SpO<sub>2</sub> values from raw PPG signals. The later part of this thesis outlines the experiments conducted to demonstrate how ANC improves the morphology of PPG signals during various physical activities. Next, the results of several ANC algorithms are discussed and compared with the goal of selecting a single motion tolerant algorithm that can be implemented in the current version of the WPO.

## 2. BACKGROUND

### 2.1. Photoplethysmography (PPG)

A pulse oximeter is a physiological monitoring system that noninvasively measures Heart Rate (HR) and arterial hemoglobin oxygen saturation ( $\text{SaO}_2$ ). The concept of pulse oximetry is based on Beer-Lambert's law, which states that the concentration of an unknown solute in a solvent can be determined by light absorption.

Oxyhemoglobin ( $\text{HbO}_2$ ) absorbs less red (R) light ( $\lambda = 660\text{nm}$ ) than reduced hemoglobin (Hb) [10], whereas  $\text{HbO}_2$  absorbs more infrared (IR) light ( $\lambda = 940\text{nm}$ ) compared to Hb. The difference in optical absorbance of  $\text{HbO}_2$  and Hb forms the basis of oxygen saturation measurement, as illustrated in Figure 2.1. By measuring the relative absorption of IR and R light, the concentration of oxygenated arterial blood can be determined noninvasively [10, 11]. Measurement of  $\text{SaO}_2$  by two wavelength pulse oximetry is termed  $\text{SpO}_2$  [7].

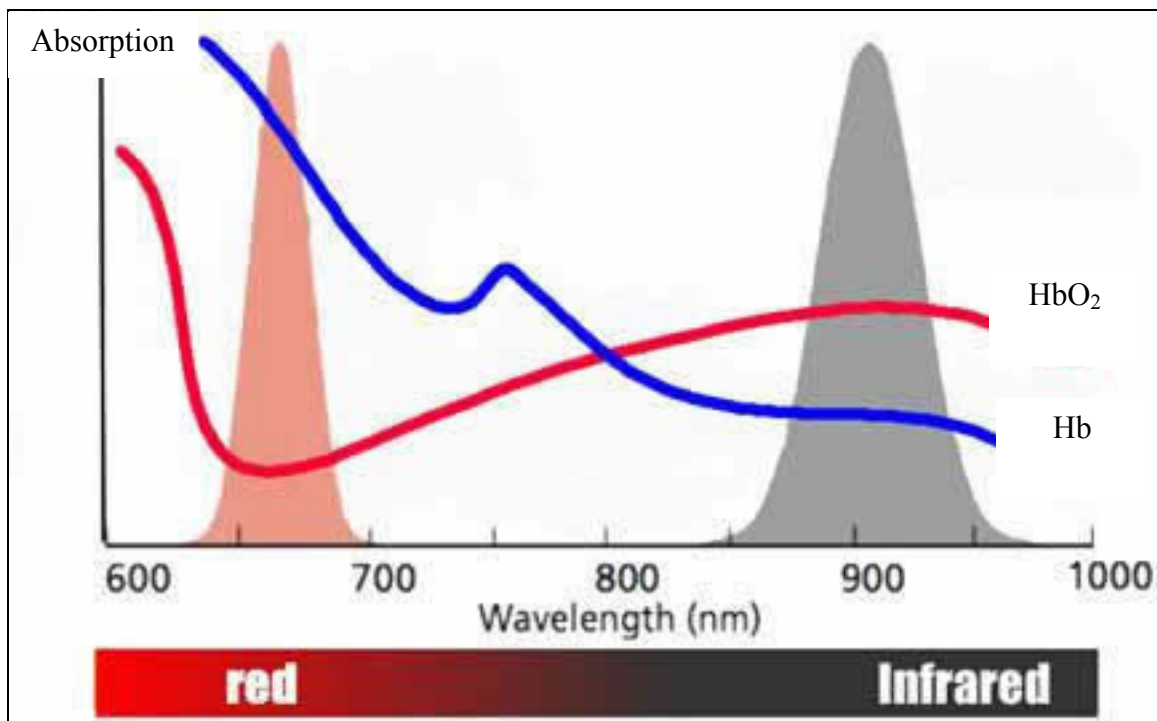


Figure 2.1: Optical absorbance spectra of  $\text{HbO}_2$  and Hb [12].



A pulse oximeter sensor consists of R and IR light emitting diodes (LED's) and a photodetector. When light is incident on the skin, some portion of the light is absorbed by body tissues while the remaining light is transmitted/reflected back to the photodetector. The light detected by the photodetector depends on skin opacity, reflection by bones, tissue scattering, and the amount of blood present in the vascular bed [13]. In this process, a constant amount of light is absorbed by tissue, bones, skin, non-pulsatile arterial and venous blood, generating a DC signal. Contrarily, the amount of light attenuated by the arterial blood varies according to the pumping action of heart [13]. As the arterial blood volume increases during systole, a greater portion of the incident light is absorbed causing a rapidly alternating signal [13]. The signal produced by this process is known as a photoplethysmographic (PPG) signal. Figure 2.2 explains the composition of the PPG signal generation process and Figure 2.3 depicts a typical sinusoidal-shaped PPG signal.

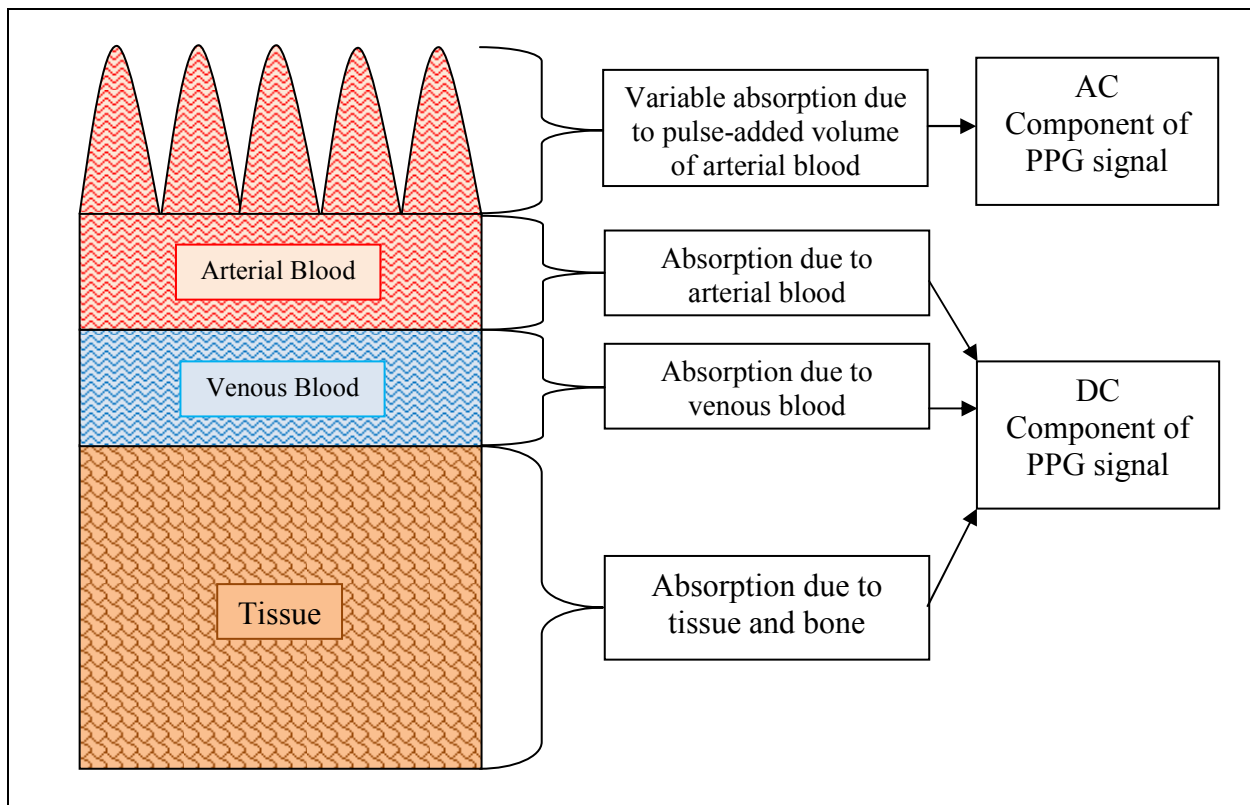


Figure 2.2: Variations in light attenuation by tissue, illustrating the PPG signal generation [13].

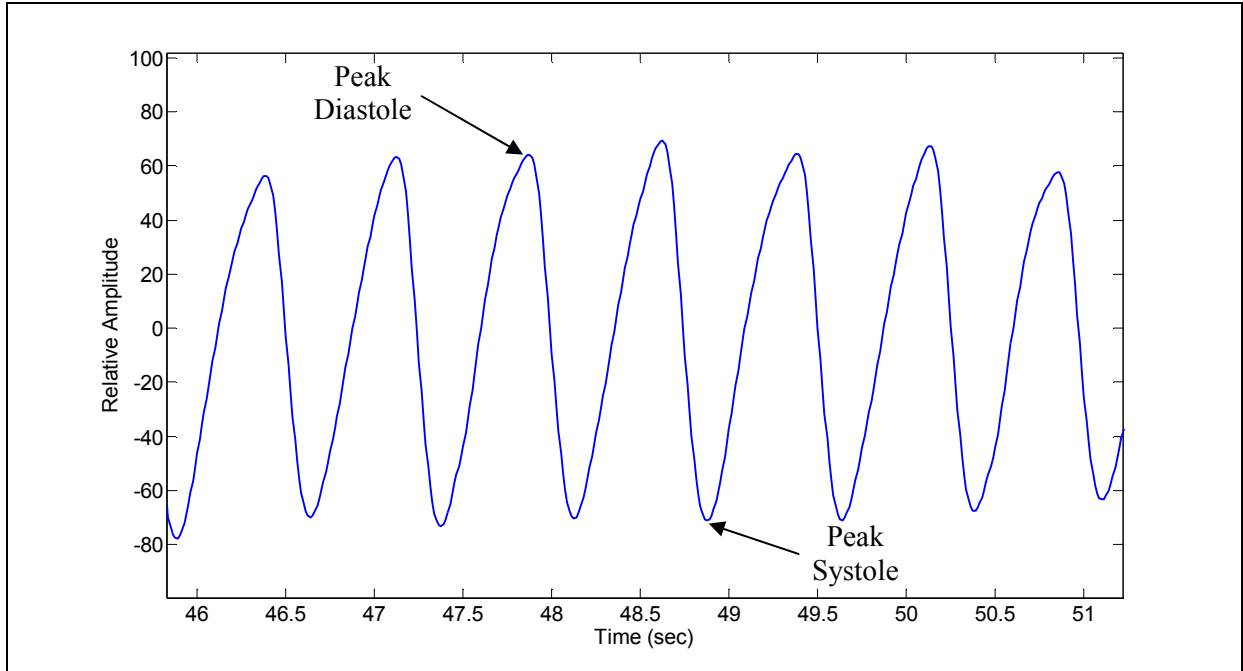


Figure 2.3: Typical PPG signal acquired during rest.

## 2.2. Operating modes and measurement sites

PPG signals can be obtained utilizing either transmittance mode or reflection mode optical transducers. As illustrated in Figure 2.4, in transmittance mode, the pulsating arterial bed is positioned between the LEDs and photodetector. The photodetector measures the portion of light that is transmitted in the forward direction. The main advantage of this mode is that it yields PPG signals with high SNR. Typical measurement sites utilized for transmittance mode oximetry are the ear lobes and finger tips.

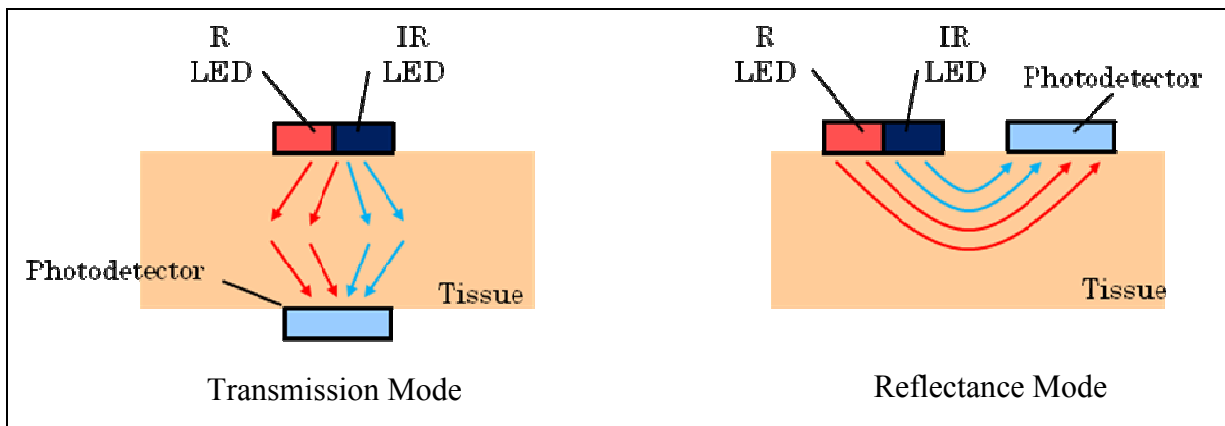


Figure 2.4: Operating modes of a pulse oximeter.

In reflectance mode, also illustrated in Figure 2.4, the LEDs and photodetector are placed side-by-side facing the skin. In this mode, the detector measures the reflected or backscattered light. For a pulse oximeter that employs a reflection mode, the optical sensor is usually attached to the forehead or temples with double-sided adhesive tapes [10]. A headband is often used to hold the sensor in position and minimize interference from the external light.

In clinical applications, PPG signals are normally acquired from the fingers. For field applications, such as physiological monitoring of soldiers or firefighters, it is more practical to implement a forehead-mounted sensor rather than finger-worn sensor. This would enable unrestricted hand movements. Moreover, the PPG signals acquired from the forehead generally have better SNR in the presence of motion artifacts [14, 15]. Therefore, we used a forehead mounted optical sensor.

## **2.3. Noninvasive arterial oxygen saturation (SpO<sub>2</sub>) measurement**

### **2.3.1. Significance**

Pulse oximeters have various clinical applications in anesthesia, surgery, critical care, exercise and other fields. For a healthy person breathing atmospheric air, SpO<sub>2</sub> readings typically range from 96% to 100%. Among the main advantages of a pulse oximeter is its ability to indicate a desaturation trend [10]. It is used to monitor a lack of O<sub>2</sub> supply to the cells. This is crucial as prolonged anoxia can result in serious brain damage and can be fatal.

### 2.3.2. Measurement Theory

As mentioned previously, SpO<sub>2</sub> values are based on the difference in optical absorbance of HbO<sub>2</sub> and Hb. Assuming that thoroughly hemolyzed blood consists of HbO<sub>2</sub> and Hb, and that light absorbance by the mixture of these two components is additive, the SpO<sub>2</sub> values can be derived from the following equations [10]:

$$SpO_2 = A - B * p \quad 2.1$$

$$p = \frac{(AC/DC)_R}{(AC/DC)_{IR}} \quad 2.2$$

In Equation 2.1, A and B are derived during empirical calibration of a pulse oximeter using the calibration curve shown in Figure 2.5.

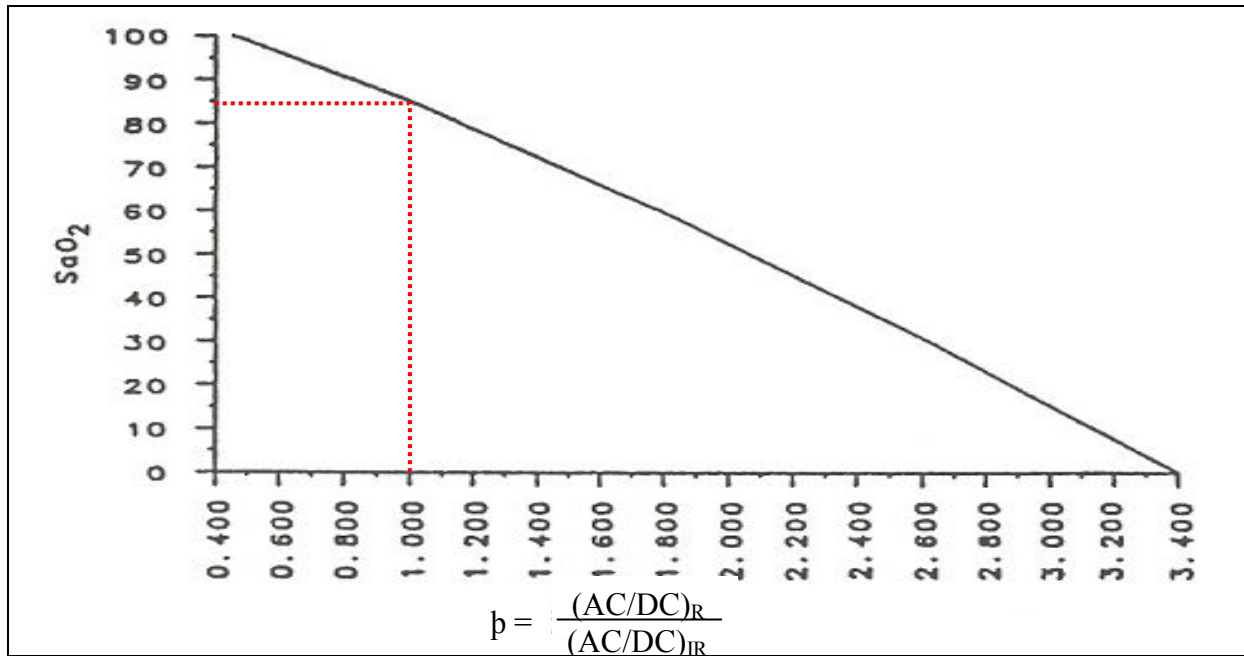


Figure 2.5: Empirical relationship between SaO<sub>2</sub> and the normalized R/IR ratio [10].

## 2.4. Heart Rate (HR)

### 2.4.1. Significance

In addition to SpO<sub>2</sub> values, pulse oximeters also measure HR. HR readings provide an early indication regarding the subject's health and indicate changes in the sympathetic nervous system.

### 2.4.2. Measurement Theory

The AC component of the PPG signal, presented in Figure 2.3, has characteristics of a sinusoidal waveform. Each peak in PPG signal corresponds to one cardiac beat. The time interval between two consecutive peaks is used to extract HR readings [1]. Specifically, if T (seconds) corresponds to the time interval between two consecutive peaks, then instantaneous HR (BPM) is calculated using Equation 2.3.

$$HR = 60 / T \quad 2.3$$

## 2.5. Limitations to Pulse Oximeter

Although pulse oximeters are highly accurate and reliable when used during rest, numerous factors have been shown to negatively affect the SNR of pulse oximeters. Factors affecting the absorbance characteristics include low pulsatile signals (e.g. low perfusion index), noise (e.g. stray lights, electromagnetic interference), and motion artifacts [3, 4, 6, 7, 10, 11, 13]. The worst case is a combination of the two factors – low perfusion index along with significant motion artifacts.

The problem of low perfusion index is biological and can be solved by the use of vasodilating drugs to enhance blood perfusion [10]. Some manufacturers take intermittent optical background readings and then subtract these from the photodetector measurements to minimize background light interference. These background readings are acquired when both the LEDs in the sensor are turned off. This greatly reduces the effects of bright light and electromagnetic

interferences [10]. Of all the factors, motion artifact has been the most troublesome in pulse oximetry.

### 3. MOTION ARTIFACT

#### 3.1. Effects of Motion Artifacts

One of the primary factor limiting the use of pulse oximetry for real-time physiological monitoring of soldiers and firefighters is its poor reliability during motion [6]. Motion affects the measurement accuracy of pulse oximeter in several ways.

Langton and Hanning correlated the force required to displace the optical sensor with the degree of motion-induced artifacts [16]. They showed that motion artifacts have the same effect on the R and IR PPG signals. When motion amplitude is very large, it masks the biological signal. These motion induced signals produce a  $\beta$ -value (Equation 2.2) that approximately equals one. As per the empirical calibration curve (Figure 2.5), a unity R-value produces  $SpO_2$  values in the range of 80% to 85%. This theory explains the sudden erroneous drop in  $SpO_2$  values to 80-85% during motion. However, it fails to explain false desaturations below 50%, also observed in the presence of motion. Additionally, the theory was not able to explain situations where the motion artifacts decrease  $\beta$ -value (Equation 2.2) to produce  $SpO_2$  values greater than 100.

One assumption in pulse oximetry is that the only pulsating component is due to arterial blood. Motion introduces additional pulsatile movements in venous blood [7, 16-18]. The pulsatile component of the PPG signal is then composed of more than just arterial blood. Contribution of deoxygenated venous blood to PPG signals reduces the final  $SpO_2$  measurements [7]. These errors induced by venous blood pulsation cannot be eliminated by PPG signal processing.

Motion artifacts also affect HR measurements since they introduce false peaks and/or attenuate the cardiac peaks. If motion artifact mimics the PPG signals, the device will be unable to differentiate between false motion peaks and true cardiac peaks, thereby producing erroneous HR readings. Such errors in HR measurements can be minimized by utilizing advanced signal processing methods.

A typical PPG waveform acquired during rest is plotted in Figure 3.1. Figure 3.2 shows the AC component of an IR PPG signal along with the reference tri-axial ACC signal acquired simultaneously during motion. An ECG waveform acquired by a Holter monitor is plotted for comparison. During motion, we can observe that the IR PPG waveform does not appear as periodic as it was during rest (see Figure 3.1). Furthermore, the amplitude of the IR PPG signal in Figure 3.2 varies to a large extent when compared to the resting state PPG signal shown in Figure 3.1. The PPG signal during rest has nearly constant amplitude. Whereas, the PPG signal presented in Figure 3.2 is distorted due to the presence of motion artifacts.

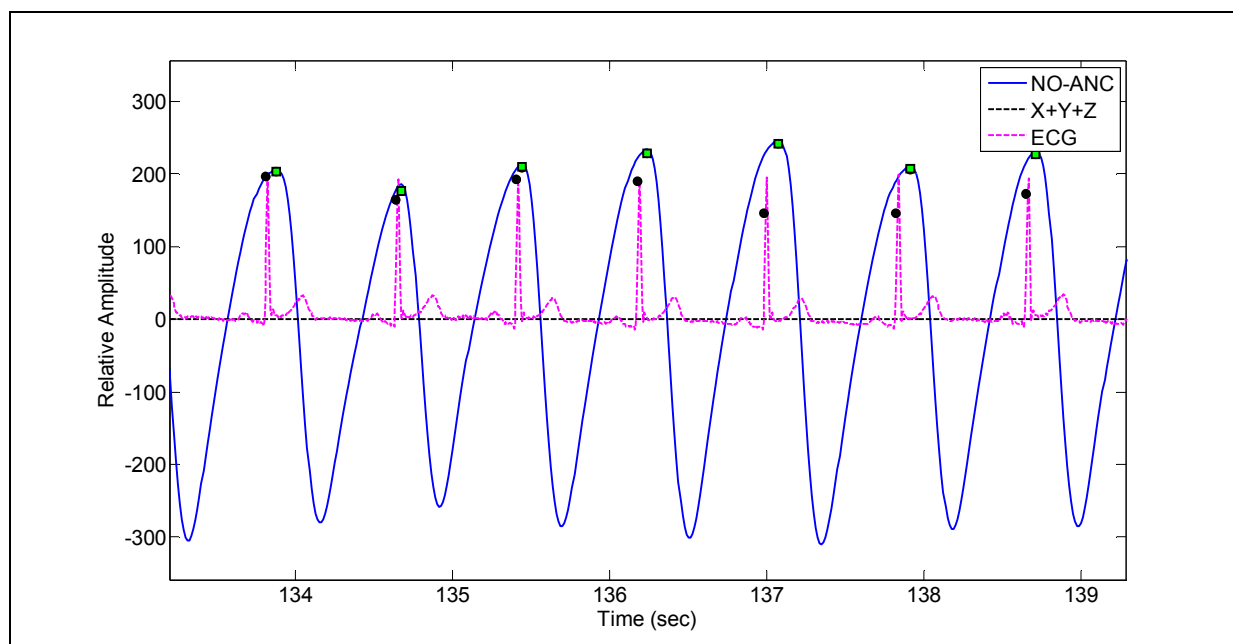


Figure 3.1: IR PPG signal during rest.



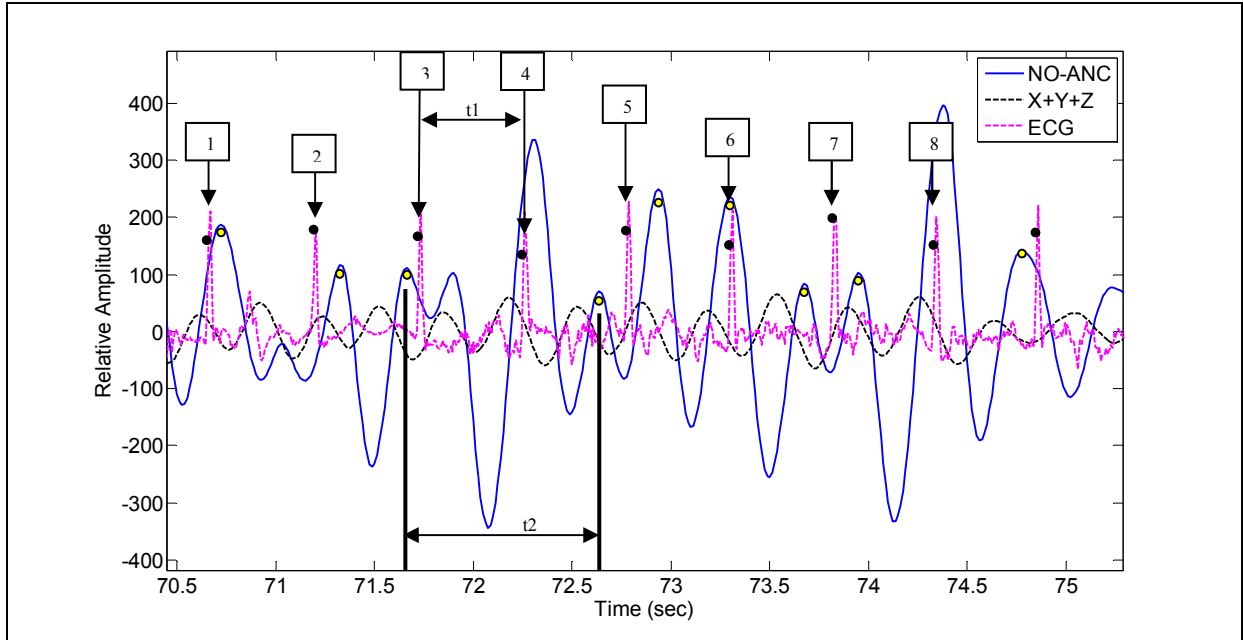


Figure 3.2: IR PPG signal affected by motion artifact. ● PPG peaks detected by the WPO (9-peaks), and ● R-waves detected from the ECG waveform (9-peaks).

To compute HR and  $SpO_2$  values, the IR and R PPG signals are processed by our custom signal processing algorithm discussed later in chapter 5. The yellow markers in Figure 3.2 indicate the peaks detected by our signal processing algorithm. These peaks are assumed to represent true cardiac beats. As both ECG and PPG signals were recorded simultaneously, cardiac peaks from the two waveforms must be closely correlated. This is apparently not true for the PPG signal shown in Figure 3.2.

As seen in Figure 3.2, both the Holter monitor and our signal processing algorithm detected 9 R-waves from the ECG waveform. However, there was no correlation between the location of some of the R-waves and PPG peaks. Consider for example the 3<sup>rd</sup> and 4<sup>th</sup> R-waves in the ECG waveform. According to the Holter monitor,  $t_1$  corresponds to the time interval between the 3<sup>rd</sup> and 4<sup>th</sup> cardiac peaks. Due to large fluctuations in the peak-to-peak amplitude seen in the PPG signal, our signal processing algorithm did not detect any PPG peaks corresponding to the 3<sup>rd</sup> and 4<sup>th</sup> R-waves. Hence, the time interval between the 3<sup>rd</sup> and 4<sup>th</sup> PPG peaks ( $t_2$ ) was larger than the actual time period ( $t_1$ ). Thus, the HR value computed based on  $t_2$  is lower than the HR value computed based on  $t_1$ . Similarly, for the 6<sup>th</sup> and 7<sup>th</sup> R-waves, our signal processing algorithm

overestimated HR values due to the shorter time period between the two PPG peaks. This resulted in an inaccuracy when HR values were determined from the motion corrupted PPG signal. Figure 3.3 represents a typical data set demonstrating the effect of motion artifacts on HR values.

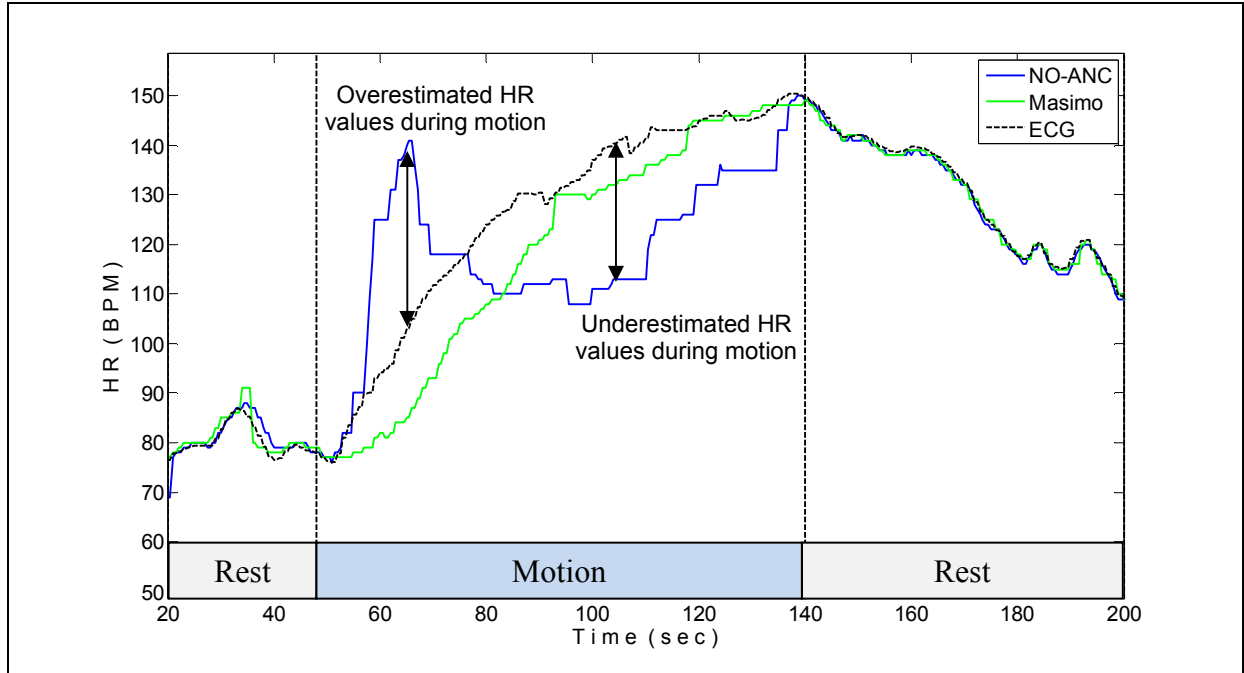


Figure 3.3: Effect of motion artifacts on HR measurements.

As explained earlier, Langton and Hanning theory quotes that if motion affects the IR and R PPG signals equally, the  $\rho$ -value (Equation 2.2) is approximately equal to 1 and  $SpO_2$  values during such time instants drop towards 80-85%. As seen in Figure 3.4, such motion peaks produce an erroneous drop in  $SpO_2$  values. Consider three PPG peaks; two are true and one produced by motion. The true cardiac peaks produce a  $SpO_2$  value of 98% each, while the motion peak produces a  $SpO_2$  value of 85%. The average of these three peaks will result in a  $SpO_2$  value of 93%, which is below the normal physiological range. Such erroneous drops should be eliminated by the use of a more robust signal processing algorithm(s).

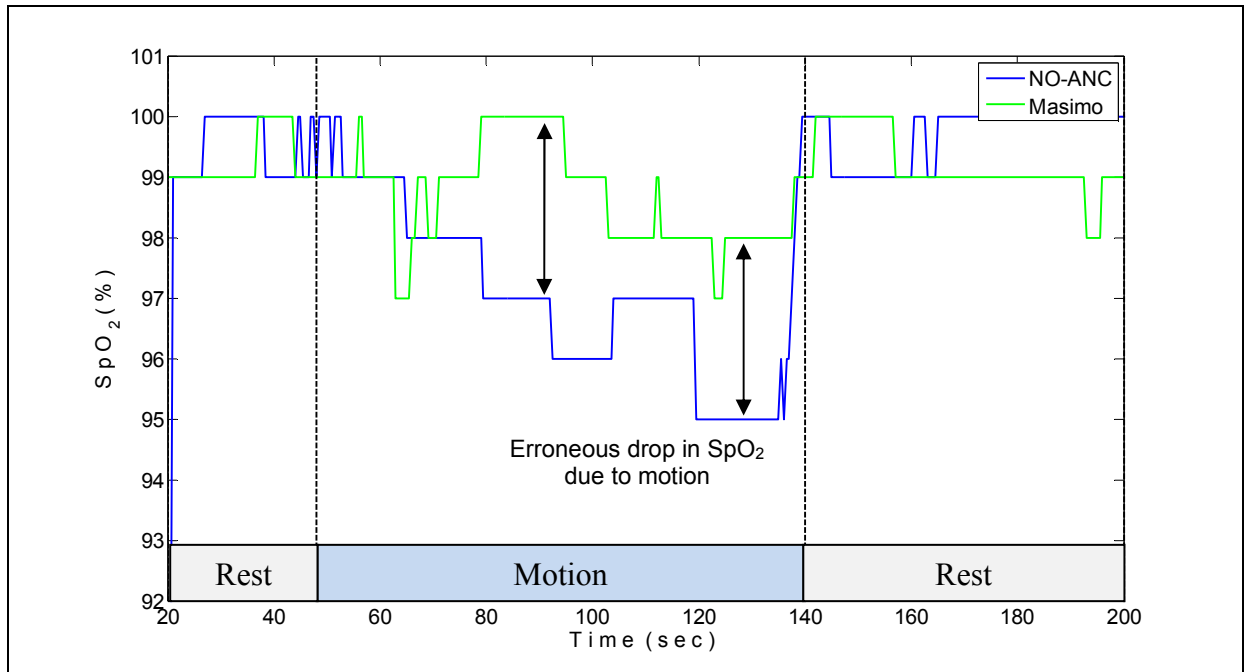


Figure 3.4: Effects of motion artifacts on SpO<sub>2</sub> measurements.

To determine the effects of motion artifacts, PPG signals were analyzed in the frequency domain. For this representative trial, HR readings were in the range of 70 BPM to 150 BPM (see Figure 3.3). In the frequency domain, the FFT of the PPG signals should therefore have peaks in the range of 1Hz to 2.5Hz, respectively. However, the frequency spectra of the IR and R PPG signals (shown in Figure 3.5 and Figure 3.6 respectively) consist of additional frequency components between 2.5Hz to 3Hz. These frequency components are due to motion artifacts and result in measurement inaccuracies. The frequency spectra of the PPG and tri-axial accelerometer signals have the same dominant motion peaks in 2.5Hz to 3Hz range. Both frequency spectra have the same motion peaks. Conclusively, these acceleration signals carry motion frequency information corrupting the PPG signals.

As illustrated above, motion artifacts can drastically affect HR and SpO<sub>2</sub> measurement accuracies. To minimize these motion artifacts and recover cleaner PPG signals, a new signal processing approach is needed. This will make the WPO more motion tolerant and improve measurement reliability.

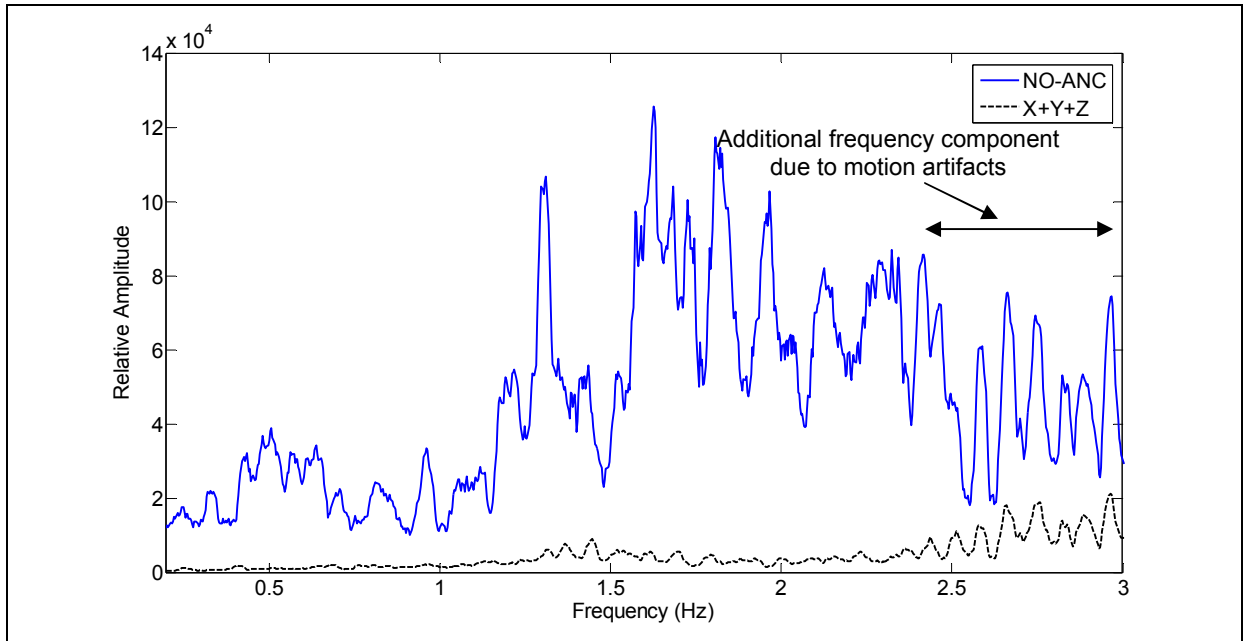


Figure 3.5: Frequency spectrum of IR PPG and reference ACC signals acquired during motion.

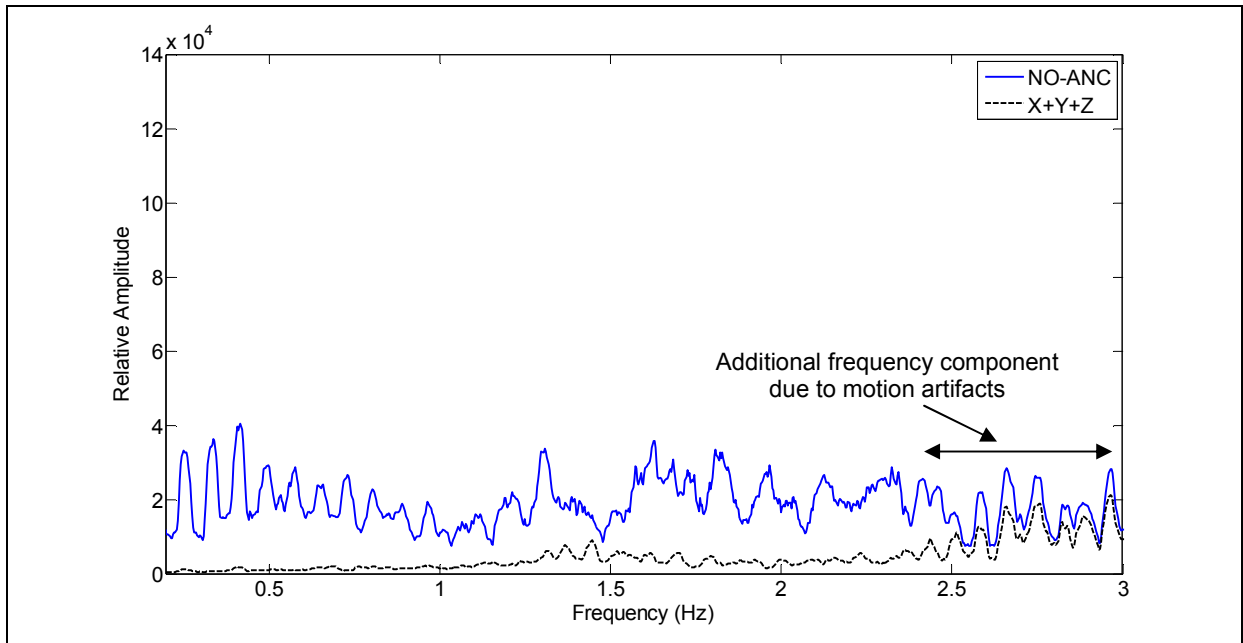


Figure 3.6: Frequency spectrum of R PPG and reference ACC signals acquired during motion.

### 3.2. Reducing the effects of motion artifacts

Removing motion artifacts from PPG signals is one of the primary challenges to be tackled before using pulse oximeters for field applications. The dominant frequency range of motion corrupting the PPG signal can overlap with the fundamental cardiac frequency range of 0.5Hz (40BPM) to 3Hz (180BPM). Hence, conventional fixed filters (LPF and HPF) cannot be used to minimize the effects of motion artifacts. Moreover, the design of fixed filters is based on prior knowledge of the noise signal – which is unknown and unpredictable. Therefore, sophisticated signal processing algorithms must be employed to reduce the effects of body motion on PPG signals.

To overcome the effects of motion artifact, several advanced signal processing techniques have been suggested in the literature. Kim and Yoo [19] used independent component analysis with a preprocessor to suppress the noise signals. This method assumes that motion artifacts and the PPG signal are independent, which is not true. Also, the complexity of the algorithm limits the feasibility of its real-time implementation in an embedded  $\mu\text{C}$  [4, 6]. Some authors suggested the use of three wavelength pulse oximetry to recover a clean PPG from motion corrupted PPG signals [20]. This technique has its own limitations since the absorption properties of the third wavelength must be independent of changes in arterial blood volume. This methodology assumes that motion artifacts result from small changes in the optical path. Also, a 3<sup>rd</sup> LED will increase the power consumption and affect the battery life. This rule outs the use of this technique for field applications which involve larger sensor movements. The technique to be used for PPG signal processing (for our application) has to be simple, robust and must quickly adapt to the changing noise frequency.

Adaptive noise cancellation (ANC) seems to be the most promising approach to minimize the effects of motion artifacts on PPG signals. This method uses a primary input containing the corrupted signal and a reference input containing noise that is correlated in some way with the primary source of noise [21]. The reference input is adaptively filtered and subsequently subtracted from the primary input to obtain the desired signal estimate [21]. Employing ACC

signals for adaptive filtering of motion corrupted PPG signals has been suggested by several investigators [3, 4, 6, 9, 21].

## 4. ADAPTIVE NOISE CANCELLATION

### 4.1. Background

The common method of eliminating additive noise from a signal is to pass the signal through a digital filter with fixed coefficients. Ideally, the filter attenuates the noise leaving the desired signal relatively unchanged [21]. Fixed digital filter design is based on prior knowledge of both the signal and noise. On the other hand, adaptive filter design requires little prior knowledge of the input signals [21]. They adjust filter parameters automatically depending upon the reference noise input. Hence, adaptive filters can be used to recover PPG signals that are corrupted by body motion.

### 4.2. Principle of ANC

Figure 4.1 presents an adaptive noise canceller that can be used for adaptive filtering of a PPG signal. The PPG signal ( $s$ ) corrupted by motion ( $n_0$ ) forms the primary input signal ( $s + n_0$ ) to the canceller. The signal ( $n_1$ ) that is uncorrelated with the desired signal ( $s$ ), but correlated with the noise signal ( $n_0$ ), is used as a reference noise input. Figure 3.5 and Figure 3.6 demonstrate that motion signal ( $X+Y+Z$ ) from the tri-axial ACC is correlated to motion corrupting the PPG signals. Hence, the ACC ( $X+Y+Z$ ) signals are used as a reference input to the adaptive noise canceller. The adaptive filter modifies the noise ( $n_1$ ) to produce an output ( $y$ ) as close a replica as possible of the primary noise ( $n_0$ ) [21]. This filter output ( $y$ ) is subtracted from the primary input ( $s+n_0$ ) to produce a system output ( $z = s + n_0 - y$ ) [21]. The adaptive process is accomplished by feeding the system output ( $e = z$ ) back to the adaptive filter and adjusting filter parameters to minimize noise ( $n_0$ ) in the desired signal ( $s$ ) [21]. The system output ( $z$ ) is also processed for HR and SpO<sub>2</sub> estimation.

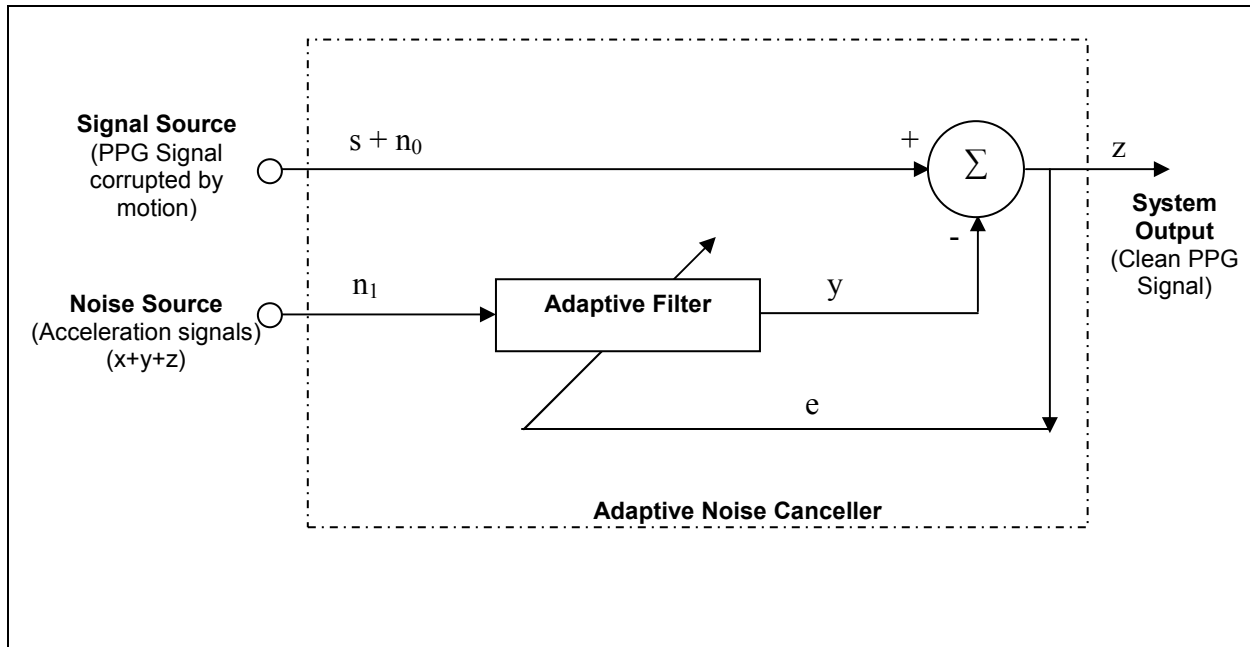


Figure 4.1: The adaptive noise cancellation concept [21].

### 4.3. Different types of ANC

The characteristics of any adaptive noise canceller primarily depend on the type of algorithm used to adjust the filter parameters. For adaptive filtering of PPG signals, we have implemented and analyzed five different types of adaptive algorithms. These include the (1) Least Mean Square (LMS), (2) Time Varying LMS (TV-LMS), (3) Normalized LMS (NLMS), (4) Modified Normalized LMS (MNLMS), and (5) Recursive Least Squares (RLS) algorithms. These algorithms are briefly discussed below.

The LMS algorithm is a well-known adaptive estimation and prediction technique. The conventional LMS algorithm is a stochastic implementation of the steepest descent algorithm. In the LMS algorithm, the adaptive filter output ( $y$ ) depends on the reference input signal ( $x$ ) and filter weights ( $\omega$ ) (also known as filter parameters or filter coefficients). Starting with arbitrary initial filter weights, the LMS algorithms will converge in order to minimize the total output power, thus causing the system output ( $y$ ) to be a best least square estimate of the desired signal. The LMS algorithm equations are summarized in Table 4.1. Detailed explanation and derivation for LMS algorithm can be found in [21, 22].



Table 4.1: LMS equations [22]

	Equations	Number of Multiplications	Number of Additions	Equation Number
System output	$y(n) = d(n) - \hat{u}^H(n) * \text{ref}(n)$ <small>(1x1) (1x1) (1xM) (Mx1)</small>	M	M	(1)
Constant	Constant = $\hat{i} * y(n)$	1	0	(2)
Update weights	$\hat{u}(n+1) = \hat{u}(n) + \text{Constant} * \text{ref}(n)$ <small>(Mx1) (Mx1) (1x1) (Mx1)</small>	M	M	(3)
	Total	2M + 1	2M	
Parameter	Definition			
$y(n)$	Filter output			
$d(n)$	Primary input signal corrupted by noise			
$\text{ref}(n)$	Reference noise signal			
$\hat{u}(n)$	Array coefficients			
H	Hermitian property			
$\hat{i}$	Filter step-size			
M	Filter order			

The performance of the LMS algorithm is highly dependent on the selected convergence parameter ( $\mu$ ) and filter order (M) [4]. A large  $\mu$  value leads to faster convergence rate, whereas, smaller values produce better accuracy [23, 24]. While selecting  $\mu$  for a conventional LMS algorithm, a compromise is made between the convergence rate and estimation accuracy. Hence, either the filter responds slowly to the changes in noise frequency or inaccurately estimates system output. This limitation is overcome by the TV-LMS algorithm [23, 24].

The main idea of the TV-LMS algorithm is to set  $\mu$  to a large value initially to speed up the algorithm convergence. As time progresses,  $\mu$  is adjusted to a smaller value so that the adaptive filter will have a smaller mean-squared error (MSE) [23, 24]. The TV-LMS algorithm is summarized in Table 4.2. Lau, Hussian and Harris derived the TV-LMS equations and explained it in greater detail [23, 24].

Table 4.2: TV-LMS equations [23, 24]

	Equations	Number of Multiplications	Number of Additions	Equation Number
System output	$y(n) = d(n) - \hat{u}^H(n) * \text{ref}(n)$ <small>(1x1) (1x1) (1xM) (Mx1)</small>	M	M	(1)
Constant	Constant = $\hat{i}_n * y(n)$	1	0	(2)
Update $\hat{i}_n$	$\hat{i}_n = \hat{a}_n * \hat{i}_0$	1	0	(3)
Update $\hat{a}_n$	$\hat{a}_n = C^{1/(1+an^b)}$	4	1	(4)
Update weights	$\hat{u}(n+1) = \hat{u}(n) + \text{Constant} * \text{ref}(n)$ <small>(Mx1) (Mx1) (1x1) (Mx1)</small>	M	M	(5)
	Total	2M + 6	2M + 1	
Parameter	Definition			
$y(n)$	Filter output			
$d(n)$	Primary input signal corrupted by noise			
$\text{ref}(n)$	Reference noise signal			
$\hat{u}(n)$	Array coefficients			
H	Hermitian property			
$\hat{i}_0$	Filter step-size			
M	Filter order			
a, b, c	Constant			
$\hat{a}_n$	Step-size variation parameter			

Another drawback of the conventional LMS algorithm is its sensitivity to scaling of the reference input (ref). This makes it very hard to choose a learning rate  $\mu$  that guarantees stability of the algorithm. The normalized least mean square algorithm (NLMS) is a variant of the LMS. The NLMS algorithm solves the scaling problem by normalizing  $\mu$  with the energy of the reference signal. Table 4.3 summarizes the NLMS algorithm equations. In these equations,  $\mu$  represents the adaptation constant,  $\|x(n)\|^2$  is the energy of the input reference signal, and  $\delta$  is a constant used to avoid divide-by-zero error. Setting  $\mu$  according to equation (3) may be viewed as using a time varying convergence factor. The interesting point about NLMS is that it exhibits potentially faster rate of convergence than the standard LMS algorithm [22, 25].

Table 4.3: NLMS equations [22, 25]

	Equations	Number of Multiplications	Number of Additions	Equation Number
System output	$y(n) = d(n) - \hat{u}^H(n) * \text{ref}(n)$ <small>(1x1) (1x1) (1xM) (Mx1)</small>	M	M	(1)
Constant	Constant = $\hat{i}_n * y(n)$	1	0	(2)
Update $\hat{i}_n$	$\hat{i}_n = \hat{i} / [\ \text{ref}(n)\ ^2 + \hat{a}]$	M+1	M	(3)
Update weights	$\hat{u}(n+1) = \hat{u}(n) + \text{Constant} * x(n)$ <small>(Mx1) (Mx1) (1x1) (Mx1)</small>	M	M	(4)
	Total	3M + 2	3M	
Parameter	Definition			
$y(n)$	Filter output			
$d(n)$	Primary input signal corrupted by noise			
$\text{ref}(n)$	Reference noise signal			
$\hat{u}(n)$	Array coefficients			
H	Hermitian property			
$\hat{i}$	Filter step-size			
M	Filter order			
$\ \text{ref}(n)\ ^2$	Energy of reference noise signal			
$\hat{a}$	Constant to avoid divide-by-zero error			

The MNLMS algorithm is a modified version of the NLMS algorithm that was developed in Matlab. In this approach,  $\mu$  is always normalized by  $(\|x(n)\|^2 + \delta)$ . For the MNLMS algorithm,  $\mu$  is normalized only if the energy of the reference signal is greater than 1. If the condition is not true,  $\mu$  is kept constant. This is the only difference between the NLMS and MNLMS algorithms.

Table 4.4: MNLMS equations

	Equations	Number of Multiplications	Number of Additions	Equation Number
System output	$y(n) = d(n) - \hat{u}^H(n) * x(n)$ <small>(1x1) (1x1) (1xM) (Mx1)</small>	M	M	(1)
Constant	Constant = $\hat{i}_n * y(n)$	1	0	(2)
Update $\hat{i}_n$	$\hat{i}_n = \hat{i} / [\ x(n)\ ^2]$	M+1	M	(3)
Update $\hat{i}_n$	$\hat{i}_n = \hat{i}$			(4)
Update weights	$\hat{u}(n+1) = \hat{u}(n) + \text{Constant} * x(n)$ <small>(Mx1) (Mx1) (1x1) (Mx1)</small>	M	M	(5)
	Total	3M + 2	3M	
Parameter	Definition			
$y(n)$	Filter output			
$d(n)$	Primary input signal corrupted by noise			
$\text{ref}(n)$	Reference noise signal			
$\hat{u}(n)$	Array coefficients			
H	Hermitian property			
$\hat{i}$	Filter step-size			
M	Filter order			
$\ \text{ref}(n)\ ^2$	Energy of reference noise signal			
$\hat{a}$	Constant to avoid divide-by-zero error			

All of the LMS algorithms discussed above are finite-impulse-response (FIR) filtering algorithms. Kwan and Tao [26] have shown that the adaptive infinite-impulse-response (IIR) based algorithms can provide significantly better performance than that of an adaptive FIR filter having the same filter order. The RLS filter is an IIR-based algorithm that is widely used for adaptive filtering, summarized in Table 4.5 [22]. The performance of the RLS algorithms primarily depends on filter order (M) and its forgetting factor ( $\lambda$ ).

Table 4.5: RLS equations [22]

	Equations	Number of Multiplications	Number of Additions	Equation Number
System output	$y(n) = d(n) - \hat{u}^T(n) * \text{ref}(n)$ <small>(1x1) (1x1) (1xM) (Mx1)</small>	M	M	(1)
Constant	$\delta(n) = P(n-1) * \text{ref}(n)$ <small>(Mx1) (MxM) (Mx1)</small>	M <sup>2</sup>	M <sup>2</sup> - M	(2)
Constant	$k(n) = [ \delta(n) ] / [ \epsilon + x^H(n) * \delta(n) ]$ <small>(Mx1) (Mx1) (1x1) (1xM) (Mx1)</small>	2M	M	(3)
Constant	$P(n) = \epsilon^{-1} [ P(n-1) - k(n) * \text{ref}^H(n) * P(n-1) ]$ <small>(MxM) (1x1) (MxM) (Mx1) (1xM) (MxM)</small>	3M <sup>2</sup>	2M <sup>2</sup> - M	(4)
Update weights	$\hat{u}(n) = \hat{u}(n-1) + y(n) * k(n)$ <small>(Mx1) (Mx1) (1x1) (Mx1)</small>	M	M	(5)
	Total	4M(M+1)	3M(M+1)	
Parameter	Definitions			
y(n)	Filter output			
d(n)	Primary input signal corrupted by noise			
T	Transpose of an array			
ref(n)	Reference noise signal			
ε	Forgetting factor			
M	Filter order			
P	Matrix of size M-by-M. Initially an identity matrix			
δ	Constant			
k	Constant			
û(n)	Filter coefficients			

## 5. SIGNAL PROCESSING ALGORITHMS

The WPO sensor operates at an 80Hz sampling frequency. Hence, every 500msec, 40 new data samples of IR PPG, R PPG, and tri-axial body acceleration signals are acquired. These signals are processed to estimate HR and SpO<sub>2</sub> values. Figure 5.1 summarizes the signal processing algorithm.

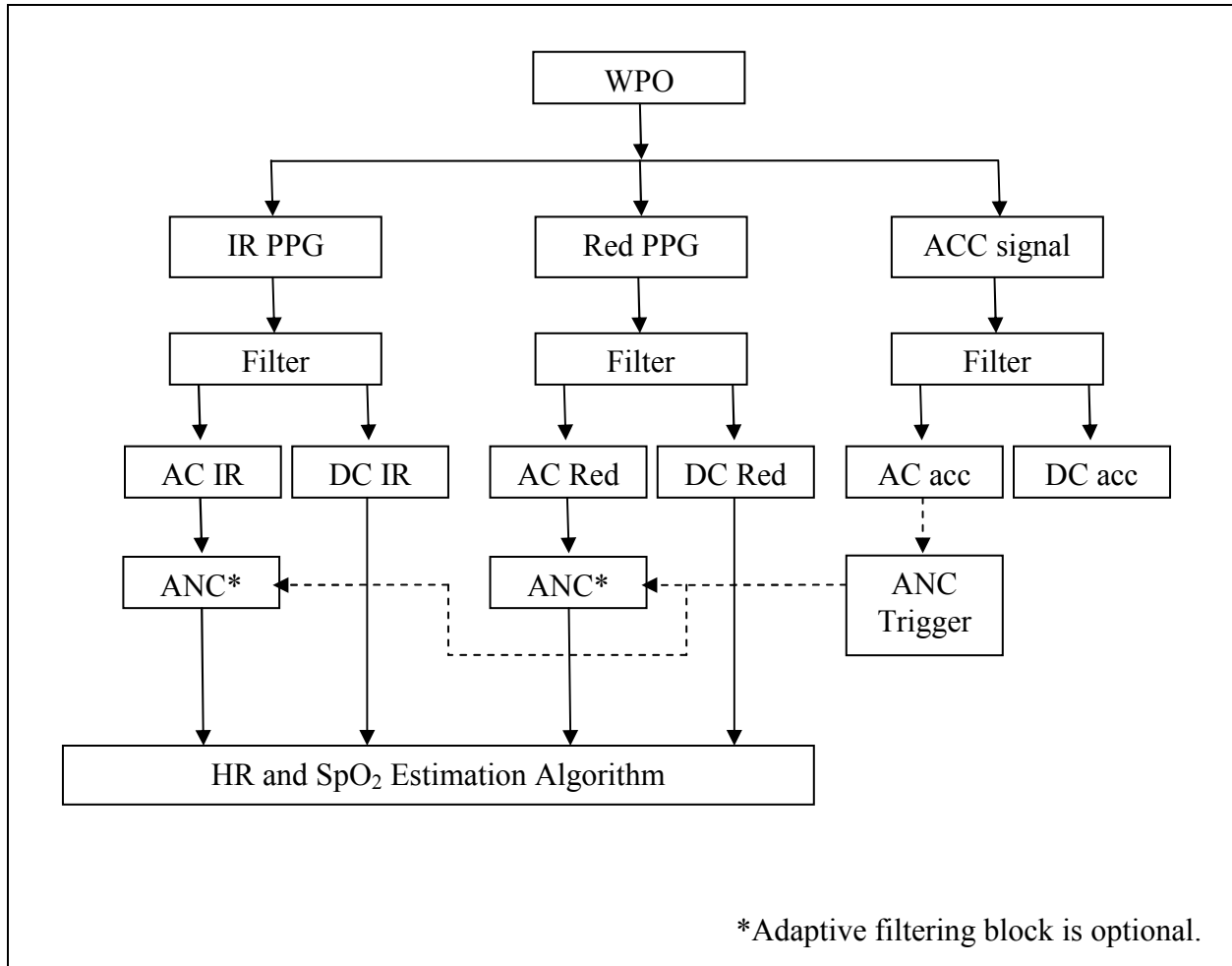


Figure 5.1: PPG signal processing flowchart.

Raw signals from the WPO are digitally filtered to separate their AC and DC components. Figure 5.2 shows the digital filtering algorithm. A 4<sup>th</sup> order band-pass Butterworth filter, having pass-band frequency ranging from 0.5Hz to 3.0Hz, was used to obtain the AC components. A 2<sup>nd</sup> order low-pass Butterworth filter with a cut-off frequency of 0.05Hz was used for DC signal extraction.

Signals from the tri-axial accelerometer were filtered using the same BP and LP filters. The AC components corresponding to body acceleration were used to determine the subjects' activity level. Body orientation was determined using the DC components of the acceleration signals. In addition to providing activity and orientation information, the AC components were used as reference noise inputs in the ANC algorithm. Instead of using the accelerometer signals directly for adaptive filtering, these signals were pre-processed by an ANC-triggered signal processing algorithm.

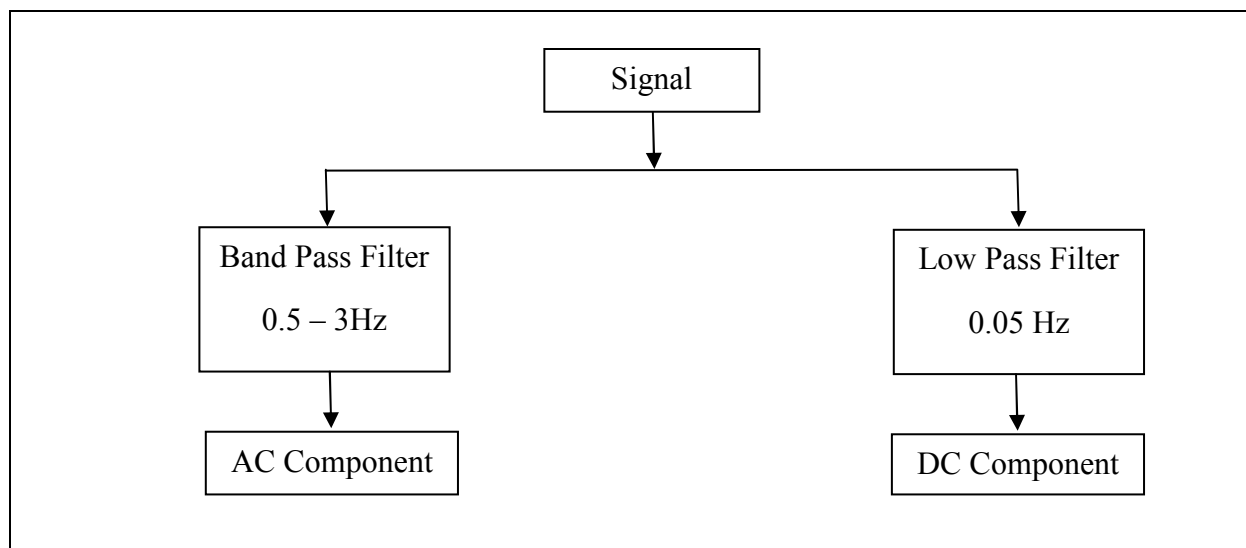


Figure 5.2: Digital filtering flow chart

The proposed ANC-triggered algorithm, shown in Figure 5.3, helped to reduce the  $\mu\text{C}$  processing time by avoiding unnecessary signal processing during rest. The energy of the reference signal, is equal to  $\|x(n)\|^2$ , where  $x(n)$  represents the reference signal. Thus, when the energy is low, it can be assumed that the motion sensor (accelerometer) is at rest. On the other hand, a higher energy indicates that the motion sensor is detecting movements. Hence, the energy of the accelerometer signal was used as a trigger to auto-start ANC when the energy of the ACC signal is above a certain threshold level. The ANC-triggered algorithm outputs a reference noise signal if energy is above certain threshold level; if not, the output is zero.

Filtered IR and R PPG signals are used for HR and  $\text{SpO}_2$  estimation. However, to eliminate motion artifacts, the AC components of the IR and R PPG signals are pre-processed by the ANC algorithm. HR and  $\text{SpO}_2$  values are then computed from the adaptively filtered PPG signals.

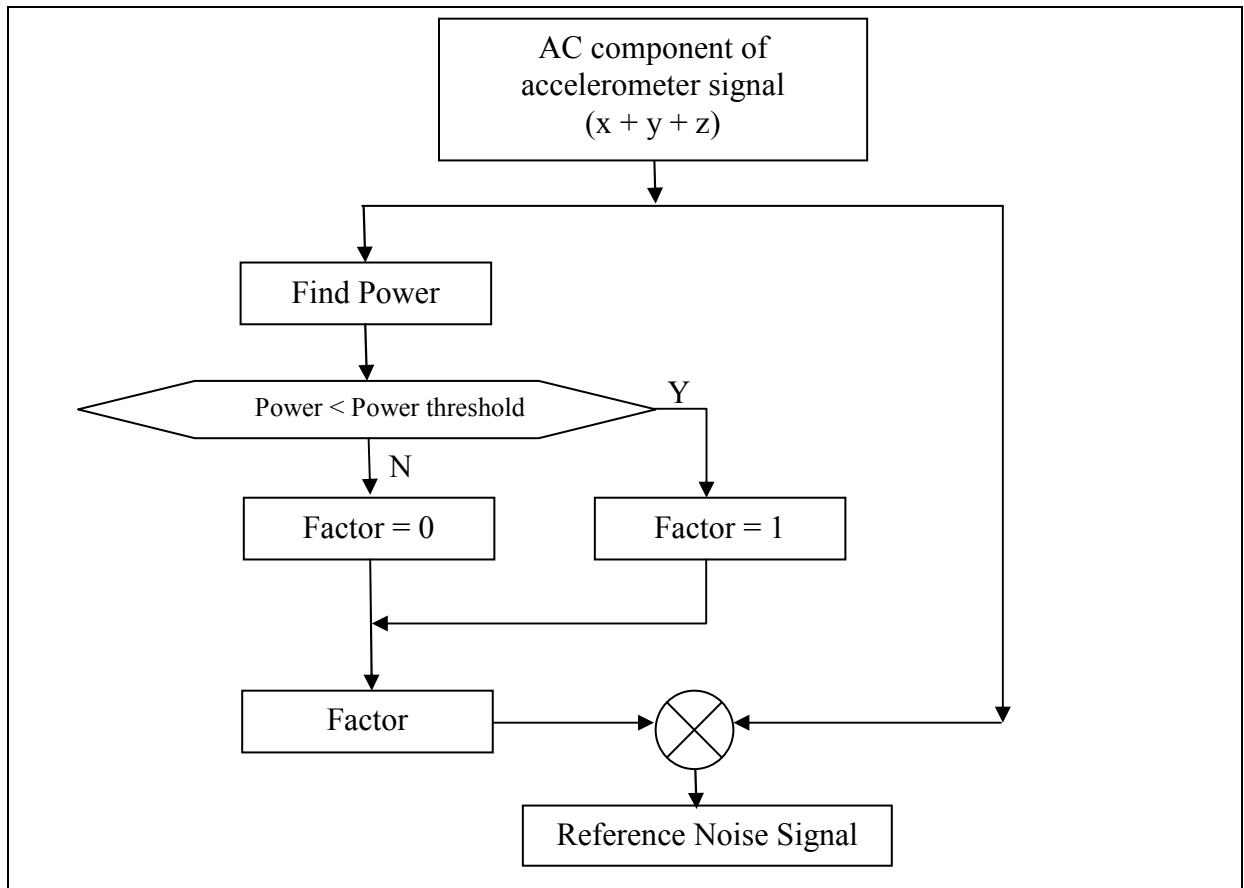


Figure 5.3: Proposed ANC-triggered algorithm.



The WPO's HR and SpO<sub>2</sub> estimation algorithms are based on signal processing methods described by Johnston [1]. The algorithms designed by Johnston were modified to improve their noise rejection capabilities and measurement accuracy. Figure 5.4 shows the modified HR and SpO<sub>2</sub> estimation algorithms.

In the HR and SpO<sub>2</sub> estimation algorithms, HR values are solely derived from the AC component of the IR PPG signal. SpO<sub>2</sub> values are estimated from the AC and DC components of the corresponding IR and R PPG signals. For each data sample, the algorithm calculates all the values of block 1 in Figure 5.4. The calculation process is interrupted if IR PPG slope toggles from a positive to a negative value, i.e. it crosses the zero-line, representing a cardiac beat. The time interval between two consecutive cardiac beats is inversely proportional to HR. False peaks are excluded from the calculation process by using several threshold conditions. A peak is considered as a true heart beat if it satisfies all the threshold conditions.

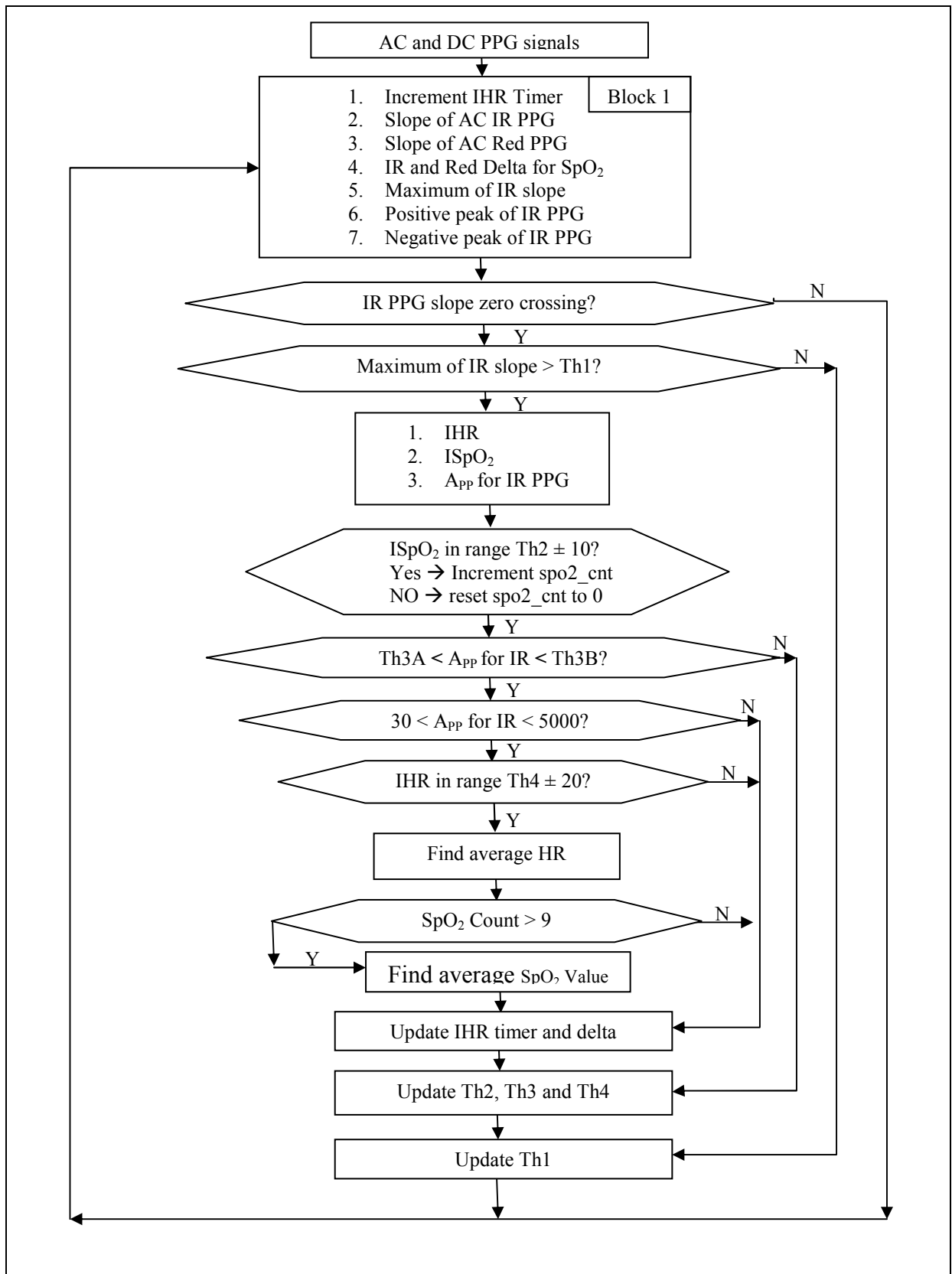


Figure 5.4: HR and SpO<sub>2</sub> estimation algorithm.

After zero-crossing detection, if the amplitude of the IR PPG slope is greater than a certain threshold level, *Th1*, then the algorithm calculates the IHR, ISpO<sub>2</sub> and IR peak-to-peak amplitude. As depicted in Table 5.1, the *Th1* value is determined based on the average of previous 10 amplitudes of the IR PPG slope. To preclude sudden changes in ISpO<sub>2</sub> and IHR values, two new threshold conditions (labeled *Th2* and *Th4* in Figure 5.4) are included in the algorithm. An ISpO<sub>2</sub> (and IHR) value, significantly (as illustrated in Table 5.1) lower or higher than the average SpO<sub>2</sub> (and HR) value is discarded in the averaging process. These modifications report more accurate SpO<sub>2</sub> and HR values.

Typically, PPG signals exhibit a sinusoidal characteristic having similar amplitude variations (see Figure 2.3). Rapid fluctuations in the peak-to-peak amplitude are generally induced due to artifacts and may result in erroneous measurements. Threshold conditions based on amplitude variations are utilized to minimize the detection of spurious cardiac peaks. These threshold conditions (*Th3A* and *Th3B*) reject false peaks to improve the estimation of HR and SpO<sub>2</sub> values. Additionally, PPG data analysis showed that in the current version of the WPO, the typical amplitude of PPG signals ranges between 30 to 5000 units (relative amplitude). Thus, as an extra precautionary step, peaks with peak-to-peak amplitude outside this range were not included in HR and SpO<sub>2</sub> estimations.

Table 5.1: Threshold condition used in HR and SpO<sub>2</sub> estimation algorithm

Threshold Condition	Formula	Effects
Th1	60% * Average of previous 10 peak-to-peak amplitude of IR PPG slope	HR and SpO <sub>2</sub>
Th2	Average SpO <sub>2</sub> values ± 10	SpO <sub>2</sub>
Th3A	40% * Average of previous peak-to-peak amplitude IR PPG	HR and SpO <sub>2</sub>
Th3B	200% * Average of previous peak-to-peak amplitude IR PPG	HR and SpO <sub>2</sub>
Th4	Average HR values ± 20	HR and SpO <sub>2</sub>

All of the threshold conditions affirm that only true cardiac peaks are used in HR and SpO<sub>2</sub> estimation. False peaks, due to motion artifacts, would not satisfy these threshold requirements and will thus be attenuated. As the physiological characteristics differ from person to person, the threshold values cannot be static. Therefore, the threshold conditions devised in our signal processing algorithm are dynamic, so the values adapt according to the user. This makes the WPO system user compatible, robust and more reliable. Several experiments were conducted to assess the accuracy of our signal processing algorithm and are discussed in the later part of this thesis.

## 6. RESEARCH OBJECTIVES

The goal of this research was to investigate if adaptive filtering using a tri-axial accelerometer can be employed in a real-time pulse oximetry system to improve HR and SpO<sub>2</sub> measurement accuracy during motion. The specific research objectives were:

**Objective 1:** To validate the accuracy of HR and SpO<sub>2</sub> estimation algorithm used by the WPO under resting conditions and compare its performance with the MPO.

**Objective 2:** To evaluate in Matlab conventional LMS, time-varying LMS, normalized LMS, modified-normalized LMS and RLS algorithms, and compare these ANC algorithms in terms of accuracy and processing time.

**Objective 3:** To implement the best ANC algorithm in a TI-MSP430  $\mu$ C for real-time filtering of motion-corrupted PPG signals utilizing reference signals obtained from a tri-axial accelerometer.

**Objective 4:** To verify the functionality of an ANC-triggered algorithm developed to improve power consumption by avoiding unnecessary signal processing.

## 7. EXPERIMENTAL SETUP

### 7.1. Resting Experiments

A few indoor experiments were conducted to verify the WPO's measurement accuracy during rest. Three apparently healthy male individuals volunteered for this study. All subjects were non-smokers with age ranging from 22-25 years.

Data were collected from a forehead-mounted WPO developed in our laboratory. Raw IR PPG, R PPG and tri-axial body acceleration (X, Y, and Z) signals were collected from the WPO using a Bluetooth enabled serial port. A custom program was utilized to store the 16-bit digital data sampled at 80Hz. For validation, reference SpO<sub>2</sub> and HR values were obtained from a fore-head worn Masimo Pulse Oximeter (MPO).

We have used the MPO as a reference pulse oximeter as it employs advanced signal extraction technology (SET) for SpO<sub>2</sub> and HR estimation. Details on how SET processes incoming signals are not available because SET algorithm is highly proprietary. But, as per the specification sheet, the MPO provides accurate HR and SpO<sub>2</sub> readings with  $\pm 2$ BPM and  $\pm 2\%$  error during rest.

Figure 7.1 shows the experimental setup for the initial bench testing of the WPO. To assess the correlation between the reference and measured HR & SpO<sub>2</sub> values, subjects were instructed to perform a breath-holding maneuver to induce hypoxemia. SpO<sub>2</sub> values were monitored during each hypoxic maneuver to ensure a detectable drop in oxygen level. If a significant drop was not induced, the datum was discarded and the experiment was repeated. Additionally, in some trials individuals were instructed to hyperventilate in an attempt to increase their HR values. This allowed comparing the values over a wide physiological range. A total of 12 successful data sets were recorded for about 3 minutes; 9 with breath-holding maneuver and 3 with hyperventilation.

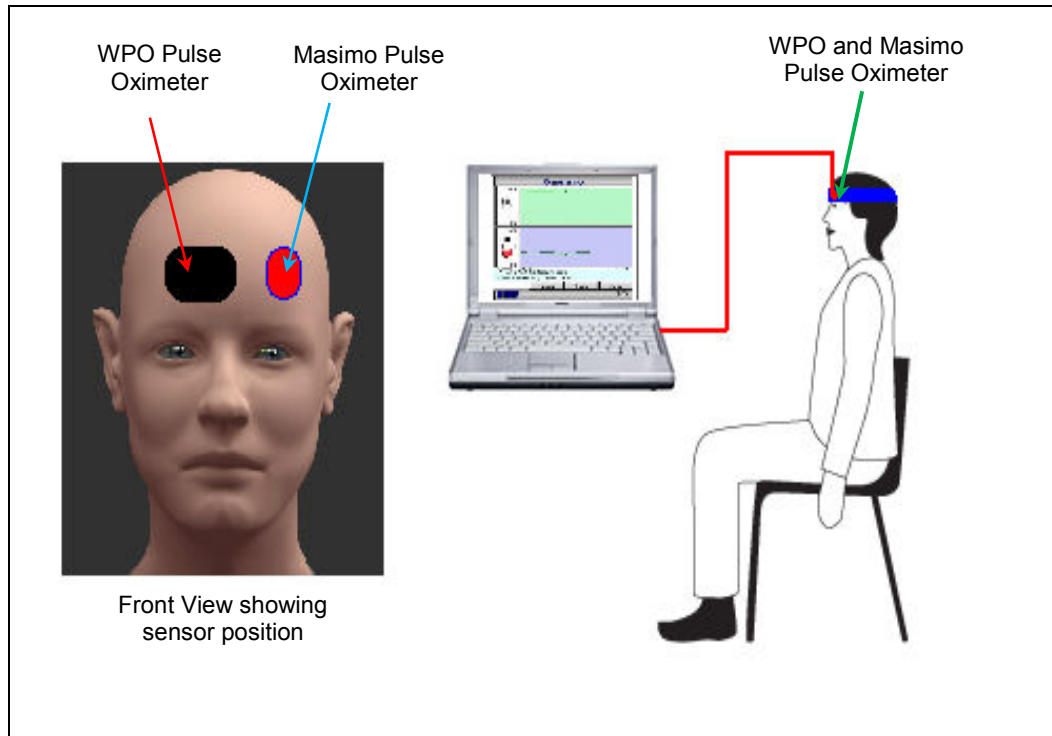


Figure 7.1: Experimental setup for initial bench testing of the WPO.

Next, in an effort to understand and develop means to reduce the effects of motion artifacts, data sets were collected while subjects were performing various physical activities. For these experiments, reference HR readings were acquired from a 3-lead Holter ECG monitor. Alcohol prep pads were used to cleanse the skin before attaching the ECG electrodes. The ECG signals were processed in Matlab to detect each R-wave and accurately calculate HR values.

The optical sensor of the MPO was placed on the right index finger to obtain reference  $SpO_2$  values. During data collection, subjects were asked to keep their index finger as stationary as possible so that the reference readings from the MPO were not affected by motion. No additional constraints were imposed on other body parts. In some trials, the MPO reported sudden erroneous drops in  $SpO_2$  values due to heavy motion. For such trials,  $SpO_2$  readings recorded at the start of motion were used as a reference. This approach of data holding is acceptable for this study as there should be no drop in  $SaO_2$  due to physical activities performed during this study. Additionally, HR readings recorded from the MPO were also included to show that even the signal extraction technique (SET) employed by Massimo to process noisy PPG signals failed to

produced accurate readings in the presence of motion artifacts. The experimental setup is illustrated in Figure 7.2.

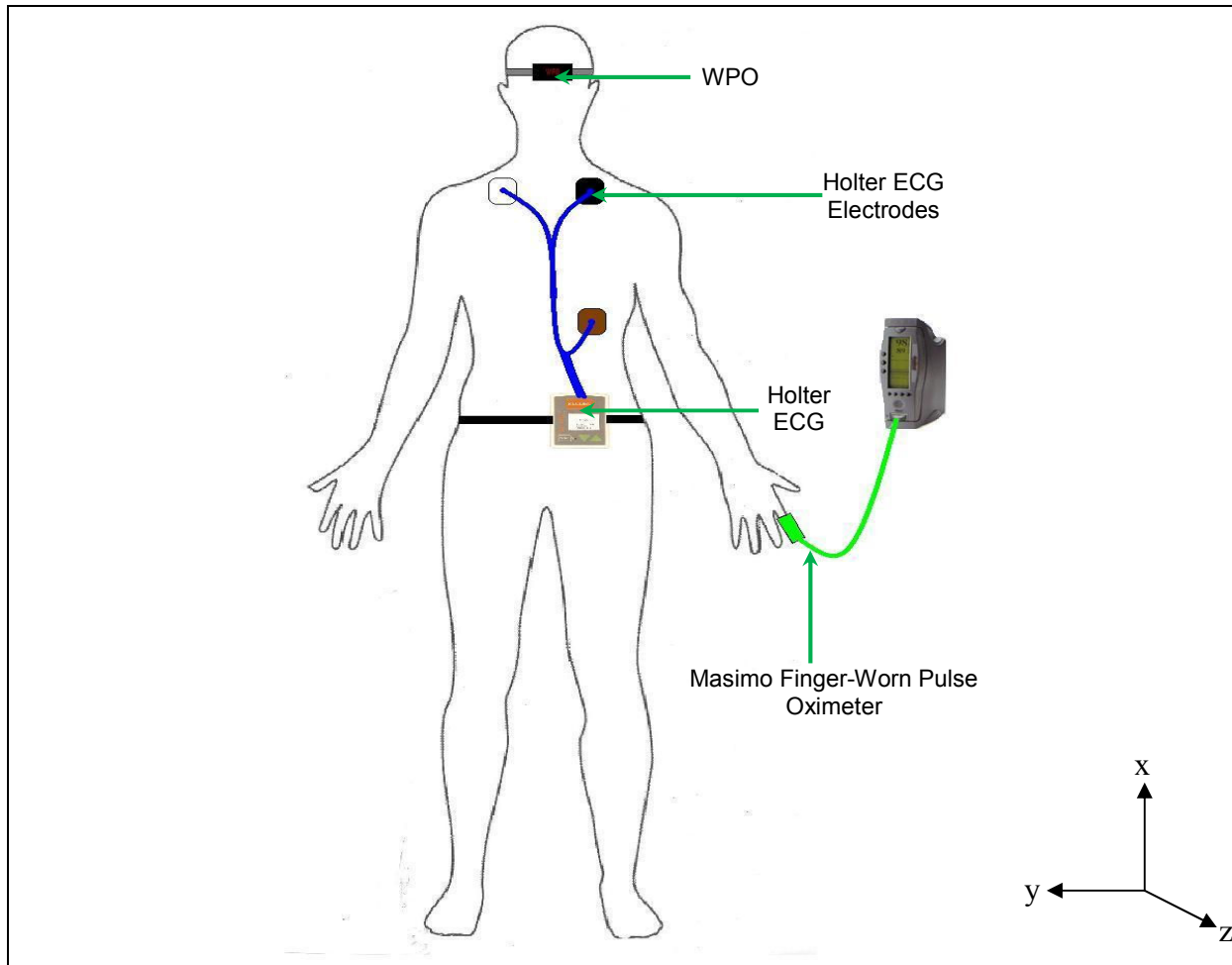


Figure 7.2: Experimental setup for data acquisition



## 7.2. Sitting Experiments

Physical activities such as running and staircase climbing were used to mimic typical activities performed by a soldier or firefighter. Along with rapid changes in HR, these activities also introduce motion artifacts. To determine the effects of motion artifacts on WPO accuracy, 9 data sets were collected from 3 subjects (3 trials per subject) while they were sitting on a chair. The experimental setup is shown in Figure 7.3.

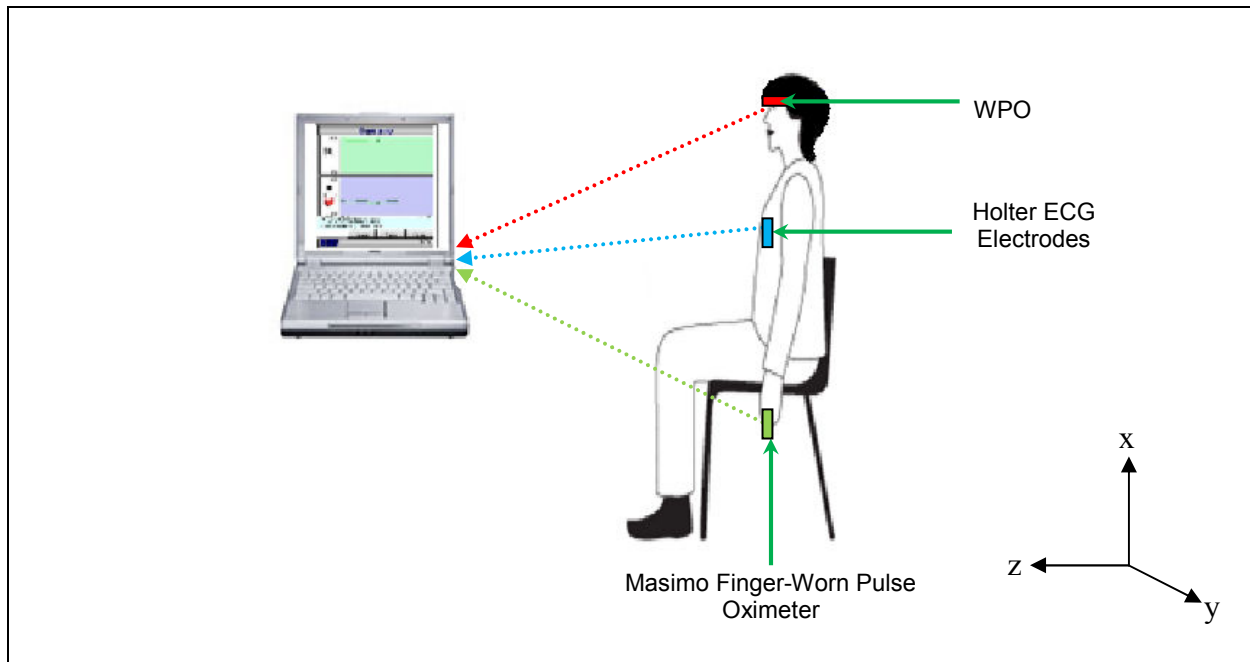


Figure 7.3: Experimental setup for data collection (sitting position).

During data collection, subjects were instructed to sit upright and breathe spontaneously. To induce motion artifacts, subjects were asked to perform three kinds of head movements. For the initial 30 seconds, subjects sat straight without any head movement. Next, subjects were asked to perform horizontal, vertical and rotational head movement for a period of 30 seconds each. This allowed us to evaluate the effects of motion on the PPG signals along all three possible axes. The timings for the sitting experiments are given in Table 7.1.

Table 7.1: Time frame for sitting experiments (one set)

Phase	Time	Subjects status
1	0 – 30 seconds	Resting
2	30 – 60 seconds	Horizontal head movement
	60 – 90 seconds	Vertical head movement
	90 – 120 seconds	Rotational head movement
3	120 – 150 seconds	Resting

### 7.3. Cycling Experiments

Data were collected from subjects while they were performing cycling exercises on a stationary bicycle. Cycling on a stationary bike hardly involves any head movement. Therefore, the collected PPG signals were affected only by rapid HR changes. This enabled us to determine if rapid HR changes affected the measurement accuracy of the WPO.

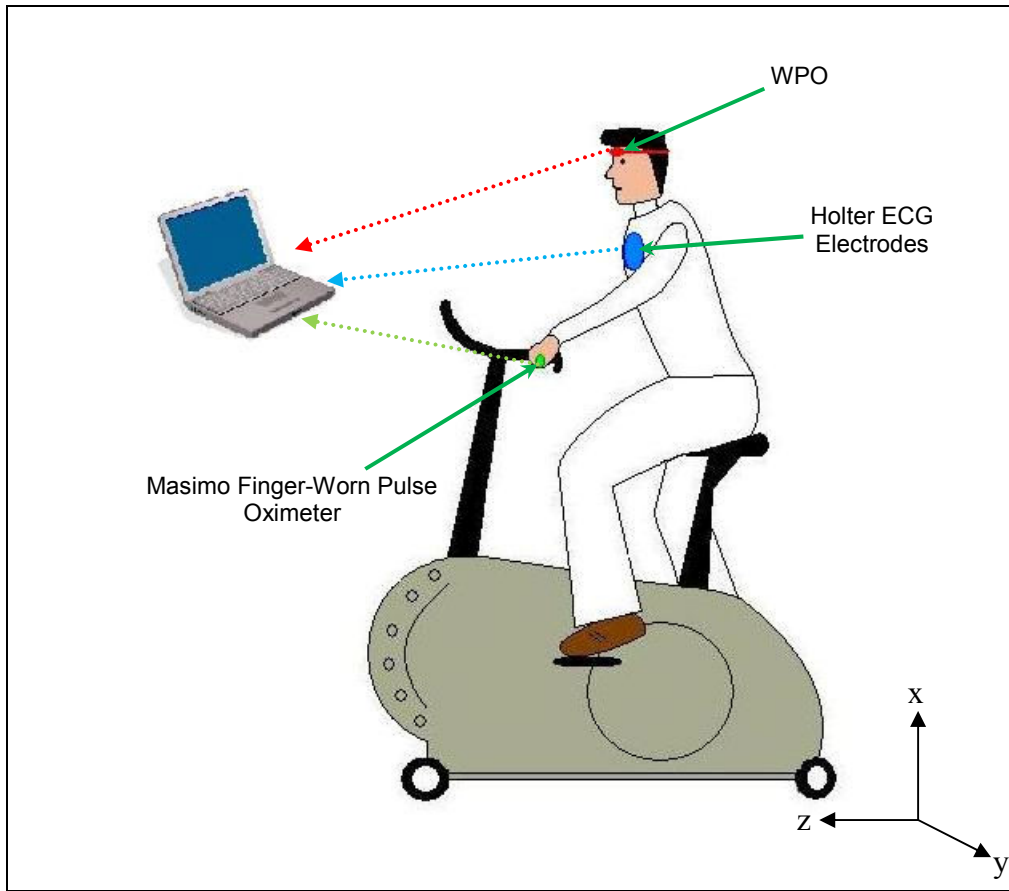


Figure 7.4: Experimental setup for cycling experiments.

For cycling experiments, 6 data trials were collected from 3 subjects. During the data collection process, subjects were seated comfortably on a stationary bicycle as illustrated in Figure 7.4. Initially, subjects were asked to sit still for 60 seconds. Subsequently, subjects were asked to perform cycling exercise for a period of 60 seconds. This again was followed by a 60 seconds of rest. The time frames for the cycling experiments are given in Table 7.2.

Table 7.2: Time frame for cycling experiments (one set)

Phase	Time	Subjects status
1	0 – 60 seconds	Resting
2	60 – 120 seconds	Cycling
3	120 – 200 seconds	Resting

#### 7.4. Treadmill Jogging, Outdoor Running and Staircase Climbing Experiments

We also collected data during treadmill jogging, outdoor running and staircase climbing as these activities mimic, more realistically, the type of motion artifacts produced during field operations. For treadmill jogging experiments, 9 trials were collected from 3 subjects. Subjects were asked to run at 2mph and 4mph. Figure 7.5 shows the experimental setup for data collection during treadmill jogging. The timings for the treadmill jogging experiments are tabulated in Table 7.3.

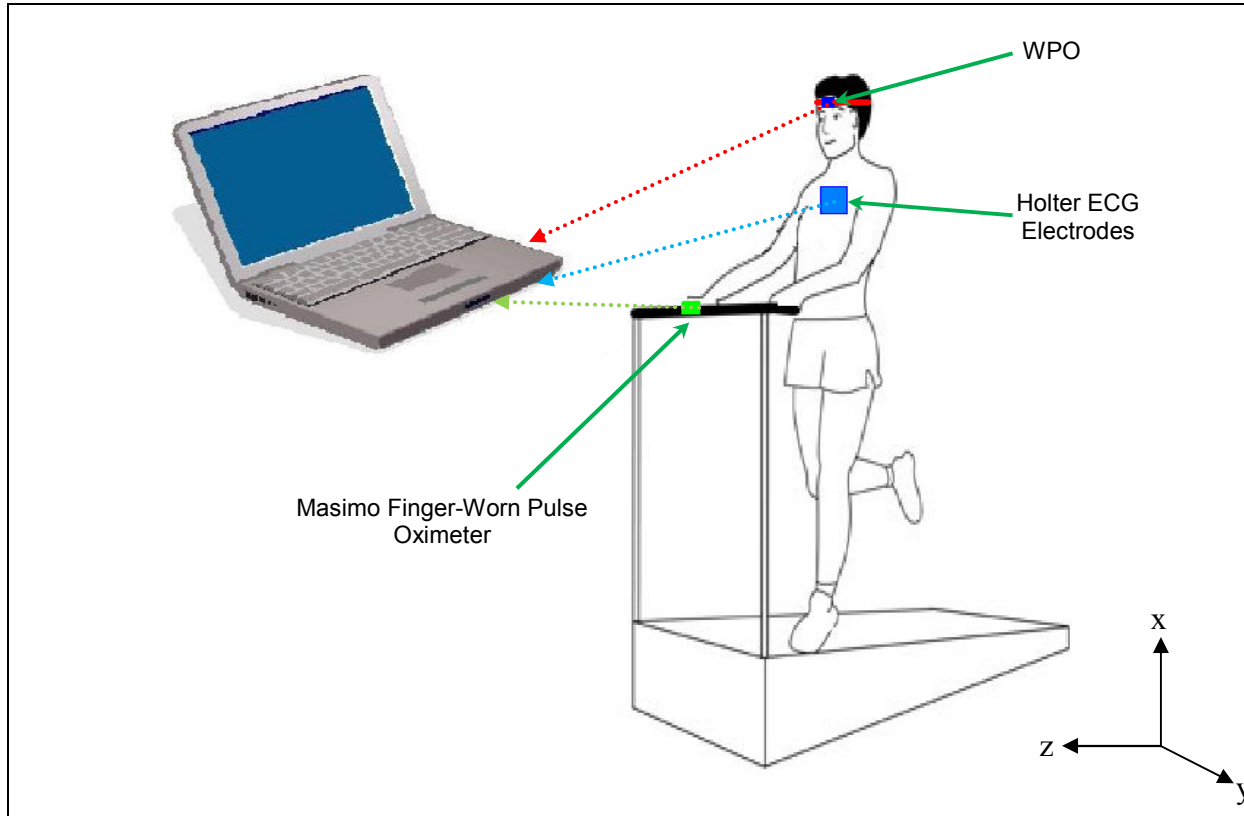


Figure 7.5: Experimental setup for data collection during treadmill jogging.

Table 7.3: Time frame for treadmill jogging experiments (one set)

Phase	Time	Subjects status
1	0 – 30 seconds	Resting
2	30 – 90 seconds	Running @ 2mph
3	90 – 180 seconds	Running @ 4mph
4	180 – 240 seconds	Running @ 2mph
5	240 seconds onwards	Resting

Similarly, 9 data sets were collected from 3 subjects while they were running outdoors. PPG data were acquired from subjects during 60 seconds of running framed by 60 seconds of resting. Table 7.4 shows the timings for the running experiments.

Table 7.4: Time frame for running experiments (one set)

Phase	Time	Subjects status
1	0 – 60 seconds	Resting
2	60 – 120 seconds	Running
3	120 – 200 seconds	Resting

Finally, 6 data sets were collected from 3 subjects (2 trials each) while running up and down a staircase. Subjects were asked to run up and down the staircase for a period of 60 seconds. The timings for the staircase climbing experiments are given in Table 7.5.

Table 7.5: Time frame for staircase experiments (one set)

Phase	Time	Subjects status
1	0 – 60 seconds	Resting
2	60 – 120 seconds	Staircase climbing
3	120 – 200 seconds	Resting

### 7.5. Real-Time ANC

As the focus of this research was to investigate the feasibility of implementing an ANC algorithm in a real-time pulse oximeter, a few data sets were collected from the WPO that was programmed with ANC. As seen in Figure 7.6, two WPO sensors were mounted side-by-side on the subjects' forehead. One of the two WPOs had an ANC algorithm to minimize the effects of motion artifacts, whereas, the other WPO was without an adaptive filtering algorithm. The HR and SpO<sub>2</sub> estimation algorithms were the same in the two WPOs.

To evaluate the performance of the ANC, 6 data sets were collected in a sitting position and 9 data sets were collected during treadmill jogging. These data sets were acquired from 3 subjects. Raw PPG data were not collected for these 15 trials due to processing time constraints in the current WPO version. Instead, final HR and SpO<sub>2</sub> values were recorded at the rate of one value per second. The timings for the sitting and treadmill jogging experiments are given in Table 7.1 and Table 7.3, respectively.

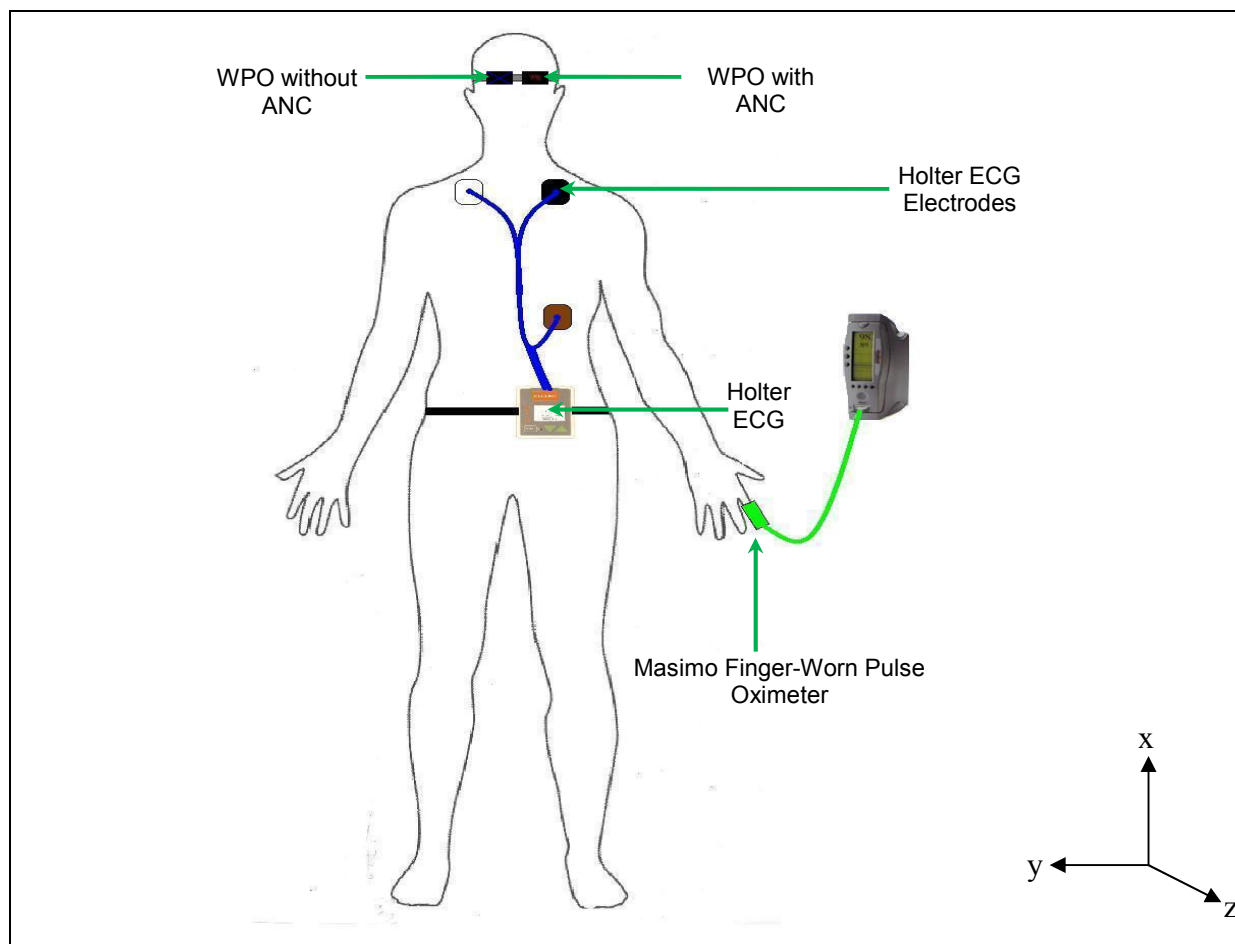


Figure 7.6: Experimental setup for data collection while testing real-time adaptive filtering.

## 8. RESULTS

### 8.1. Resting Experiments

HR and SpO<sub>2</sub> values were derived from IR and R PPG signals utilizing a custom signal processing algorithm explained in chapter 5. Figure 8.1 shows representative HR readings obtained during rest followed by a voluntary hypoxic period. HR readings recorded during hyperventilation are plotted in Figure 8.2. These figures demonstrate that HR readings obtained from the WPO and reference readings recorded from the MPO followed a similar trend. Figure 8.3 confirmed that SpO<sub>2</sub> values reported by the WPO closely track the readings obtained from the MPO.

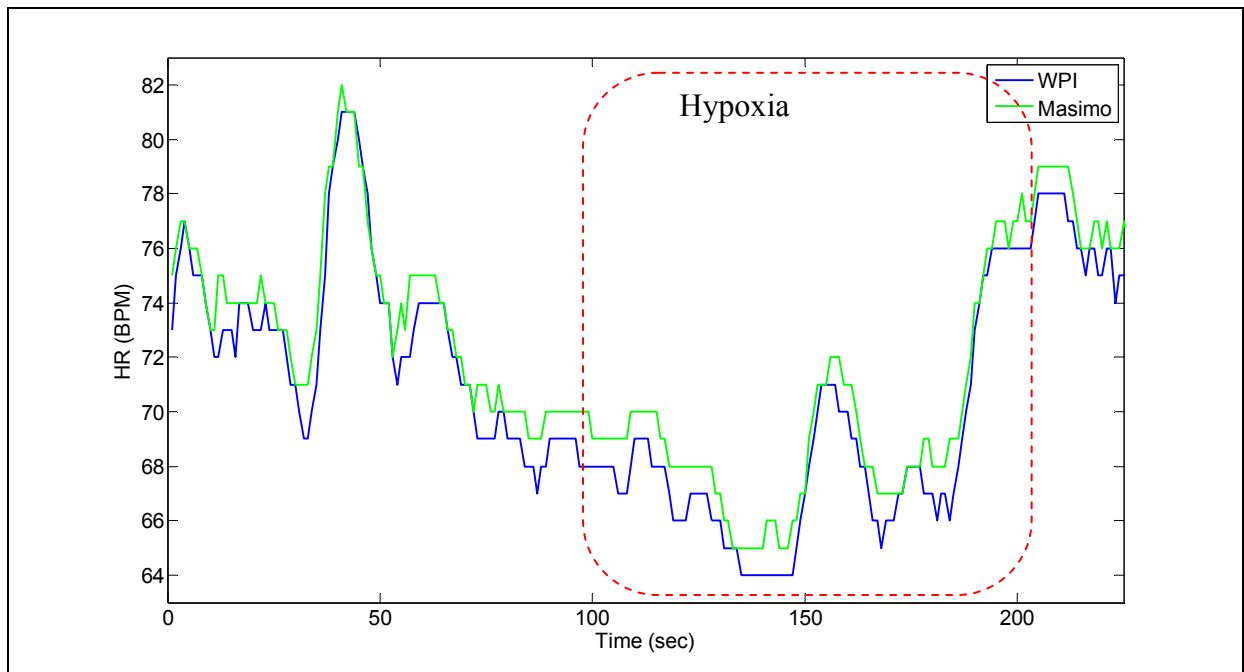


Figure 8.1: Typical HR measured simultaneously from the WPO (blue) and MPO (green) during a resting experiment.

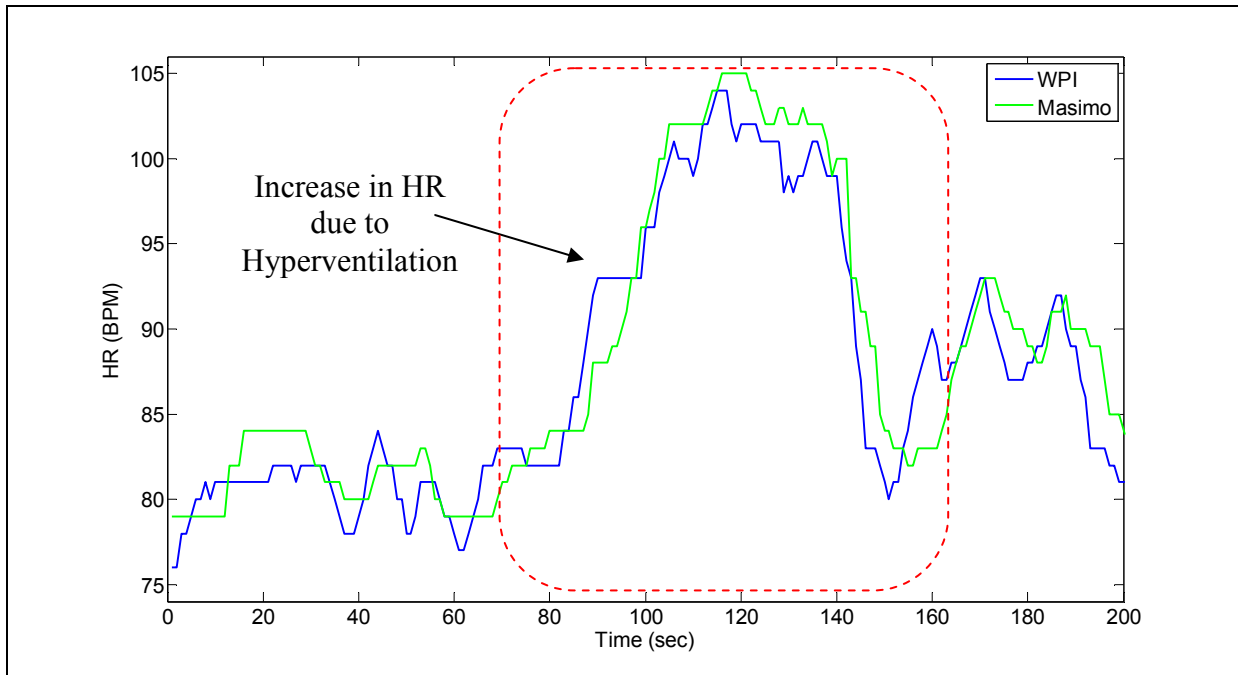


Figure 8.2: Typical HR measured simultaneously from the WPO (blue) and MPO (green) during a resting experiment. The highlighted region marks the period of hyperventilation that resulted in increase in HR values.

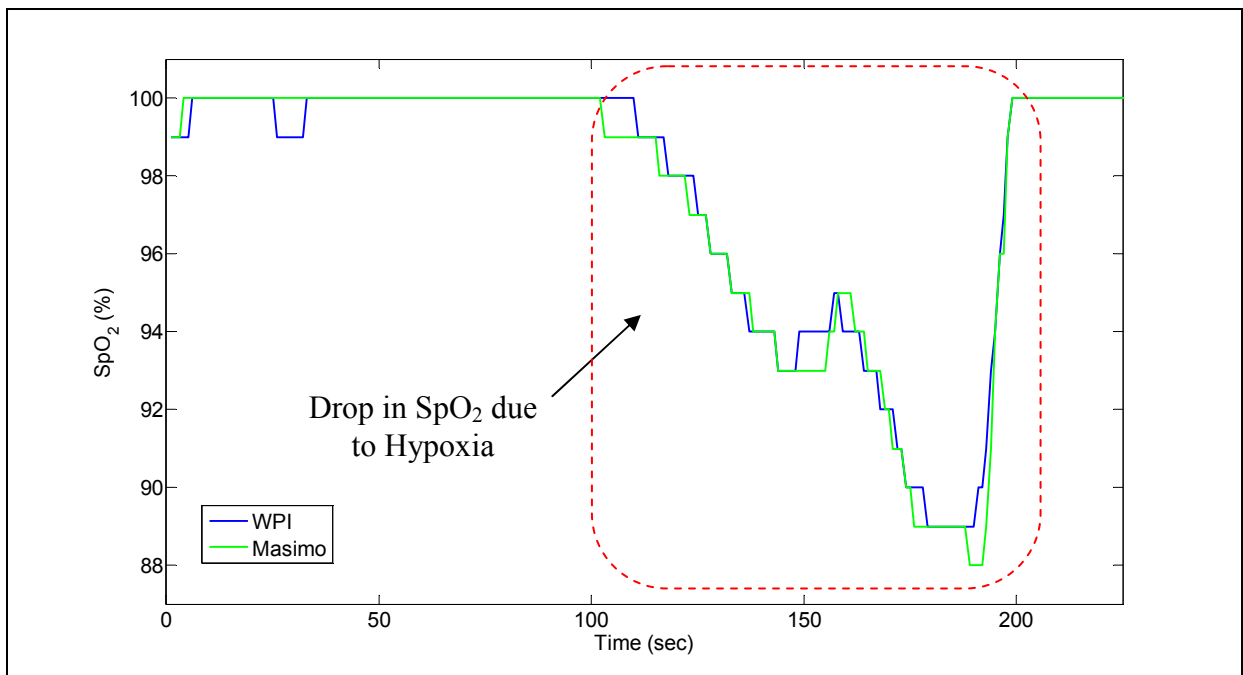


Figure 8.3: Typical SpO<sub>2</sub> measured simultaneously from the WPO (blue) and MPO (green) during a resting experiment. The highlighted region marks the breath holding episodes to induce hypoxia.



Regression analysis was performed to estimate the correlation between the WPO and MPO. The regression plot for HR values obtained from the WPO and MPO is presented in Figure 8.4. The CC between the WPO and MPO readings was 0.99. Figure 8.5 and Figure 8.6 plots the differences in HR and SpO<sub>2</sub> readings obtained from the WPO and MPO. The WPO – MPO difference is plotted against the reference readings from the MPO. For SpO<sub>2</sub> readings, the mean difference between the WPO and MPO was approximately 1%. Results for individual trials are summarized in Table 8.1. These results indicate that HR and SpO<sub>2</sub> values estimated by our signal processing algorithm using the WPO are in close agreement with the readings obtained from the MPO.

In regression plots, the color chart on the right represents the frequency of data points. The vertical bars indicate  $\pm 1$  SD. Additionally, the regression line (solid black) and the line of identity (dashed-black trace) are plotted for direct comparison of values obtained from the WPO and MPO.

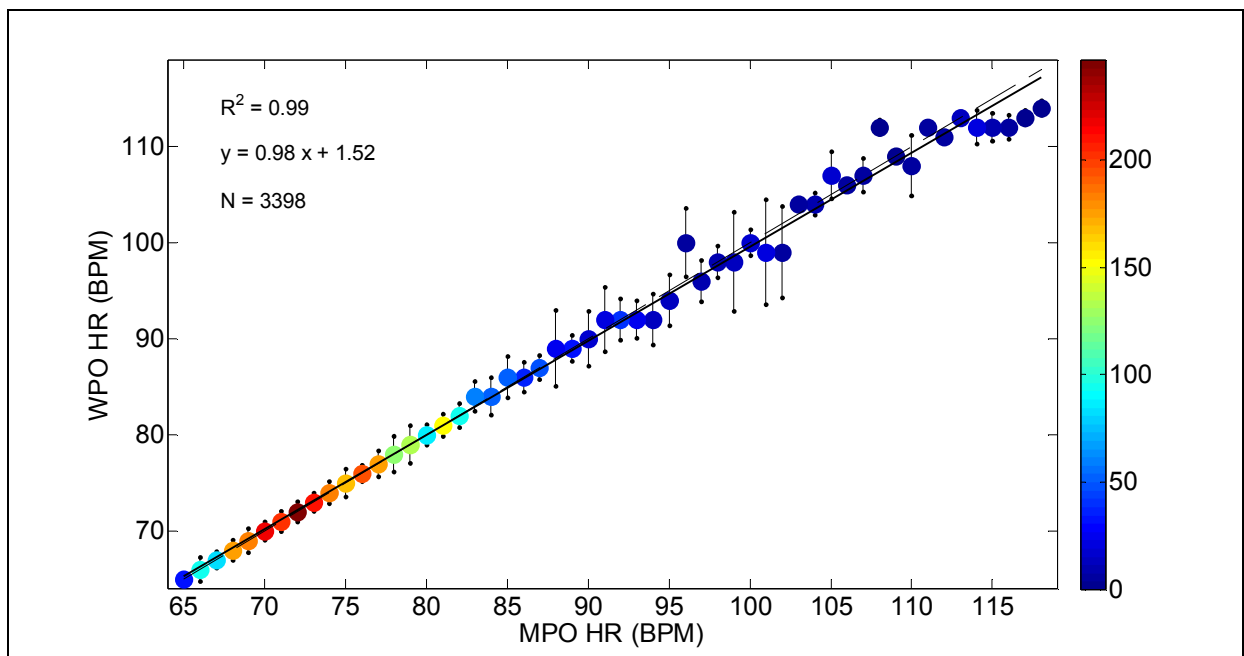


Figure 8.4: Comparison of HR values measured by the WPO and MPO during rest. The color chart on the right represents the frequency of data points.

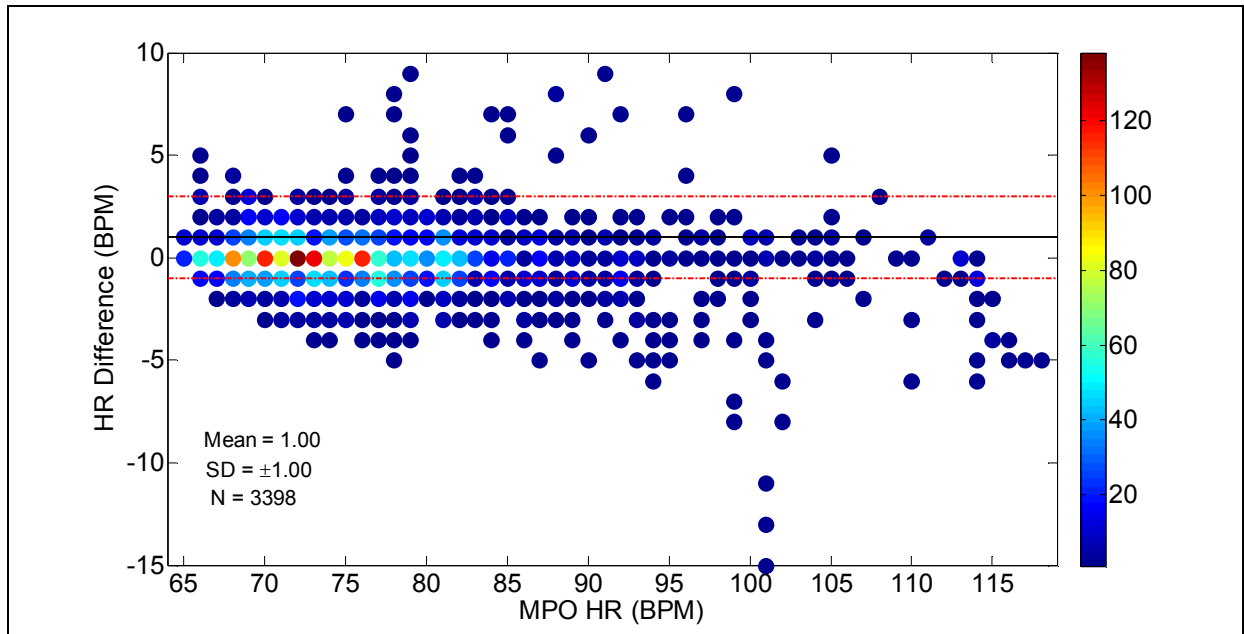


Figure 8.5: Difference between HR readings from the WPO and MPO plotted against MPO values. The red lines indicate  $\mu \pm 2SD$  values.

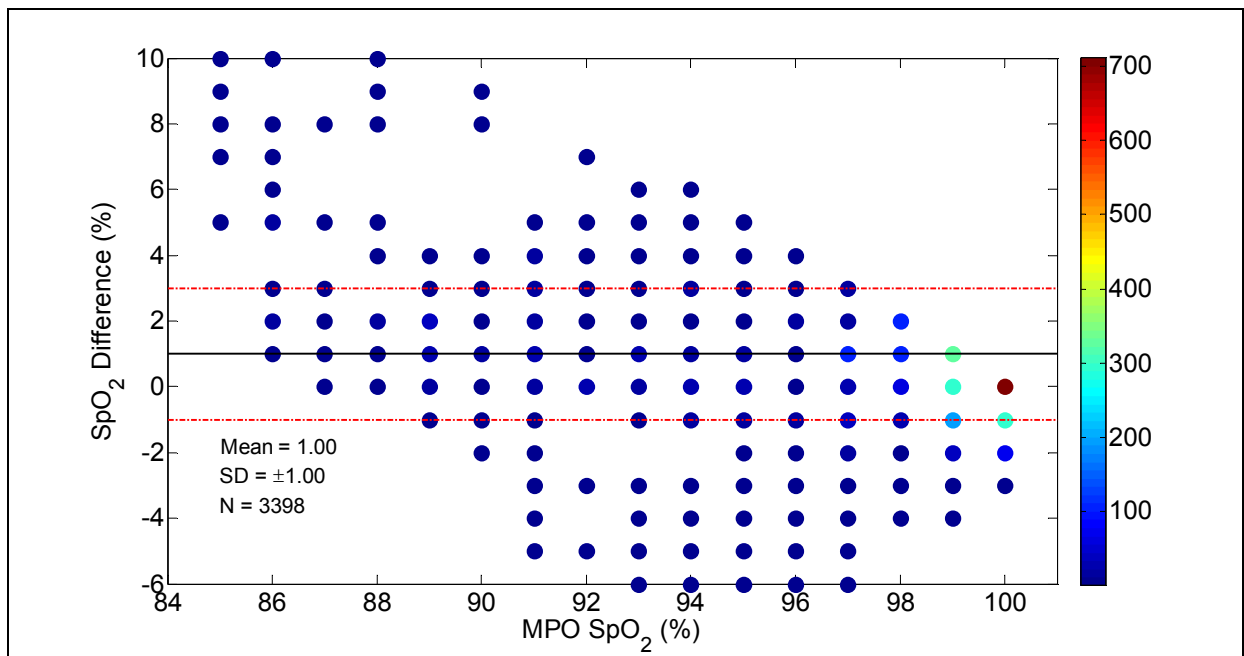


Figure 8.6: Difference between SpO<sub>2</sub> readings from the WPO and MPO plotted against MPO values. The red lines indicate  $\mu \pm 2SD$  values.

Table 8.1: Comparison of HR and SpO<sub>2</sub> values obtained from the WPO and MPO during rest.

Trials	Heart Rate (BPM)			SpO <sub>2</sub> (%)	
	MSE	SD	R <sup>2</sup>	MSE	SD
1	1	1	1	1	1
2	3	1	1	6	2
3*	4	2	1	1	1
4	9	2	1	10	2
5	8	2	1	3	1
6*	1	1	1	0	0
7	2	1	1	1	1
8	1	1	1	11	2
9*	0	1	1	1	1
10	1	1	1	1	1
11	1	1	1	3	1
12	0	1	1	1	1
<b>Average</b>	<b>3</b>	<b>1</b>	<b>1</b>	<b>3</b>	<b>1</b>

Note: \* Represents hyperventilation trial.

## 8.2. LMS Algorithm

### 8.2.1. Step-size ( $\mu$ ) selection

For a conventional LMS algorithm, selection of a constant  $\mu$  is critical since it controls the stability and speed of convergence. A small  $\mu$  leads to slow convergence rate; conversely, a large  $\mu$  leads to large errors. In order to find an optimal  $\mu$  value, several PPG data sets were processed by the LMS filter in Matlab. Data were analyzed with a LMS filter having a fixed order (M) and variable  $\mu$ .  $\mu$  was incremented from 0 to 0.05 in steps of 0.002. A 16<sup>th</sup> order LMS filter was chosen for this study as Comtois [4] showed that improvements in HR and SpO<sub>2</sub> values were almost constant for  $M \geq 16$ .

A similar method was used by Comtois [4] to determine  $\mu$ , but his study comprised of motion generated only during jogging. This study is based on motion artifacts generated during treadmill jogging (7 tests), outdoor running (6 tests), staircase climbing (5 tests), cycling on stationary bicycle (6 tests), and head movements (7 tests). Hence, the  $\mu$  value found from the

above tests is more representative and can be used for ANC during various physical activities rather than just jogging.

The effectiveness of the LMS algorithm with varying  $\mu$  was determined based on improvements in the MSE for HR and SpO<sub>2</sub> estimations. Percentage improvement graphs for HR and SpO<sub>2</sub> values are plotted in Figure 8.7 and Figure 8.8, respectively. HR errors were greatly reduced when  $0 < \mu < 0.03$ . Adaptive filtering reported an average improvement of 40% in SpO<sub>2</sub> readings over the entire range of  $\mu$  values. Given the similar performance, a larger  $\mu$  value was selected to achieve faster adaptation rate. An LMS algorithm having a constant  $\mu$  of 0.01 was selected for adaptive filtering of the PPG signals because this step-size significantly reduced the errors in HR and SpO<sub>2</sub>.

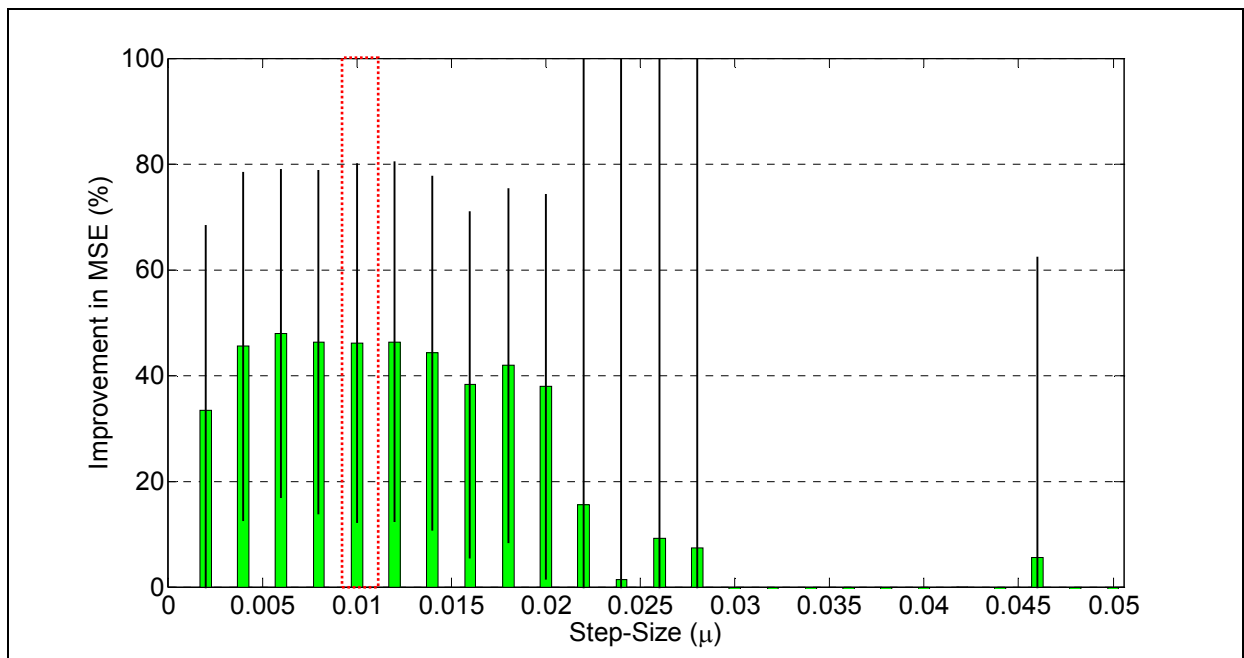


Figure 8.7: Average MSE improvement in HR for a 16<sup>th</sup> order LMS filter with varying step-size ( $\mu$ ). The error bars indicate  $\pm 1SD$ . The shaded region corresponds to  $\mu$  value that was selected for further study.

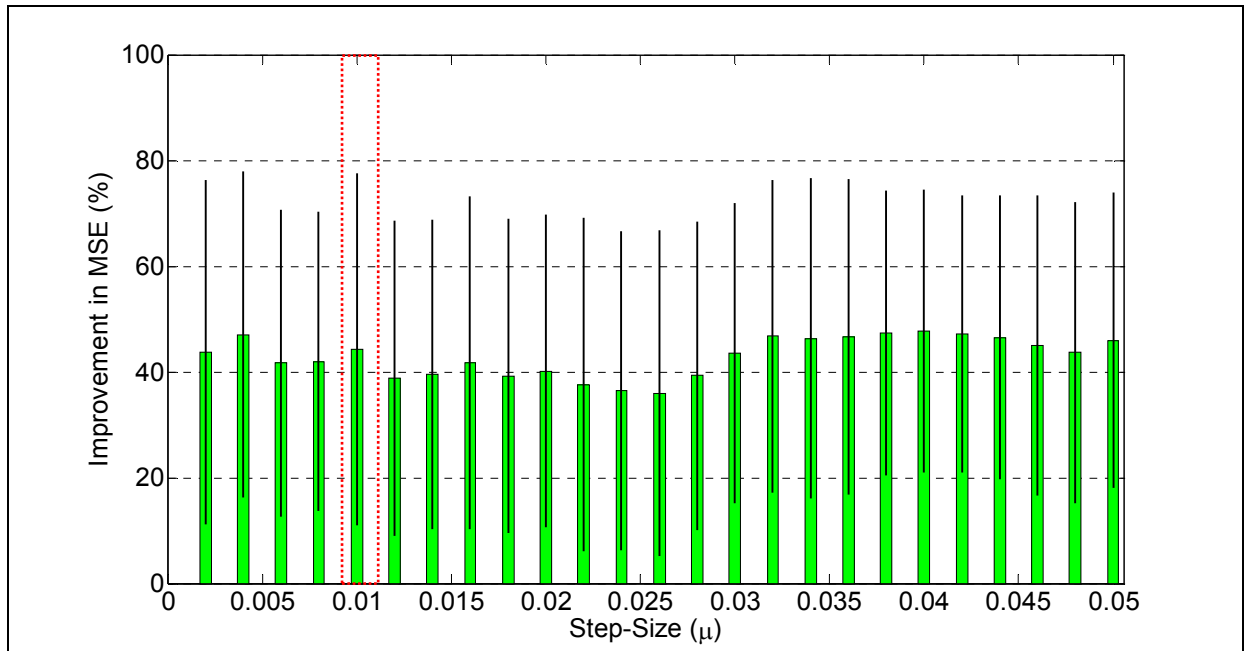


Figure 8.8: Average MSE improvement in SpO<sub>2</sub> for a 16<sup>th</sup> order LMS filter with varying step-size ( $\mu$ ). The error bars indicate  $\pm 1SD$ . The shaded region corresponds to  $\mu$  value that was selected for further study.

### 8.2.2. Filter Order (M) selection

After estimating an optimal  $\mu$  value, the next step in the LMS filter design was to select the filter order (M). To determine an optimal filter order, an approach similar to the one used for estimating  $\mu$  value was followed. A LMS filter with a constant  $\mu$  of 0.01 and varying M was studied in Matlab. M was varied from 0 to 32, where M = 0 implies no adaptive filtering.

For different M values, the percent improvements in HR and SpO<sub>2</sub> are graphically shown in Figure 8.9 and Figure 8.10, respectively. The results confirmed that HR and SpO<sub>2</sub> values estimated after adaptive filtering were more accurate compared to the values estimated before adaptive filtering. With a 16<sup>th</sup> order ANC filter, HR and SpO<sub>2</sub> errors were reduced by 50% and 40%, respectively. These improvements were relatively constant for M > 16.

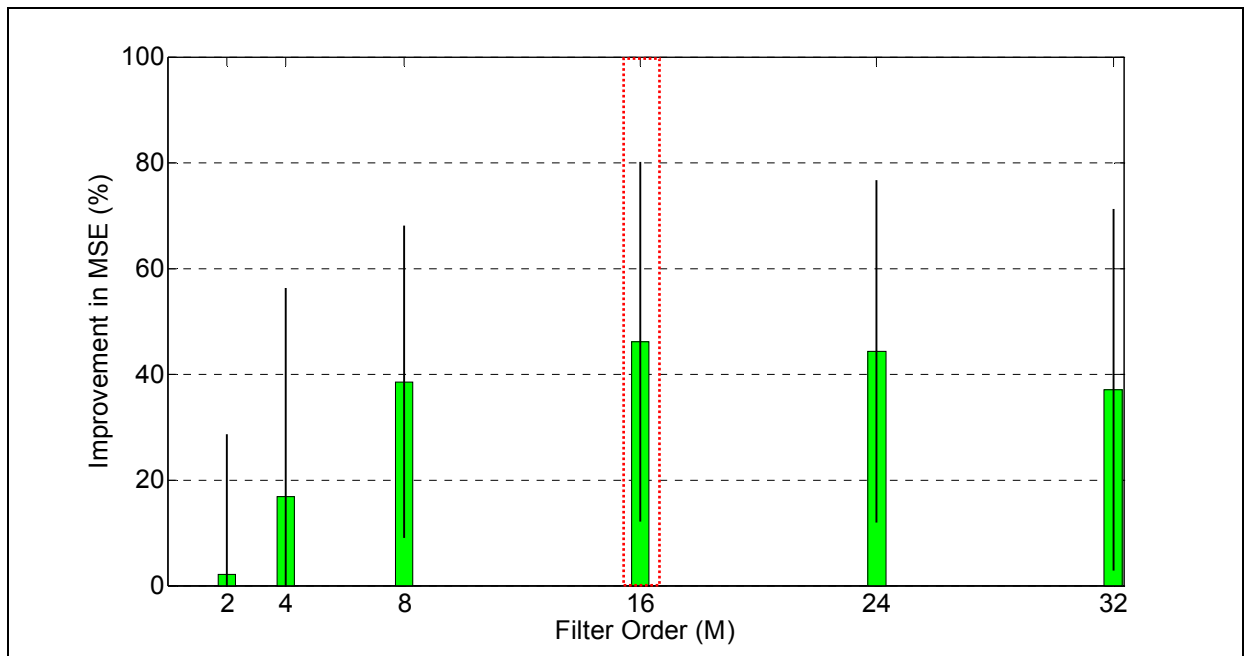


Figure 8.9: Average MSE improvement in HR for a LMS filter with a  $\mu = 0.01$  and varying filter order (M). The error bars indicate  $\pm 1SD$ . The shaded region corresponds to M that was selected for further study.

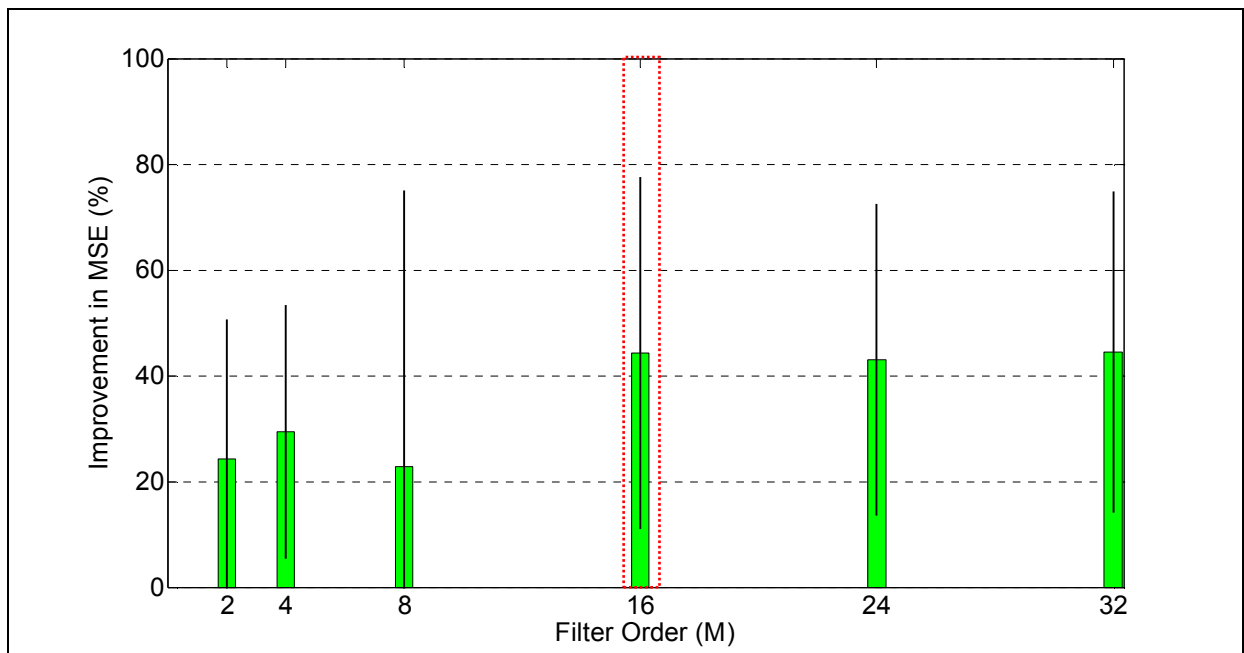


Figure 8.10: Average MSE improvement in SpO<sub>2</sub> for a LMS filter with a  $\mu = 0.01$  and varying filter order (M). The error bars indicate  $\pm 1SD$ . The shaded region corresponds to M that was selected for further study.

### 8.2.3. LMS – Sitting Experiments

Figure 8.11 to Figure 8.13 show the AC component of typical IR PPG signals, the reference acceleration signal from the ACC, and an ECG signal obtained during one of the sitting experiments. During the resting phase of the experiment (Phase-1 and Phase-3), it is evident that the number of cardiac peaks detected by the WPO matches the number of R-waves in the ECG waveform. This again verifies the ability of the WPO to report accurate readings in the absence of motion artifacts.

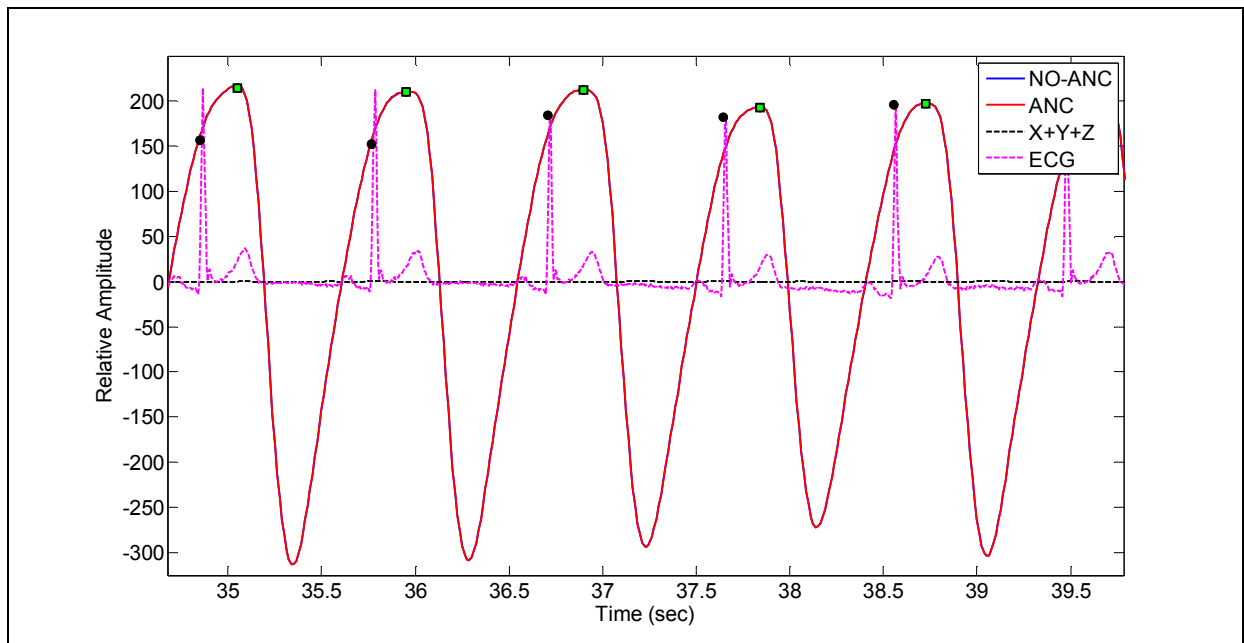


Figure 8.11: Typical IR PPG signals during rest (Phase-1 of sitting experiment), before (Blue) and after (Red) ANC. Note that the blue and red traces completely overlap in this figure. ■ marks PPG peaks detected by the WPO after ANC (6-peaks) and ● denotes R-waves detected from the ECG waveform (6-peaks).

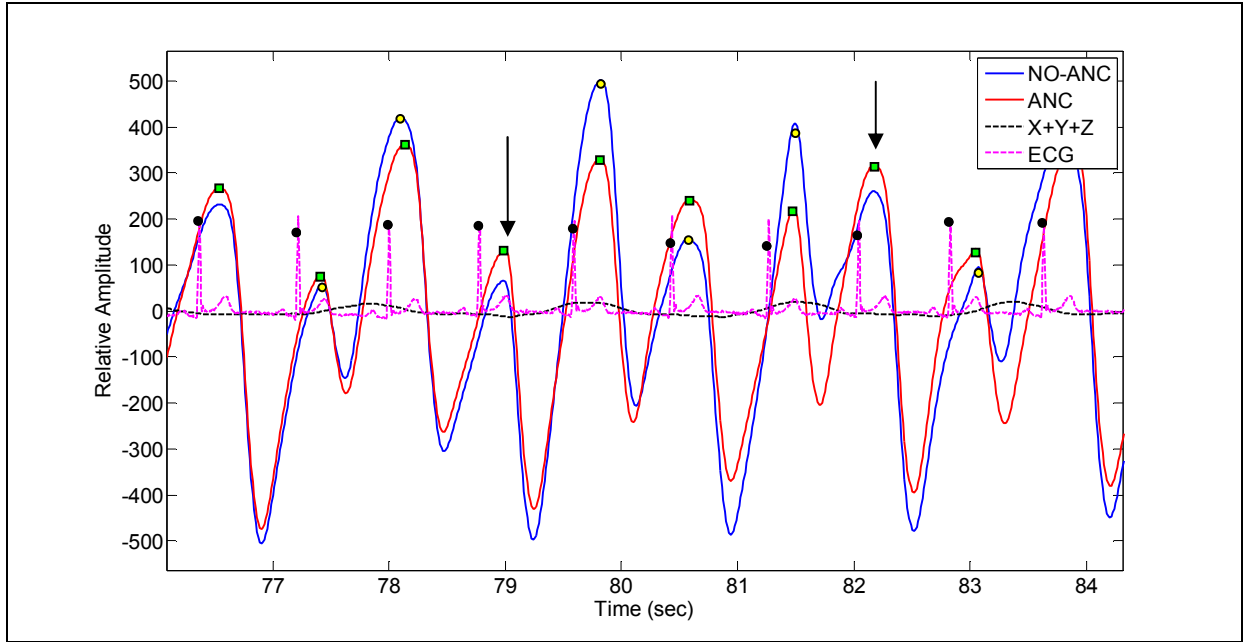


Figure 8.12: Typical IR PPG signals during Phase-2 of sitting experiment, before (Blue) and after (Red) ANC. The arrows indicate the additional peaks that were detected only after adaptive filtering. ■ marks PPG peaks detected by the WPO after ANC (9-peaks), ● denotes PPG peaks detected without ANC (7-peaks), and ● represents R-waves detected from the ECG waveform (9-peaks).

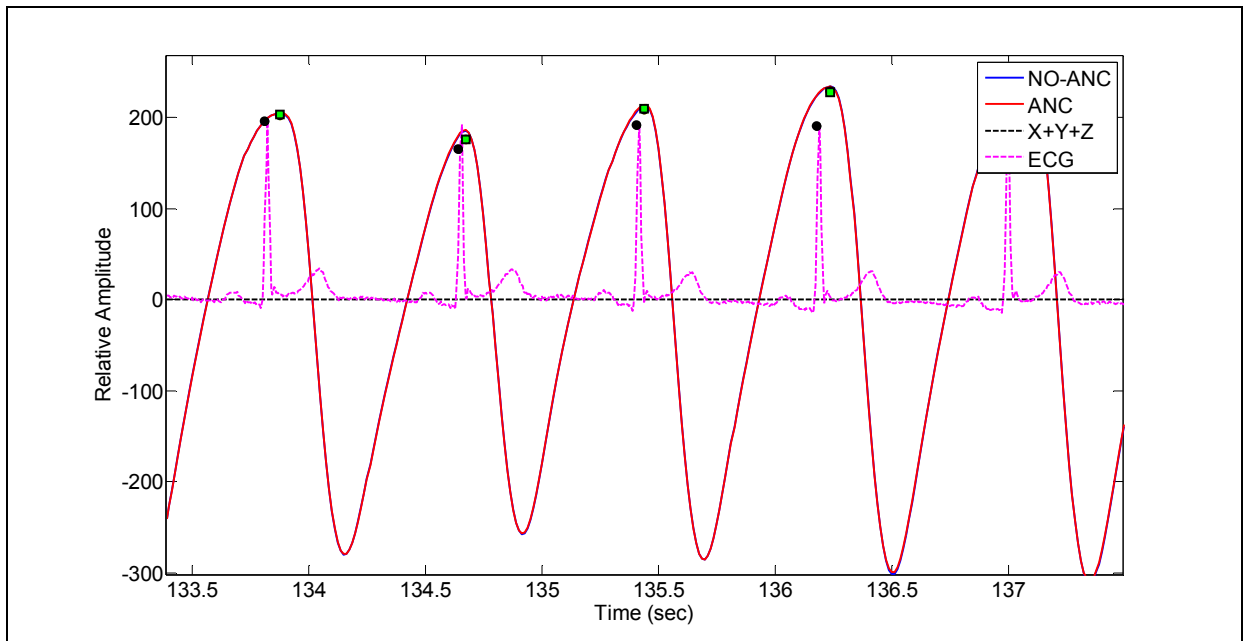


Figure 8.13: Typical IR PPG signals during rest (Phase-3 of sitting experiment), before (Blue) and after (Red) ANC. Note that the blue and red traces completely overlap in this figure. ■ PPG marks peaks detected by the WPO after ANC (4-peaks), and ● represents R-waves detected from the ECG waveform (4-peaks).



During rest, the motion signals from the tri-axial ACC have relatively low amplitude. Hence, the adaptive LMS filter has no significant effect on the PPG signals. During the 2<sup>nd</sup> phase of the experiment, the tri-axial ACC generates high amplitude signals corresponding to the voluntary head movements. These motion signals, when used as reference noise, result in effective filtering of the motion corrupted PPG signals. In Figure 8.12, the arrows indicate the extra peaks that were detected by the WPO after adaptive filtering of the PPG signal. These peaks were not included in the HR and SpO<sub>2</sub> estimation before adaptive filtering due to large variations in the PPG amplitude during motion. The results demonstrate that the LMS algorithm was effective in recovering the clean PPG signal from the motion corrupted signal.

The frequency spectra of the AC components of IR and R PPG signals are shown in Figure 8.14 and Figure 8.15, respectively. Since the subject's HR for this particular trial was in the range of 70BPM – 75 BPM, the PPG frequency spectra showed a dominant cardiac peak between 1Hz and 1.3Hz. Some additional frequency components, between 0.25Hz and 1Hz, are observed in the frequency spectra of the unprocessed PPG signal (blue trace). The body acceleration signal (black trace) verifies that the dominant motion frequency corresponds with the dominant noise frequency present in the PPG signal. Therefore, the primary cause of the reduced measurement accuracy during head motion is due to the contribution of the body acceleration signals to the spectral content of PPG signal. In order words, the adaptive filter attenuated these noise frequencies without distorting the cardiac frequency components, thereby improving the PPG signals quality.

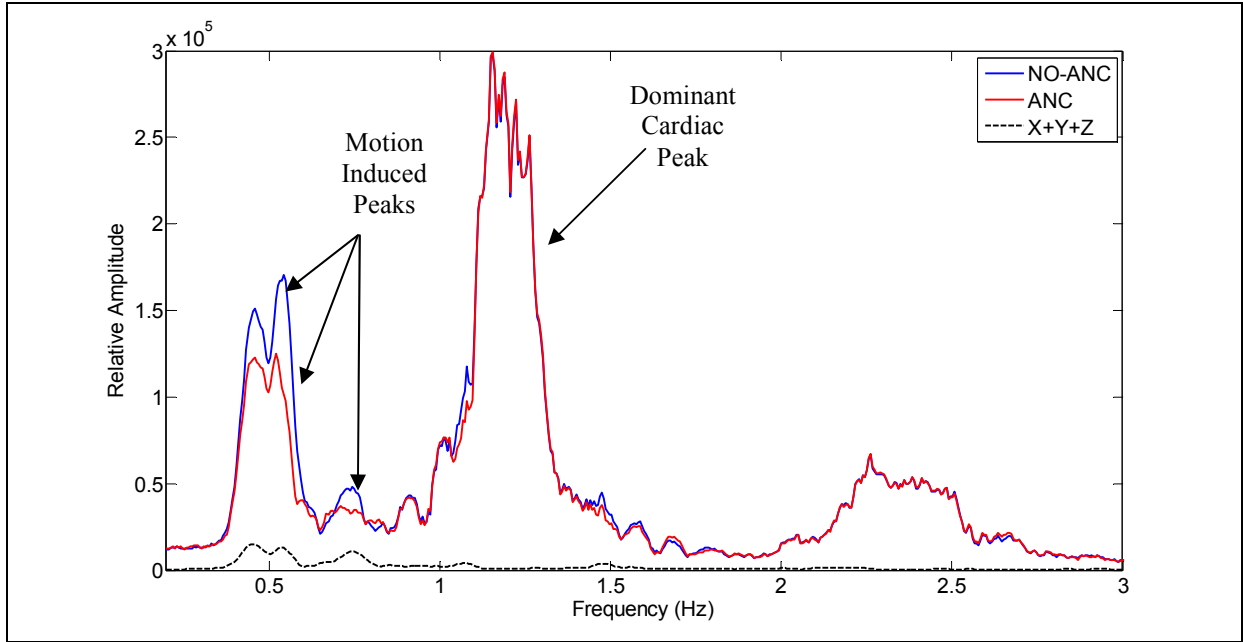


Figure 8.14: Characteristic frequency spectrum of an IR PPG signal during a sitting experiment.

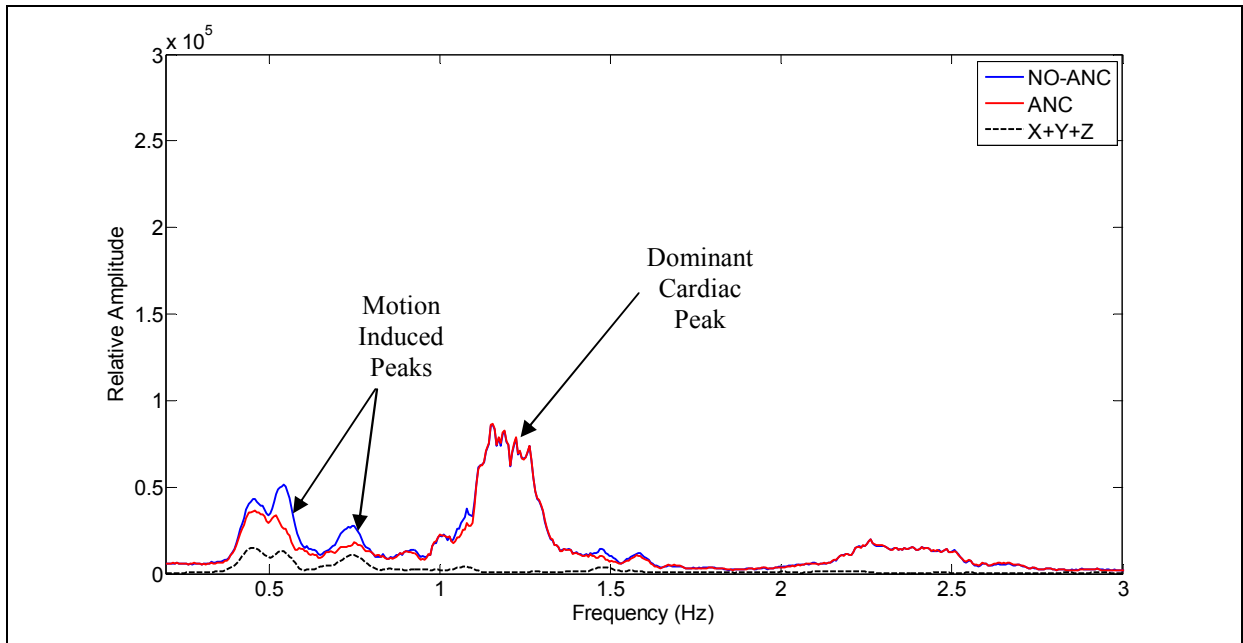


Figure 8.15: Characteristic frequency spectrum of an R PPG signal during a sitting experiment.

HR readings obtained from the WPO, MPO and Holter monitor are compared in Figure 8.16. During rest (phase-1 and phase-3), HR values estimated from the WPO closely matches the HR values obtained from the other two reference sources, whereas during head movements, the WPO underestimates the reference HR. This is mainly due to the additional (lower than cardiac frequency) frequency components induced in the PPG signals during head movements. ANC was effective in attenuating these additional frequency components and successfully recovered the cardiac peaks from the motion corrupted PPG signals. Thus, HR errors were significantly reduced by adaptive filtering of the PPG signals.

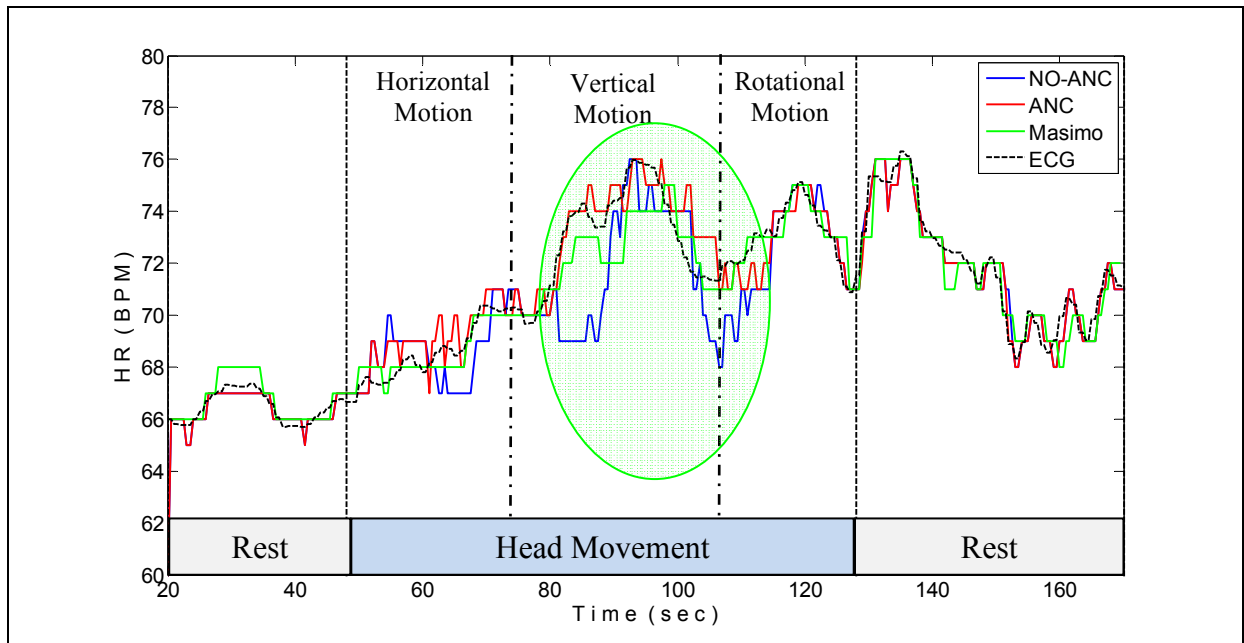


Figure 8.16: HR measurements without and with ANC during a sitting experiment. The green highlighted region shows the improvement in HR estimation after ANC.

Figure 8.17 shows  $SpO_2$  values reported by the WPO and MPO. It is evident that  $SpO_2$  measured from the WPO tend to match  $SpO_2$  acquired from the MPO with an acceptable error of  $\pm 1\%$ . For this particular trial, motion did not produce significant drop in  $SpO_2$  values. As a result, there was no significant effect of ANC on  $SpO_2$  for this trial.

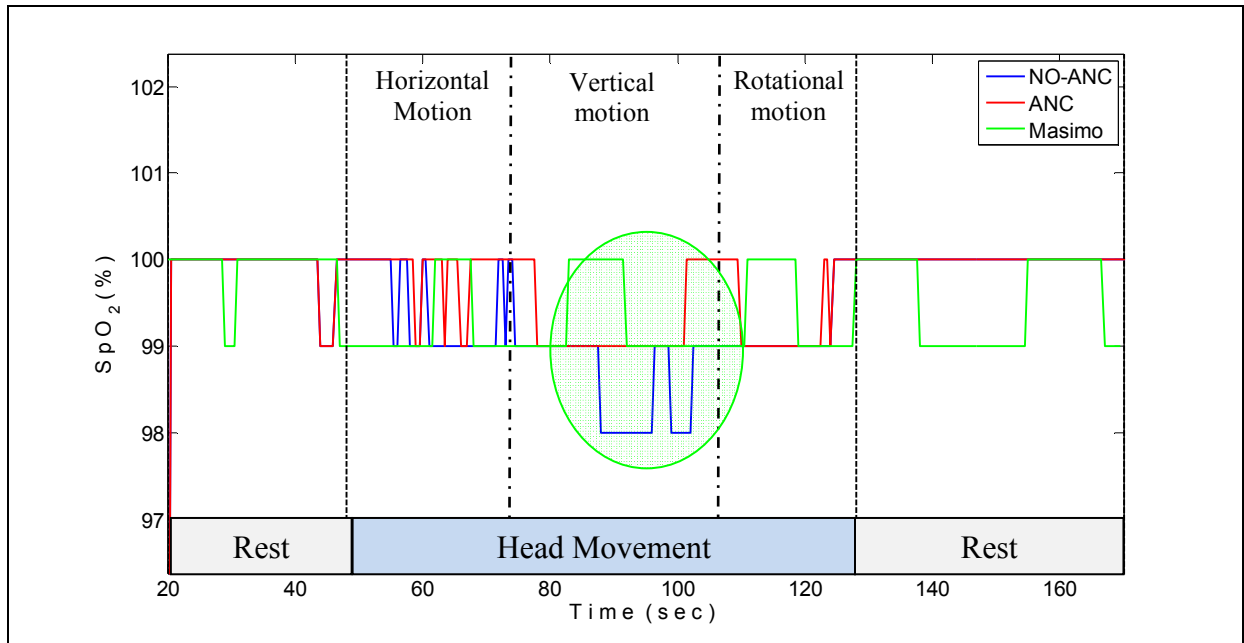


Figure 8.17: SpO<sub>2</sub> values without and with ANC during a sitting experiment.

The regression plot between HR readings obtained from the WPO and Holter monitor before ANC is shown in Figure 8.18. Figure 8.19 shows the regression plot for the same data set after ANC. These figures confirmed that ANC improved the correlation coefficient from 0.57 to 0.91, an improvement of 37% in HR estimation.

Figure 8.20 and Figure 8.21 show the differences between HR values obtained from the WPO and Holter monitor. The differences are plotted against reference readings from the Holter ECG monitor. The mean difference before adaptive filtering was 3BPM with SD corresponding to 5BPM. Interestingly, ANC filtering of PPG signals produced mean difference of 2BPM with SD of 2BPM.

Figure 8.22 and Figure 8.23 illustrate the differences in SpO<sub>2</sub> readings obtained from the WPO and MPO plotted against readings obtained from the MPO. From these two figures it can be observed that the mean SpO<sub>2</sub> difference is reduced from 2% to 1% due to adaptive filtering.

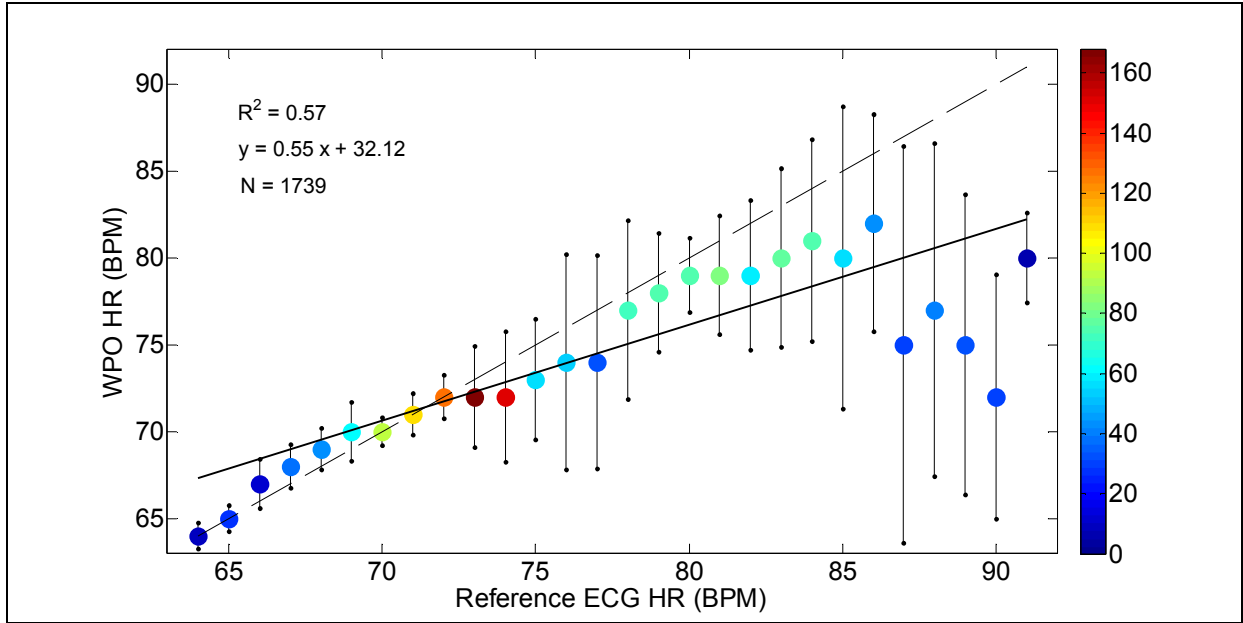


Figure 8.18: Comparison of HR measured by the WPO and an ECG as a reference source, before ANC (sitting experiment).

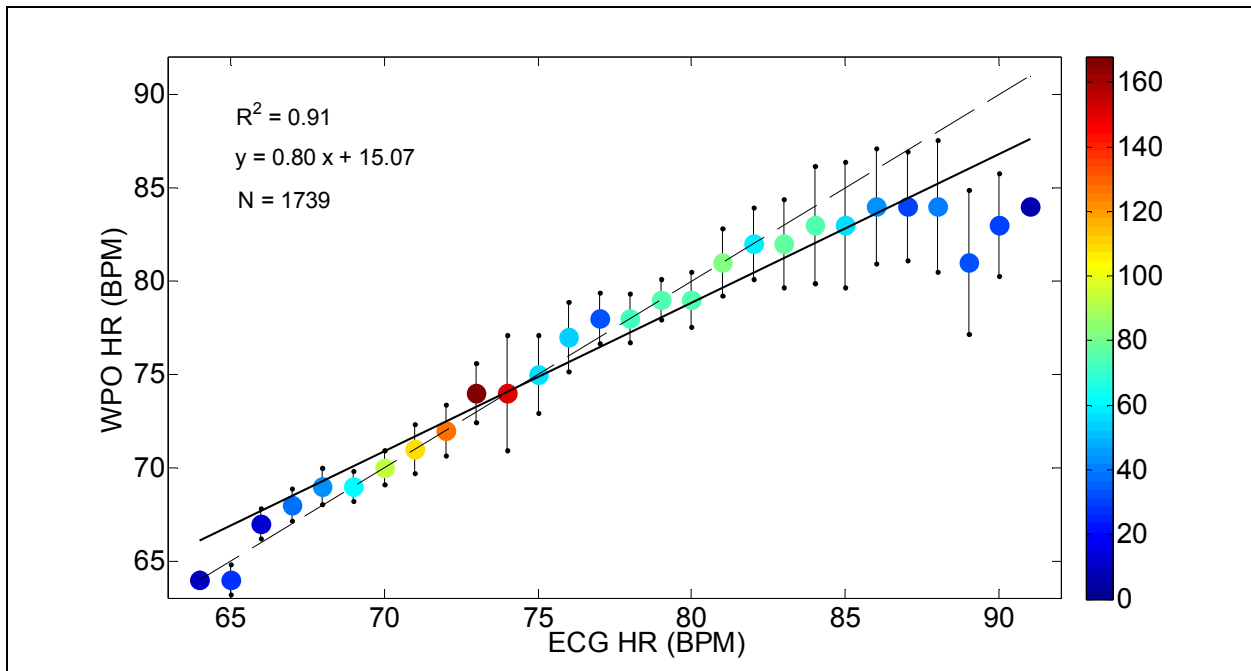


Figure 8.19: Comparison of HR measured by the WPO and an ECG reference source after ANC (sitting experiment).

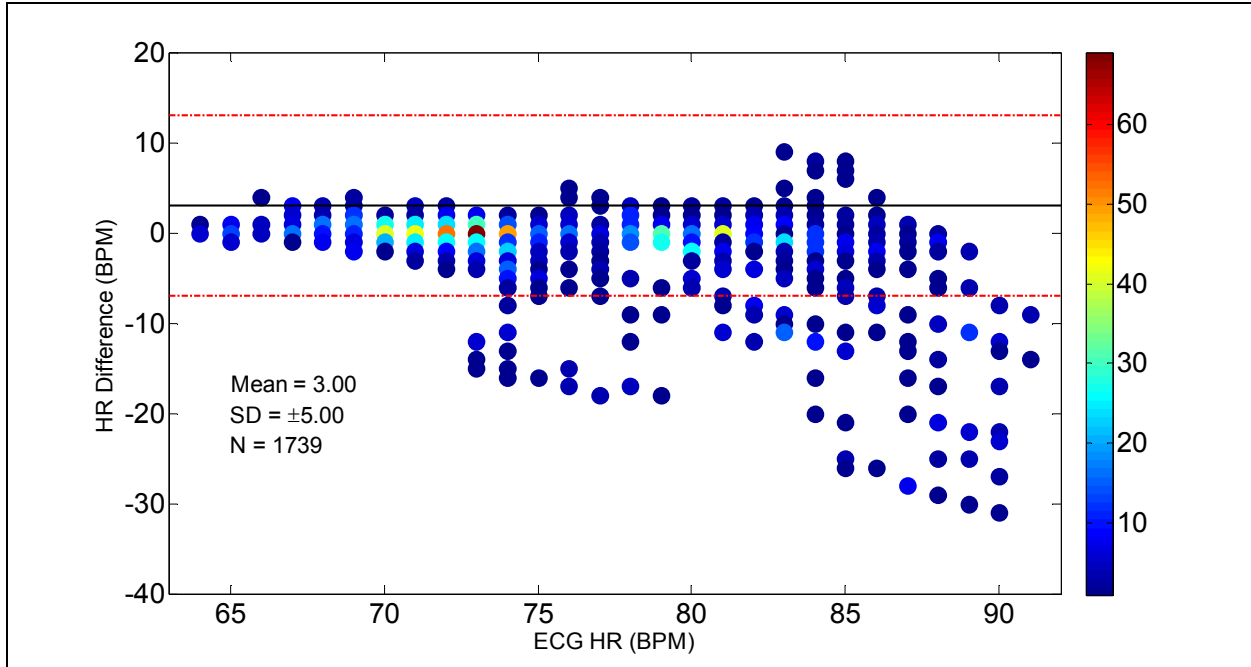


Figure 8.20: Difference in HR readings measured by the WPO and the ECG Holter Monitor without ANC (sitting experiment). The red lines indicate the  $\mu \pm 2SD$  values.

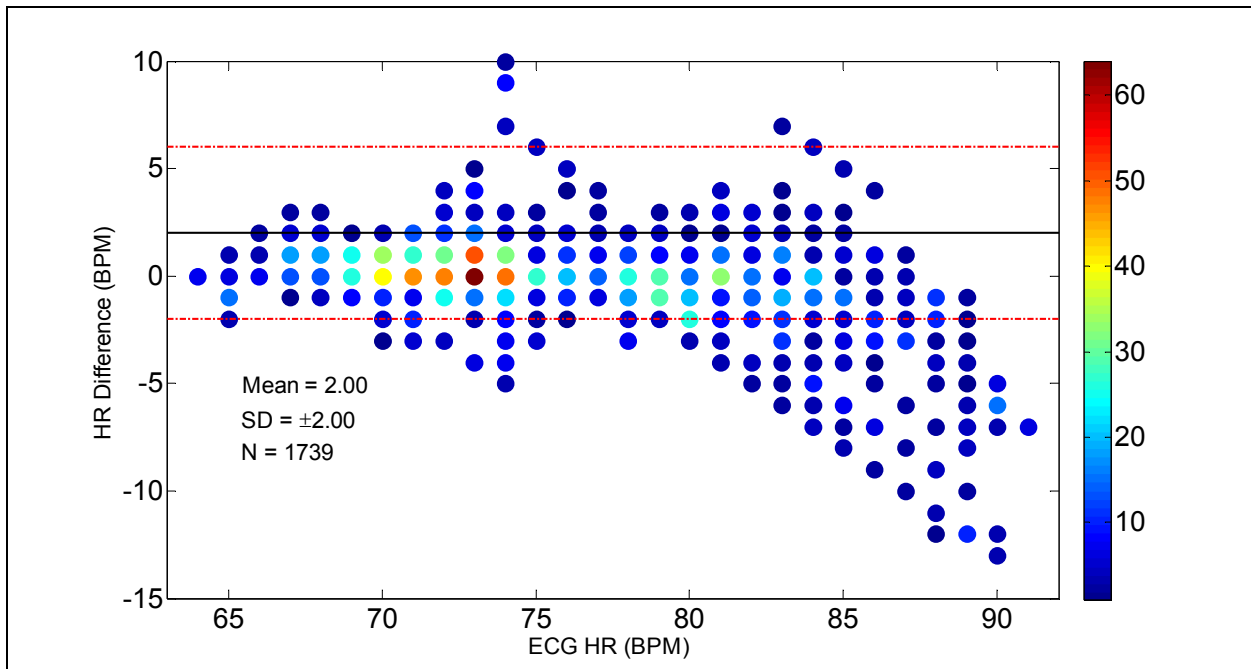


Figure 8.21: Difference in HR readings measured by the WPO and the ECG Holter Monitor with ANC (sitting experiment). The red lines indicate the  $\mu \pm 2SD$  values.

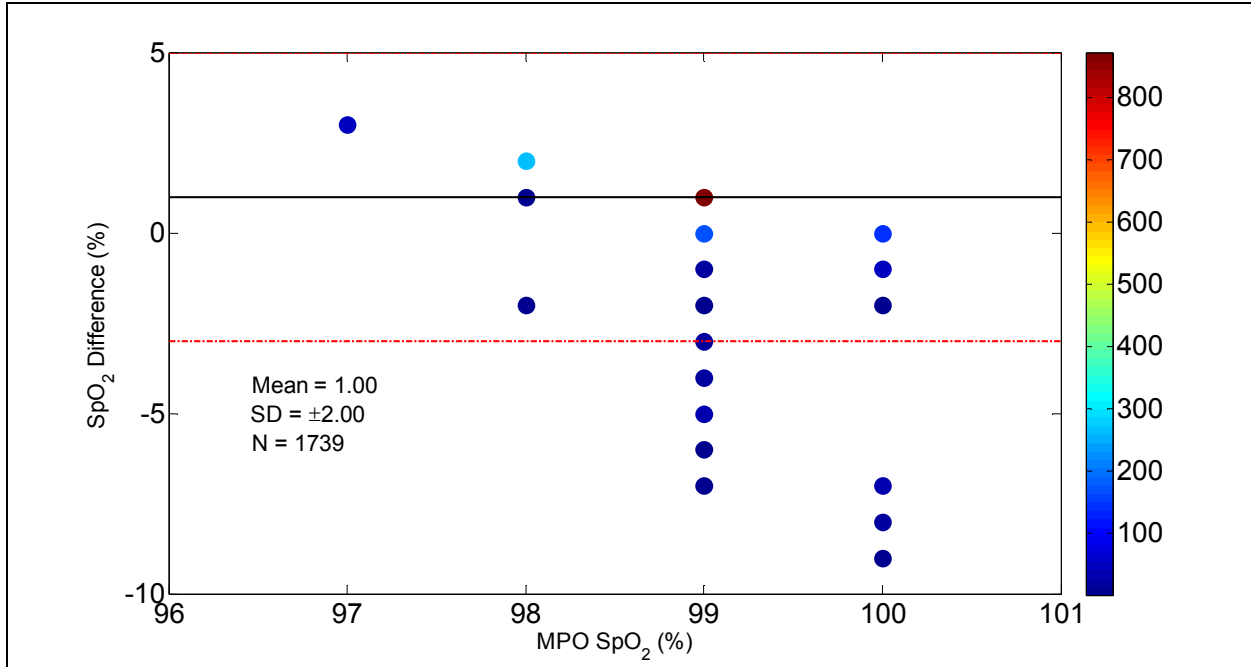


Figure 8.22: Difference between SpO<sub>2</sub> readings acquired from WPO and MPO plotted against MPO values without ANC (sitting experiment). The red lines indicate the  $\mu \pm 2SD$  values.

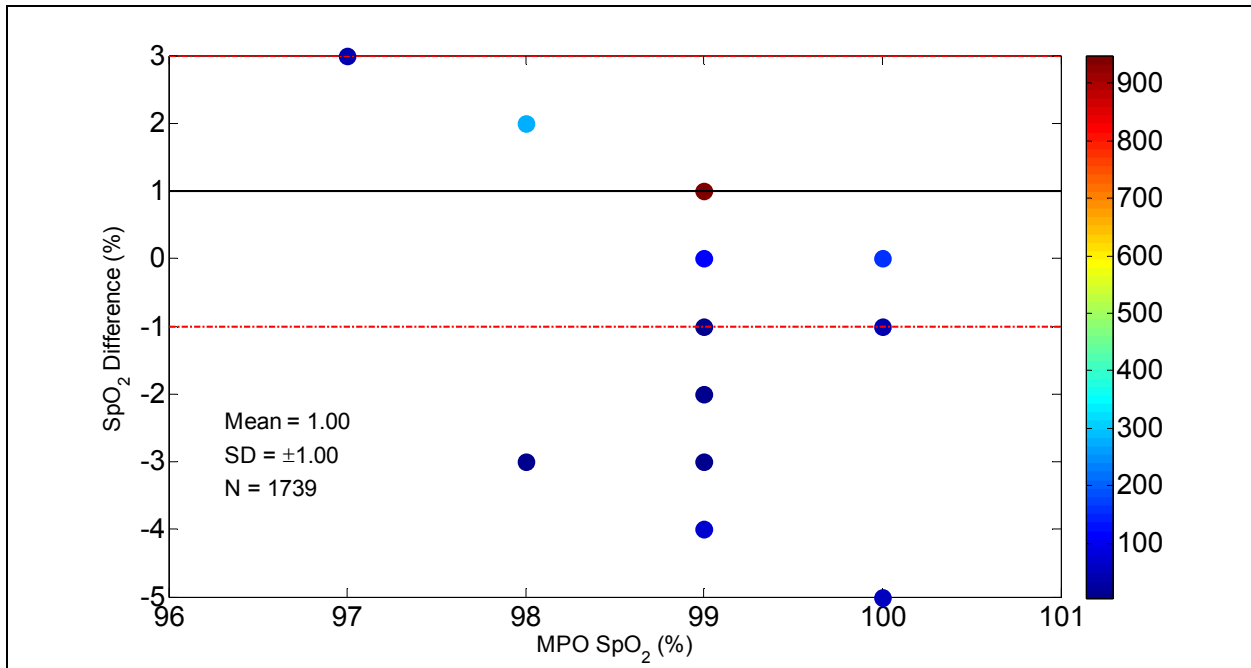


Figure 8.23: Difference between SpO<sub>2</sub> readings acquired from WPO and MPO plotted against MPO values with ANC (sitting experiment). The red lines indicate the  $\mu \pm 2SD$  values.

The results from each trial are summarized in Table 8.2. From these experiments it was found that ANC reduces the average HR errors by 56%, whereas the SD and  $R^2$  were improved by 27% and 44%, respectively. Similarly, for  $SpO_2$  values the MSE and SD were reduced by 7% and 36% respectively.

Table 8.2: Comparison of HR and  $SpO_2$  values obtained after and before LMS type ANC.  $M = 16$  and  $\mu = 0.01$  (Sitting experiments)

Trial	% Improvement					
	ECG - HR			MPO $SpO_2$		Change in $SpO_2$
	MSE	SD	$R^2$	MSE	SD	
1	0	0	-0.41	0	0	NC
2	33	0	3.69	0	0	NC
3	67	0	16.05	0	100	<2%
4	50	0	10.20	0	100	<2%
5	70	50	100.00	0	0	NC
6	93	75	100.00	0	0	<2%
7	83	67	80.55	47	50	<2%
Average	56	27	44.30	7	36	



#### 8.2.4. LMS – Cycling Experiments

Results from cycling experiments showed that PPG signals (Figure 8.24 to Figure 8.26) hardly differ from the signals obtained during rest. The only noticeable difference is that cycling PPG signals have a higher frequency content compared to resting signals. Since cycling on a stationary bicycle does not involve head movements that distort the PPG signals, the increased cardiac frequency is not associated with motion artifacts.

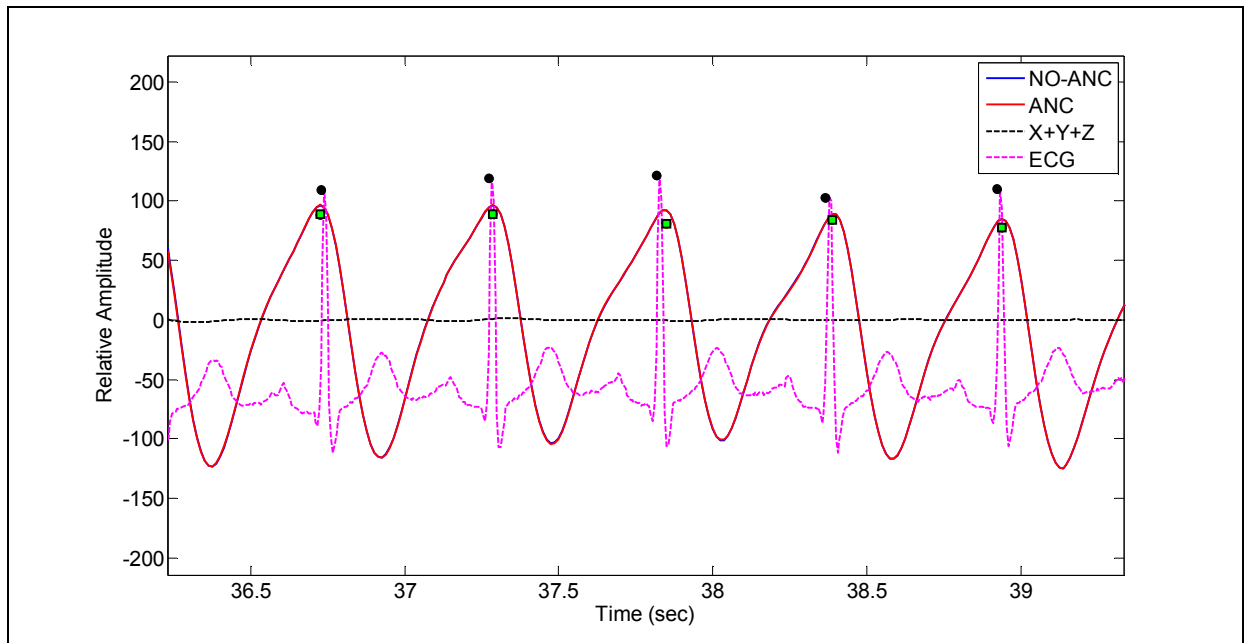


Figure 8.24: Typical IR PPG signals during Phase-1 of cycling experiment, before (Blue) and after (Red) ANC. Note that the blue and red traces completely overlap in this figure. ■ marks PPG peaks detected by the WPO after ANC (5-peaks), and ● represents R-waves detected from the ECG waveform (5-peaks).

Since minimal sensor motion was observed during cycling, the acceleration signals have very low amplitude and thus the morphology of the PPG signals was not affected. This is noticeable in Figure 8.25 which shows that the PPG waveform has a similar morphology before and after ANC.

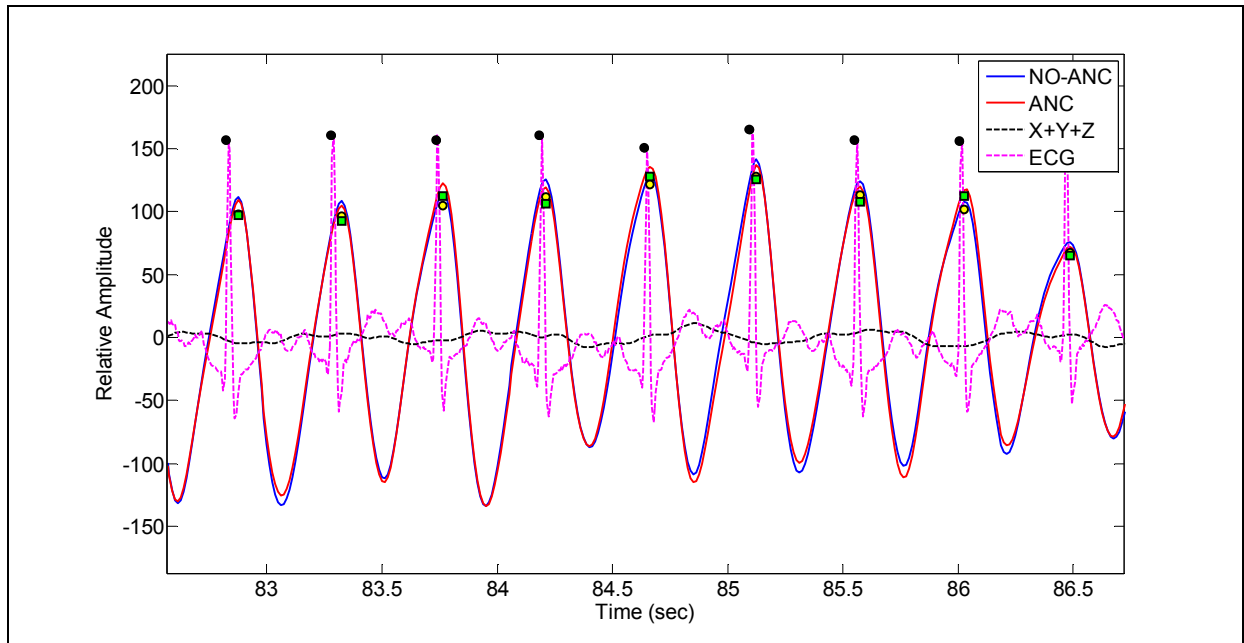


Figure 8.25: Typical IR PPG signals during Phase-2 of cycling experiment, before (Blue) and after (Red) ANC. Note that the blue and red traces overlap in this figure. ■ marks PPG peaks detected by the WPO after ANC (9-peaks), ● denotes PPG peaks detected without ANC (9-peaks), and ● represents R-waves detected from the ECG waveform (9-peaks).

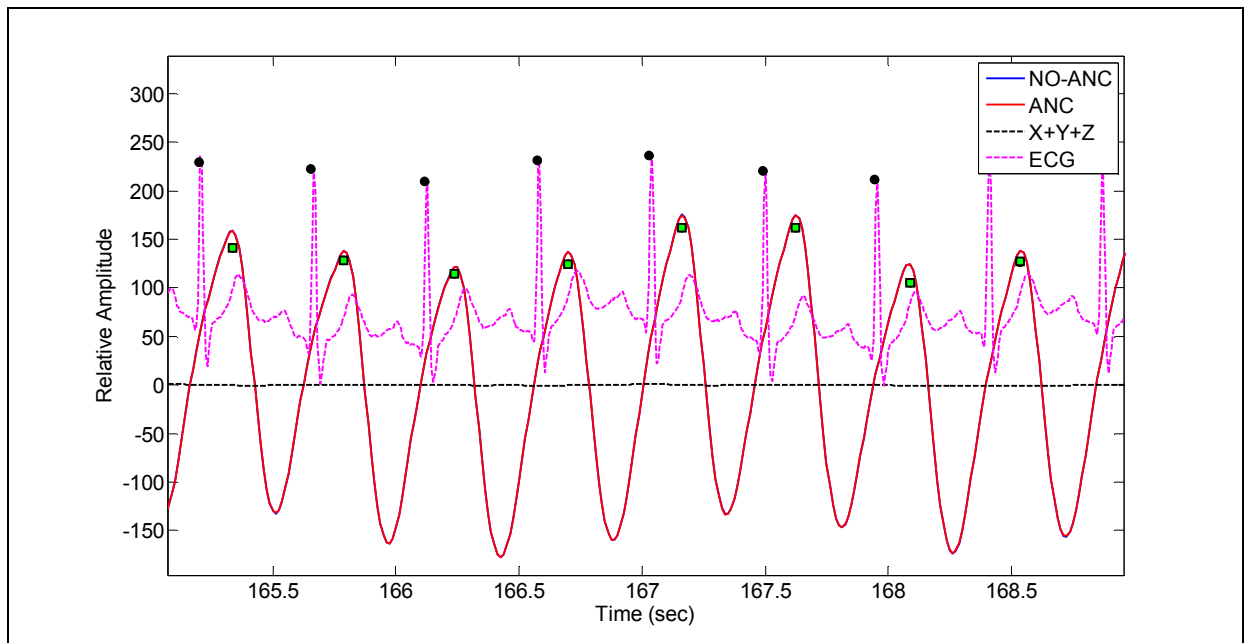


Figure 8.26: Typical IR PPG signals during Phase-3 of cycling experiment, before (Blue) and after (Red) ANC. Note that the blue and red traces overlap in this figure. ■ marks PPG peaks detected by the WPO after ANC (8-peaks), and ● represents R-waves detected from the ECG waveform (8-peaks).

The frequency plots, shown in Figure 8.27 and Figure 8.28, indicate that the frequency of the PPG signal obtained during cycling were free from motion artifacts. As shown in these figures, the red and blue traces completely overlap, further verifying that ANC has no significant effect on the PPG signals during cycling. Results obtained from these cycling experiments suggest that adaptive filtering of the PPG signals during no/minimal head motion is not required.

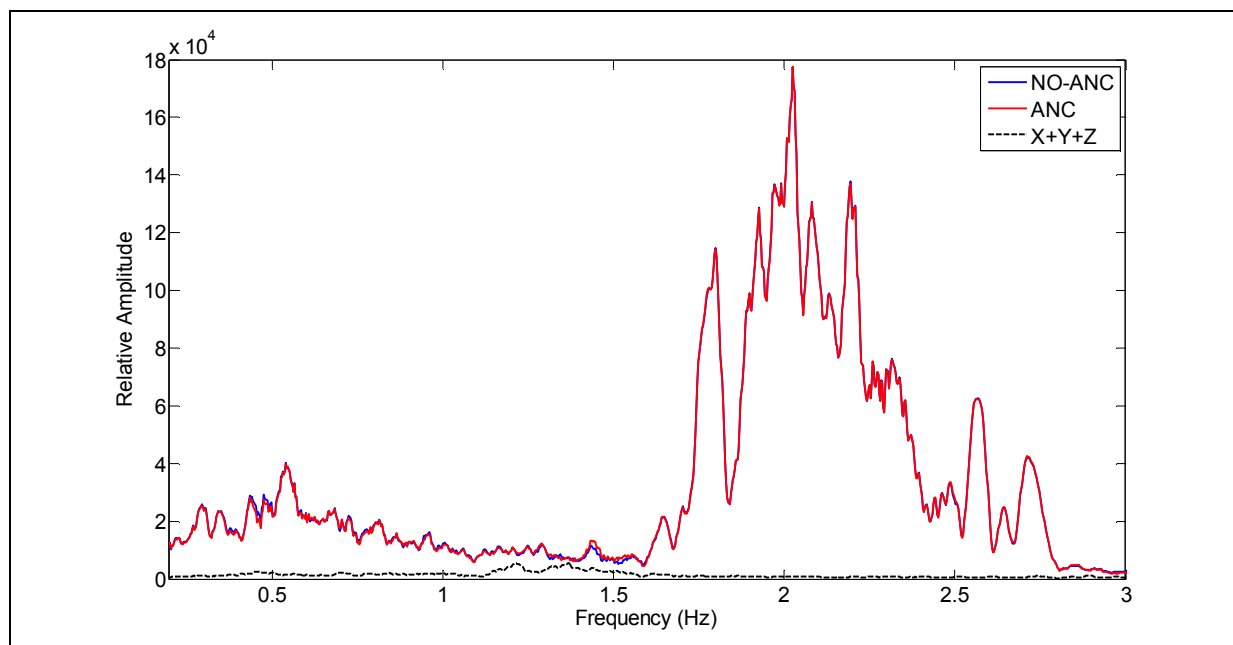


Figure 8.27: Typical frequency spectrum of an IR PPG obtained during cycling. Note that the red and blue traces overlap completely.

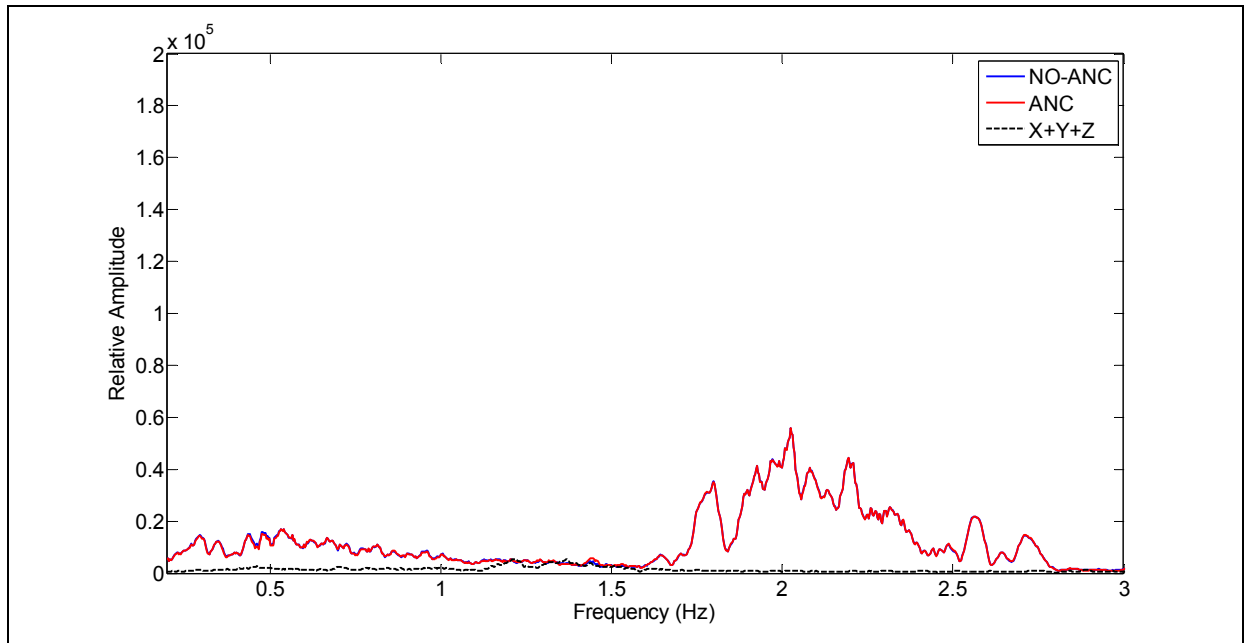


Figure 8.28: Typical frequency spectrum of an R PPG obtained during cycling. Note that the red and blue traces overlap completely.

Since there was no change in the PPG signal during cycling, HR and SpO<sub>2</sub> measurements remained unaltered after ANC. Figure 8.29 and Figure 8.30 verify that HR and SpO<sub>2</sub> values obtained from the WPO closely matched the measurements from the reference sources, hence no further improvements were needed.

The high CC values obtain from the regression analysis confirmed that measurements obtained from the WPO produced accurate estimation of HR & SpO<sub>2</sub> values and can also track rapid changes in these parameters. The results of the regression analysis are plotted in Figure 8.31 to Figure 8.36.

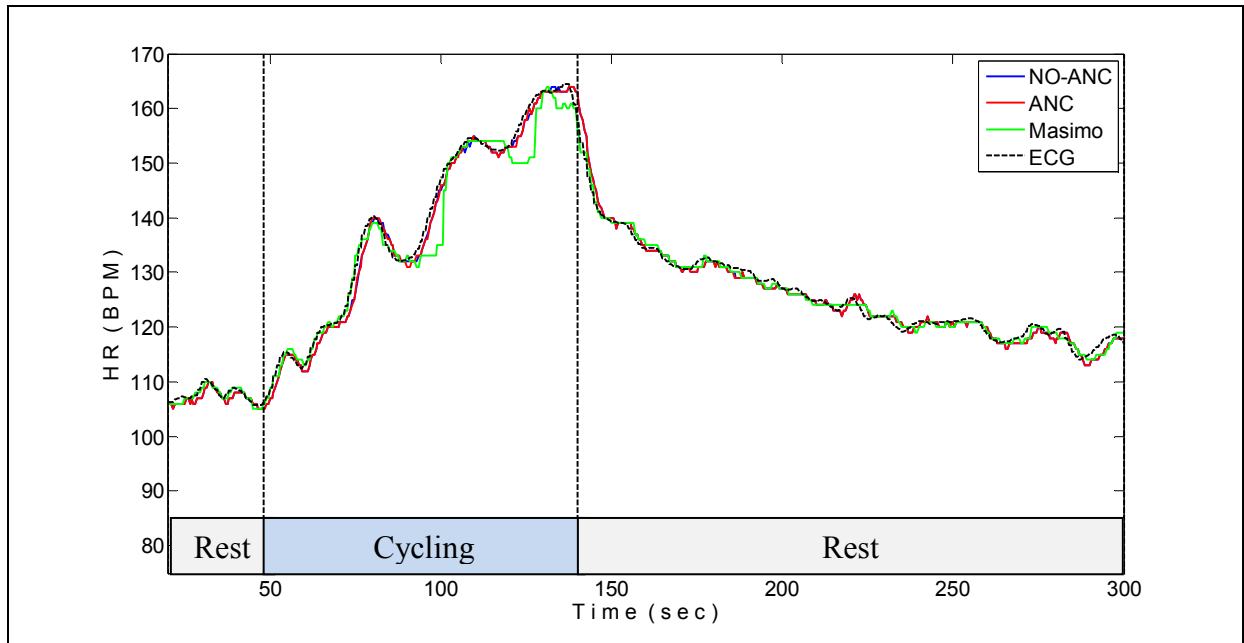


Figure 8.29: HR measurements without and with ANC during cycling. Note that the red and blue traces overlap completely.

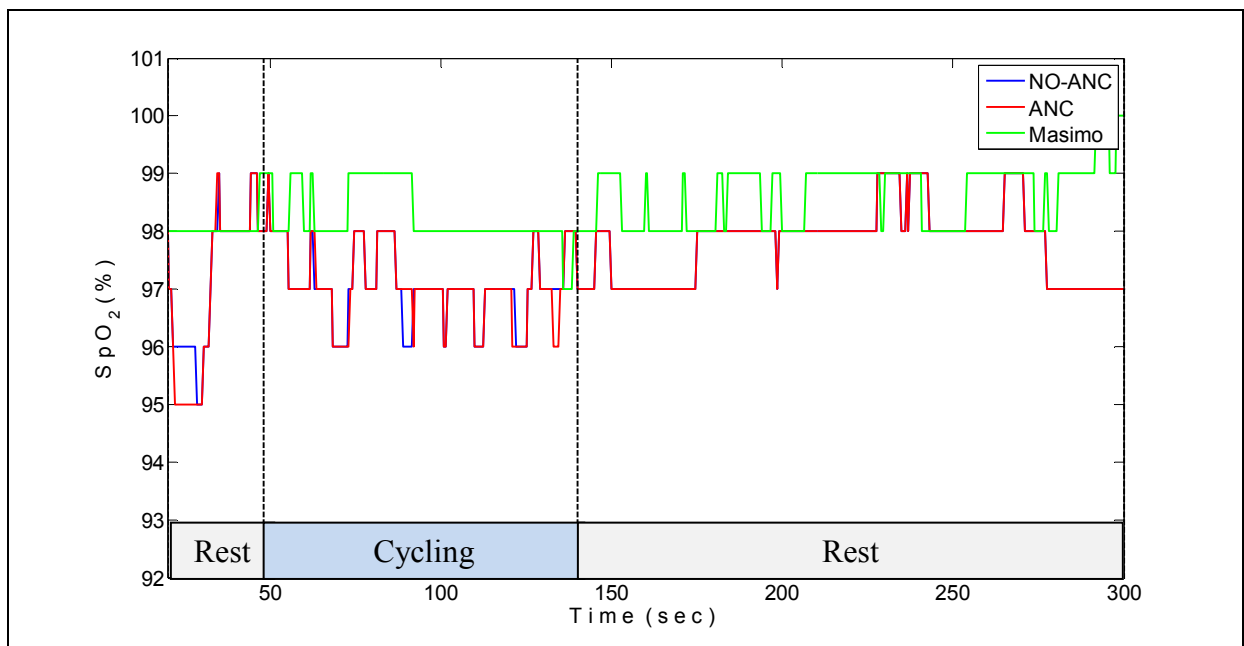


Figure 8.30: SpO<sub>2</sub> measurements without and with ANC during cycling. Note that the red and blue traces overlap completely.

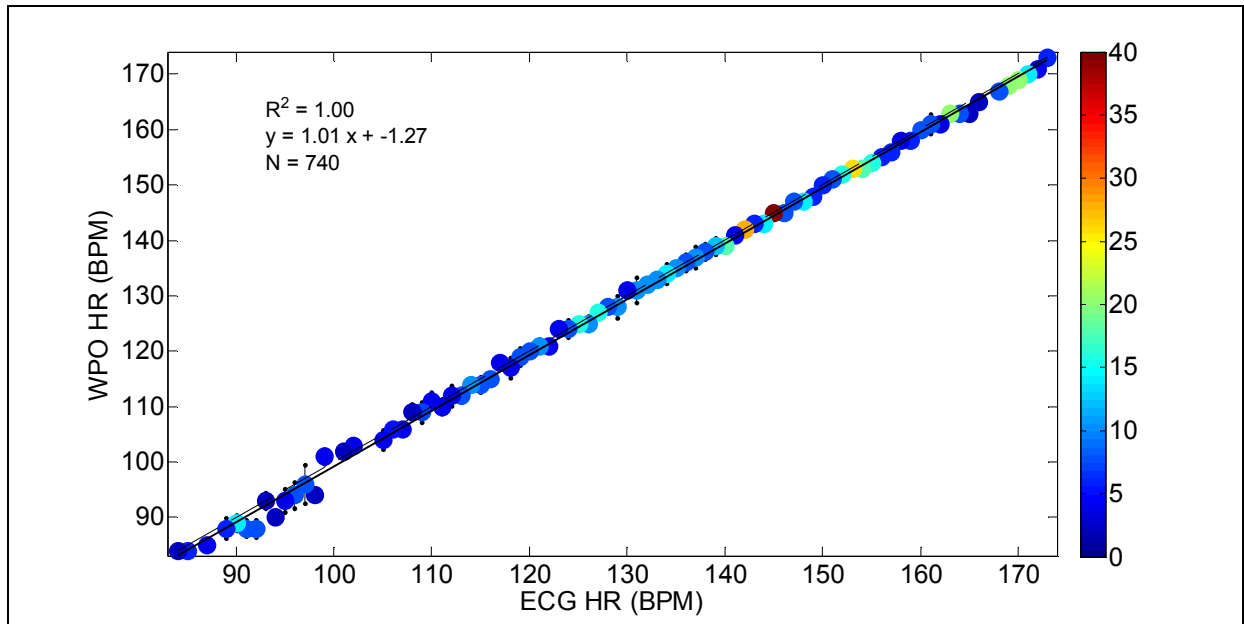


Figure 8.31: Comparison of HR measured by the WPO and reference source during cycling before ANC.

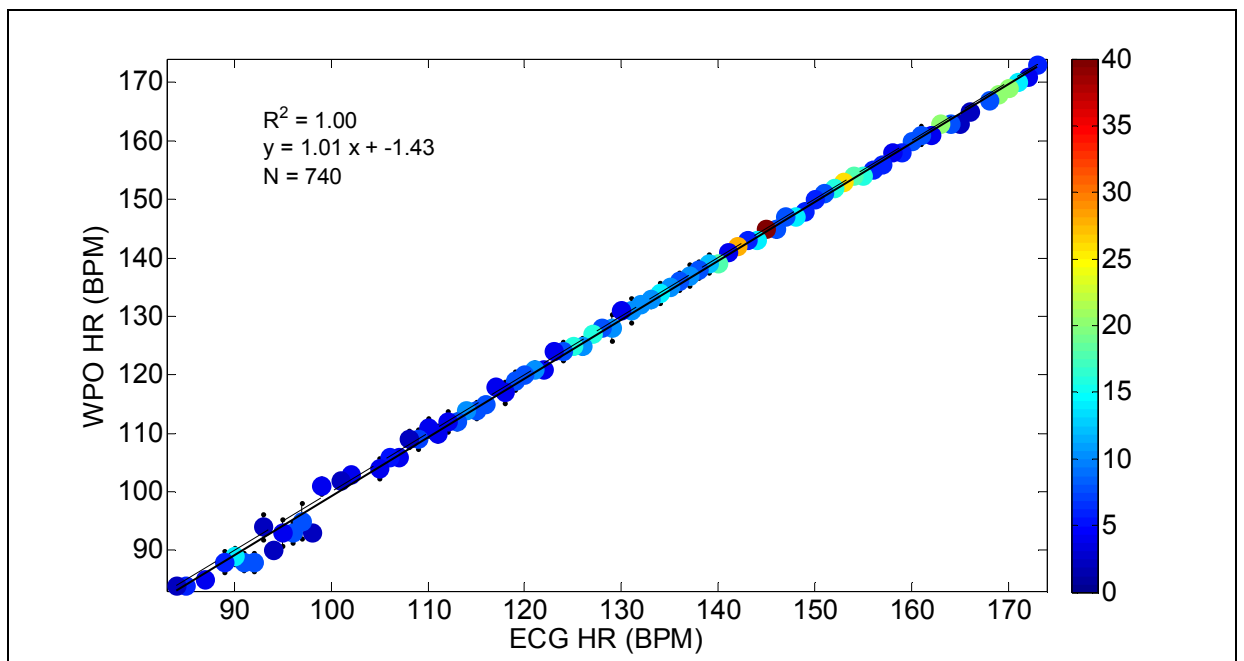


Figure 8.32: Comparison of HR measured by the WPO and reference source during cycling after ANC.

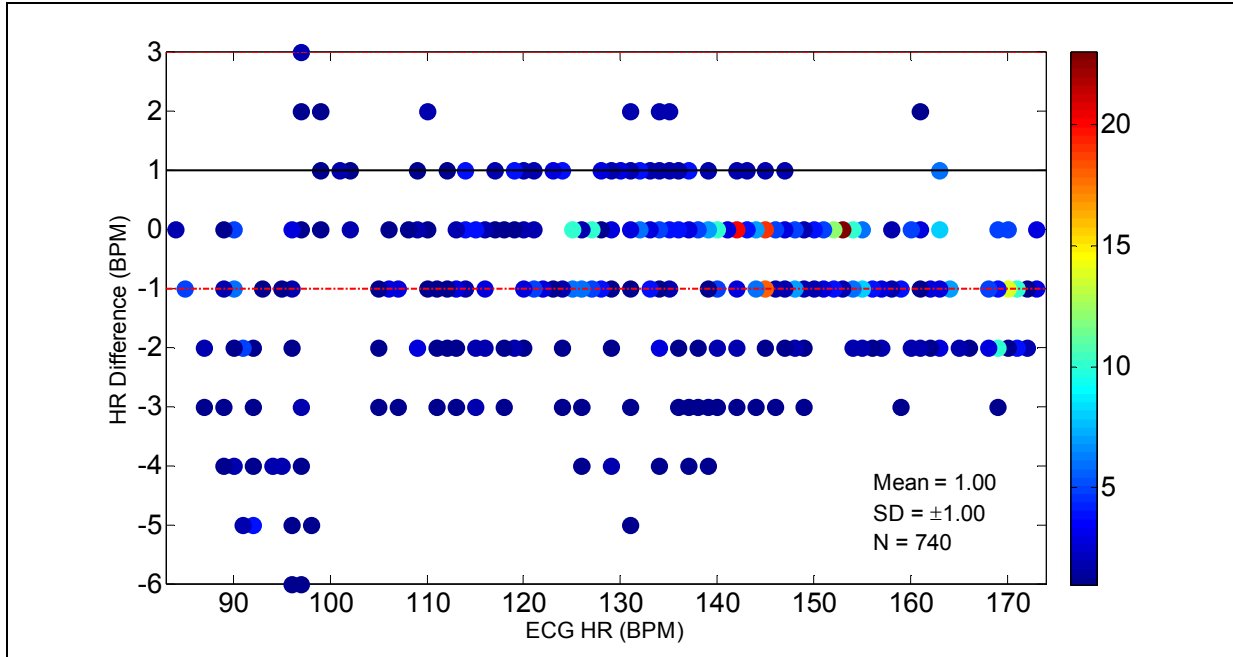


Figure 8.33: Difference in HR readings measured by the WPO and ECG Holter Monitor during cycling without ANC. The red lines indicate the  $\mu \pm 2SD$  values.

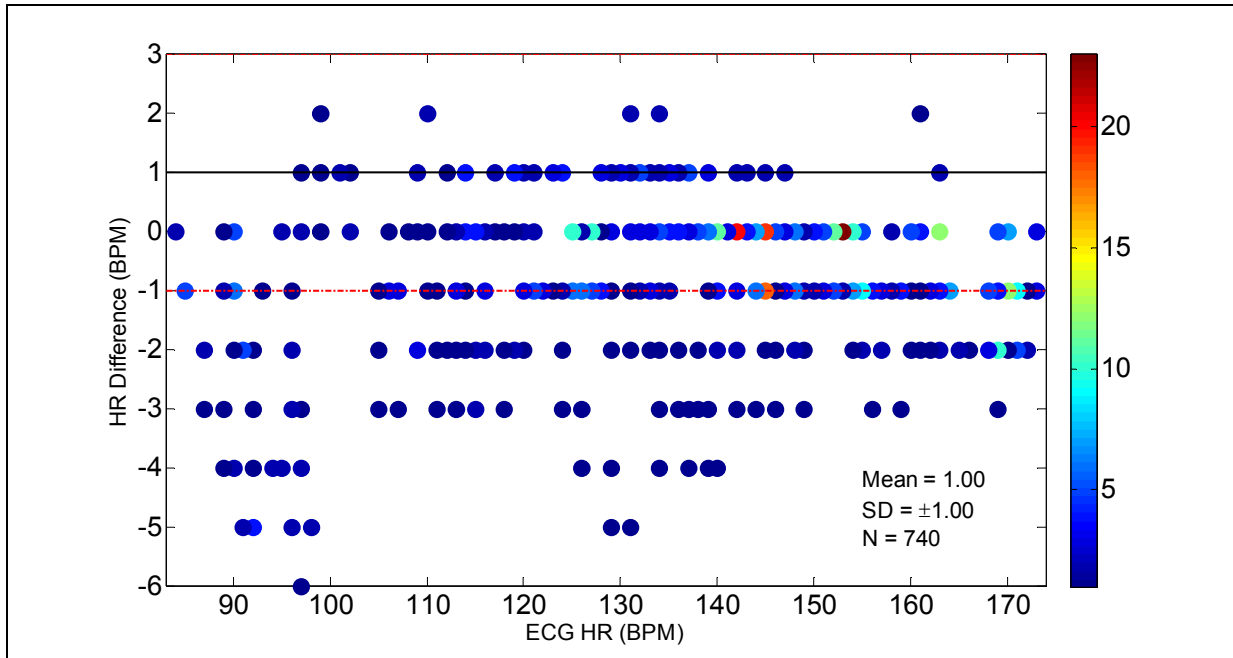


Figure 8.34: Difference in HR readings measured by the WPO and ECG Holter Monitor during cycling with ANC. The red lines indicate the  $\mu \pm 2SD$  values.

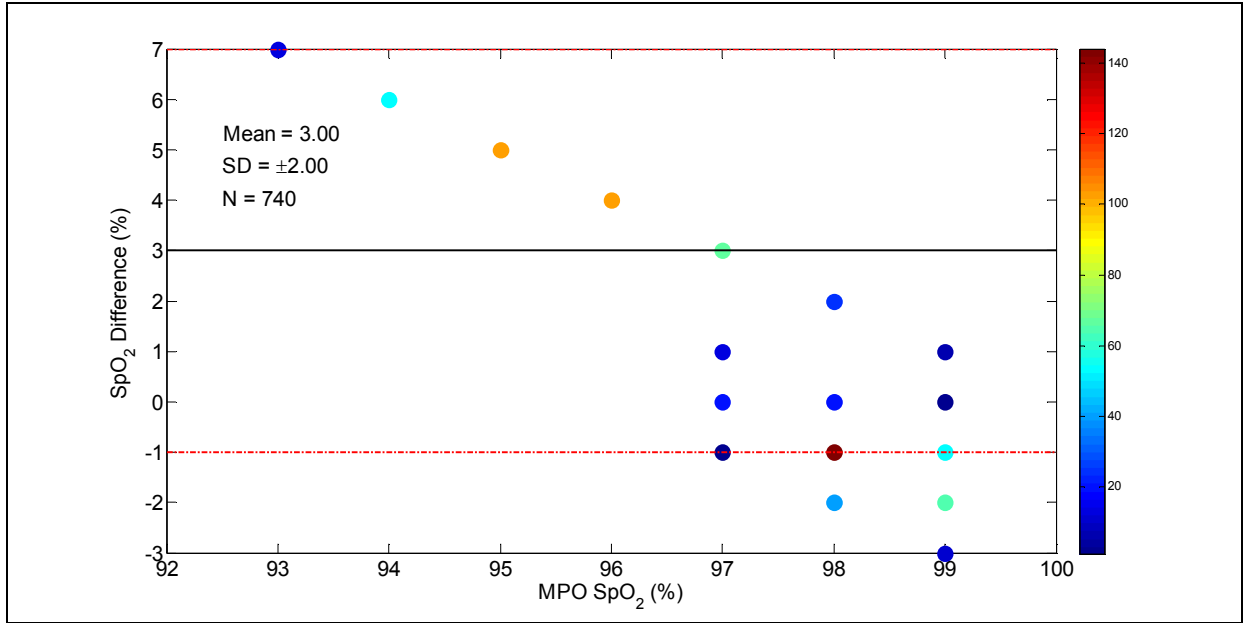


Figure 8.35: Difference in SpO<sub>2</sub> measured by the WPO and MPO during cycling without ANC. The red lines indicate the  $\mu \pm 2SD$  values.

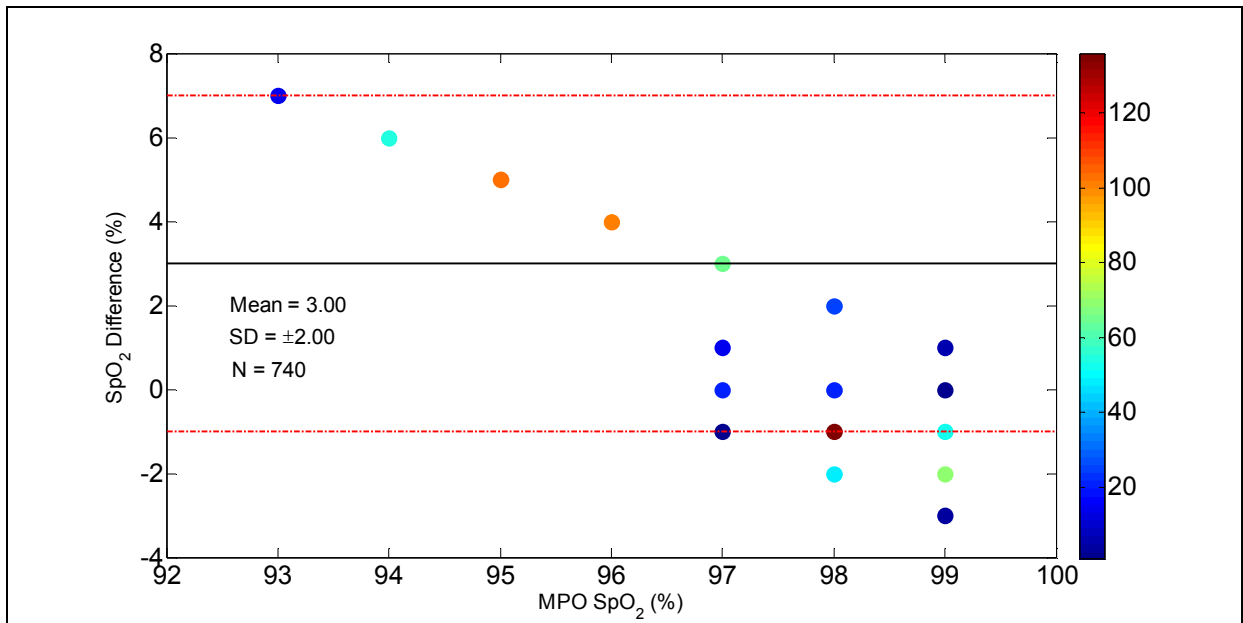


Figure 8.36: Difference in SpO<sub>2</sub> measured by the WPO and MPO during cycling with ANC. The red lines indicate the  $\mu \pm 2SD$  values.



Results of individual tests are summarized in Table 8.3. The table shows that even without adaptive filtering, measurements obtained from the WPO are of high accuracy in the absence of motion artifacts. There were no significant differences in HR and SpO<sub>2</sub> values before and after adaptive filtering. Therefore, physical activities involving little/no head motion do not affect the accuracy of our WPO.

Table 8.3: Comparison of HR and SpO<sub>2</sub> values obtained before and after ANC using a LMS filter. M =16 and  $\mu = 0.01$  (cycling experiments)

Trial	% Improvement					
	ECG - HR			MPO SpO <sub>2</sub>		Change in SpO <sub>2</sub>
	MSE	SD	R <sup>2</sup>	MSE	SD	
1	0	0	-0.01	0	0	NC
2	0	0	0.01	0	0	NC
3	0	0	0	0	0	NC
4	0	0	0	0	0	NC
5	8	0	0.78	6	33	<2%
6	36	0	0.33	0	0	NC
Average	7	0	0.19	1	6	

Note that in trial#6, the subject was moving a lot while cycling. Due to excessive motion, the ACC generated high amplitude signals and the LMS filter had a noticeable effect on the morphology of the PPG signals. As seen in Figure 8.37, ANC improved HR values by 36% for trial #6. Also, note that the MPO reported false HR readings for this trial due to excessive finger movements.

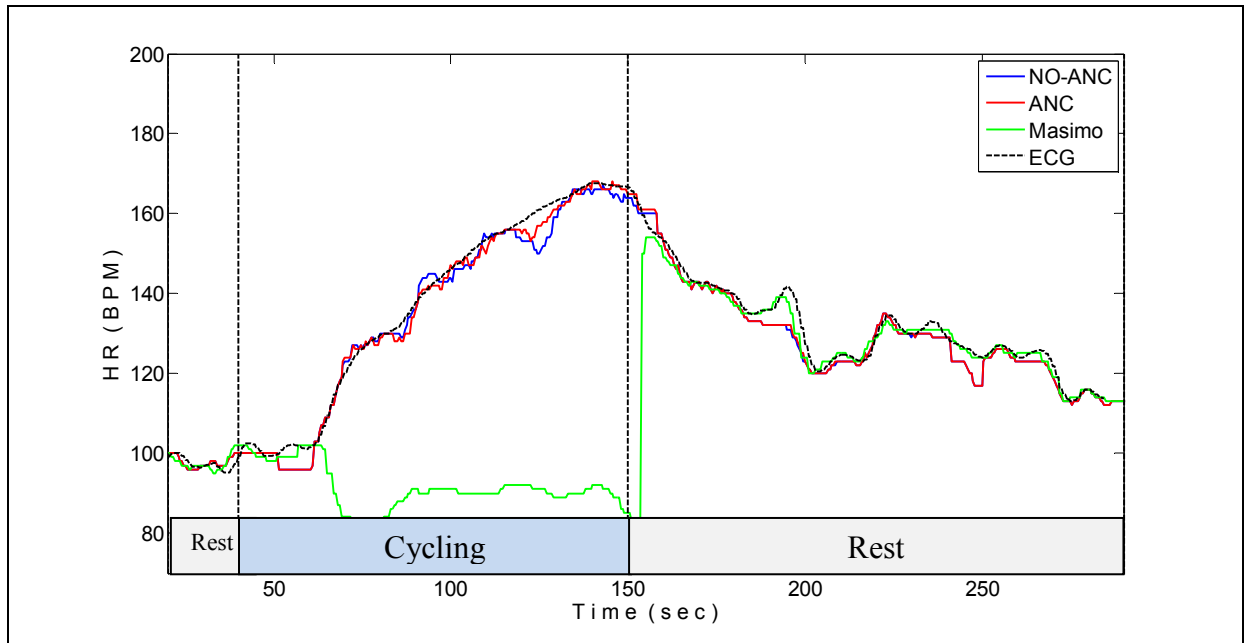


Figure 8.37: HR readings for trial#6.

#### 8.2.5. LMS – Treadmill Jogging Experiments

Figure 8.38 to Figure 8.42 summarize the experimental results of a typical data set obtained during treadmill jogging. These figures include the AC component of the IR PPG signals, ACC signals and the output of the LMS adaptive filter during different phases of the experiment.

During rest (phase-1 and phase-5) it was found that the PPG signals were not contaminated by motion, thus HR and SpO<sub>2</sub> readings were accurate. Jogging at 2mph (phase-2 and phase-4) increased the amplitude of the accelerometer signals. From Figure 8.39 and Figure 8.41 it was observed that motion induced by jogging at 2mph had an insignificant effect on the shape and frequency of the PPG waveform. Hence, jogging at low speeds such as 2mph did not degrade the SNR of the PPG signals and did not affect the accuracy of the WPO.

PPG signals acquired during running at 4mph (phase-3) are presented in Figure 8.40. It was observed that before ANC, the PPG signal had 6 noticeable peaks; each peak corresponds to one heart beat. After ANC, the same signal processing algorithm detected 9 cardiac peaks, matching the number of R-waves in the ECG waveform. The three peaks were recovered due to adaptive

filtering of the PPG signals. Thus, adaptive filtering while jogging was shown to improve the SNR of the PPG signals.

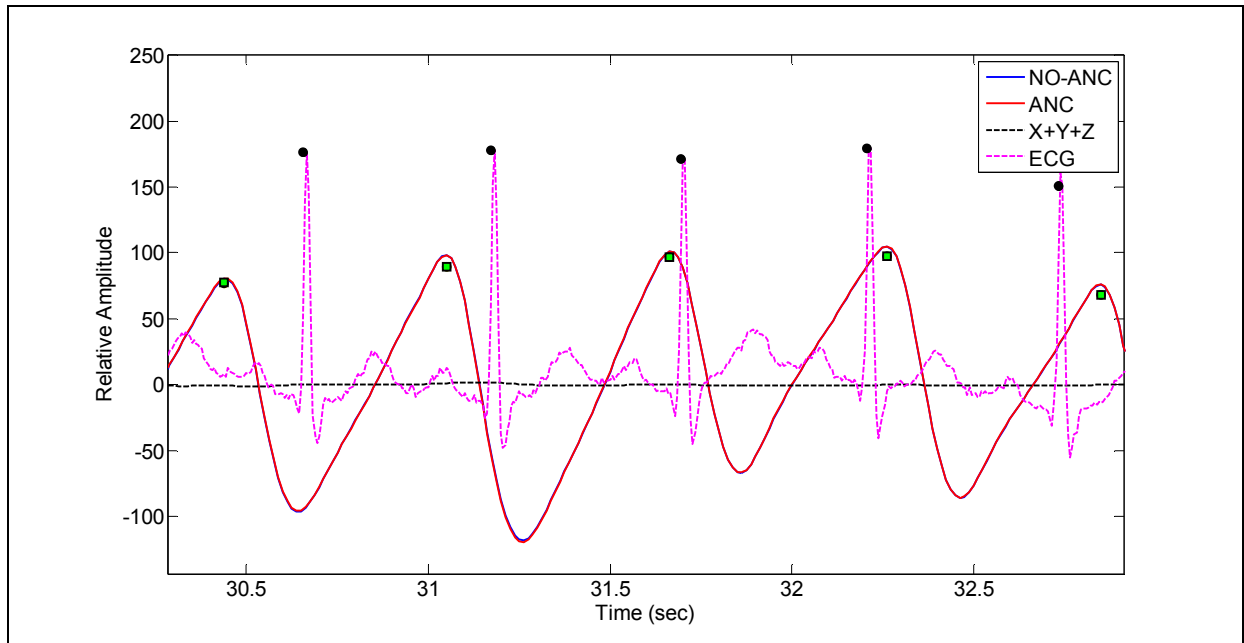


Figure 8.38: Typical IR PPG signals during Phase-1 of treadmill jogging experiment, before (Blue) and after (Red) ANC. Note that the blue and red traces completely overlap in this figure. ■ marks PPG peaks detected by the WPO after ANC (5-peaks), and ● represents R-waves detected from the ECG waveform (5-peaks).

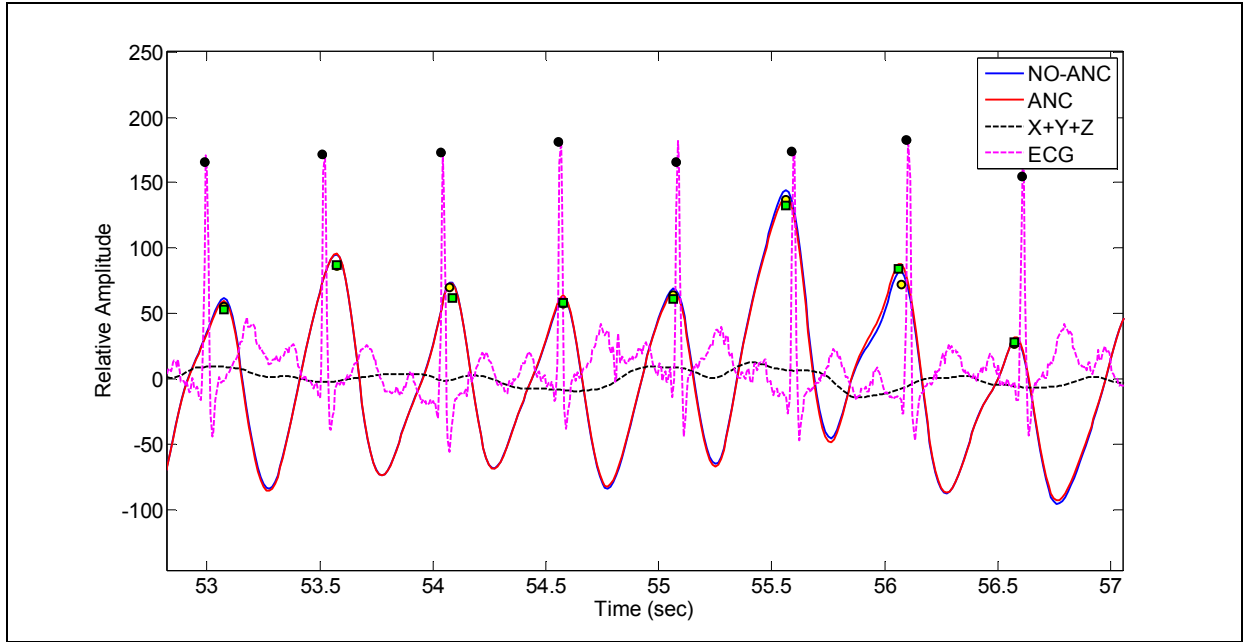


Figure 8.39: Typical IR PPG signals during Phase-2 of treadmill jogging experiment, before (Blue) and after (Red) ANC. Note that the blue and red traces completely overlap in this figure. ■ marks PPG peaks detected by the WPO after ANC (8-peaks), ● denotes PPG peaks detected without ANC (8-peaks), and ● represents R-waves detected from the ECG waveform (8-peaks).

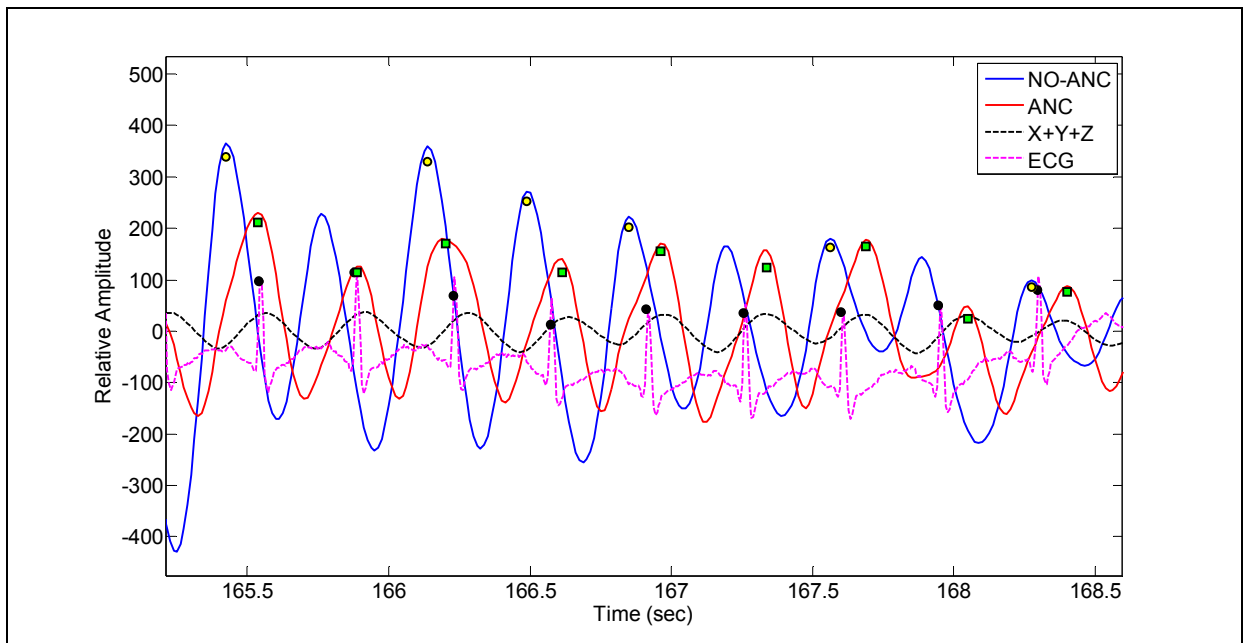


Figure 8.40: Typical IR PPG signals during Phase-3 of treadmill jogging experiment, before (Blue) and after (Red) ANC. ■ marks PPG peaks detected by the WPO after ANC (9-peaks), ● denotes PPG peaks detected without ANC (9-peaks), and ● represents R-waves detected from the ECG waveform (9-peaks).

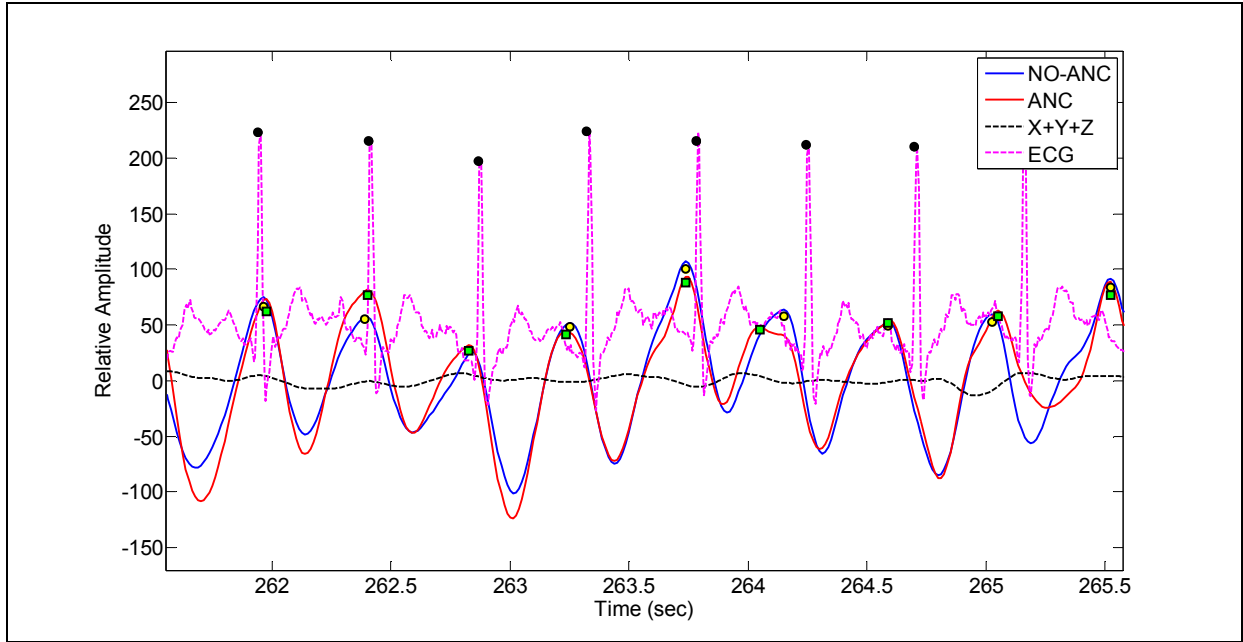


Figure 8.41: Typical IR PPG signals during Phase-4 of treadmill jogging experiment, before (Blue) and after (Red) ANC. Note that the blue and red traces overlap. ■ marks PPG peaks detected by the WPO after ANC (9-peaks), ● denotes PPG peaks detected without ANC (9-peaks), and ● represents R-waves detected from the ECG waveform (9-peaks).

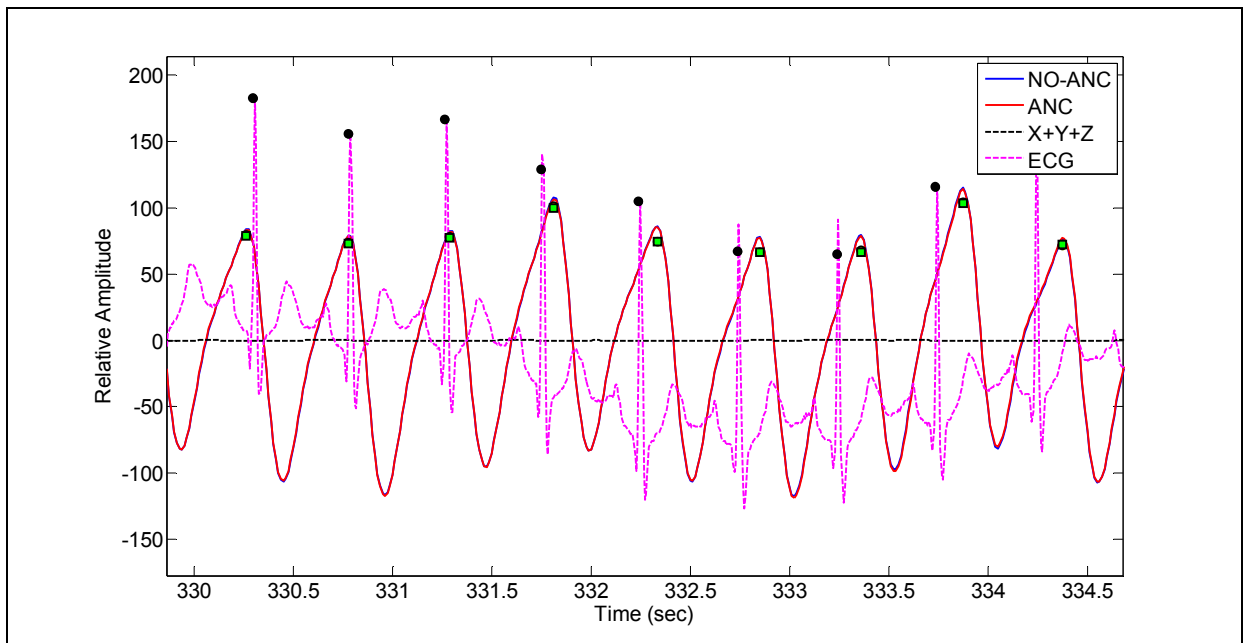


Figure 8.42: Typical IR PPG signals during Phase-5 of treadmill jogging experiment, before (Blue) and after (Red) ANC. Note that the blue and red traces completely overlap in this figure. ■ marks PPG peaks detected by the WPO after ANC (9-peaks), and ● represents R-waves detected from the ECG waveform (9-peaks).

The frequency spectra of the signals (Figure 8.43 and Figure 8.44) clearly show an additional frequency component induced by motion artifacts. Note that the amplitude of this motion induced frequency is higher than the frequency corresponding to the cardiac activity. This leads to measurement errors when the algorithm calculates SpO<sub>2</sub> and HR values. The figures also illustrate that the ANC algorithm was able to remove the dominant frequency components corresponding to motion artifacts. The red trace shows that the cardiac spectrum was not distorted by the ANC.

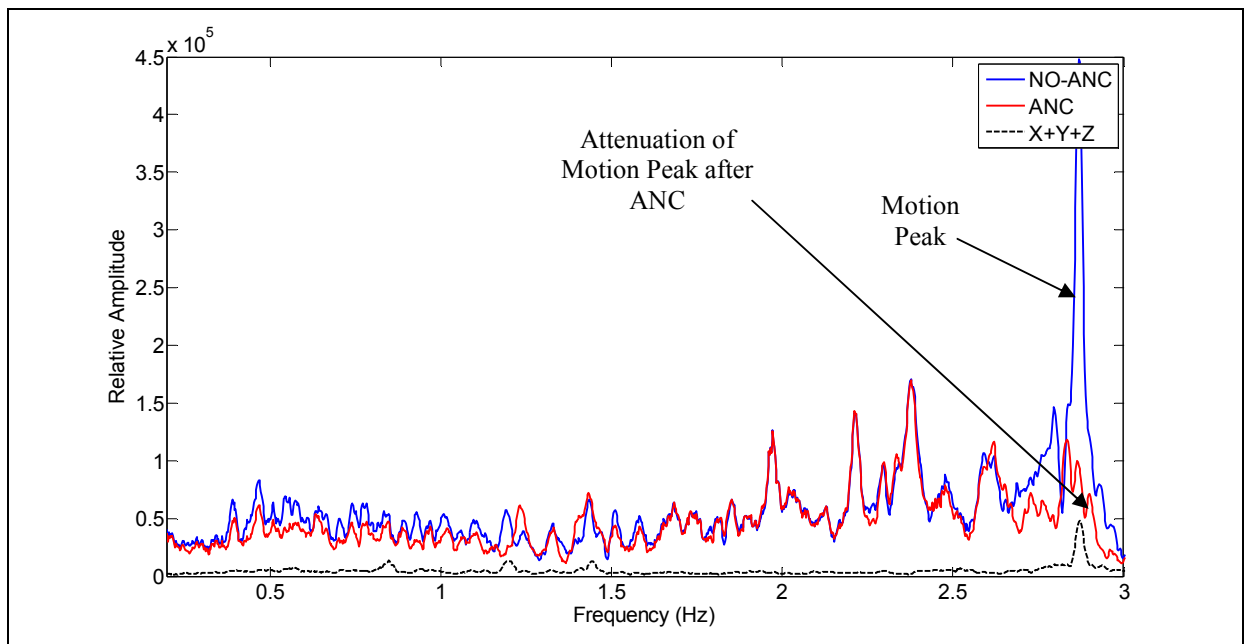


Figure 8.43: Frequency spectrum of IR PPG during treadmill jogging.

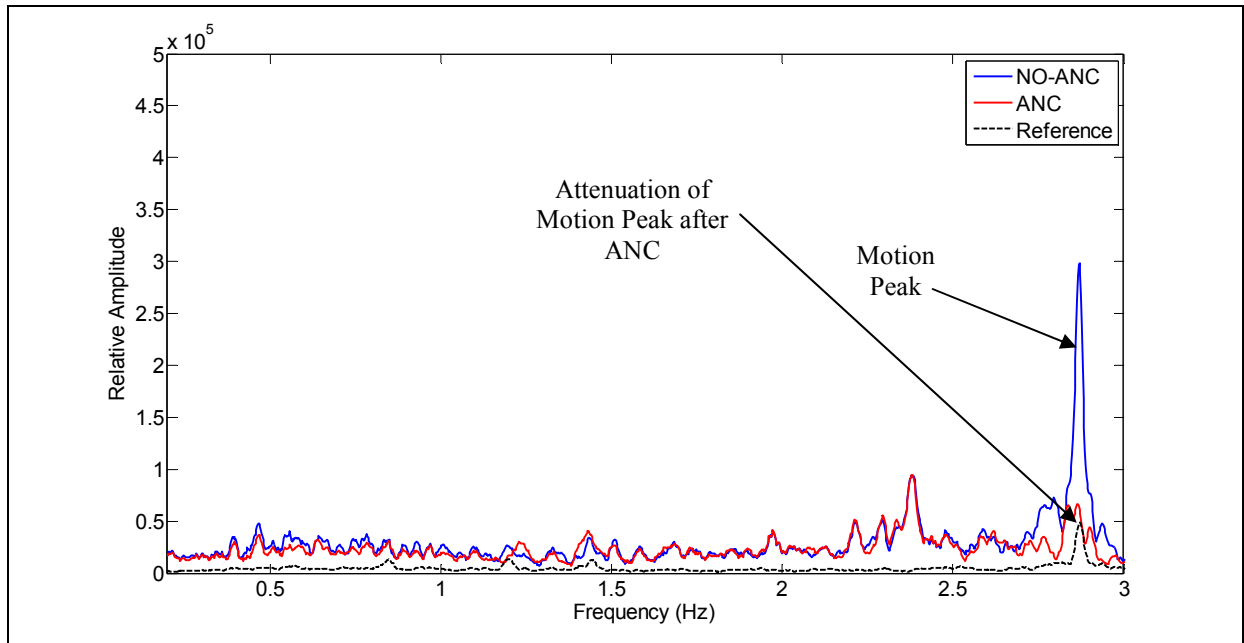


Figure 8.44: Frequency spectrum of Red PPG during treadmill jogging.

HR readings obtained from one of the jogging tests are plotted in Figure 8.45. After ANC the HR values from the WPO closely match the readings from the reference Holter monitor. This was due to the additional peaks that were detected only after adaptive filtering.

Similarly, tests revealed that the performance of the ANC-based SpO<sub>2</sub> algorithm was improved compared to the performance of the non-ANC algorithm. Figure 8.46 shows the results of representative tests in which the non-ANC SpO<sub>2</sub> values dropped to 65% due to body motion. Post adaptive filtering values were closer to the normal physiological range of 96-98%. Hence, the analysis confirmed that measurements obtained after adaptive filtering are more accurate than measurements obtained from non-ANC signals. This was further confirmed by the regression results.

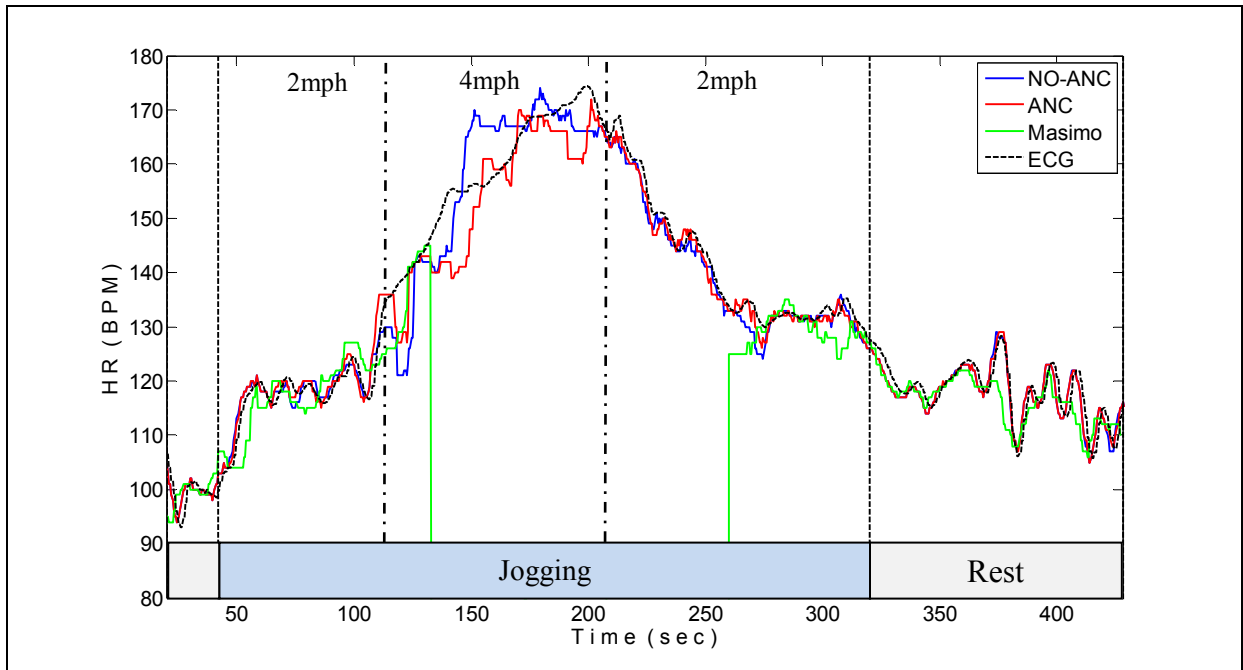


Figure 8.45: HR measurements during treadmill jogging without and with ANC.

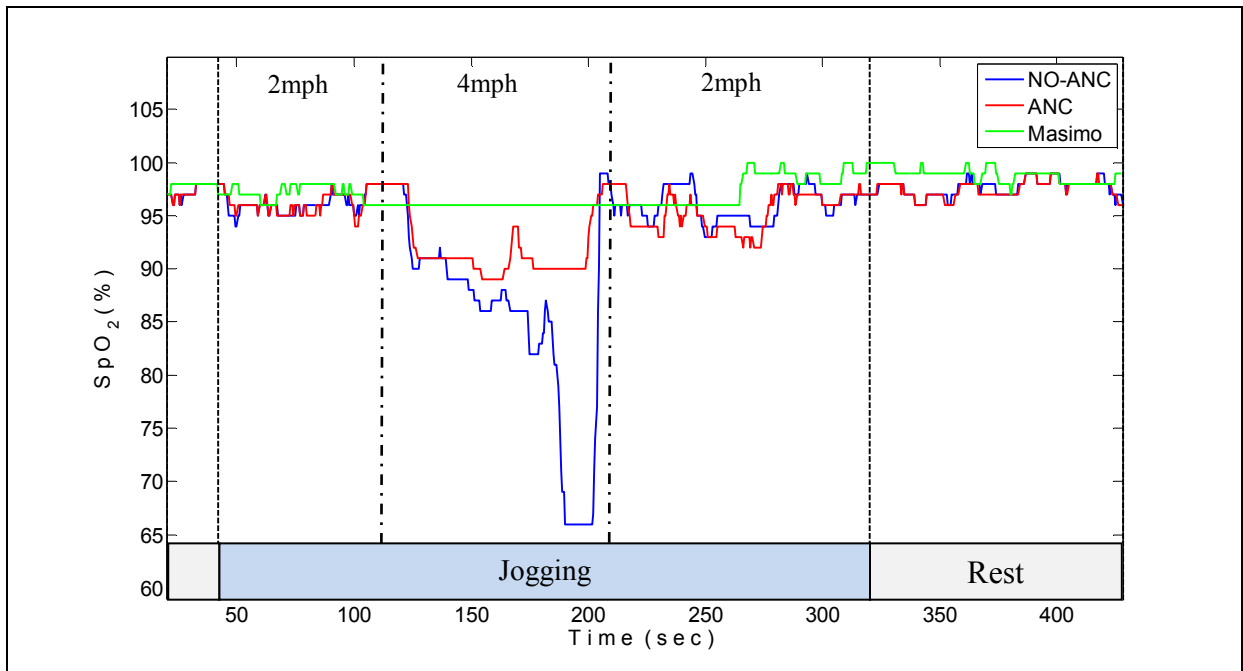


Figure 8.46: SpO<sub>2</sub> values during treadmill jogging without and with ANC.



HR values measured by the WPO were plotted against reference HR values (Figure 8.47 and Figure 8.48). We found that the CC between HR values obtained from the WPO and reference HR values was improved from 0.87 to 0.97 after adaptive filtering. The residual HR plots, shown in Figure 8.49 and Figure 8.50, illustrate that the mean difference was reduced from 7 BPM to 3 BPM after adaptive filtering. Similar improvements were also observed for SpO<sub>2</sub> measurements. As plotted in Figure 8.51 and Figure 8.52, the mean SpO<sub>2</sub> difference reduced from 3% to 2% after ANC.

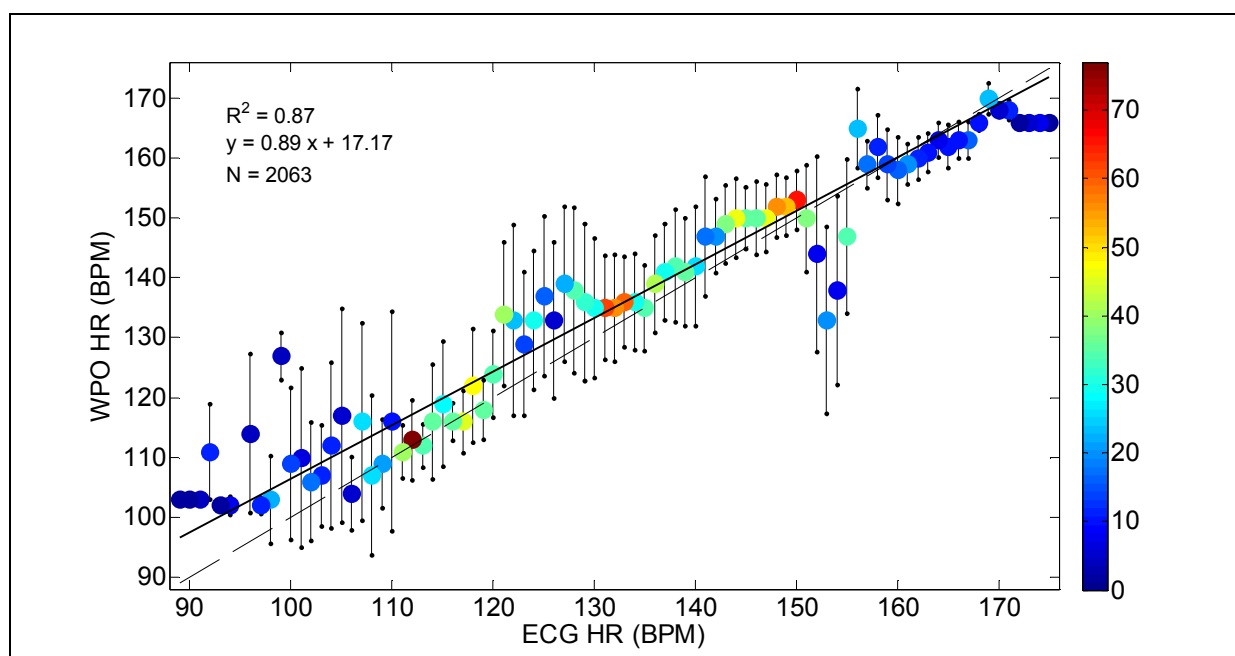


Figure 8.47: Comparison of HR measured during treadmill jogging by the WPO and reference source before ANC.

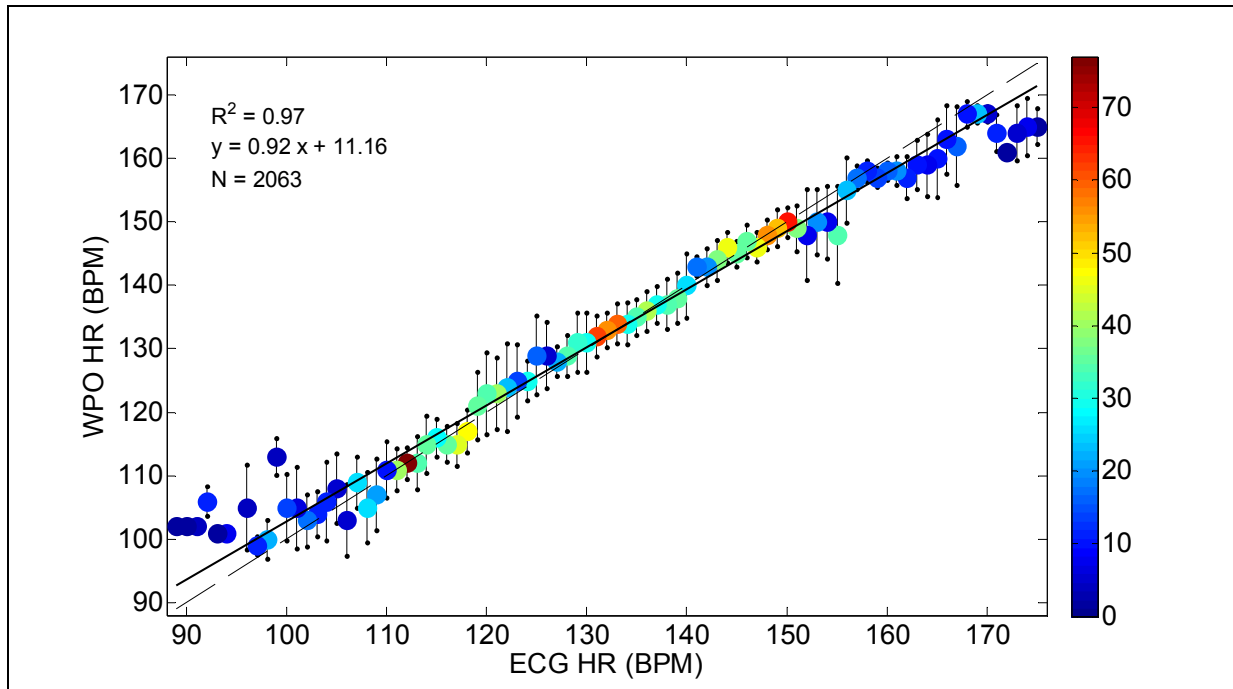


Figure 8.48: Comparison of HR measured during treadmill jogging by the WPO and reference source after ANC.

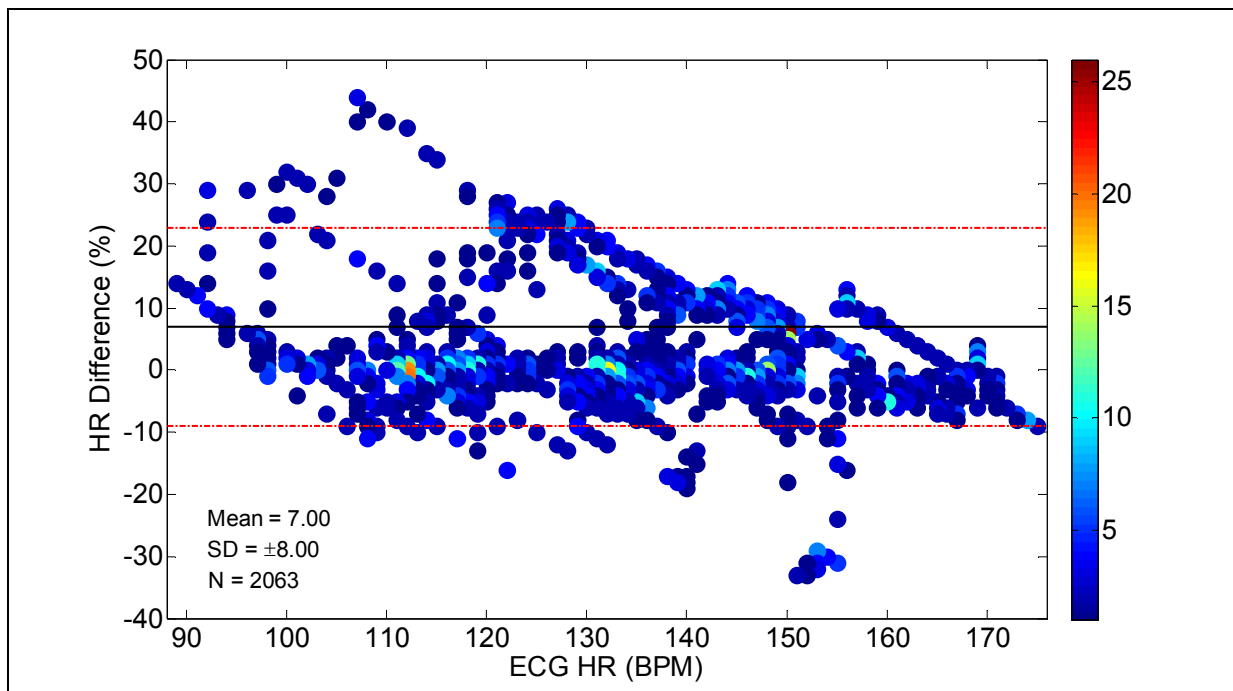


Figure 8.49: Difference in HR readings measured by the WPO and the ECG Holter Monitor without ANC (treadmill jogging). The red lines indicate the  $\mu \pm 2SD$  values.

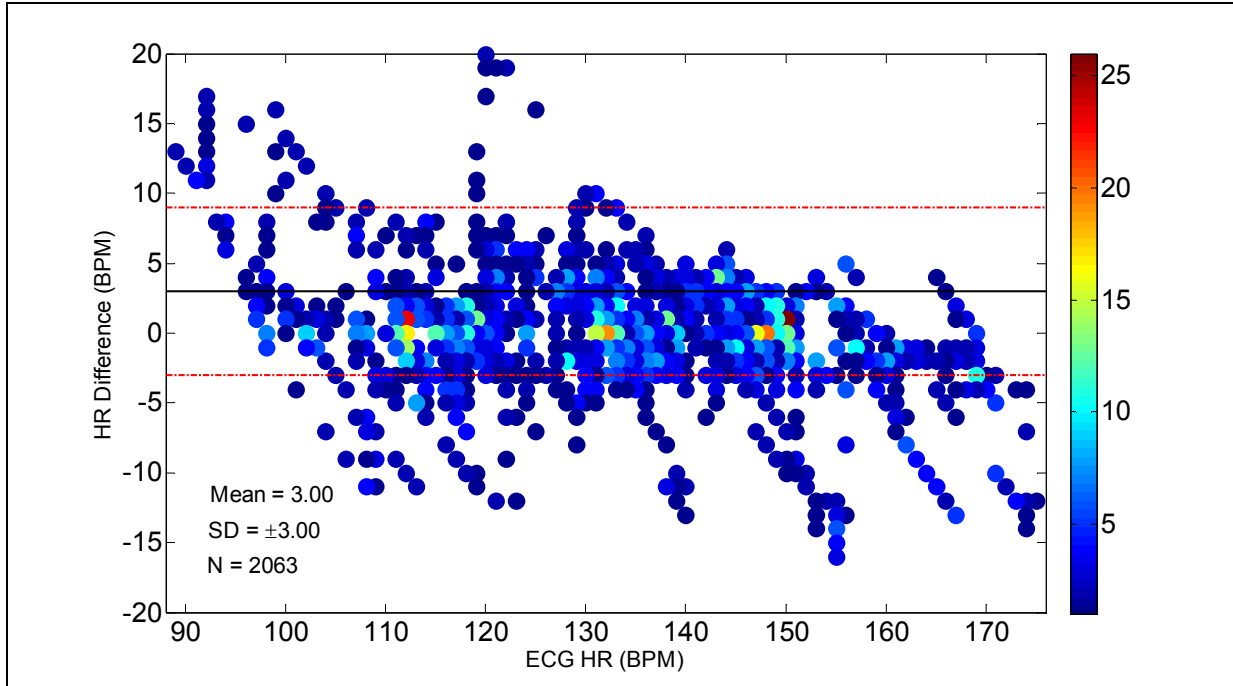


Figure 8.50: Difference in HR readings measured by the WPO and the ECG Holter Monitor with ANC (treadmill jogging). The red lines indicate the  $\mu \pm 2SD$  values.

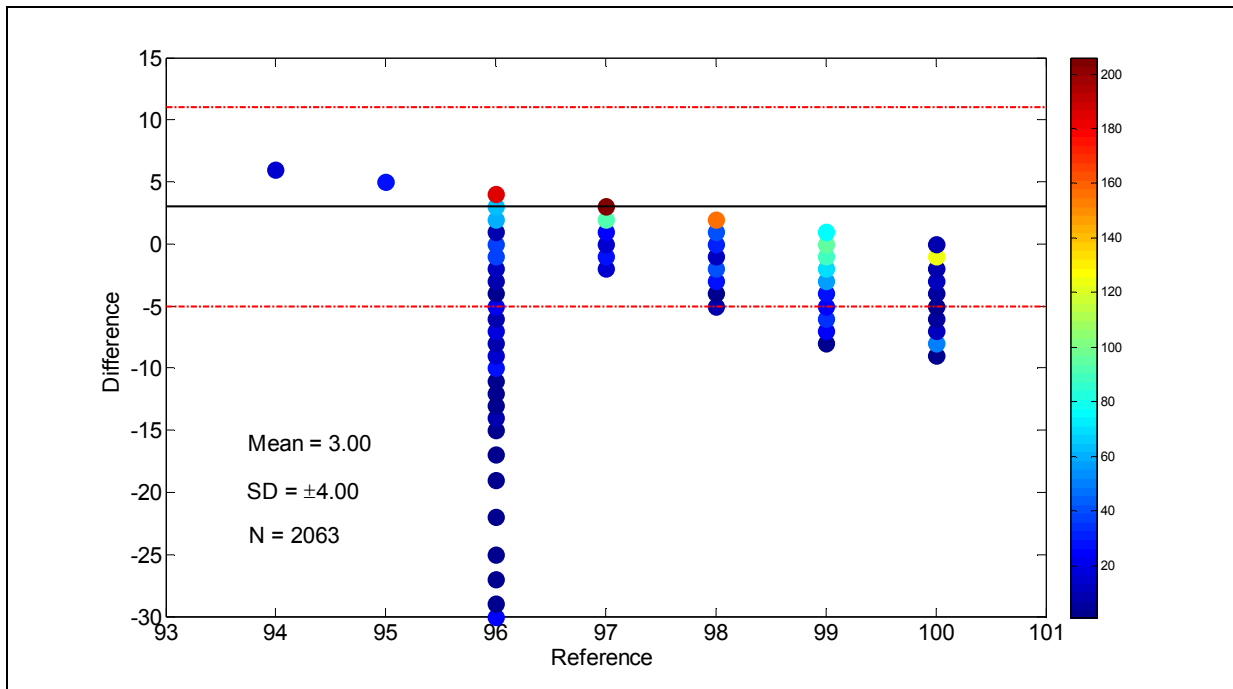


Figure 8.51: Difference in SpO<sub>2</sub> readings measured by the WPO and MPO without ANC (treadmill jogging). The red lines indicate the  $\mu \pm 2SD$  values.

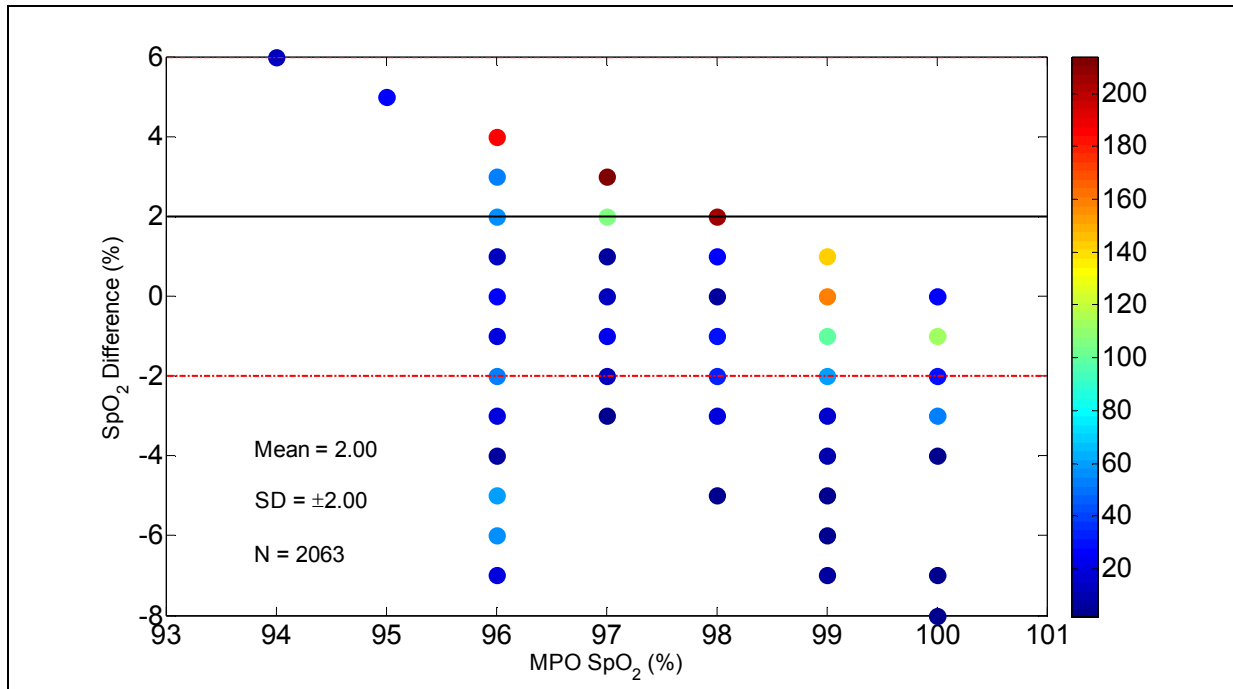


Figure 8.52: Difference in SpO<sub>2</sub> readings measured by the WPO and MPO with ANC (treadmill jogging). The red lines indicate the  $\mu \pm 2SD$  values.

Table 8.4 summarizes analysis results for each trial. These HR data confirmed that ANC improved the MSE by 71%, the SD was improved by 51% and R<sup>2</sup> was improved by 11%. For SpO<sub>2</sub>, the error was reduced by 50%, whereas SD was improved by 27%.

Table 8.4: Comparison of HR and SpO<sub>2</sub> values obtained before and after a LMS type ANC. M =16 and  $\mu = 0.01$  (treadmill jogging)

Trial	% Improvement					
	ECG - HR			MPO SpO <sub>2</sub>		Change in SpO <sub>2</sub>
	MSE	SD	R <sup>2</sup>	MSE	SD	
1	72	57	5.98	0	0	NC
2	93	75	14.38	85	67	
3	54	0	-0.59	100	0	
4	88	71	7.51	83	50	
5	93	77	35.43	0	0	<2%
6	84	50	12.26	0	0	NC
7	13	25	0.85	83	71	
Average	71	51	10.83	50	27	

### 8.2.6. LMS – Outdoor Running Experiments

The results of outdoor running experiments were similar to the results of the treadmill jogging experiments. Table 8.5 summarizes the results for all running tests. In case of HR estimation, it was found that adaptive filtering yields better results in terms of MSE, SD and CC. Post adaptive filtering results showed an improvement of 35% for MSE, 31% for SD and 8% for  $R^2$  values. SpO<sub>2</sub> measurement accuracy was also improved by adaptive filtering. An average improvement of 12% was noted for SpO<sub>2</sub> values.

Table 8.5: Comparison of HR and SpO<sub>2</sub> values obtained before and after a LMS type ANC. M =16 and  $\mu = 0.01$  (outdoor running)

Trial	% Improvement					
	ECG – HR			MPO SpO <sub>2</sub>		Change in SpO <sub>2</sub>
	MSE	SD	R <sup>2</sup>	MSE	SD	
1	59	40	3.01	50	0	NC
2	13	33	2.17	-100	-100	
3	69	56	23.17	43	0	
4	60	40	8.89	17	0	
5	15	20	3.25	57	0	
6	-4	0	8.00	7	0	<2%
Average	35	31	8.08	12	-17	

In trial#2, we noticed that ANC degraded the SpO<sub>2</sub> measurement accuracy. HR and SpO<sub>2</sub> plots corresponding to trials#2 are shown in Figure 8.53 and Figure 8.54, respectively. After adaptive filtering, SpO<sub>2</sub> values dropped to 91%. Also, there was no significant change in the HR values due to adaptive filtering. The ability of the ANC to improve HR measurements, but degrade the SpO<sub>2</sub> accuracy, is not yet understood and is therefore a potential issue that requires further studies.

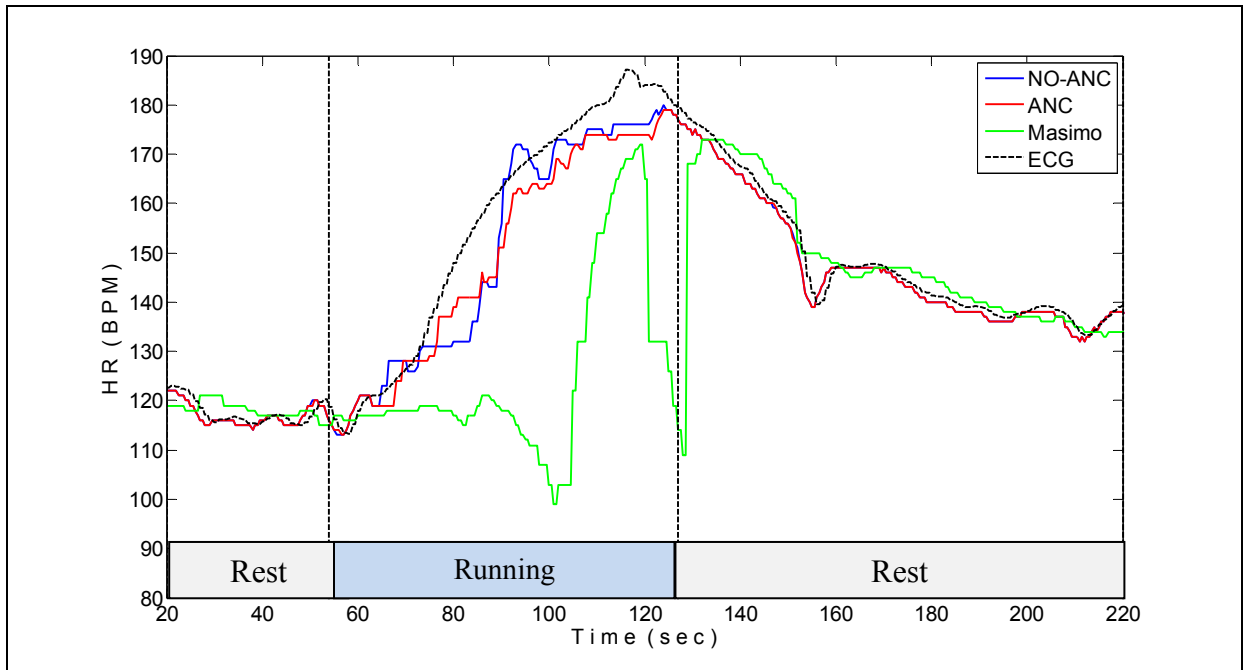


Figure 8.53: HR readings for trial#2 during outdoor running.

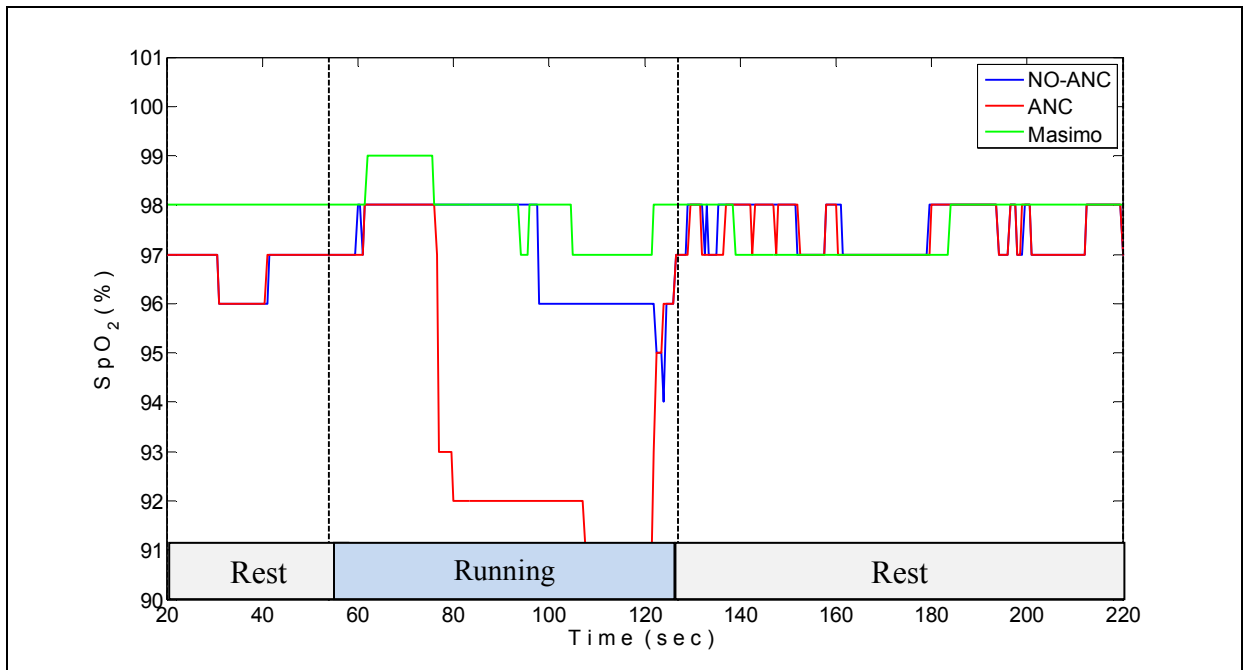


Figure 8.54: SpO<sub>2</sub> readings for trial#2 during outdoor running.

### 8.2.7. LMS – Staircase Climbing Experiments

PPG waveforms collected during staircase experiments are shown in Figure 8.55 to Figure 8.57. During rest (phase -1 and phase-3), there are no motion artifacts to cause PPG signal distortions. Hence, the adaptive filtering has no effect on the PPG waveform. However, staircase climbing induces motion artifact to cause significant PPG distortions, thus degrading measurement accuracy. Figure 8.56 highlights the peak that was successfully recovered by adaptive filtering.

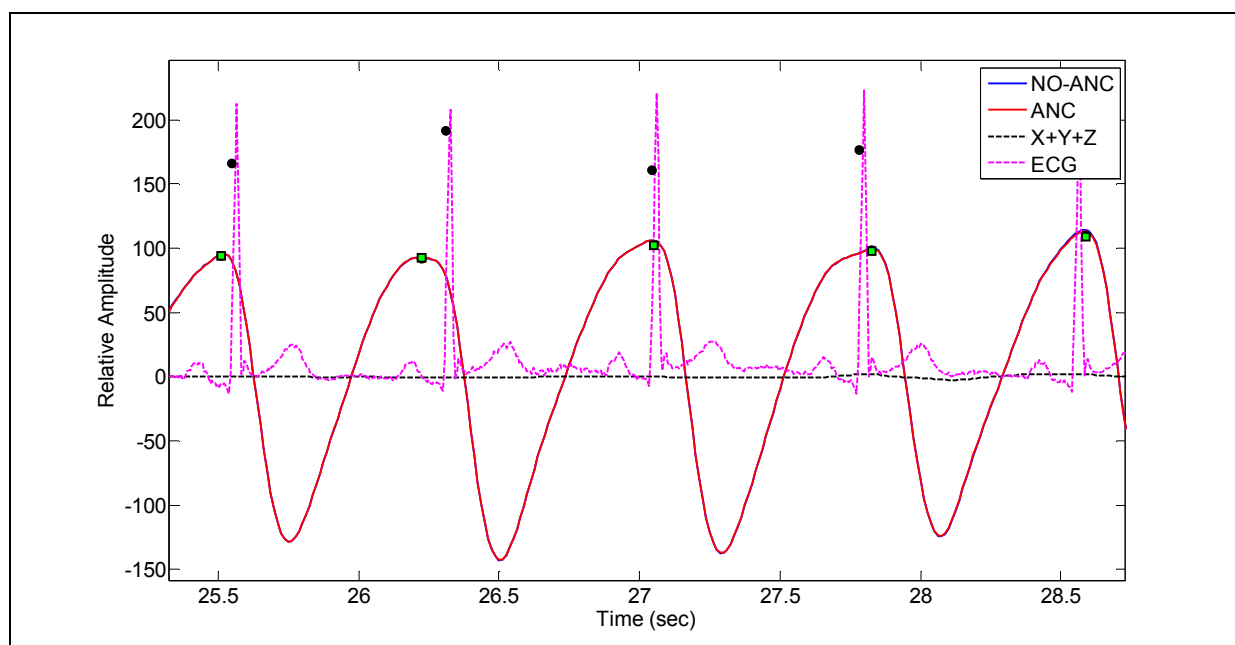


Figure 8.55: Typical IR PPG signals during Phase-1 of staircase climbing, before (Blue) and after (Red) ANC. Note that the blue and red traces overlap in this figure. ■ marks PPG peaks detected by the WPO after ANC (5-peaks), and ● represents R-waves detected from the ECG waveform (5-peaks).

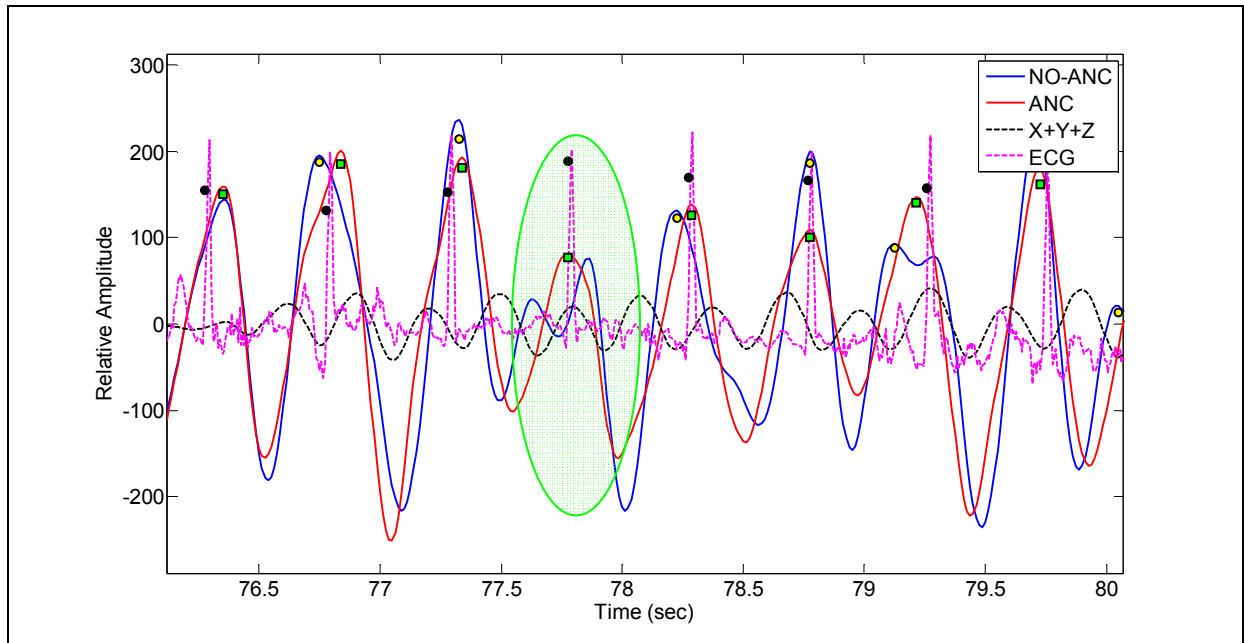


Figure 8.56: Typical IR PPG signals during Phase-2 of staircase climbing experiment, before (Blue) and after (Red) ANC. ■ marks PPG peaks detected by the WPO after ANC (8-peaks), ● denotes PPG peaks detected without ANC (7-peaks), and ● represents R-waves detected from the ECG waveform (8-peaks).

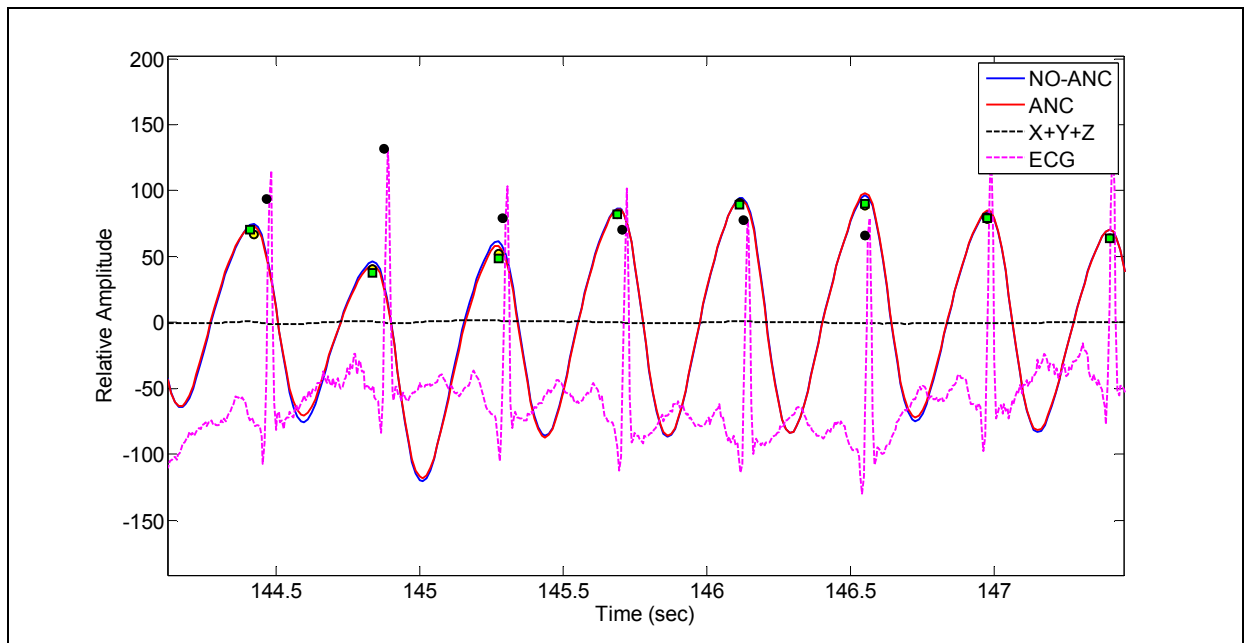


Figure 8.57: Typical IR PPG signals during Phase-2 of staircase climbing experiment, before (Blue) and after (Red) ANC. Note that the blue and red traces overlap in this figure. ■ marks PPG peaks detected by the WPO after ANC (8-peaks), and ● represents R-waves detected from the ECG waveform (8-peaks).



Frequency analysis of PPG signals collected during staircase climbing experiments illustrate that several motion induced peaks were present. These peaks yielded inaccurate HR and SpO<sub>2</sub> measurements. Figure 8.58 and Figure 8.59 demonstrate that ANC was able to successfully attenuate these frequencies. The two figures also demonstrate that ANC is effective in filtering several motion frequencies, and hence can be used for real-time applications where generally more than one motion frequency component can affect the PPG quality.

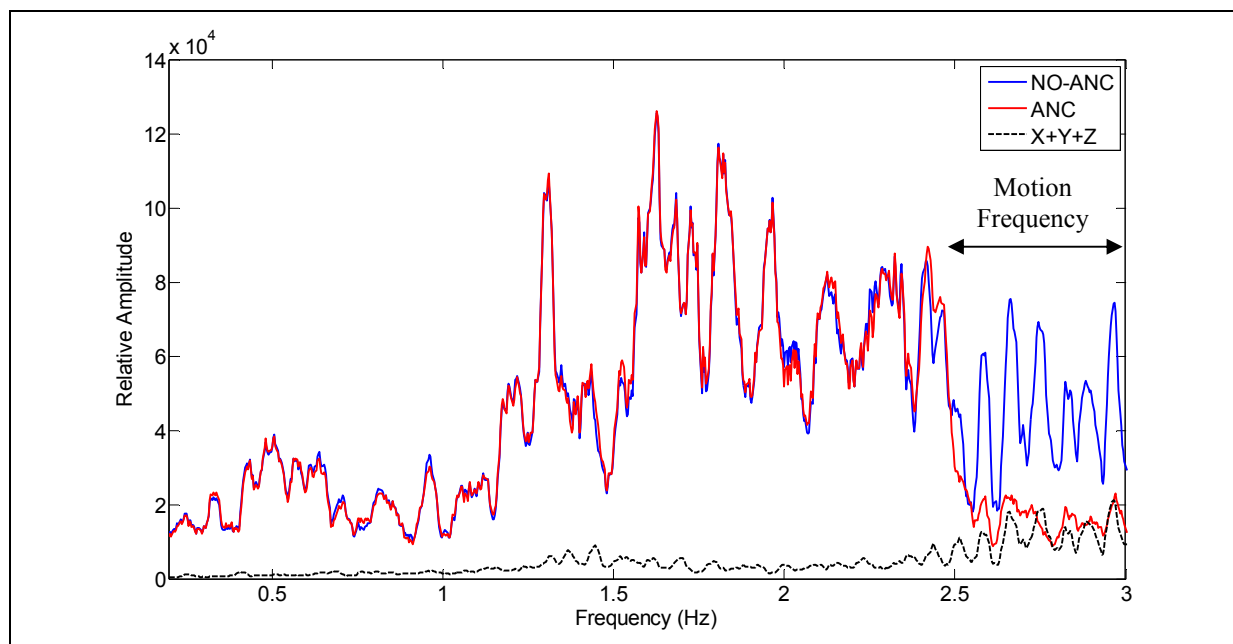


Figure 8.58: Frequency spectrum of IR PPG during staircase climbing.

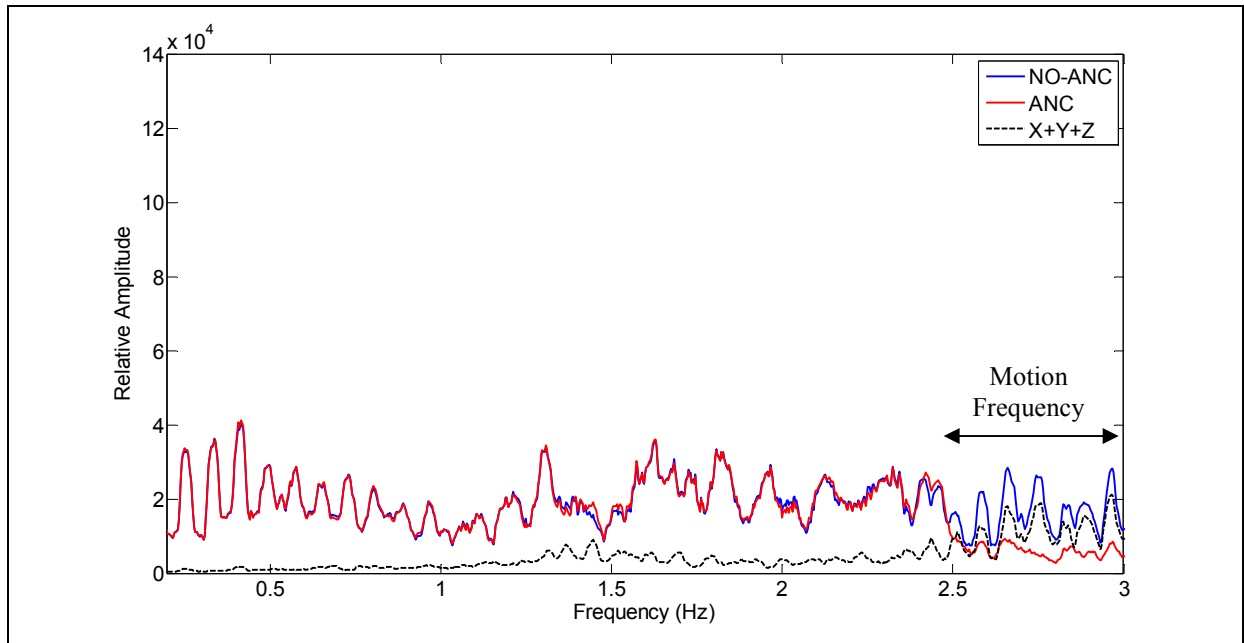


Figure 8.59: Frequency spectrum of Red PPG during staircase climbing.

Unprocessed PPG signals, used for HR measurements, produced erroneous results because the algorithm detects false peaks and /or missed some true cardiac peaks during motion. Figure 8.60 shows HR readings estimated from pre and post adaptively filtered PPG signals. At the beginning of the adaptation process, the adaptive filter weights are zero and start to change according to the motion frequency. Since the adaptation takes time, initially, the HR values do not match the reference HR readings. Once the filter weights are adapted to the motion frequency, HR readings become more accurate and closely match the actual HR. Similar observations were made for SpO<sub>2</sub> measurements.

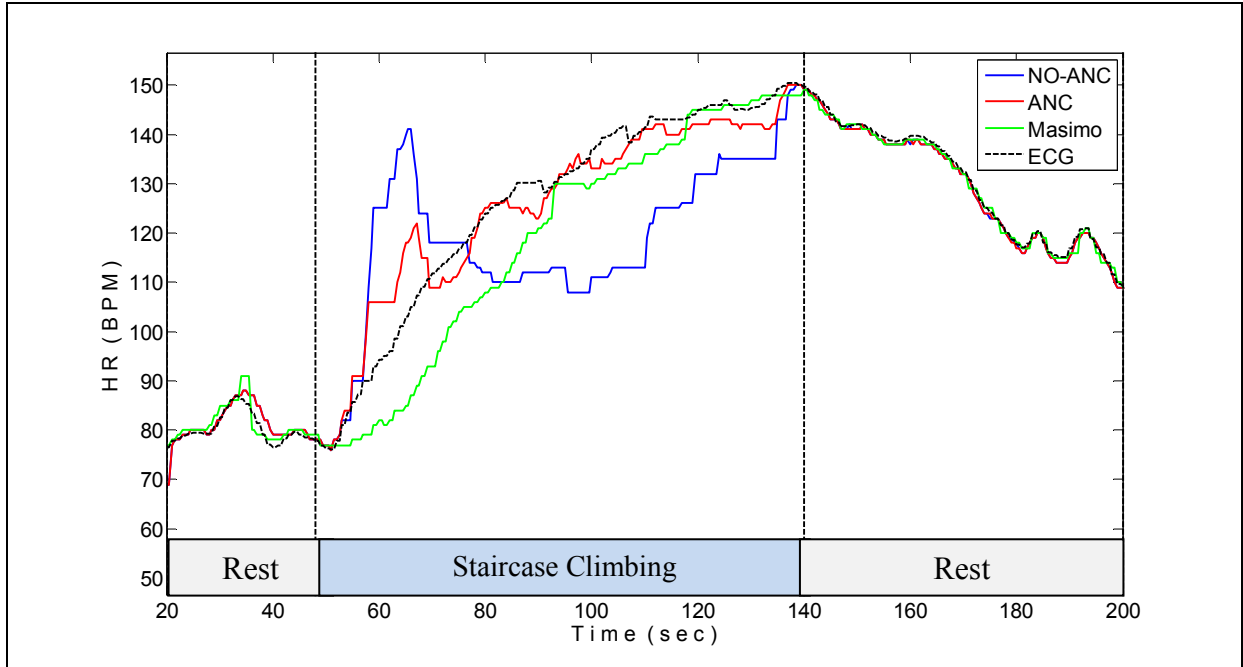


Figure 8.60: HR measurements without and with ANC during a staircase climbing experiment.

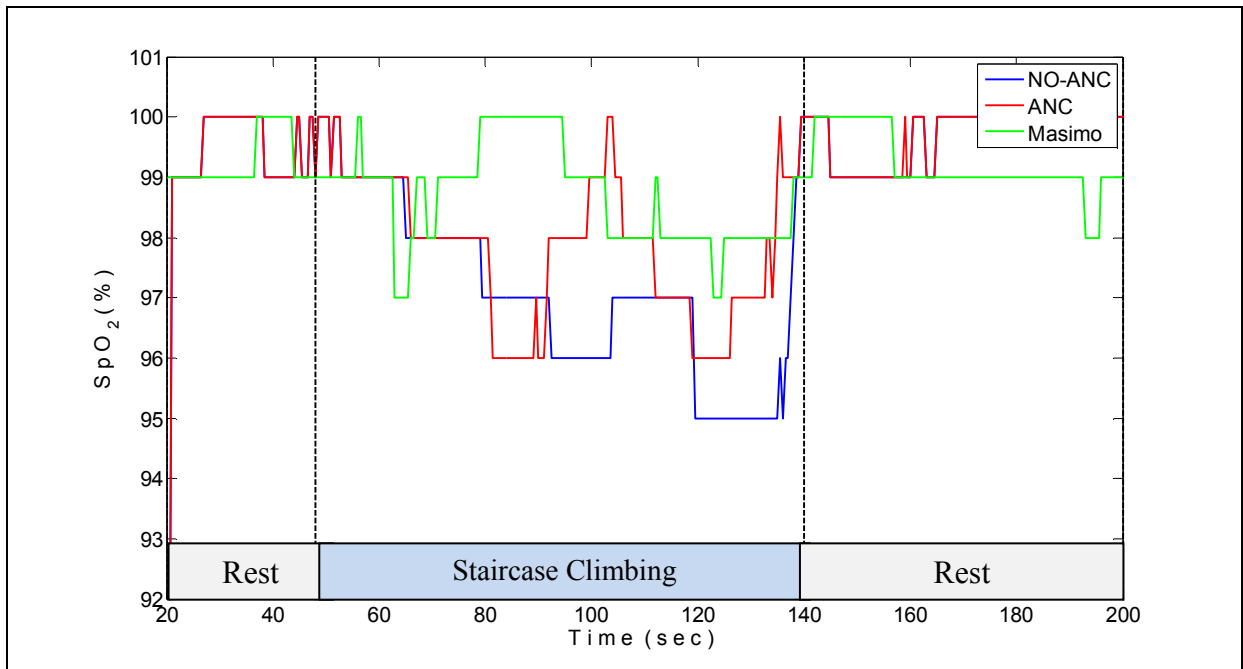


Figure 8.61: SpO<sub>2</sub> measurements without and with ANC during a staircase climbing experiment.

Plots of regression analysis are shown in Figure 8.62 and Figure 8.67. The results indicate that ANC improves the HR CC by 8%. The mean difference between HR values measured by the WPO and actual HR values was improved by 52%. The mean difference in SpO<sub>2</sub> was improved by 17%. Table 8.6 summarizes the results for each trial. From this table, it can be concluded that ANC helps to improve the accuracy of pulse oximeters during staircase climbing.

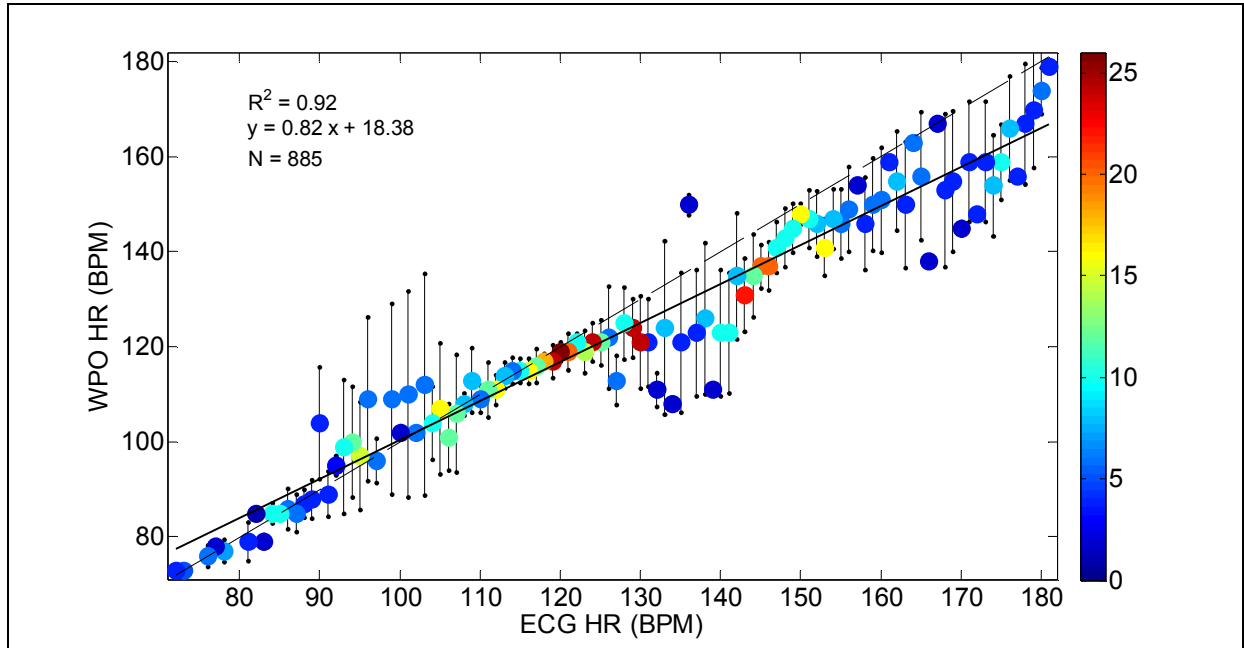


Figure 8.62: Comparison of HR measured during staircase climbing by the WPO and reference source before ANC.

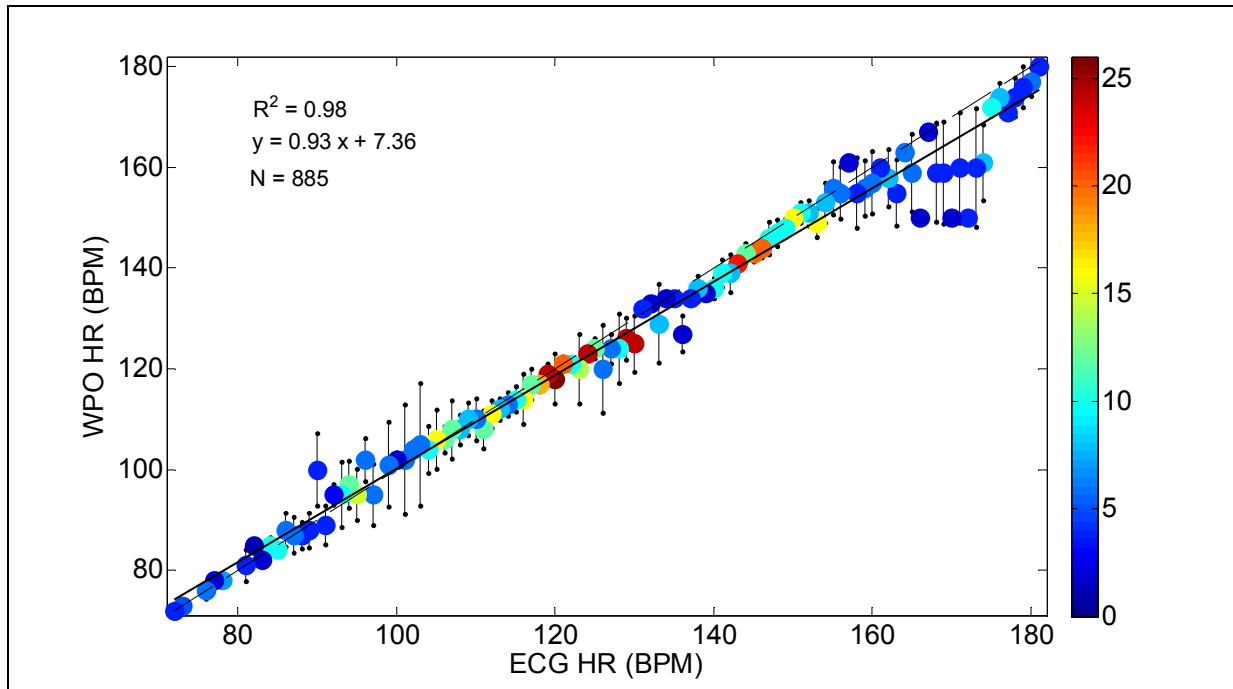


Figure 8.63: Comparison of HR measured during staircase climbing by the WPO and reference source after ANC.

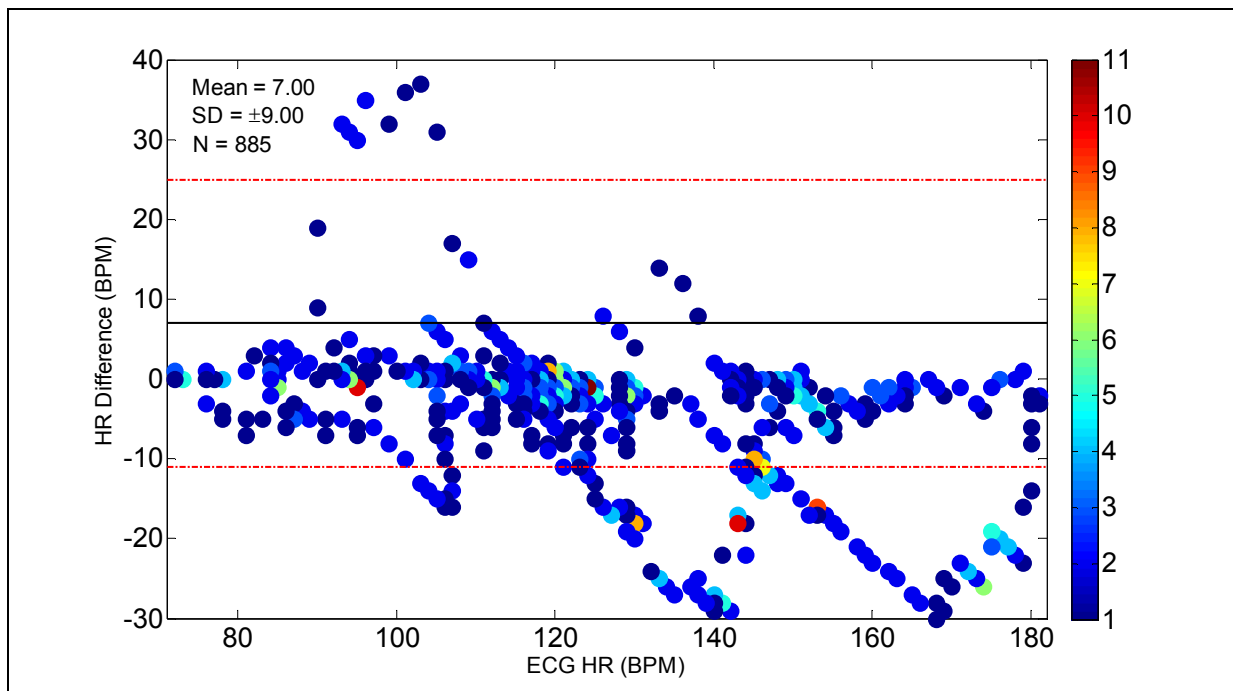


Figure 8.64: Difference in HR readings measured by the WPO and the ECG Holter Monitor without ANC (staircase climbing). The red lines indicate the  $\mu \pm 2\text{SD}$  values.

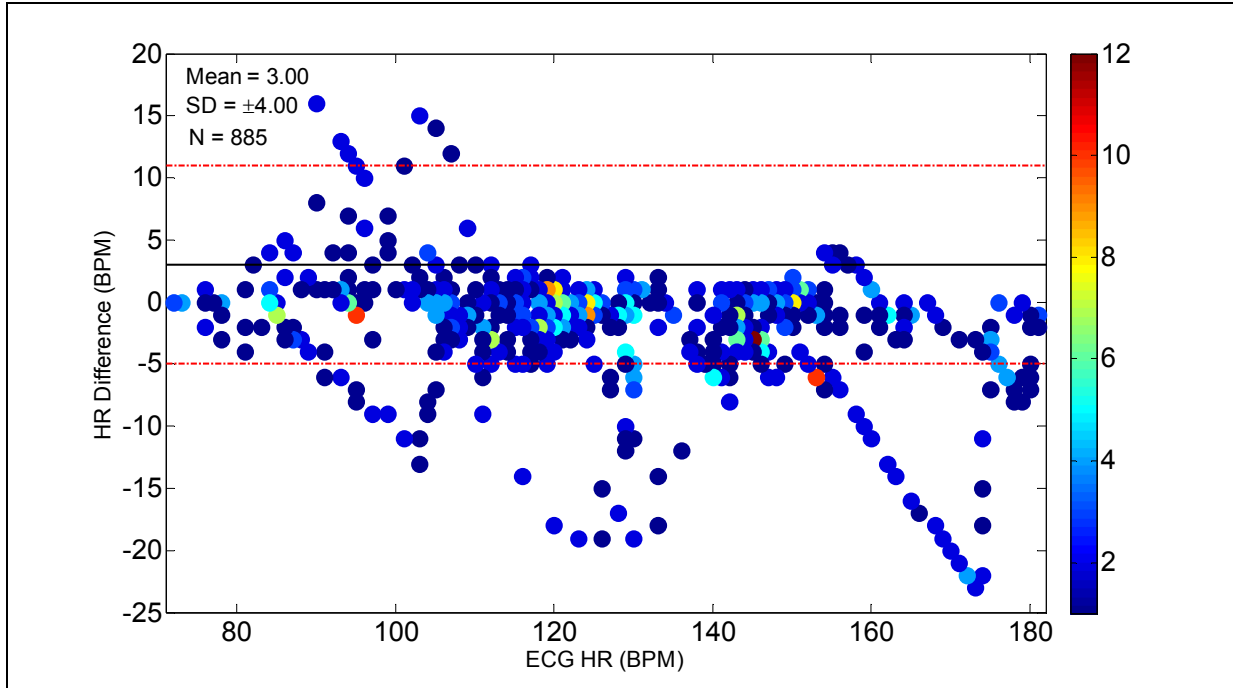


Figure 8.65: Difference in HR readings measured by the WPO and the ECG Holter Monitor with ANC (staircase climbing). The red lines indicate the  $\mu \pm 2SD$  values.

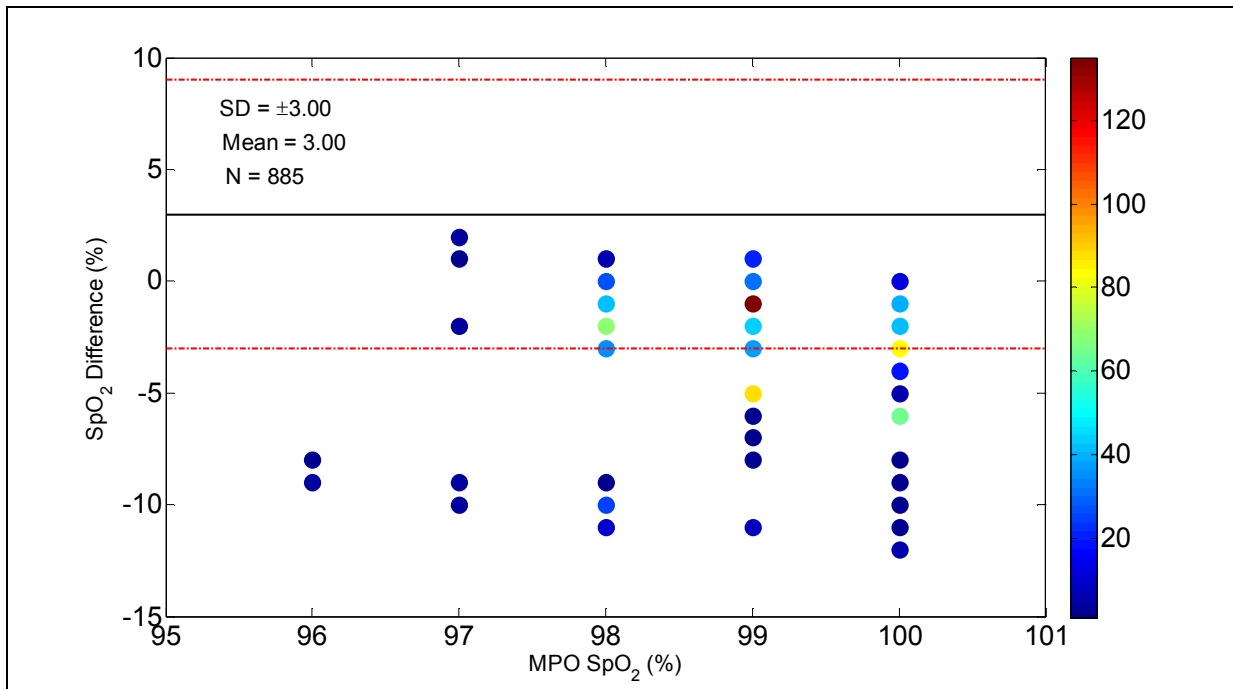


Figure 8.66: Difference in SpO<sub>2</sub> readings measured by the WPO and MPO without ANC (staircase climbing). The red lines indicate the  $\mu \pm 2SD$  values.

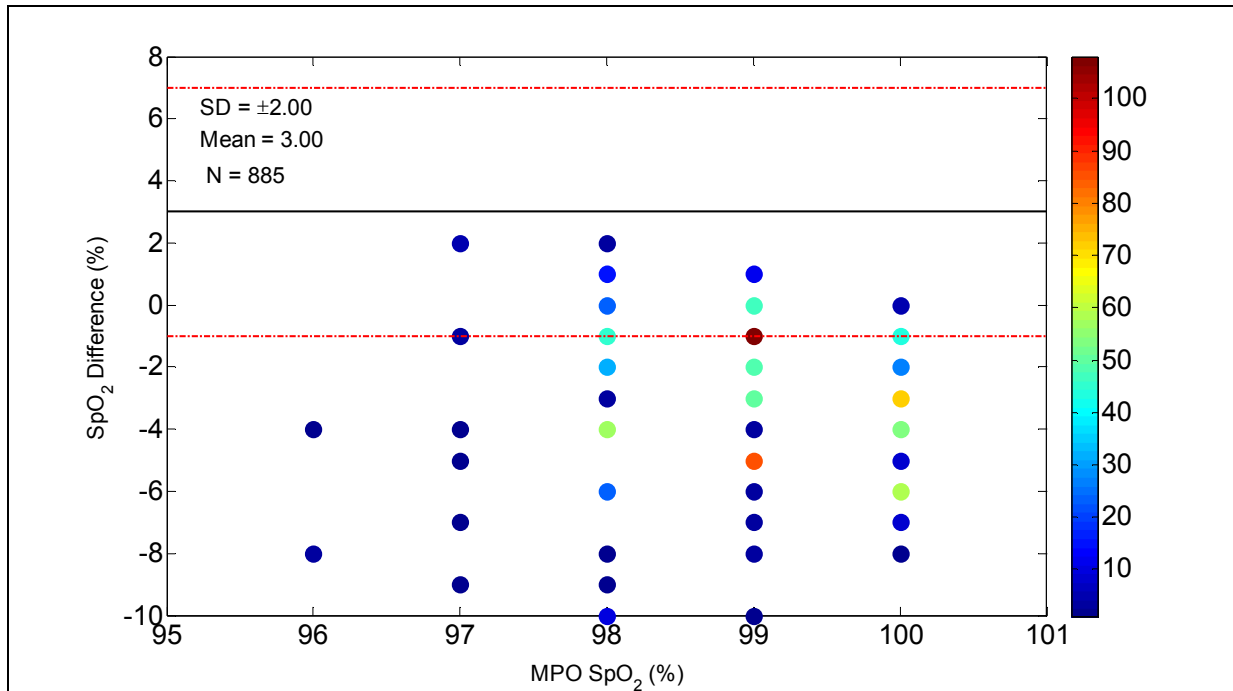


Figure 8.67: Difference in SpO<sub>2</sub> readings measured by the WPO and MPO with ANC (staircase climbing). The red lines indicate the  $\mu \pm 2SD$  values.

Table 8.6: Comparison of HR and SpO<sub>2</sub> values obtained before and after a LMS type ANC. M =16 and  $\mu = 0.01$  (Staircase climbing experiments)

Trial	% Improvement					
	ECG - HR			MPO SpO <sub>2</sub>		Change in SpO <sub>2</sub>
	MSE	SD	R <sup>2</sup>	MSE	SD	
1	92	60	33.61	40	0	
2	68	25	2.16	46	25	
3	0	0	-0.26	0	0	<2%
4	43	33	0.30	0	0	<2%
5	57	30	6.21	0	0	NC
Average	52	30	8.40	17	5	

### 8.3. Conventional LMS Results Summary

The results obtained from this study revealed that processing motion corrupted PPG signals by conventional LMS improves HR and SpO<sub>2</sub> accuracy. ANC can improve the MSE for HR values by a factor of 54%. The CC for HR measurements was improved by 19%. Similarly, an improvement of 35% was observed in SD. MSE and SD for SpO<sub>2</sub> measurements were improved by 22 % and 15%, respectively.

### 8.4. TV-LMS

#### 8.4.1. Step-Size Selection

The TV-LMS algorithm is similar to the conventional LMS algorithm, except for a time dependent convergence parameter [23]. In the TV-LMS algorithm, the  $\mu$  is initially set to a large value in order to speed up the convergence. As time progresses, the parameter is adjusted to a smaller value to decrease the MSE.

The initial  $\mu$  value was determined based on the results of the 31 data sets. These are the same data sets that were used to estimate  $\mu$  for the conventional LMS filter. Data were analyzed by a 16<sup>th</sup> order TV-LMS filter with a variable  $\mu$ .  $\mu$  was varied from 0 to 0.05 in steps of 0.002. Table 4.2 summarizes the TV-LMS equations. The constants C, a, and b are set to 2, 0.01 and 0.7 respectively [23]. These parameters determine the magnitude and rate of  $\alpha_n$  decrease.

The effectiveness of the TV-LMS filter, with varying  $\mu$ , was determined based on the improvement in HR and SpO<sub>2</sub> errors. Figure 8.68 and Figure 8.69 show the calculated MSE  $\pm$  1 SD for HR and SpO<sub>2</sub>. MSE improvement in HR was noticeable for  $0 < \mu < 0.03$ . For  $\mu > 0.03$ , the improvements were insignificant. Similarly, maximum MSE improvement for SpO<sub>2</sub> was observed for  $0.008 < \mu < 0.012$ . Maximum improvements for HR and SpO<sub>2</sub> were observed for  $\mu = 0.01$ .



Initial value of filter order ( $M = 16$ ) was kept the same as in the conventional LMS filter because, as stated previously, the only difference between LMS and TV-LMS is the use of a dynamic  $\mu$  in the latter algorithm. Hence, a 16<sup>th</sup> order TV-LMS filter with a  $\mu$  of 0.01 was implemented in Matlab.

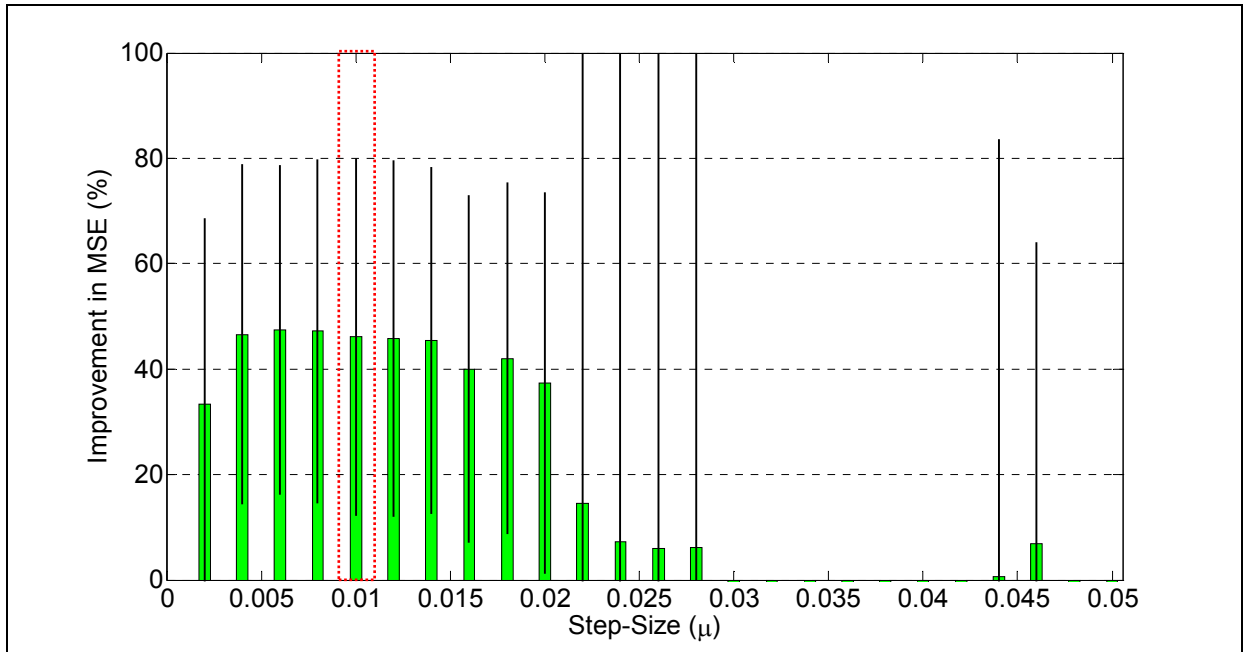


Figure 8.68: Average MSE improvement in HR for a 16<sup>nd</sup> order TV-LMS filter with varying step-size ( $\mu$ ). The error bars indicate  $\pm 1SD$ . The shaded region corresponds to  $\mu$  value that was selected for further study.

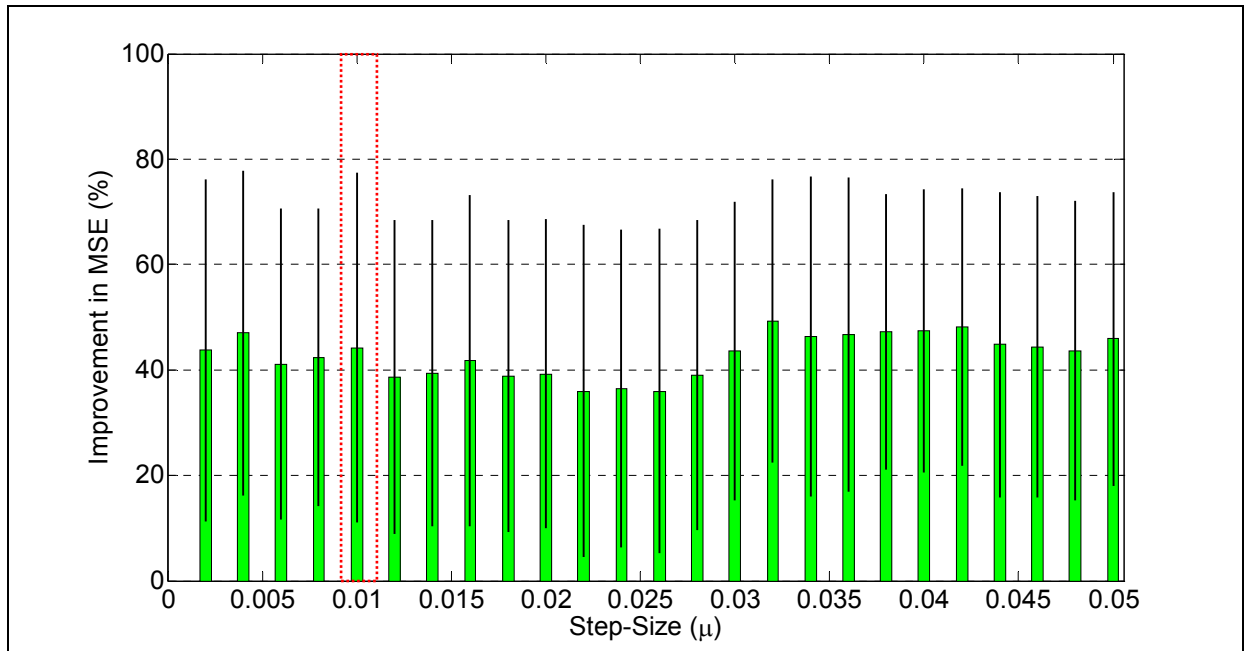


Figure 8.69: Average MSE improvement in SpO<sub>2</sub> for a 16<sup>th</sup> order TV-LMS filter with varying step-size ( $\mu$ ). The error bars indicate  $\pm 1SD$ . The shaded region corresponds to  $\mu$  value that was selected for further study.

#### 8.4.2. Results of TV-LMS filter

Data collected during sitting experiments, treadmill jogging, outdoors running and staircase climbing were adaptively filtered using a 16<sup>th</sup> order TV-LMS algorithm. The results obtained after adaptive filtering demonstrated that the TV-LMS is also effective in reducing the effects of motion artifacts. HR data analysis showed that the MSE was improved by 56%, SD by 35% and CC by 19%. In the case of SpO<sub>2</sub>, MSE was improved by 25%, whereas SD was improved by 23%.

### 8.5. NLMS and MNLMS

#### 8.5.1. Step-Size and Filter Order Selection

In NLMS, the gradient step factor  $\mu$  is normalized by the energy of the reference input signal. The NLMS equations are given in Table 4.3. To find an ideal value for  $\mu$ , NLMS was implemented in Matlab and was used to filter all 31 data sets. The filter order was kept constant at 16, whereas  $\mu$  was varied from 0 to 0.05 in steps of 0.002.

The results, depicted in Figure 8.70 and Figure 8.71, indicate that the NLMS filter produced better performance when  $\mu = 0.006$ . Similar data analysis showed that a 16<sup>th</sup> order NLMS filter having a convergence parameter of 0.006 produced the most accurate HR and SpO<sub>2</sub> measurements during motion. Figure 8.72 and Figure 8.73 show that, for HR, the NLMS algorithm with  $M = 16$  improved the MSE by 50%, whereas for SpO<sub>2</sub>, MSE was improved by 40%. Since the MNLMS algorithm is a modified version of the NLMS algorithm, the same filter parameters were selected for implementing the MNLMS algorithm.

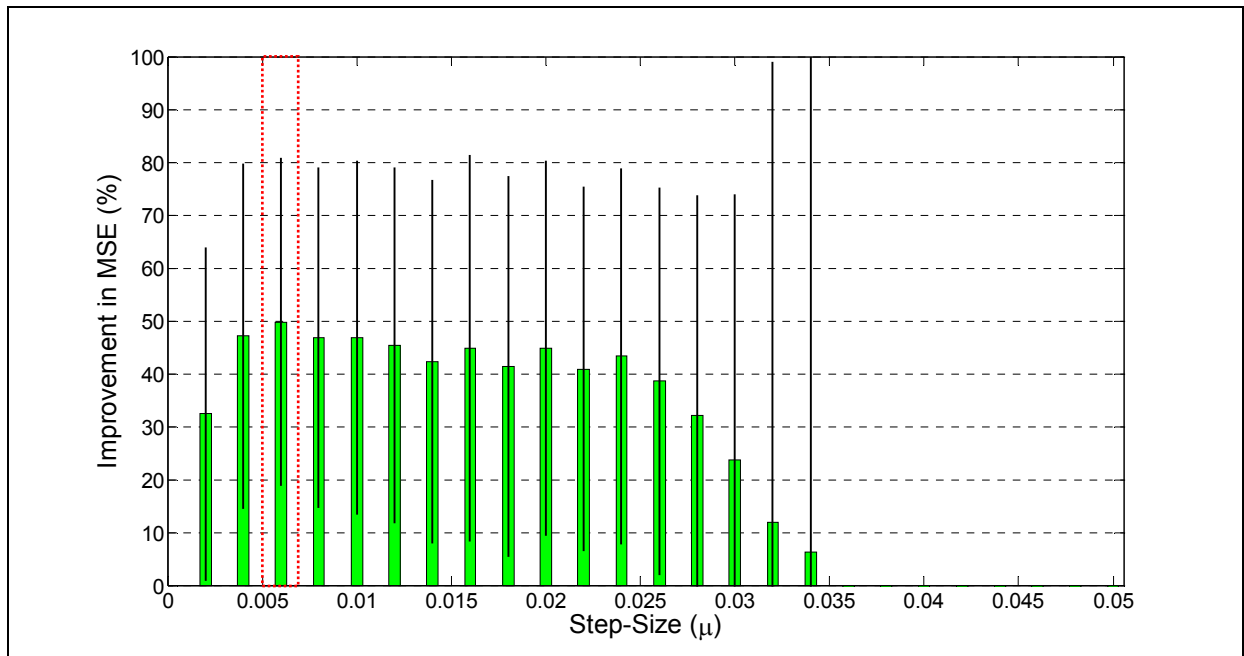


Figure 8.70: Average MSE improvement in HR for a 16<sup>th</sup> order NLMS filter with varying step-size ( $\mu$ ). The error bars indicate  $\pm 1SD$ . The shaded region corresponds to  $\mu$  value that was selected for further study.

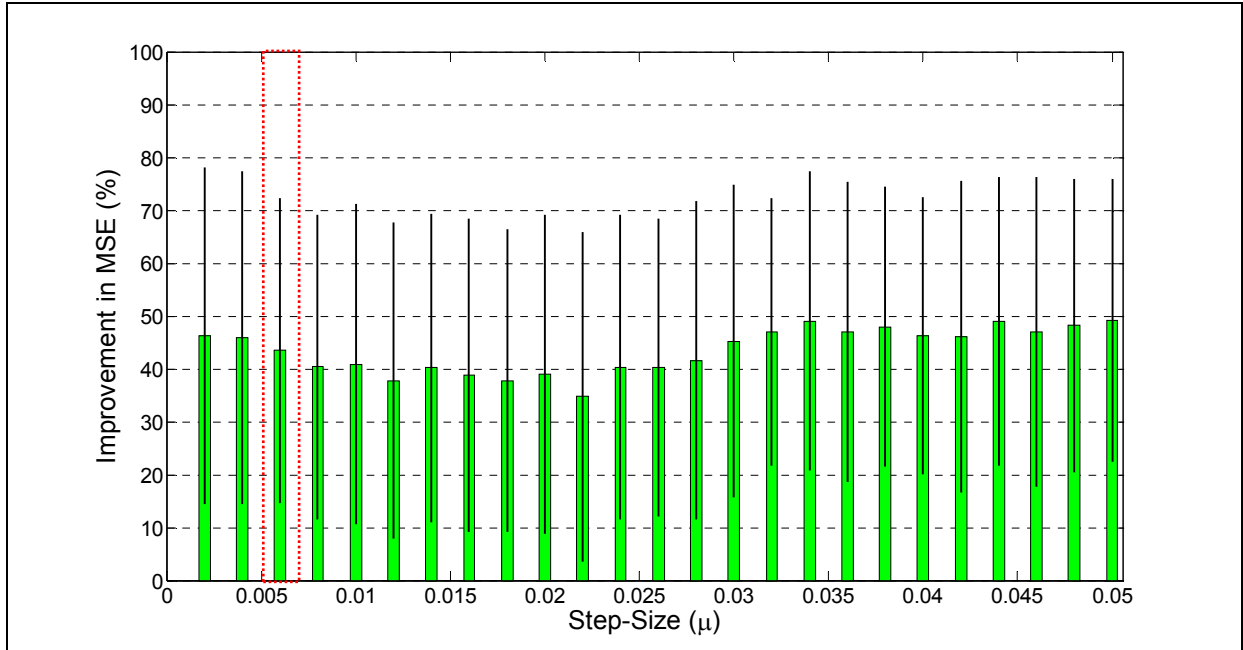


Figure 8.71: Average MSE improvement in SpO<sub>2</sub> for a 16<sup>th</sup> order NLMS filter with varying step-size ( $\mu$ ). The error bars indicate  $\pm 1SD$ . The shaded region corresponds to  $\mu$  value that was selected for further study.

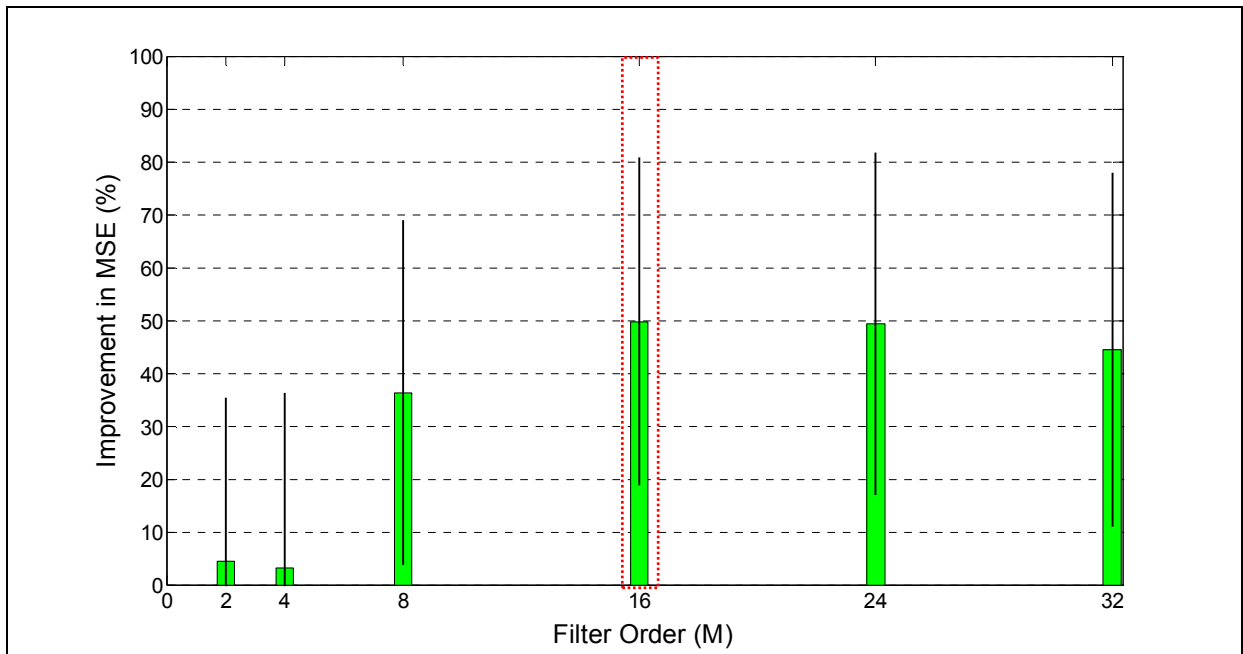


Figure 8.72: Average improvement in HR MSE for a NLMS filter with a constant  $\mu = 0.006$  and varying filter order ( $M$ ). The error bars indicate  $\pm 1SD$ . The shaded region corresponds to  $M$  value that was selected for further study.

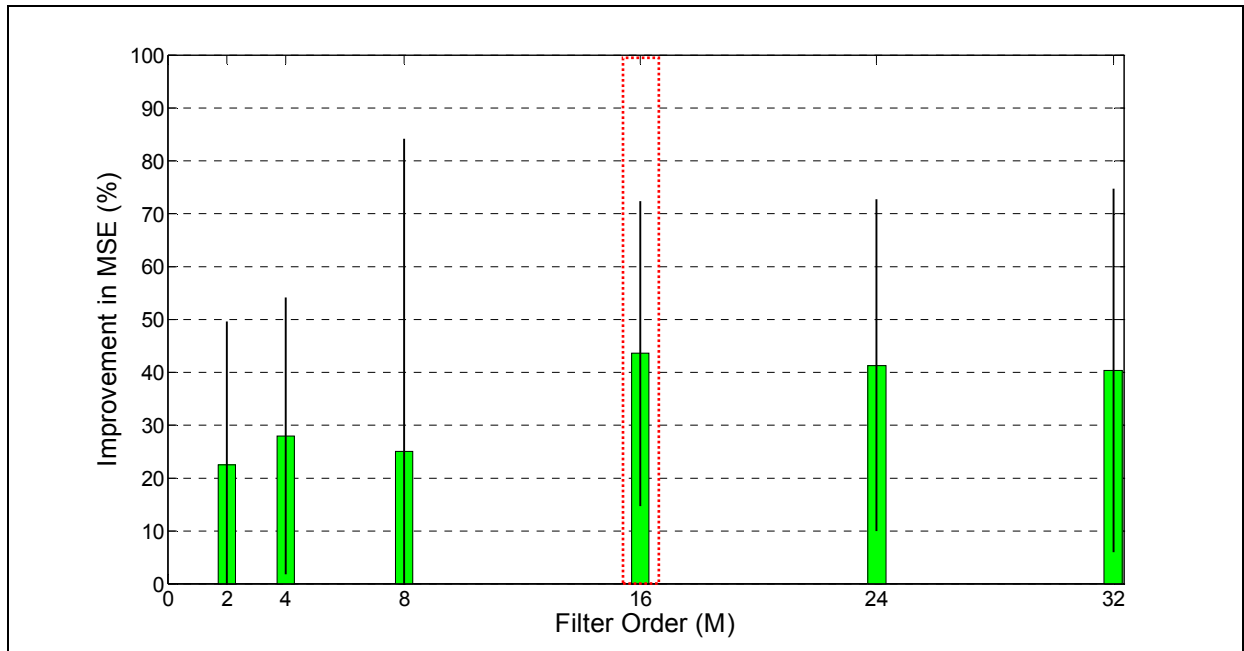


Figure 8.73: Average improvement in SpO<sub>2</sub> MSE for a NLMS filter with a constant  $\mu = 0.006$  and varying filter order (M). The error bars indicate  $\pm 1SD$ . The shaded region corresponds to M value that was selected for further study.

#### 8.5.2. Results of NLMS and MNLMS filter

Data analysis confirmed that the performance of the NLMS and MNLMS algorithm were similar to the results obtained by the conventional LMS filter. For HR estimation, MSE was improved by 60% by both algorithms. SD and  $R^2$  showed an improvement of 42% and 13%, respectively. For SpO<sub>2</sub> estimations, both algorithms increased the MSE accuracy by 22% and SD by 21%.

## 8.6. RLS Algorithm

### 8.6.1. Forgetting factor and Filter Order Selection

RLS filter output solely depends on the filter order ( $M$ ). The forgetting factor ( $\lambda$ ) is generally kept constant (close to 1). To determine an ideal filter order, the MSE performance of the RLS filter was observed as the filter order ( $M$ ) was varied from 0 to 32 with a constant  $\lambda = 1$ .

Figure 8.74 and Figure 8.75 show improvement in MSE for HR and SpO<sub>2</sub> values due to RLS adaptive filtering with various filter orders. Results show that for HR and SpO<sub>2</sub>, a 4<sup>th</sup> order RLS filter produced a 55% and 35% improvement in MSE, respectively. This suggests that a 4<sup>th</sup> order RLS algorithm with  $\lambda = 1$  could be implemented to improve measurement accuracy during motion. This filter was implemented in Matlab for further analysis.

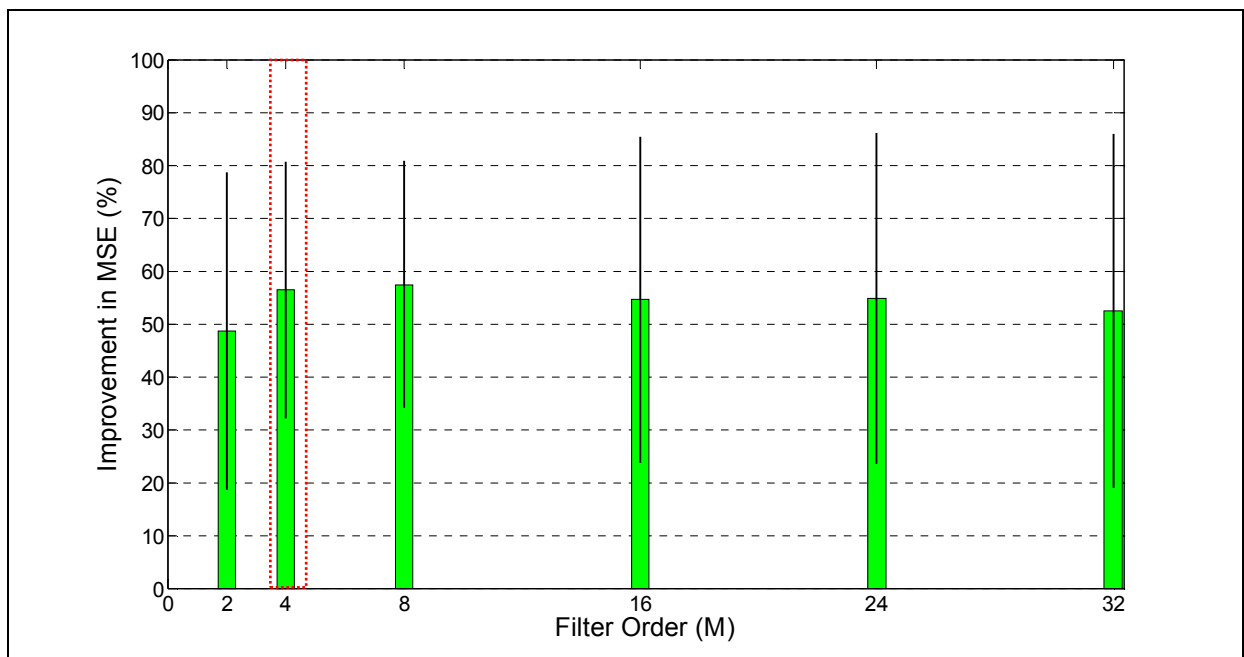


Figure 8.74: Average MSE improvement in HR for a RLS filter with  $\lambda = 1$  and varying  $M$ . The error bars indicate  $\pm 1SD$ . The shaded region corresponds to  $M$  value that was selected for data analysis.

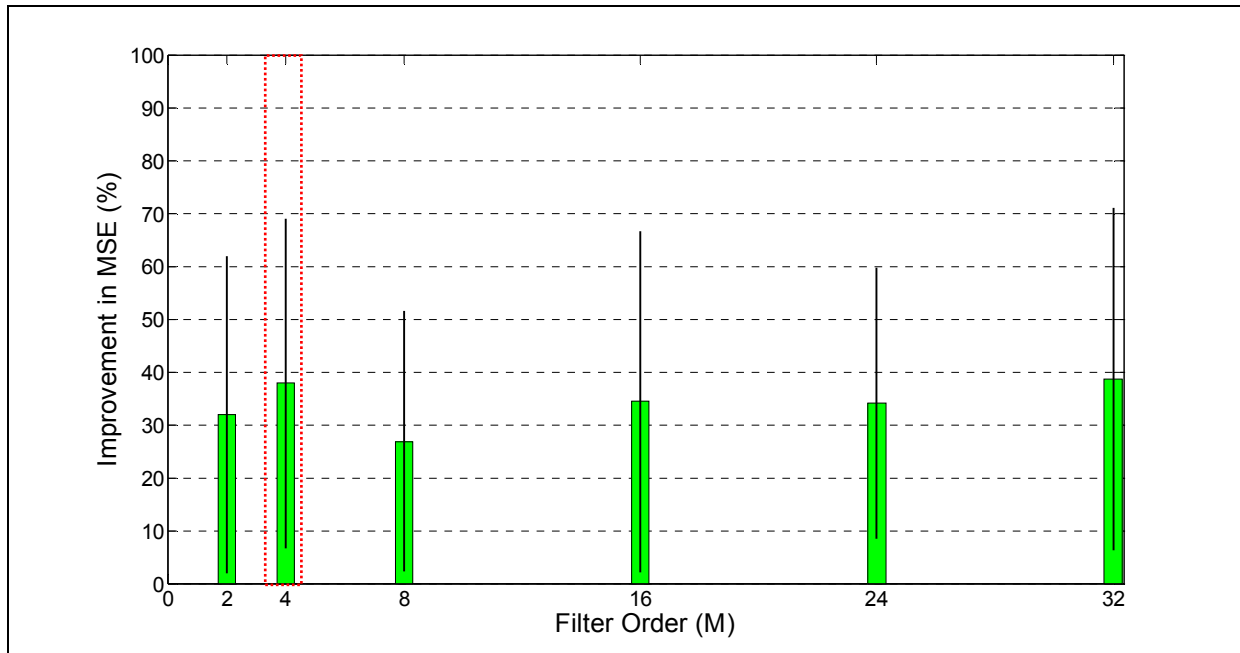


Figure 8.75: Average MSE improvement in SpO<sub>2</sub> for a RLS filter with  $\lambda = 1$  and varying M. The error bars indicate  $\pm 1SD$ . The shaded region corresponds to M value that was selected for data analysis.

### 8.6.2. Results of RLS filter

Adaptive filtering using 4<sup>th</sup> order RLS algorithm resulted in 50% improvement in the MSE for HR values along with a 30% improvement in the SD and a 16% improvement in the R<sup>2</sup> value. SpO<sub>2</sub> estimation also showed a 24% and 5% improvements in the MSE and SD, respectively.

Analysis showed that all of the ANC algorithms helped to improve the accuracy of the WPO. Processing the motion corrupted PPG signals by each algorithm produced slightly different improvements. Given similar performances, it is important to take into consideration the complexity of the adaptive algorithms before implementing ANC in real-time. A comparative study between these algorithms will suggest which algorithm should be implemented for real-time adaptive filtering.

## 8.7. Comparative Study of Different ANC Algorithms

The principle goal of this research was to implement ANC to improve the performance of our customized WPO during motion. This will make the WPO more robust against motion induced disturbances. An ideal algorithm must be fast enough to quickly adapt to changes in motion frequencies and must provide significant improvement in HR and SpO<sub>2</sub> accuracy. At the same time, it must be efficient in terms of algorithmic complexity and computation time. Table 8.7 summarizes the results of different ANC algorithms, and also compares them in terms of algorithmic efficiency. The LMS algorithm was selected because of its simplicity and reasonable performance.

Table 8.7: Comparison of different ANC algorithms

		LMS	RLS	TV-LMS	NLMS	M-NLMS
HR (BPM)	MSE improvement	54%	50%	56%	60%	60%
	SD improvement	35%	63%	35%	42%	42%
	R <sup>2</sup> improvement	19%	16%	19%	13%	13%
SpO <sub>2</sub> (%)	MSE improvement	22%	24%	25%	22%	22%
	SD improvement	15%	5%	23%	21%	21%
Filter Parameters	Number of Additions	2M	3M(M+1)	2M+1	3M	3M
	Number of Multiplications	2M+1	4M(M+1)	2M+6	3M+2	3M+2
	Ideal filter parameter value	$\hat{i} = 0.01$	$\hat{e} = 1$	$\hat{i} = 0.01$	$\hat{i} = 0.006$	$\hat{i} = 0.006$
	Ideal Filter Order	M = 16	M = 4	M = 16	M = 16	M = 16



## 8.8. Accelerometer Axis selection

In order to determine the potential effect of ACC axis selection on measurement accuracy, the collected data sets were adaptively filtered (16<sup>th</sup> order LMS filter) using each axis as a reference noise signal. Improvements in HR and SpO<sub>2</sub> errors were obtained by utilizing each acceleration axis separately as well as the summed combination of the three axes (X+Y+Z). Additionally, a multi-noise input adaptive filter was also studied and implemented in Matlab.

The results summarized in Table 8.8 show that for all the data sets the MSE for HR was improved by approximately 30% irrespective of the axis that was used as a reference noise input. It was found that the best performance was obtained by the summation of all reference signals (X+Y+Z). For HR and SpO<sub>2</sub>, a MSE improvement of 46% and 13% was noticed, respectively. Thus, results indicate that using the additive X+Y+Z axis signals as noise reference inputs provided significant improvement in measurement accuracy. These results are in agreement with Comtois [4].

Table 8.8: Percentage improvement in HR and SpO<sub>2</sub> after adaptive filtering using different reference noise signals.

Axis	HR (BPM)		SpO <sub>2</sub> (%)	
	MSE	SD	MSE	SD
X	39	26	15	6
Y	26	15	18	13
Z	32	24	10	9
X,Y,Z	26	12	11	4
<b>X+Y+Z</b>	<b>46</b>	<b>29</b>	<b>13</b>	<b>13</b>

## 8.9. Validation of Real-time ANC

Results from a series of indoor and outdoor experiments revealed that a conventional LMS algorithm can considerably improve the WPO's measurement accuracy during motion. Hence, for real-time application, the LMS algorithm was implemented in the embedded TI-MSP430  $\mu\text{C}$ .

To validate the functionality of the LMS algorithm in the TI-MSP430  $\mu\text{C}$ , adaptively filtered and unfiltered IR PPG data were collected. Due to processing time limitations in the current version of the hardware, a 4<sup>th</sup> order LMS filter was implemented in the  $\mu\text{C}$ . Raw IR PPG data were processed (offline) in Matlab utilizing the built-in 4<sup>th</sup> order LMS-ANC algorithm. Typical PPG signals processed in real-time by ANC algorithm and offline using the same processing are shown in Figure 8.76. The figure revealed that the two PPG waveforms matched exactly, verifying the functionality of the LMS algorithm implemented inside the TI-MSP430  $\mu\text{C}$ .

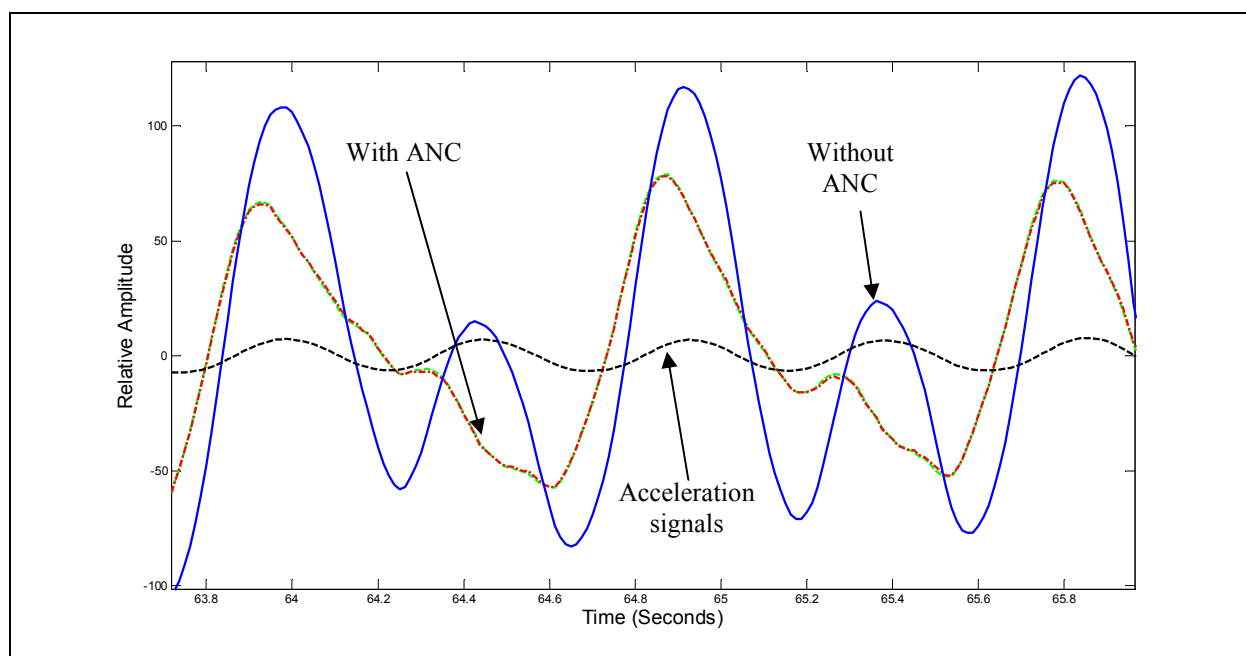


Figure 8.76: PPG waveforms obtained from a 4<sup>th</sup> order LMS adaptive filter implemented in real-time. Note that the Matlab (green) and  $\mu\text{C}$  (red) outputs overlap completely.

## 8.10. ANC Processing Time

The current version of the WPO receives a raw PPG data packet (80 sample vector) from the optical sensor every 500msec. Hence, signal processing must be completed in less than 500msec before the  $\mu$ C receives a new data packet. Table 8.9 summarizes the execution time for different sections of the signal processing algorithm. According to the timing shown in the table, the adaptive filtering process must be fast enough to be completed in less than 210msec. Processing time associated with various filter orders were recorded. In general, we observed that processing time increases linearly with the filter order. As shown in Figure 8.77, with the current hardware version of the WPO, an 8<sup>th</sup> order LMS filter can be implemented. Hence, an 8<sup>th</sup> order LMS filter having a step-size of 0.01 was implemented in the final version of the WPO.

Table 8.9: Execution time of the signal processing algorithm inside the WPO

Process	Time (msec)
IR and R PPG –LPF	38.0
IR and R PPG –BPF	60.0
ACC signals –BPF	30.0
HR and SpO <sub>2</sub> estimation	12.0
Other signal processing	150
Total	290
Processing time for ANC	500-290 = 210

*\*Note: Times were measured at a 4MHz clock frequency.*

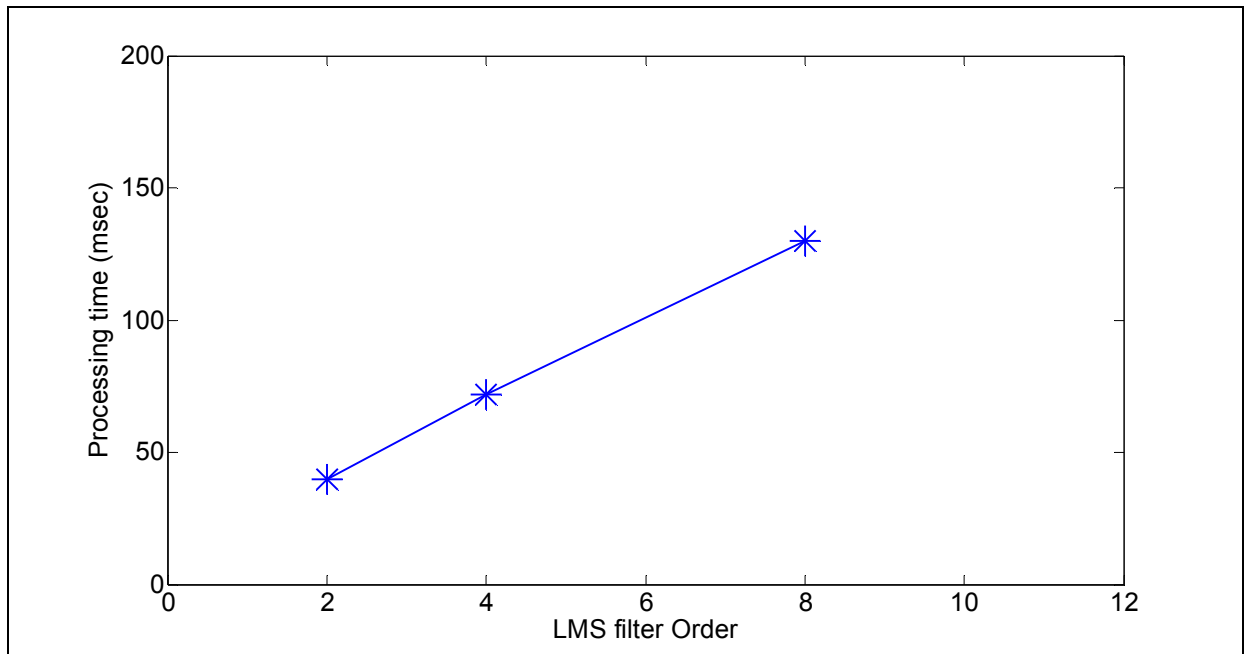


Figure 8.77: LMS filter processing time for various filter orders inside the TI-MSP430  $\mu$ C.

### 8.11. Auto-triggering of ANC

From Table 8.9 and Figure 8.77, it is observed that adaptive filtering increases the processing time of the system. As explained in the signal processing flowchart, the energy of the accelerometer signal is used as a trigger to start ANC when the energy of the ACC signal is above a certain threshold level.

In real-time implementation, the energy threshold value was set to 100. This value was chosen based all the collected data sets. In the real-time system implementation, the triggering method activated the ANC only when there was sufficient sensor motion. For example, in one of the jogging trails (shown in Figure 8.78), ANC process was inactive during resting state and was automatically activated during jogging at 4mph. Due to mixed energy levels during low motion activities, the ANC trigger algorithm did not work effectively. It triggers ANC for short periods of time and then deactivates it, as observed in Figure 8.78. However, as explained earlier, ANC has no effect on measurement accuracy during low motion activities like jogging at 2mph. Thus, short activation period of ANC has no effect on HR and SpO<sub>2</sub> measurement accuracy of the WPO.

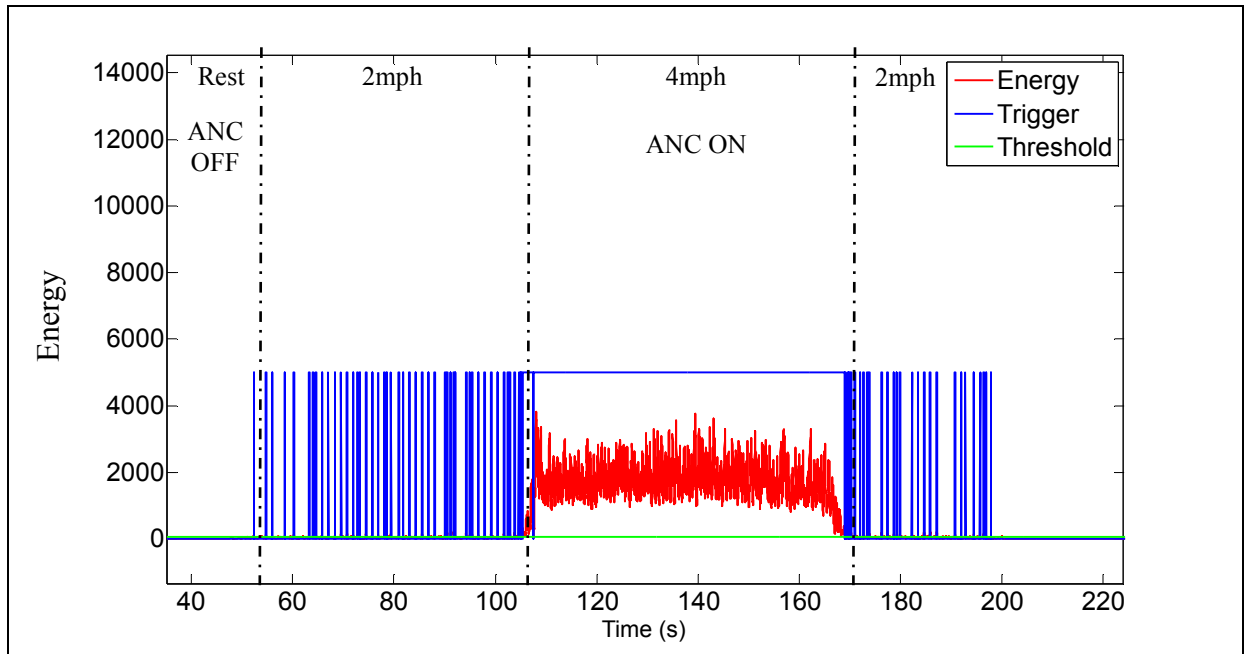


Figure 8.78: Auto-triggering of ANC in one of the jogging tests.

The proposed method to trigger ANC reduces unnecessary signal processing in the  $\mu\text{C}$  and thus reduces the processing time. During resting conditions, the auto-trigger ANC saves about 110 milliseconds. This will eventually increase the battery life. The processing timings for WPO are summarized in Table 8.10.

Table 8.10: Processing time of the auto-triggered ANC method.

LMS (8 <sup>th</sup> order, $\mu = 0.01$ )	Constantly ANC	Auto-triggered ANC
Rest	130msec	14msec
Motion	130msec	130msec

## 8.12. Real-time ANC results

The final ANC algorithm implemented in real-time consisted of an 8<sup>th</sup> order LMS filter with  $\mu = 0.01$ . Additionally, auto-triggering of the ANC was also implemented to reduce the processing time during low motion conditions.

Figure 8.79 and Figure 8.80 show the experimental tests during which HR measurements reported significant improvement due to adaptive LMS filtering during motion. In these tests, the ACC-based ANC algorithm provided more accurate measurements than the non-adaptively filtered signals. Percentage improvements in MSE for HR values are summarized in Table 8.11 and Table 8.12. The results revealed that HR errors are reduced by 81% during head motion and by 37% during treadmill jogging.

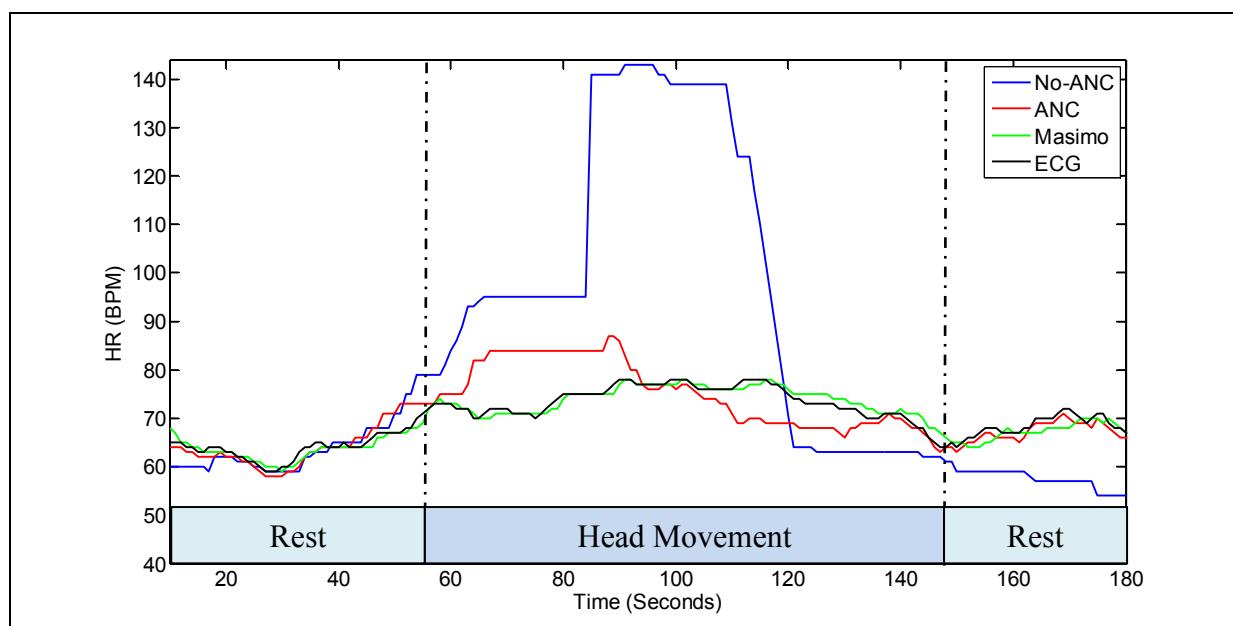


Figure 8.79: HR measurements with and without ANC from one of the head motion experiments.

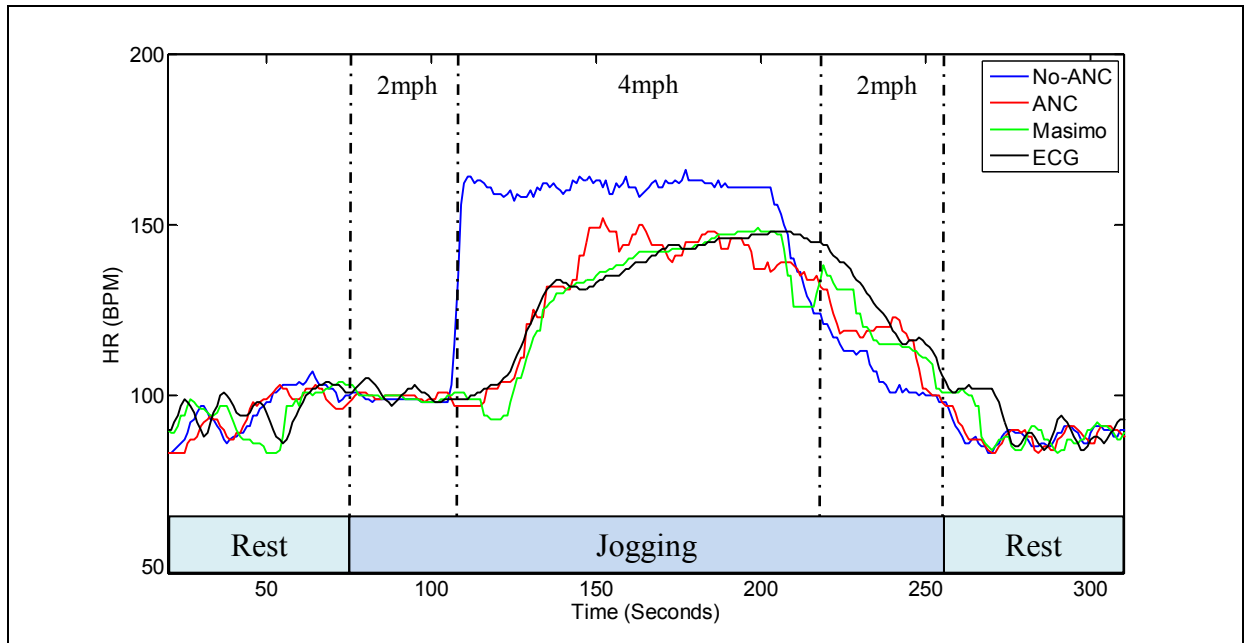


Figure 8.80: HR measurements with and without ANC from one of the jogging tests.

Table 8.11: Percentage improvement in WPO measurement accuracy after ANC (Head Movement)

Trial	HR (BPM)			SpO <sub>2</sub> (%)	
	MSE	SD	R <sup>2</sup>	MSE	SD
1	95	70	43	33	50
2	96	80	-2	43	0
3	96	80	3	39	0
4	83	57	-6	45	67
5	64	41	29	73	75
6	51	33	5	96	86
<b>Average</b>	<b>81</b>	<b>60</b>	<b>12</b>	<b>55</b>	<b>46</b>

Table 8.12: Percentage improvement in WPO measurement accuracy after ANC (Treadmill Jogging)

Trial	HR (BPM)			SpO <sub>2</sub> (%)	
	MSE	SD	R <sup>2</sup>	MSE	SD
1	55	33	-3	92	50
2	46	43	2	87	50
3	9	-6	-1	55	11
4	85	64	17	43	50
5	10	0	1	72	33
6	16	0	1	85	60
<b>Average</b>	<b>37</b>	<b>22</b>	<b>3</b>	<b>72</b>	<b>42</b>

Similar improvements were also observed for SpO<sub>2</sub> measurements during motion. The results are summarized in Figure 8.81 and Figure 8.82. For head motion tests, an average improvement of 55% was observed. During treadmill jogging, the MSE was improved by 72%. All of the results verified that ANC improved SpO<sub>2</sub> accuracy in the presence of motion artifacts.

Note that in Figure 8.82 a 5% drop in SpO<sub>2</sub> was observed around 200 seconds post adaptive filtering. We speculate that this drop was due to distortion of the PPG signals during frequency overlap lasting for a few seconds.

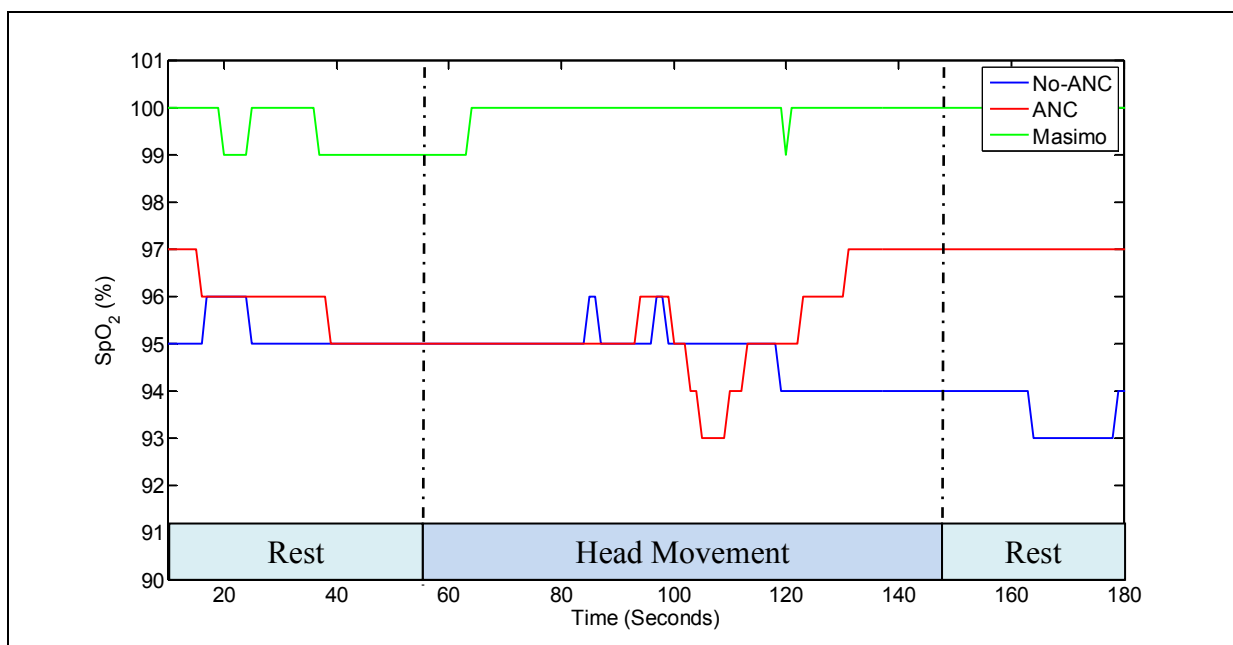


Figure 8.81: SpO<sub>2</sub> measurements with and without ANC from one of the head motion experiments.



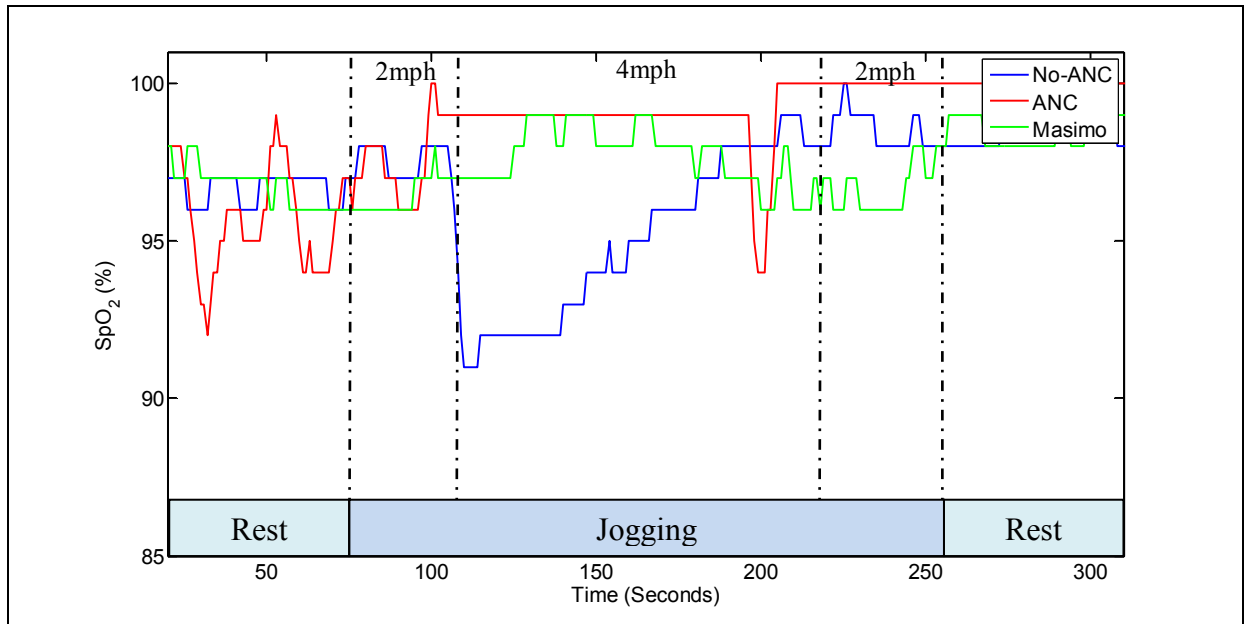


Figure 8.82: SpO<sub>2</sub> measurements with and without ANC from one of the jogging tests.

### 8.13. Limitation of ANC

In pulse oximetry, the adaptively filtered PPG signals could remain distorted when the cardiac and motion frequencies overlap. Consider for example a subject having an initial HR of 60BPM (cardiac frequency of 1Hz). Next, the subject starts exercising and produces 1.33Hz motion artifacts. The cardiac frequency will gradually increase to meet the additional oxygen demand due to increased physical activity, as illustrated in Figure 8.83. As the HR increases from 1Hz to 1.33Hz, at time  $t_1$ , the cardiac frequency will overlap with the motion frequency. Hence from time  $t_1$ , adaptive filtering would distort the PPG signals, resulting in erroneous HR and SpO<sub>2</sub> measurements. The worst case occurs when the two signal components are of opposite phase [26]. This suggests that adaptive filtering should be avoided when the frequency of the reference signal coincides with the cardiac frequency.

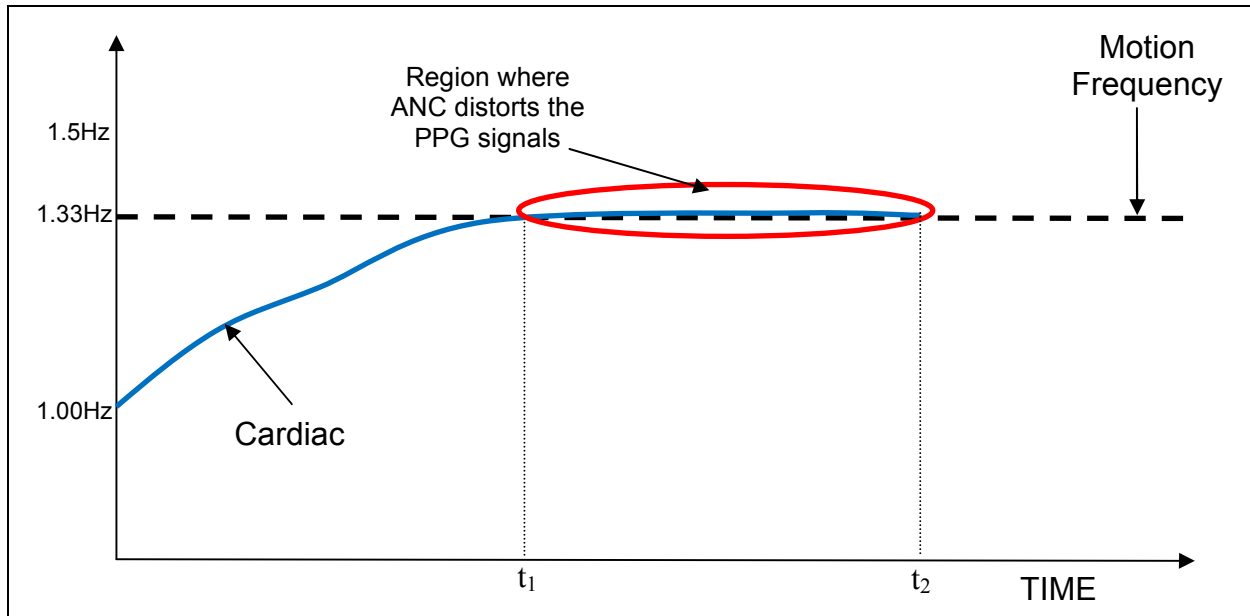


Figure 8.83: Cardiac and motion frequency overlap.

In our studies, the frequency overlap data consisted of 2 treadmill jogging tests, 3 outdoor running tests, and 1 staircase climbing trial. In case of real-time adaptive filtering, frequency overlaps were observed in 3 out of 9 treadmill jogging tests. Figure 8.84 shows typical IR PPG signals before and after ANC during frequency overlap. Before adaptive filtering, the frequency of the IR PPG signal (blue trace) closely matches the frequency of the reference motion signals from the tri-axial accelerometer (black trace). Hence, adaptive filtering techniques results in distortion of the IR PPG signals. Distortion of the PPG has a significant negative effect on measurement accuracy, as observed in Figure 8.85 and Figure 8.86.

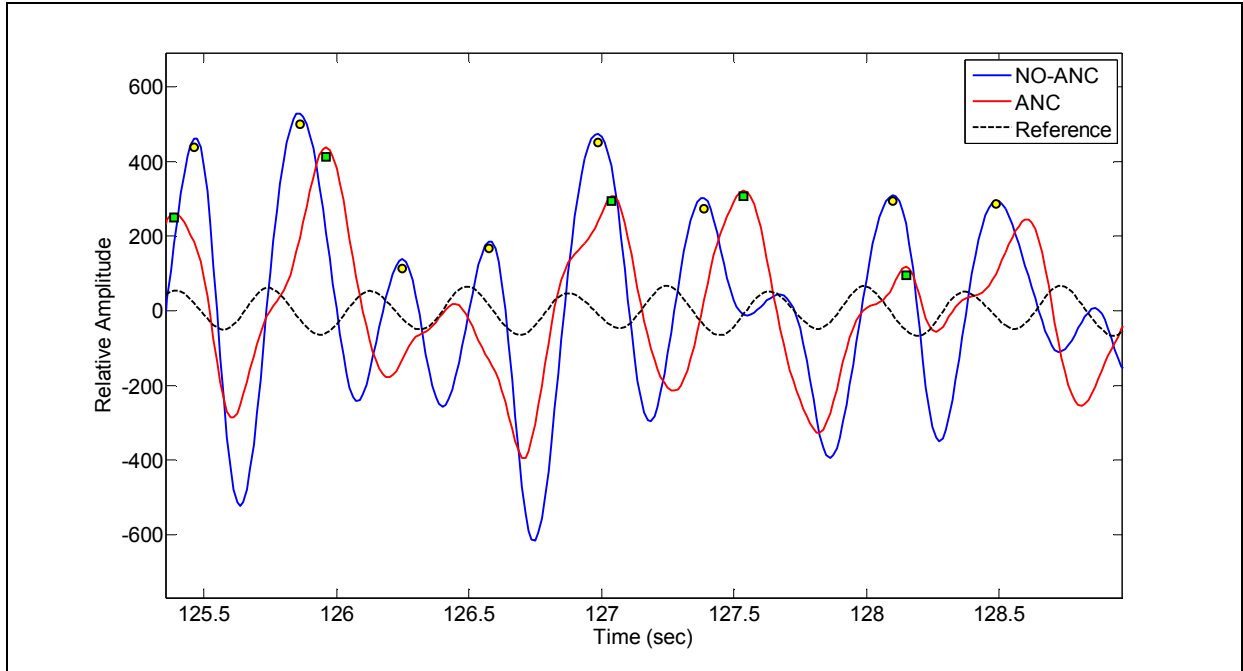


Figure 8.84: Effects of ANC process in case of frequency overlap.

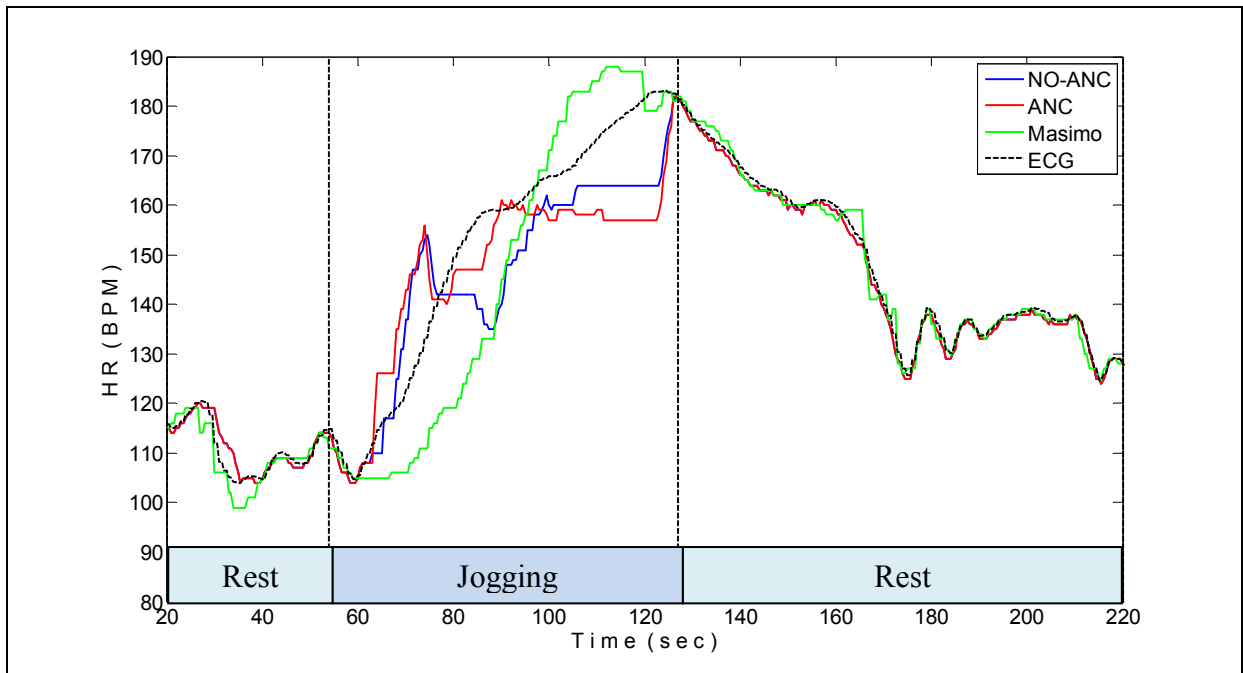


Figure 8.85: Effect of frequency overlap on HR measurements.

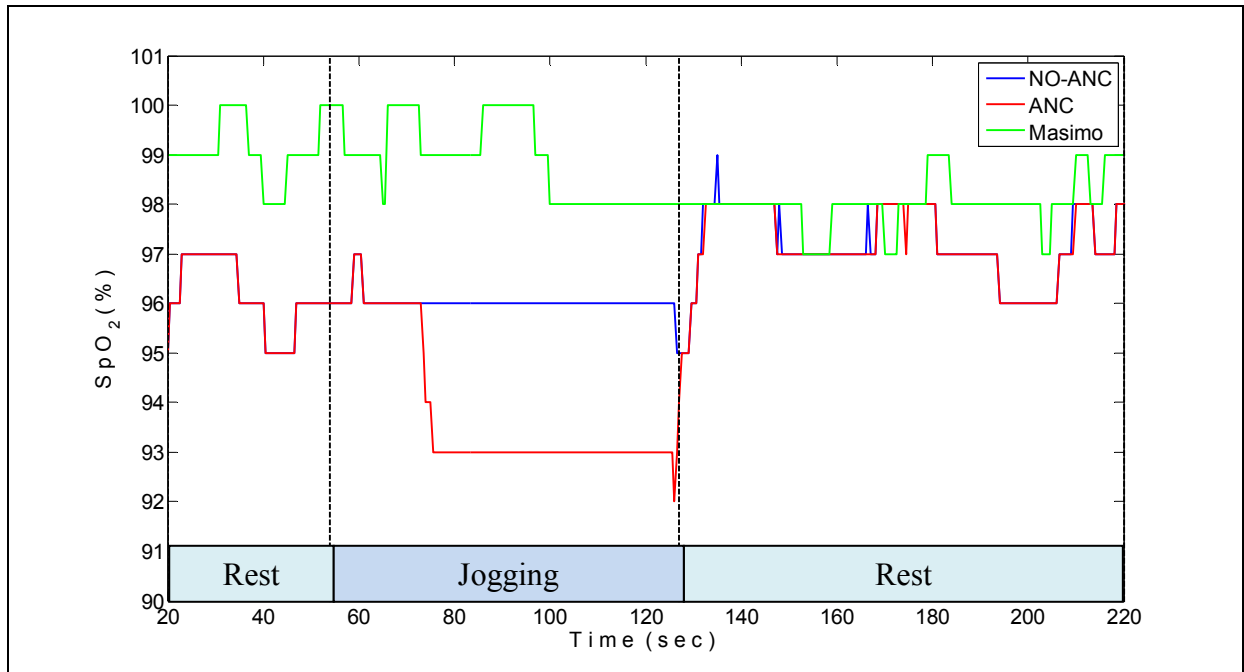


Figure 8.86: Effect of frequency overlap on SpO<sub>2</sub> measurements.

## 9. DISCUSSION

### 9.1. Resting Experiments

Physiological information from a WPO can help to keep track of soldiers and firefighters vital signs, allowing continuous real-time monitoring by medical experts. This section describes the initial bench testing of a WPO and compares its performance with that of the MPO.

Figure 8.1 and Figure 8.2, illustrate that average steady-state difference between HR values recorded from the WPO and MPO are within an acceptable clinical range of  $\pm 2\%$  [27]. During rest, the WPO was able to accurately track changes in HR values that took place during hypoxia and hyperventilation. Similarly, the transient  $SpO_2$  changes recorded by our WPO during breath holding maneuver matched the readings from the MPO.

The regression plot in Figure 8.4 demonstrates that the HR measured by the WPO and MPO are closely correlated between 65BPM – 95BPM. However, the variations are comparatively large for HR values greater than 95BPM, but the number of data points showing large variations is very small. The main reason for this disagreement is sensor movement during data collection. In order to induce hypoxia, subjects were requested to perform a breath holding maneuver which resulted in some sensor movements. Additionally, motion artifacts were also induced during hyperventilation. Sensor motion, induced during hypoxia and hyperventilation, resulted in small HR discrepancies.

### 9.1.1. Systolic versus diastolic peak detection

The first sentence is obvious!

HR and SpO<sub>2</sub> measurements can be obtained by identifying either the systolic or diastolic peaks in the PPG, as shown in Figure 2.3. Figure 9.1 and Figure 9.2 confirms that HR and SpO<sub>2</sub> computed from either peak produce similar readings. To assess whether the mean readings produced are statistically different, a t-test was performed for each measurement. The high  $p$ -value of 0.58 for HR and 0.28 for SpO<sub>2</sub> confirmed that there was no significant difference between the two methods. The results are summarized in Table 9.1. Therefore, only diastolic peaks were used to estimate HR and SpO<sub>2</sub> in this thesis.

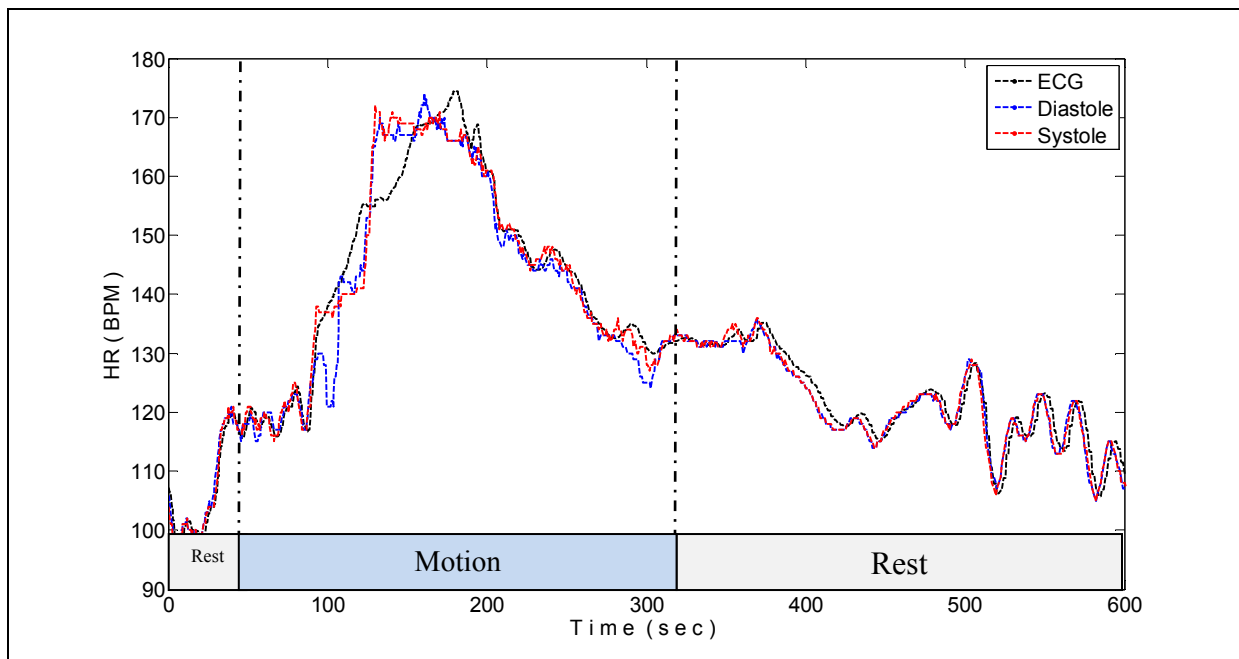


Figure 9.1: HR estimated from systolic and diastolic peaks during one of the jogging trials.

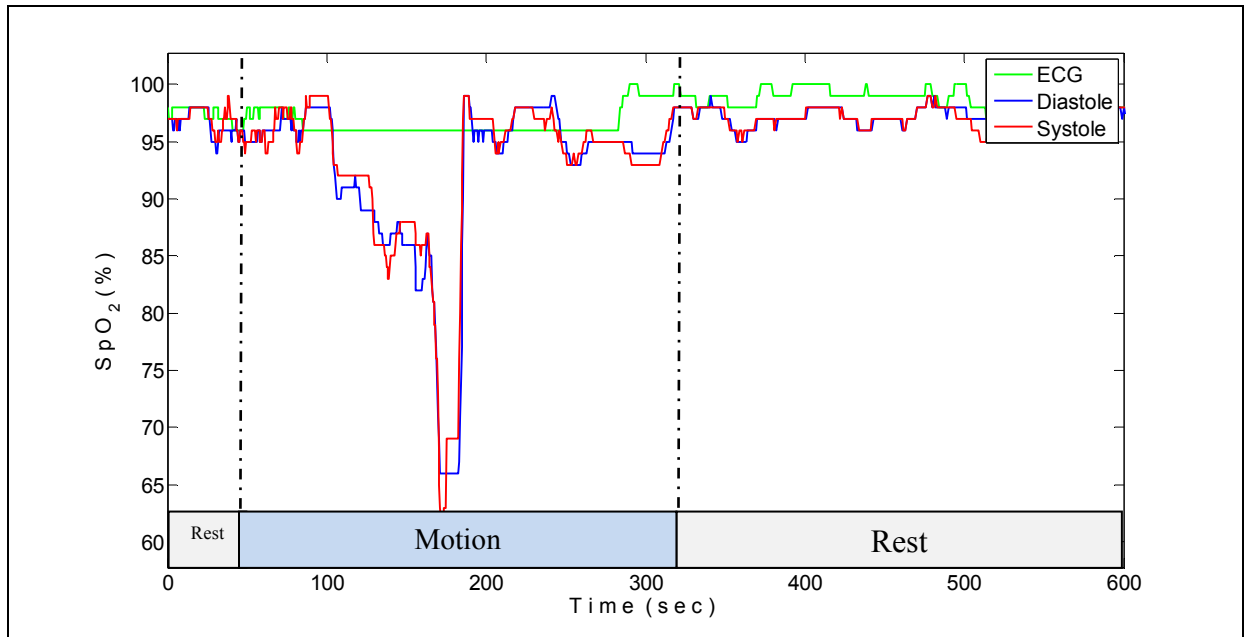


Figure 9.2: SpO<sub>2</sub> estimated from systolic and diastolic peaks during one of the jogging trials.

Table 9.1: Data analysis for HR and SpO<sub>2</sub> values computed from systolic and diastolic peaks.

	HR (BPM)		SpO <sub>2</sub> (%)	
	Systolic	Diastolic	Systolic	Diastolic
Mean	116	116	98	98
SD	29	29	4	4
<i>p</i> -value	0.52		0.28	

## 9.2. LMS Algorithm

### 9.2.1. Step-size ( $\mu$ ) selection

The main design parameter for a LMS algorithm is the selection of the step-size,  $\mu$ . A small value for  $\mu$  is desirable since this provides an LMS algorithm with a relatively low error [22]. However, a small  $\mu$  value yields a slower convergence rate. A faster convergence rate (or adaptation factor) can be achieved by utilizing a larger value of  $\mu$ , but at the expense of a larger adjustment error [22]. Thus, selection of a constant  $\mu$  value for a conventional LMS algorithm is a tradeoff between convergence rate and reduction in adjustment errors.

The data analysis results in section 8.2.1 showed that for HR values, the improvement in the MSE were significant for  $0 < \mu < 0.03$ . These values provide an improvement of 30% to 50% in the presence of motion artifacts. The improvements in the MSE for HR values were found to be insignificant for  $\mu > 0.03$ . This verifies that the adjustment error increases with larger  $\mu$  values. Improvement in the MSE for SpO<sub>2</sub> did not vary significantly as a function of  $\mu$ . These results concur with similar observations by Comtois [4, 6].

The results also indicate that the adaptive filters have a greater effect on HR than SpO<sub>2</sub> values. HR values are estimated based on time demarcations coinciding with PPG peaks. Hence, even slight PPG signal modification due to adaptive filtering can have a prominent effect on the instantaneous HR values. On the contrary, SpO<sub>2</sub> values are based on averaged values of the respective AC and DC components of the IR and R PPG signals. Averaging minimizes the direct qualitative effect of adaptive filtering on SpO<sub>2</sub> calculations. Hence, in general we observe that the adaptive filtering algorithms have a more significant effect on HR as compared to SpO<sub>2</sub> measurements.

### 9.2.2. Filter Order (M) selection

The performance of any filter depends on the number of coefficients utilized in the computation process, i.e. filter order (M). Filter order not only affects the measurement errors but also the



required computational time. Computational time increases with increase in the filter order [4, 6, 22].

To find an ideal value of  $M$  for a conventional LMS algorithm,  $M$  was varied while  $\mu$  was kept constant at 0.01. For different values of  $M$ , Figure 8.9 and Figure 8.10 show the average improvement in MSE for HR and SpO<sub>2</sub> values, respectively. From these figures we found that the degree of improvement depends on the filter order. The highest improvement observed was for  $M = 16$ . We also found that the mean improvement diminishes for  $M > 24$ . These results are in agreement with Comtois [4, 6].

Data indicate that a 16<sup>th</sup> order conventional LMS adaptive filter with  $\mu = 0.01$  can significantly reduce HR and SpO<sub>2</sub> estimation errors. Hence, this filter was selected for further evaluations.

### 9.2.3. LMS – Sitting Experiments

Motion artifacts are known to be the primary contributor to errors and high rates of false alarm in pulse oximeters. To understand the effects of motion artifacts on PPG signals and pulse oximetry accuracy, a series of head movement experiments were performed. The main purpose behind carrying out these experiments was to better understand the effects related exclusively to sensor movement.

During the resting phase of the experiment, when the head remained still, there were no motion artifacts that corrupted the PPG signals. The PPG signals depicted in Figure 8.11 and Figure 8.13 have cardiac peaks that exactly match the R-waves in the ECG waveform. The difference in time response is due to different sampling frequency of the WPO and Holter monitor. Moreover, the two recordings were supposed to start simultaneously, but this did not occur due to human error. This adds on the time difference between the two waveforms. However, PPG signals are not contaminated by any artifacts during rest.

During rest, the adaptive filtering had no significant effect on the morphology of the PPG signals as the motion signals had significantly low amplitude. Nonetheless, irrespective of whether adaptive filtering was implemented or not, HR and SpO<sub>2</sub> measurements during rest were in

complete agreement with readings obtained from the reference sources. The data confirmed that the adaptive filtering algorithm has no effect on pulse oximetry accuracy in the absence of motion artifacts. Thus, processing clean PPG signals with ANC is an unnecessary waste of  $\mu\text{C}$  processing time and battery power.

During phase 2 of the sitting experiment, morphological distortions of the underlying PPG waveform begin with head movements. The peak-to-peak amplitude variation increases significantly in the presence of motion artifacts. Distortion of the PPG signals, from which HR and  $\text{SpO}_2$  values are derived, leads to measurement errors and frequent dropouts when subjects remain active. From Figure 8.16, it is evident that the WPO (blue trace) underestimated HR while the subject was performing head movements. We also noticed pronounced fluctuations in  $\text{SpO}_2$ , although to a lesser extent, that was recorded by the WPO during motion. The effects of motion artifacts are also visible in the frequency spectra of the IR and R PPG signals.

To improve the performance of the WPO during motion, we have investigated the effectiveness of an ACC-based adaptive LMS algorithm. The morphology of an adaptively filtered PPG signal appeared to have more consistently shaped peaks as compared to a PPG signal before adaptive filtering (blue trace). Figure 8.12 shows that the noisy portion of the IR PPG appeared to be corrected such that the peak (marked by an arrow) was identified as a cardiac peak in the adaptively filtered signal (red trace).

The frequency spectra of the IR and R PPG showed that the LMS algorithm was effective in attenuating the frequency associated with body motion. Thus, it increases the SNR of the PPG signals. Analysis of HR and  $\text{SpO}_2$  data acquired during sitting experiments showed that the LMS algorithm improves considerably the accuracy of the WPO, as highlighted in Figure 8.16 and Figure 8.17.

The regression plot of HR readings before and after adaptive filtering, depicted in Figure 8.31 and Figure 8.32, clearly demonstrate the effectiveness of ANC. Before adaptive filtering, the points on the regression plot were scattered away from the regression line, producing a CC of 0.57. Adaptive algorithm shifted the HR data points towards the linear regression line, showing

an improvement of 40% in the CC. SpO<sub>2</sub> regression plots were not studied as the range of values was very small (95% to 100%). The residual plots for SpO<sub>2</sub> values depict that utilizing LMS adaptive filtering can minimize the mean difference between the WPO and MPO.

Since, head movements varied from trial to trial, the improvements in HR and SpO<sub>2</sub> varied as well. In some trials, the improvement was as high as 90%, whereas in other trials the improvement was insignificant. We believe that this was caused by the variable nature of the motion artifacts that corrupted the PPG signals. If the motion involved is periodic, the adaptive filter will adjust its coefficients precisely at the motion frequency and will have a more significant effect on the PPG signal. On the contrary, if the motion frequency varies instantaneously, the adaptive filter cannot fully adapt to rapidly changing frequencies and will therefore not be efficient. Thus, in some cases, the adaptive filtering of the PPG signals yielded more than 70% improvement, while in other cases the improvement was clinically insignificant. Since the extent of motion corrupting the PPG signals cannot be predicted, the improvement due to adaptive filtering can never be predicted in real-time pulse oximetry. This is true for all the experiments included in this study. However, the results from Table 8.1 indicate that ANC using a LMS algorithm can help to improve the accuracy of the WPO in the presence of motion artifacts.

#### 9.2.4. LMS – Cycling Experiments

The purpose of this study was to determine the effects of rapid changes in HR on the accuracy of the WPO. The experimental results showed that the morphology of the PPG signals obtained during stationary bicycling and rest were very similar. As mentioned earlier, the only difference was the increase in the cardiac frequency to meet the additional oxygen demand by the body.

From the frequency spectra of the IR and R PPG, the dominant frequency components are in the range of 1.6Hz – 2.8Hz, which corresponds to HR values between 100BPM – 170BPM. Since cycling on a stationary bicycle causes negligible head motion, the PPG signal did not contain any spectral band outside the dominant cardiac frequency range. When compared to the frequency spectra of the ACC signals acquired during head motion, the ACC signal during cycling

consisted of low energy. This suggests that the degree of movement occurring during stationary bicycling was significantly smaller compared to head motion.

During cycling, the signal processing algorithm was able to accurately locate all of the cardiac beats that matched the R-waves from the Holter monitor. The plots in Figure 8.29 and Figure 8.30 suggest that accurate HR and SpO<sub>2</sub> readings can be acquired during stationary cycling.

HR regression plots confirmed that the HR acquired from the WPO and Holter monitor are in complete agreement (CC of 1.00). The results for the resting experiments (section 8.1) and cycling experiments proved that the WPO is capable of measuring accurate HR values over a range of 65BPM to 170BPM when subjects remain at rest.

We also noticed that, PPG signals associated with cycling on a stationary bicycle were not affected by motion artifacts but rather by changes in the physiology. This suggests that while performing any physical activity, PPG signal distortions are primarily caused by body motion rather than rapid changes in HR. Additionally, the analysis showed that there is no need to apply adaptive filtering during activities involving no/little head movements, such as cycling. By avoiding ANC processing when the sensor remains stationary, battery life can be extended.

#### 9.2.5. LMS – Treadmill Jogging Experiments

During rest, due to lack of head movements, the PPG signals were not contaminated by artifacts. These PPG signals tend to produce accurate HR and SpO<sub>2</sub> readings that are in close agreement with the HR and SpO<sub>2</sub> values recorded from the Holter monitor and MPO, respectively. LMS adaptive filtering has no significant effect on measurement accuracy during rest as motion detected by the tri-axial ACC produced very low amplitude signals. As soon as a subject starts walking at the speed of 2mph, we noted an increase in the amplitude of the ACC signals.

Although the amplitude of the motion signal increased while the subject was jogging at 2mph, the motion was sufficiently low to produce any discernable distortion of the PPG signals. As shown in Figure 8.39 and Figure 8.41, the PPG signals before and after the application of LMS filtering have similar characteristics including the number and location of the cardiac peaks. This

suggest that HR and SpO<sub>2</sub> derived from unprocessed (non adaptive) PPG signals remain accurate. HR and SpO<sub>2</sub> plots during phase-2 and phase-4 of the experiment, as illustrated in Figure 8.45 and Figure 8.46, confirmed these results since the HR and SpO<sub>2</sub> readings from the WPO and reference overlap.

We also notice that the IR PPG signal acquired during jogging at 4mph, shown in Figure 8.40, has an inconsistent morphology due to motion artifacts. The large peak-to-peak amplitude of the ACC signal indicates the presence of heavy motion artifacts during phase-3 of the experiment. These motion signals, when used as reference noise during adaptive filtering, help to recover clean PPG signals. It should be emphasized that before adaptive filtering, the signal processing algorithm was not able to differentiate between true cardiac peaks and motion induced peaks due to large variations in peak-to-peak amplitude. Adaptive filtering produced cleaner PPG signals, such that the peaks were easily identified by the signal processing algorithm.

In the frequency domain, the FFT of IR and R PPG signals revealed that the PPG signals during phase-3 of the experiment were dominated by frequencies corresponding with body acceleration (i.e. 2.8Hz). These additional motion induced frequency components are the primary cause for reduced measurement accuracy. We found that LMS adaptive filtering was effective in removing the motion related frequency corrupting the PPG signals. This also demonstrated that signals obtained from the integrated ACC were effective as a noise reference input to the adaptive LMS algorithm.

The effectiveness of the LMS filtering routine is clearly observed in Figure 8.45 and Figure 8.46. It is evident that HR readings before ANC were higher as the motion related spectral components were in the higher frequency range. These figures also revealed that the MPO, which employs advanced signal extraction technology (SET) designed to greatly extend its utility into high motion environments [27], was clearly unable to accurately track HR values while the subject was jogging at 4mph. HR readings derived from the ECG waveform were comparatively more reliable. Even in the presence of motion artifacts, R-waves were distinctly visible in the ECG waveform, as evident in Figure 8.40. Hence, HR readings computed based on the ECG waveform were used as a standard reference.

The percent improvements in HR and SpO<sub>2</sub> (Table 8.4) support the observation made in section 9.2.3. We found that the improvements are significantly greater for some tests, whereas in other trials the results produced by adaptive filtering were not clinically significant. As mentioned earlier, the improvements depend on the nature of the motion artifacts. Overall analysis suggests that ANC is effective in increasing the accuracy of the WPO when motion artifacts are present.

#### 9.2.6. LMS – Outdoor Running Experiments

Running outdoors is similar to running/jogging on a treadmill. Thus, the LMS algorithm should have a similar effect on the PPG signals during outdoor running as it did during indoor treadmill jogging. The results from section 8.2.5 confirmed that HR readings during outdoor running were improved by 35%, while SpO<sub>2</sub> values were improved by 12%.

We noticed that the mean percentage improvement for running experiments was very low compared to improvement during treadmill jogging. The frequency of motion induced during jogging/running on a treadmill was relatively constant. This frequency depends on the speed and to a very large extent on running style. Treadmill experiments involve running at a constant speed, and hence we generally can see a single dominant motion frequency in the frequency spectrum of the PPG. In Figure 8.43, the dominant motion frequency was around 2.8Hz. On the contrary, speed does not remain constant while outdoors running. Thus, the motion affecting the PPG signal quality is not centered at a single frequency. As shown in Figure 9.3, the motion frequency cannot be easily identified by looking at the FFT of a motion corrupted signal. Since the motion frequency is not constant and can vary rapidly while running outdoors, the adaptive filter never fully adapts to the motion frequency. Hence, noise attenuation is reduced and the mean percentage improvement is not as high as during treadmill jogging. Still, utilizing LMS adaptive filtering was helpful to minimize some motion artifacts.

Out of the 6 experimental tests, we noticed that trial#2 displayed a different behavior. For this particular trial, the HR values were improved by 12%, while there was degradation in SpO<sub>2</sub> accuracy. This behavior is not fully understood and requires further investigations.

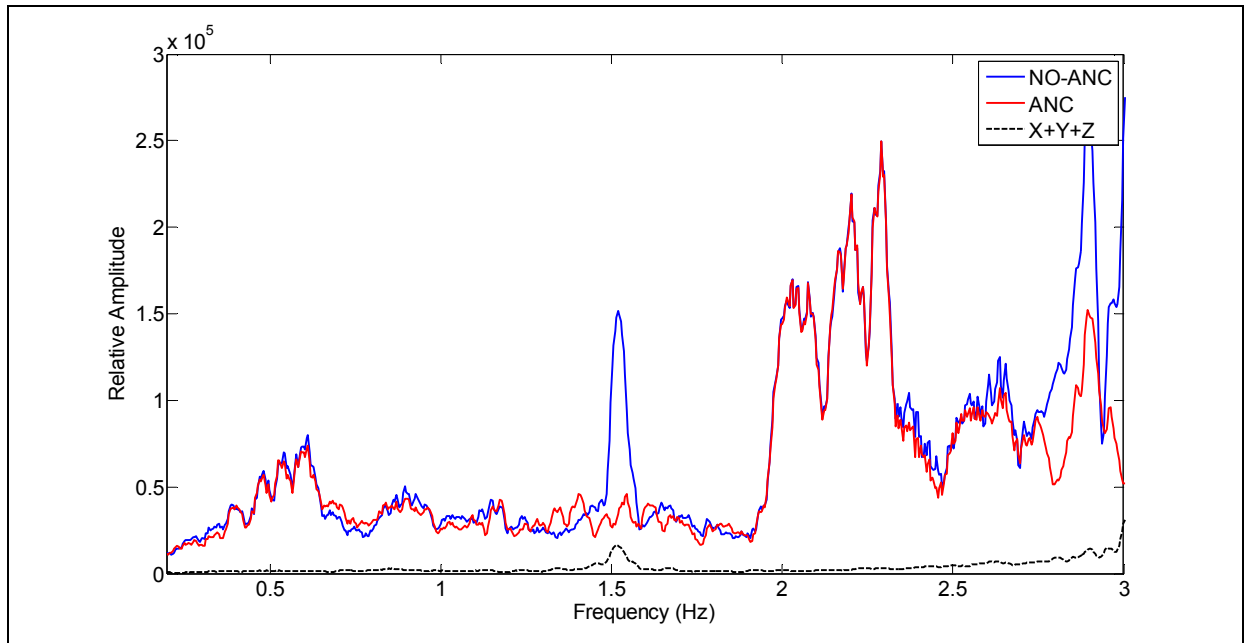


Figure 9.3: Frequency spectrum of IR PPG waveform during outdoor running.

#### 9.2.7. LMS – Staircase Climbing Experiments

Soldier and firefighters often have to climb up and down stairs during routine missions. Therefore it is important to better understand the behavior of the WPO during stair climbing. We noticed that the motion affected the PPG signals and deteriorated the WPO's accuracy. Once again, the application of LMS algorithm was beneficial in recovering clean PPG signals. Post adaptive filtering produced more accurate HR and SpO<sub>2</sub> readings.

The FFT of PPG and ACC signals during staircase experiment revealed another interesting aspect of ANC. According to the HR values in Figure 8.60, the HR corresponds to frequencies between 1.1Hz – 2.5Hz. All frequencies outside this range are considered noise signals mainly contributed by motion artifacts. The frequency spectra of the PPG and motion signal consist of a band of motion frequencies between 2.5Hz – 3Hz. These additional frequencies were successfully attenuated by the LMS algorithm. Hence, the ANC is capable of eliminating several motion related frequency components that occur simultaneously.

### 9.3. TV-LMS

The conventional LMS algorithm works effectively in reducing the effects of motion artifacts. However, the performance of this algorithm is highly dependent on the selected convergence parameter,  $\mu$ . Lau and Hussain have devised a novel approach for the LMS estimation algorithm [23, 24]. This approach utilizes a time-varying convergence parameter rather than using a fixed  $\mu$ . The developed algorithm is known as a Time-varying LMS (TVLMS) algorithm. In their study [23], the TVLMS showed better performance than the conventional LMS algorithm. To determine if the TVLMS algorithm is better than the conventional LMS for pulse oximetry applications, we implemented the TVLMS in Matlab. The first step in the implementation was to determine an initial value for  $\mu$ .

#### 9.3.1. Step-Size Selection

The TVLMS and LMS algorithms work similarly, except for a time varying convergence factor,  $\mu_n$ , which is used in the TVLMS algorithm [23]. In the TVLMS approach, the convergence parameter is set to a large value in the initial state in order to speed up the algorithm convergence. Then, the value convergence parameter is reduced as the time progresses to produce a smaller mean-squared error [23, 24]. The equations and formulas for the TVLMS are summarized in Table 4.2.

The steps involved in estimating an ideal starting value,  $\mu_0$ , is explained in section 8.4.1. The results in Figure 8.68 and Figure 8.67 are similar to the results in section 8.2.1. The plots indicate that the mean improvement in HR and SpO<sub>2</sub> is best for  $\mu_0 = 0.01$ . Therefore, this value was chosen for further evaluation. For proper comparison, we use the same filter ( $M = 16$ ) order for the two LMS algorithms.

#### 9.3.2. Results of TV-LMS filter

The collected PPG data sets were adaptively filtered using the TVLMS algorithm. Both algorithms provided similar results. We found that the TVLMS algorithm performed slightly better than the conventional LMS algorithm. The LMS provided mean percentage improvements of 54% and 22% for HR and SpO<sub>2</sub>, respectively. On the other hand, the TVLMS algorithm



provided HR and SpO<sub>2</sub> improvements of 56% and 25%, respectively. However, the additional 2% improvement is clinically insignificant. Since both algorithms produced similar improvements, implementation of a conventional LMS algorithm is preferred since it is simpler and requires fewer operations.

#### 9.4. NLMS and MNLMS

The conventional LMS algorithm having a constant  $\mu$  produced acceptable results. However, it has a shortcoming. Usually the signal conditions are not static and vary with time. In such cases, the filter will not have enough time to adapt at constant convergence rate. That is, the convergence parameter must be varied depending on the input signal. The NLMS is a variant of the conventional LMS that deals with this shortcoming more effectively since it introduces a variable adaptation rate as explained previously in section 4.3.

The MNLMS algorithm is a slightly modified version of the NLMS algorithm. In the NLMS algorithm, to avoid a divide-by-zero error, a small delta value is added. To avoid error induced by this delta, the MNLMS algorithm was implemented. In the MNLMS algorithm, the delta is added only if the energy of the input reference signal is zero. This is incorporated to reduce the adaptation error when the reference energy is non-zero. All the other equations and parameters of the MNLMS algorithm are the same as the NLMS algorithm.

##### 9.4.1. Step-Size and Filter Order Selection

Although the convergence parameter is variable in the NLMS algorithm, a constant  $\mu$  value has to be selected. The ideal  $\mu$  value was estimated by analyzing the data sets with a variable  $\mu$  and a constant  $M$  of 16. The results in section 8.5.1 show that the best percentage improvements are obtained with  $\mu = 0.006$ . For  $\mu$  values greater than 0.035, the improvements in HR were insignificant. These results are similar to the LMS algorithm. The NLMS filter order was also determined in a similar way.  $\mu$  was kept constant and  $M$  was varied to obtain the best performance. The best performance was observed for  $M = 16$ . Thus, we implemented a 16<sup>th</sup> order NLMS filter having a  $\mu$  of 0.006 and compared its performance with that of other adaptive algorithms.

Since the MNLMS algorithm is the same as the NLMS algorithm, it was implemented with the same filter parameters i.e.  $\mu = 0.006$  and  $M = 16$ . The results for the NLMS and MNLMS algorithm are discussed below.

#### 9.4.2. NLMS and MNLMS filter results

PPG signals processed using the NLMS and MNLMS algorithms produced better results than the LMS and TVLMS algorithms. Due to faster convergence rates of the NLMS and MNLMS algorithms, HR values showed an improvement of 60% during motion. SpO<sub>2</sub> values were improved by 22%. These results confirmed that varying  $\mu$  yielded better performance during real-time implementation. However, the processing required in calculating the reference energy signal increases the computational complexity of the signal processing algorithm. The NLMS and MNLMS algorithms require  $M$  additional computations than the LMS algorithm in its basic form.

### 9.5. RLS Algorithm

The RLS algorithm is one of the two most popular adaptive filtering algorithms. The RLS algorithm has a fast convergence rate compared to the LMS algorithm [22]. Being an IIR filter, the RLS filter is not always stable and this limits its applications compared to the LMS filter. However, by selecting proper filter parameters, a stable RLS filter can be implemented.

#### 9.5.1. Forgetting factor and filter order selection

The performance of the RLS adaptive algorithm is highly dependent on its filter order  $M$ . It also depends on the forgetting factor  $\lambda$  [22]. Specifically, for the RLS algorithm,  $0.99999 \leq \lambda \leq 1$  is typically utilized. Relente and Sison suggest using this range to reduce the effects of motion on the PPG [8]. For this thesis, we used  $\lambda = 1$ .

The execution time of the RLS algorithm increases more rapidly with filter order than any other LMS algorithms [4, 6, 22, 23]. As the execution time of the RLS algorithm increases non-linearly with filter order, the selection of filter order is based on a trade-off between the performance and execution time. Our data showed that improvement in HR and SpO<sub>2</sub> by the

RLS algorithm was steady for  $M > 4$ . Hence, a 4<sup>th</sup> order RLS algorithm with  $\lambda = 1$  was implemented.

### 9.5.2. Results of RLS filter

The ANC implemented using the RLS algorithm helped to significantly improve the accuracy of the WPO during motion. We found that the performance of a 4<sup>th</sup> order RLS algorithm was similar to that of a 16<sup>th</sup> order LMS filter. Still, the processing time of the LMS algorithm is faster than the RLS algorithm. For example, a 16<sup>th</sup> order LMS filter requires 32 additions and 33 multiplications, whereas a 4<sup>th</sup> order RLS filter requires 60 additions and 80 multiplications. Hence, the implementation of a LMS algorithm is preferred over a RLS algorithm.

## 9.6. Comparative Study of Different ANC Algorithms

This study was designed to investigate the performance of different ANC algorithms to minimize HR and SpO<sub>2</sub> errors induced by movements. The results revealed that adaptive filtering of motion corrupted PPG signals can effectively reduce motion-induced HR and SpO<sub>2</sub> errors.

HR and SpO<sub>2</sub> measurements estimated from adaptively filtered PPG signals have a lower MSE and SD than unfiltered PPG signals (see Table 8.7). Every adaptive algorithm produced similar improvements in HR and SpO<sub>2</sub> during motion. While implementing an adaptive algorithm in real-time, we have to compromise between the mean percent improvements in measurement accuracy, convergence rate and filter order. For example, the performance of a 4<sup>th</sup> order RLS algorithm is very similar to a 16<sup>th</sup> order LMS filter. Additionally, the RLS algorithm has a faster convergence rate compared to the LMS algorithm which is essential in real-time applications. However, this comes at the expense of a longer computation time since the RLS algorithm requires  $M^2$  ( $M$  is filter order) operations per iterations.

The literature shows that the performance of the TV-LMS [23, 24], NLMS [22, 25], and RLS [22, 26] algorithms is better than a conventional LMS algorithm. For real-time adaptive filtering of PPG signals, Table 8.7 reveals that a conventional LMS algorithm will be the best choice in terms of performance, computation and simplicity. Hence, a conventional LMS algorithm was implemented in the TI-MSP430  $\mu$ C for real-time adaptive filtering.

## 9.7. Accelerometer Axis selection

Selection of an appropriate reference noise is crucial for adaptive filtering of PPG signals. Many research groups have demonstrated the use of tri-axial accelerometer signals as an effective reference noise for pulse oximeters [3, 4, 6, 8]. This study was carried out to determine which axis out of the three should be used as a reference input to the adaptive filter. Although Comtois showed that utilizing the summation signals (X+Y+Z) yield best results in terms of MSE performance, his study was limited to motion artifacts generated from treadmill jogging [4]. This included data collected from head motion along all the three axes, treadmill jogging, outdoor running and staircase climbing. Additionally, we evaluated the performance of a multi-input adaptive filter using motion signals along all three axes simultaneously.

The results in section 8.8 illustrate that the X-axis (vertical) was the most dominant plane of acceleration. This was expected since sensor motion associated with head movement is mainly in the vertical direction. The data indicated that the X-axis motion provided the most significant improvement in HR and SpO<sub>2</sub>. The next major contributor to accuracy improvement was the Z-axis signal, and the Y-axis contributed the least.

Data analysis revealed that the combination X+Y+Z provided the best results in terms of MSE improvement. These results are in agreement with Comtois [4]. The results obtained from the multi-input ANC were not as significant as the combination of X+Y+Z. With multi-input ANC, an improvement of 26% and 13% was observed for HR and SpO<sub>2</sub> values, respectively. Thus, we used the summation of all tri-axial signals as a reference noise input to the ANC algorithm.

However, using the summation of all tri-axial signals for ANC has one disadvantage since the energy and morphology of the reference signal becomes phase dependent. Hence, if two or more signals are out of phase, they will cancel each other. In that case, the adaptive filtering will not be very effective and it could also negatively affect the PPG signals. This is a potential area for future work. In spite of this limitation, it would be advantageous to utilize the summation of the tri-axial ACC signals as a reference noise input for ANC.

## 9.8. Validation of Real-time ANC algorithm

After choosing the adaptive LMS filter for real-time implementation in TI-MSP430  $\mu\text{C}$ , its performance was tested by comparing the results with the Matlab's LMS filter. As the main was to validate the C-code, comparison of HR and  $\text{SpO}_2$  values before and after ANC was not necessary.

The waveforms plotted in Figure 8.76 show that the PPG waveform processed by the  $\mu\text{C}$  and offline matched completely. The 4<sup>th</sup> order LMS filter implemented in real-time successfully attenuated the motion peaks. Processing using the same input signals by Matlab's LMS filter yielded the same results.

## 9.9. ANC processing time

The main focus of this thesis was the real-time implementation of an ANC algorithm for minimizing the effects of motion artifacts. After testing each adaptive algorithm, it was found that the LMS algorithm is the most optimal algorithm for real-time implementation. We also found that a LMS algorithm with  $\mu = 0.01$  would produce the best results in terms of reducing HR and  $\text{SpO}_2$  errors. Moreover, a 16<sup>th</sup> order filter should be implemented for real-time ANC. However, some time constraints restrict implementation of a 16<sup>th</sup> order LMS filter in the current version of the WPO sensor.

Table 8.9 shows the execution time required by the TI-MSP430  $\mu\text{C}$  to estimate HR and  $\text{SpO}_2$ . Accordingly, the LMS algorithm must complete processing within 210msec. As per the processing time chart (Figure 8.77) the projected execution time for a 16<sup>th</sup> order LMS filter is 260msec. This is beyond the available processing time. Hence, an 8<sup>th</sup> order LMS filter was implemented in the current WPO sensor.

## 9.10. Auto-triggering of ANC

Auto-triggering of the ANC algorithm was proposed to avoid unnecessary processing during rest and thus save battery power. The explanation presented in section 8.11 clearly highlights the

simplicity of the proposed algorithm. If the motion signal has high amplitude, it will have high energy and will automatically start the adaptive processing.

The application of this method results in saving 110msecs of processing time for an 8<sup>th</sup> order LMS algorithm. Normally, an 8<sup>th</sup> order LMS algorithm, if processed continuously, consumed 130msec out of the 500msec processing time. With the application of the proposed method, during low head movements, the ANC process consumed only 14msec. This time is required to compute the energy of the motion signal. There was no reduction in the percentage of HR and SpO<sub>2</sub> improvement as the ANC process was initiated when heavy motion was detected. Due to its effectiveness in avoiding unnecessary signal processing, this method was also implemented in the WPO.

### **9.11. Real-time ANC results**

Several groups have suggested the use of ANC based on a noise reference signal obtained from an ACC that is integrated into the sensor to represent body movements [3, 4, 6, 8, 9]. These groups have demonstrated promising feasibility for motion induced artifact rejection. These groups have presented results based on offline processing of PPG data acquired using their custom pulse oximeters. They did not present quantifiable data showing whether ACC-based ANC resulted in more accurate estimation of HR and SpO<sub>2</sub> during real-time applications.

A series of head motion and jogging experiments were performed to compare the benefits of ANC using two WPO sensors placed side-by-side on the forehead. The sensor with ANC estimated HR and SpO<sub>2</sub> values that were more accurate compared to values obtained from the reference sources. Figure 8.79 and Figure 8.80 showed that a traditional non-adaptive signal processing algorithm overestimated HR values when motion artifacts were present.

During the initial phase of the experiments, while the subjects were at rest, HR and SpO<sub>2</sub> values from the two sensors matched closely within  $\pm 2\%$ . These small errors are acceptable as the two sensors were placed side-by-side rather than at the same position. Once the physical activities were completed, the two sensors must report approximately the same HR and SpO<sub>2</sub> values.

However, there was a certain time delay before the values from the two sensors matched. This delay is due to the processing time involved in computing the average HR and SpO<sub>2</sub> values.

To conserve battery life, an auto-triggered algorithm was also implemented inside the  $\mu$ C. Percentage improvements shown in Table 8.11 and Table 8.12 validated the functionality of the algorithms. The percentage improvements varied significantly for each trial as the nature of motion was different in each trial. These results clearly highlight the effectiveness of ANC for real-time pulse oximetry. Data from this study were limited to head movements and treadmill jogging only. Further studies must be conducted to assess potential of the ANC for obtaining more accurate readings during other types of activities. It would be more beneficial to test the WPO on the field during more rigorous training exercises.

### **9.12. Limitation of ANC**

Our results clearly demonstrate the advantages of using ANC in real-time pulse oximetry. However, ANC also has some drawbacks. Wood & Asada [9] and Comtois [4] have shown that spectral overlap between ACC and motion corrupted PPG signals could reduce the effectiveness of the ACC-based ANC. ANC-based filtering implements an adaptive notch filter with a notch frequency corresponding to the motion frequency. Hence, overlap of cardiac and movement-induced motion frequencies attenuates the fundamental cardiac frequency, and also reduces HR and SpO<sub>2</sub> accuracy.

According to Comtois [4], spectral overlap cannot have a significant effect on the accuracy of HR and SpO<sub>2</sub> during motion since there was a low probability that the PPG and acceleration signals overlap during movement. Therefore, there should be no negative effect when ANC is utilized. However, the results presented in this thesis contradict his findings. Our results clearly demonstrate the negative effect of adaptive filtering on HR and SpO<sub>2</sub> measurements when frequency overlap was present. The data also showed that HR values are more prominently affected in trials where body motion and cardiac signals are synchronized.

Methods to overcome this basic limitation must be devised in order to make the system more robust. An algorithm that can determine phase difference between PPG signals reference motion

signals should be investigated. However, such an algorithm will consume more  $\mu\text{C}$  processing time and will further the battery life. More studies must be in future to develop a time-efficient digital phase detector that avoids adaptive filtering in the case of spectral overlap.



## 10. CONCLUSION

Remote physiological monitoring of individuals working in dangerous and high-risk environments may provide a valuable means for saving their life in critical conditions. It would also help medical personnel and first responders to better prioritize medical intervention when the sources are limited.

Pulse oximeters can measure arterial oxygen saturation ( $SpO_2$ ) along with heart rate (HR), heart rate variability (HRV) and respiration rate (RR) noninvasively. However, commercially available pulse oximeters are not reliable in the presence of motion artifacts that are expected in field applications. Hence, a motion tolerant battery-operated wireless pulse oximeter (WPO) has been developed. The main goal of this thesis was to implement an adaptive filtering technique for real-time pulse oximetry to minimize HR and  $SpO_2$  errors during motion. A tri-axial accelerometer (ACC) was integrated into our WPO to capture motion signals that diminished the accuracy of the WPO. The motion signals acquired from the ACC were used to determine body activity and orientation.

To investigate the effects of motion artifacts on Photoplethysmograph (PPG) signals, several experiments were conducted during rest, cycling, treadmill jogging, outdoor running and staircase climbing exercises. These experiments were performed since intense motion artifacts are known to affect the performance of a pulse oximeter.

The results from the cycling experiments proved that the inaccuracies are attributed mainly to sensor movement rather than rapid changes in HR values. First, it was determined that the WPO was able to accurately measure HR and  $SpO_2$  during rest and cycling on a stationary bicycle. During physical activities, motion contributes directly to the degradation of the infrared (IR) and red (R) PPG signals. Hence, HR and  $SpO_2$  errors increase during movements. Generally, sudden drastic drops were observed in  $SpO_2$  readings. We found that HR values were either overestimated or underestimated depending on the extent of motion.

To attenuate the motion induced noise, various ANC algorithms were implemented in Matlab. These included the LMS, TVLMS, NLMS, MNLMS and RLS algorithms. A summation of 3 planar acceleration signals (X+Y+Z) were used as a reference input for the adaptive filters as they provided the best results. This suggests that ANC can be used to extract more accurate readings from the WPO during motion.

For a 16<sup>th</sup> order conventional LMS algorithm with a step-size ( $\mu$ ) of 0.01, HR and SpO<sub>2</sub> values showed a mean percent improvement of 55% and 22%, respectively. Variants of the LMS algorithm also showed similar improvements. A 4<sup>th</sup> order RLS filter with a forgetting factor ( $\lambda$ ) equal to 1 improved the WPO performance similar to a 16<sup>th</sup> order LMS filter. A comparative study was performed to select an appropriate algorithm for real-time implementation. The RLS algorithm has a faster adaptation rate and requires a lower filter order which is essential in real-time applications. However, it comes at the expense of a longer computational time. Thus, the conventional LMS algorithm is more appropriate for real-time adaptive filtering since it requires significantly less operations.

A 16<sup>th</sup> order LMS algorithm with  $\mu = 0.01$  proved to be the best algorithm for recovering clean PPG signals. However, due to processing time constraints in the current hardware version, a lower order LMS filter was implemented inside the TI-MSP430  $\mu$ C. The final algorithm that was developed for minimizing the effects of motion artifacts comprised an 8<sup>th</sup> order LMS filter with  $\mu = 0.01$  along with an auto-triggering algorithm. The auto-triggering algorithm was devised to initiate ANC only when motion signals were above a certain threshold level. This algorithm avoids unnecessary PPG processing during little motion and extends battery life.

Unlike processing time, program memory does not appear to be a limiting factor. The PPG signals required for adaptive filtering are already stored in memory for subsequent calculation of HR and SpO<sub>2</sub>. Additional memory is required to store the motion signals that are used as reference noise signals by the ANC algorithm. Since the sample frequency of our WPO is 80Hz, forty 16-bit digital samples of motion signal must be stored in the RAM of the  $\mu$ C. This requires approximately 160 bytes of RAM. On average, the implementation of the noise cancellation

algorithm will require approximately 500 bytes for storing the vectors used in the calculation process. This memory requirement would not limit the feasibility of implementing this adaptive noise cancellation algorithm since 10KB of RAM is typically available in the TI-MSP430F1611  $\mu$ C.

As a final test, a few data sets were collected with the real-time ANC routine while the subjects performed various head movements and treadmill jogging exercises. HR and SpO<sub>2</sub> values were recorded from two WPOs placed side-by-side on the subject's forehead. With ANC, we found that HR errors were reduced from 12BPM to 6BPM for reading ranging between 60 to 180BPM. Similarly, SpO<sub>2</sub> errors were reduced from 5% to 2% during ambient breathing. These improvements clearly demonstrated that HR and SpO<sub>2</sub> measurements are more reliable from an ANC-based WPO during motion.

Despite these promising results, the effectiveness of the ACC-based adaptive filtering technique is limited to certain activities and depends on the type of motion artifacts. Reduction of noise could be limited during motions that are less repetitive. Moreover, if the motion frequency shifts rapidly over a wide spectral band, the adaptive filter would be less effective due to a slower adaptation rate. ANC might also deteriorate measurement accuracy when cardiac and motion frequencies overlap.

## 11. FUTURE RECOMMENDATIONS

The studies conducted in this thesis evaluated the effectiveness of adaptive filtering during head movement, cycling on a stationary bicycle, treadmill jogging, outdoor running, and staircase climbing. Although these activities represent typical movements that are commonly associated with field operations, additional studies must be conducted to confirm the effectiveness of the ANC algorithms. Specifically, the results presented demonstrated the effectiveness of the ANC algorithm during short periods of movements. It would be useful to determine the feasibility of these algorithms during longer durations.

Furthermore, the results showed that cardiac and movement induced spectral overlap limits the effectiveness of the ANC algorithm. It could be reasonable to develop additional software routines that prevent PPG signal processing in case of frequency overlap. For example, a digital phase detector as shown in Figure 11.1 can be used to determine the phase difference between the PPG and motion signals. If the two signals are in phase or  $180^\circ$  out of phase, adaptive filtering should be avoided.

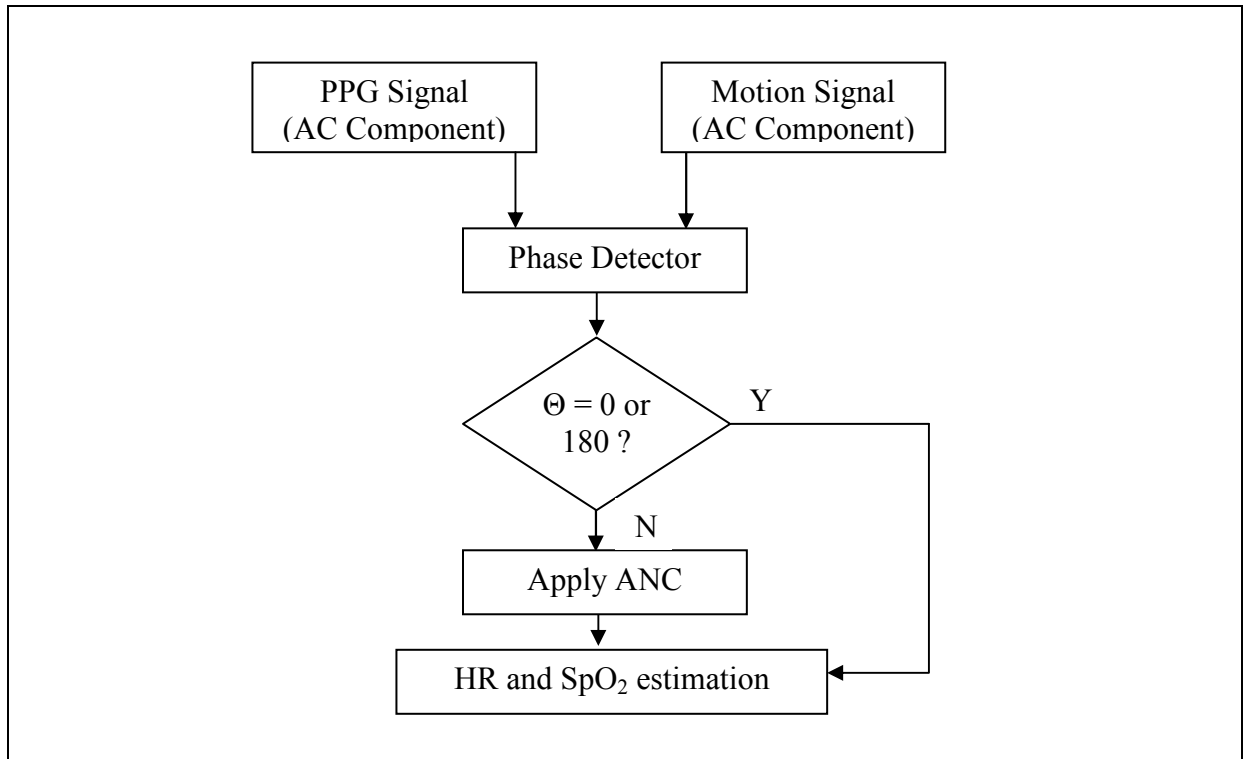


Figure 11.1: Implementation of a phase detector algorithm to bypass ANC during frequency overlap.

Although previous results presented in this thesis suggest that the use of tri-axial acceleration (X+Y+Z) signals are appropriate, there are some limitations in using all three axes as a reference noise signal for adaptive filtering. For instance, our adaptive filtering algorithm will fail if two or more signals are out of phase as they will tend to cancel each other. We also assume that each axis contributes equally towards the distortion of the PPG signal which is not always true. Hence, more effective methods should be developed to determine proper reference signals depending on the type of motion involved.

SpO<sub>2</sub> measurements are computed based on the AC and DC components of the IR and R PPG signals. Although it was shown that ANC algorithms were effective in improving SpO<sub>2</sub> measurements during motion, these improvements were limited to adaptive filtering of the AC components of each PPG signal. No signal processing has been applied to minimize the effects of artifacts on the corresponding DC components. Additional signal processing algorithms could be designed to minimize the effects of motion artifacts on the DC components, as this may lead to further improvements in SpO<sub>2</sub> measurements.

Finally, PPG signals used to estimate HR and SpO<sub>2</sub> can also be used predict respiration rate (RR) and heart rate variability (HRV). This thesis investigated the effects of ANC to improve HR and SpO<sub>2</sub> during motion. Further studies should be conducted to determine the effects of ANC on RR and HRV measurements.

## 12. REFERENCES

- [1] W. S. Johnston, "Development of a Signal Processing Library for Extraction of SpO<sub>2</sub>, HR, HRV, and RR from Photoplethysmographic Waveforms," M.S. Thesis, Department of Biomedical Engineering, Worcester Polytechnic Institute, Worcester, MA, 2006
- [2] R. Zajtcuk and G. R. Sullivan, "Battlefield Trauma Care: Focus on Advanced Technology," *Military Medicine*, Vol. 160, pp. 1-7, 1995
- [3] H. H. Asada, J. Hong-Hui and P. Gibbs, "Active noise cancellation using MEMS accelerometers for motion-tolerant wearable bio-sensors," *Engineering in Medicine and Biology Society*, 2004. IEMBS '04. 26th Annual International Conference of the IEEE, Vol.3, pp 2157-2160, 2004
- [4] G. Comtois, "Adaptive Noise Cancellation Utilizing Accelerometer to Reduce the Effects of Motion Artifact in Wearable Reflectance Mode Pulse Oximetry," M.S. Thesis, Department of Biomedical Engineering, Worcester Polytechnic Institute, Worcester, MA, 2007
- [5] G. Comtois and Y. Mendelson, "A Wearable Wireless Reflectance Pulse Oximeter for Remote Triage Applications," *Bioengineering Conference*, 2006. Proceedings of the IEEE 32nd Annual Northeast, pp 53-54, 2006
- [6] G. Comtois, Y. Mendelson and P. Ramuka, "A Comparative Evaluation of Adaptive Noise Cancellation Algorithms for Minimizing Motion Artifacts in a Forehead-Mounted Wearable Pulse Oximeter," *Engineering in Medicine and Biology Society*, 2007. EMBS 2007. 29th Annual International Conference of the IEEE, pp 1528-1531, 2007
- [7] M. T. Petterson, V. Begnoche and J. M. Graybeal, "The Effect of Motion on Pulse Oximetry and Its Clinical Significance," *International Anesthesia Research Society*, Vol. 105/6, December 2007.
- [8] A. R. Relente and L. G. Sison, "Characterization and adaptive filtering of motion artifacts in pulse oximetry using accelerometers," [Engineering in Medicine and Biology, 2002. 24th Annual Conference and the Annual Fall Meeting of the Biomedical Engineering Society] EMBS/BMES Conference, 2002. Proceedings of the Second Joint, 2, pp 1769-1770 vol.2, 2002
- [9] L. B. Wood and H. H. Asada, "Noise Cancellation Model Validation for Reduced Motion Artifact Wearable PPG Sensors Using MEMS Accelerometers," *Engineering in Medicine and Biology Society*, 2006. EMBS '06. 28th Annual International Conference of the IEEE, pp 3525-3528, 2006
- [10] Y. Mendelson, "Pulse Oximetry: Theory and Applications for Noninvasive Monitoring," *Clinical Chemistry*, Vol. 38/9, pp. 1601-1607, 1992.

- [11] J. F. Kelleher, "Pulse Oximetry," Journal of Clinical Monitoring, Vol. 5/pp. 37-62, 1989.
- [12] Web page, "<http://oximeter.holisticphysio.com/indexE.html>".
- [13] Y. Mendelson and B. D. Ochs, "Noninvasive pulse oximetry utilizing skin reflectance photoplethysmography," Biomedical Engineering, IEEE Transactions on, Vol. 35/10, pp. 798-805, 1988.
- [14] W. S. Johnston, P. C. Branche, C. J. Pujary and Y. Mendelson, "Effects of motion artifacts on helmet-mounted pulse oximeter sensors," Bioengineering Conference, 2004. Proceedings of the IEEE 30th Annual Northeast, pp 214-215, 2004
- [15] A. Nagre and Y. Mendelson, "Effects of motion artifacts on pulse oximeter readings from different facial regions," Bioengineering Conference, 2005. Proceedings of the IEEE 31st Annual Northeast, pp 220-222, 2005
- [16] J. Langton and C. Hanning, "Effect of motion artefact on pulse oximeters: evaluation of four instruments and finger probes," Br J Anaesth, 65:564-70, 1987
- [17] S. Barker and N. Shah, "The effect of motion on the performance of pulse oximeters in volunteers (Revised publication)," Anesthesiology, 86:101-8, 1997
- [18] J. Goldman, M. Petterson, R. Kopotic and S. Barker, "Masimo Signal Extraction Pulse Oximetry," J Clin Monit, 16:475-83, 2000
- [19] B. S. Kim and S. K. Yoo, "Motion artifact reduction in photoplethysmography using independent component analysis," Biomedical Engineering, IEEE Transactions on, Vol. 53/3, pp. 566-568, 2006.
- [20] M. J. Hayes and P. R. Smith, "A new method for pulse oximetry possessing inherent insensitivity to artifact," Biomedical Engineering, IEEE Transactions, Vol. 48/4, pp. 452-461, 2001.
- [21] B. Widrow, J. R. J. Glover, J. M. McCool, J. Kaunitz, C. S. Williams, R. H. Hearn, J. R. Zeidler, E. Dong and R. C. Goodlin, "Adaptive noise cancelling: Principles and applications," Proceedings of the IEEE, Vol. 63/12, pp. 1692-1716, 1975.
- [22] S. S. Haykin., "Adaptive Filter Theory," NJ: Prentice-Hall, 2002.
- [23] Y. S. Lau, Z. M. Hussian and R. Harris, "Performance of Adaptive Filtering Algorithms: A Comparative Study," Australian Telecommunications, Networks and Applications Conference (ATNAC), Melbourne, 2003
- [24] Y. S. Lau, Z. M. Hussian and R. Harris, "A Time-Varying Convergence Parameter for the LMS Algorithm in the presence of White Gaussian Noise," Submitted to the Australian Telecommunications, Networks and Applications Conference (ATNAC), Melbourne, 2003



- [25] D. L. Jones, "Normalized LMS," Connexion Module: m11915, Vol. 2004.
- [26] H. K. Kwan and L. Tao, "Adaptive IIR digital filtering using an analog neural network," Electrical and Computer Engineering, 1999 IEEE Canadian Conference, Vol. 2/pp. 827-830, 1999.
- [27] Masimo, "Radical SET Pulse Oximeter Operator's Manual," 2004.